Imperial College London

Faculty of Engineering

Department of Chemical Engineering

# Framework-based Nanofiltration Membranes for Liquid Separation

By

**Mengjiao Zhai**

Supervisor: Professor Kang Li

A Thesis Submitted for the Degree of Doctor of Philosophy and the Diploma of Imperial College London

April 2025

## Declaration of Originality

I hereby declare that this thesis and the work reported herein were composed by and originated entirely from me. I used ChatGPT-4o, a generative AI tool developed by OpenAI (https://chat.openai.com), for the refinement of language in writing this thesis; the tool was used solely to improve grammar and clarity. Information derived from the published and unpublished work of others has been acknowledged in the text, and the relevant references are included in this thesis.

Mengjiao Zhai

Imperial College London

April 2025

## Copyright Declaration

The copyright of this thesis rests with the author. Unless otherwise indicated, its contents are licensed under a Creative Commons Attribution-Non Commercial 4.0 International Licence (CC BY-NC).

Under this licence, you may copy and redistribute the material in any medium or format. You may also create and distribute modified versions of the work. This is on the condition that: you credit the author and do not use it, or any derivative works, for a commercial purpose.

When reusing or sharing this work, ensure you make the license terms clear to others by naming the license and linking to the licence text. Where a work has been adapted, you should indicate that the work has been changed and describe those changes.

Please seek permission from the copyright holder for uses of this work that are not included in this licence or permitted under UK Copyright Law.

Mengjiao Zhai

Imperial College London

April 2025

## Abstract

Crystalline frameworks, primarily metal organic frameworks (MOFs) and covalent organic frameworks (COFs), have demonstrated great potential in membrane separation. These materials can effectively overcome the inherent limitations of conventional polymeric materials because of their tuneable porous structures and versatile functionalities. However, the controllable fabrication of framework-based membranes remains challenging, compromising their structural integrity, separation performance, and practical applicability in industrial processes. In this thesis, the controllable fabrication of different framework-based membranes for liquid separations is presented.

First, a water-stable MOF-303 membrane with a crystallographic preferred orientation (CPO) is fabricated on alumina hollow fibres (HFs) via a novel dual-source (DS) seeding method. The achieved (110) CPO provides straight permeation channels, ensuring high water permeance in nanofiltration and pervaporation. Additionally, the robust attachment between the substrate and the MOF membrane leads to high structural integrity over the long-term test.

Second, a highly permeable loose nanofiltration (LNF) membrane is fabricated by combining nonsolvent-induced phase separation (NIPS) with the combined crystallization and diffusion (CCD) method. A homogeneous COF-polyethersulfone (PES) solution is prepared by dissolving PES in a single phase-solution containing synthesized DABA-TFP colloids. Dye-salt separation tests reveal a promising selectivity with an exceptional permeance.

Finally, confined growth of a two-dimensional (2D) MOF, CuBDC, within the laminar structure of a porous graphene oxide (PGO) membrane is achieved via a contra diffusion approach. The oxygen-coating groups present on the PGO nanosheets, which are capable of coordinating with metal clusters, are adjusted by decreasing the flake size to control the loading of the MOFs. This controlled coordination significantly enhances the structural robustness of the composite membrane, ensuring the stabilization of the PGO membrane during desalination tests.

Overall, these strategies effectively address key challenges associated with the fabrication and practical application of MOF/COF-based membranes from multiple perspectives, paving the way for their widespread application in advanced liquid separation technologies.

## Acknowledgement

After navigating both expected and unexpected challenges, my doctoral journey is finally nearing its completion. I would like to take this opportunity to sincerely and wholeheartedly thank everyone who has supported and guided me along the way.

First of all, I would like to express my sincere gratitude to my supervisor, Professor Kang Li. As an insightful and responsible supervisor, he not only places great emphasis on cultivating my abilities as an independent researcher, but also spares no effort in providing invaluable guidance, suggestions, and support whenever I encounter significant challenges. Moreover, Professor Li genuinely cares about the mental well-being of his students, and I feel truly grateful and fortunate to have had the opportunity to be part of his research group.

Additionally, I am deeply grateful to my family for their unwavering emotional support and companionship. My acknowledgement goes to Fuling Li, Xinhua Zhai, Bingxin Guo, Yuping Zhai and Yanyun Wang. Their wholehearted love has always been my source of motivation, and their encouragement and trust are the most precious treasures in my life.

I am sincerely grateful to my colleagues and friends, Boyuan Hao, Zouaoui Taqwa, Yuting Wu, Zihao Li, Oloyede Olukayode, Dr. Kornkamol Banjerdteerakul, Dr. Hao Peng, Dr. Jialin Yu, Dr. Farhad Moghadam, Dr. Xiang Li, Dr. Zhiwei Jiang, Dr. Vatsal Shah, and Dr. Tongrong Wu for their invaluable support, encouragement, and companionship. Their kindness, and intelligence have not only enriched my research experience but also profoundly impacted my personal growth. I will always remember the time we spent together.

In addition, I also gratitude to others who has helped me in my research, Gosiamemang, Tsaone, Chaoyue Zhang, Jingdong Xu, Zhipeng Lin, Shitong Zhou, Dr. Kaho Cheung, Dr. Carry Patricia and Dr. Liana Zoumpouli.

Finally, I am grateful for this PhD journey and all its joys and sorrows, which would be precious experience in my life. May I always remain gentle, kind, and true, never letting go of love and dreams throughout my life.

## Table of Content

**Declaration of Originality** ..... **1**

**Copyright Declaration** ..... **2**

**Abstract** ..... **3**

**Acknowledgement** ..... **4**

**List of Figures** ..... **8**

**List of Tables** ..... **11**

**List of Equations** ..... **13**

**Chapter 1: Introduction** ..... **14**

1.1 Background ..... 14

1.2 Thesis Objectives ..... 15

1.3 Thesis structure and presentation ..... 17

References ..... 18

**Chapter 2: Literature Review** ..... **19**

2.1 Reticular Chemistry ..... 19

2.2 Metal Organic Frameworks ..... 20

2.3 Covalent Organic Frameworks ..... 26

2.4 Continuous Frameworks Membranes ..... 31

2.5 Discontinuous Framework Membranes ..... 58

2.6 Conclusion ..... 77

References ..... 79

**Chapter 3: Experimental** ..... **101**

3.1 Materials ..... 101

3.2 Preparation of The Alumina-based Substrate ..... 101

3.3 Framework-based Membranes Preparation ..... 102

3.4 Characterizations and Performance tests..... 106

References ..... 112

**Chapter 4: Facile Fabrication of MOF-303 Hollow Fibre Membranes with Controlled Orientation for Nanofiltration ..... 114**

4.1 Abstract..... 114

4.2 Introduction ..... 115

4.3 Material and Methods ..... 116

4.4 Results and Discussion ..... 117

4.5 Conclusion ..... 137

References ..... 138

**Chapter 5: Loose Nanofiltration PES/DABA-TFP Membrane Fabricated by NIPS-CCD Method with Ultrapermeable Selectivity for Dye/Salt Separation ..... 143**

5.1 Abstract..... 143

5.2 Introduction ..... 144

5.3 Material and Methods ..... 146

5.4 Results and Discussion ..... 149

5.5 Conclusion ..... 166

References ..... 166

**Chapter 6: Confined Growth of 2D MOF Nanosheets within Porous Graphene Oxide Membranes for Long-term Stable Desalination ..... 172**

6.1 Abstract..... 172

6.2 Introduction ..... 173

6.3 Material and Methods ..... 176

6.4 Results and Discussion ..... 178

6.5 Conclusion ..... 199

References ..... 199

**Chapter 7: Conclusion and Future Plan ..... 206**

7.1 Conclusion ..... 206

7.2 Future Plan ..... 207

References ..... 208

**List of Publication ..... 210**

Journal Publications ..... 210

Conference Presentation ..... 210

**Permissions for the Reproduction of Copyright Materials ..... 211**

## List of Figures

Figure 2.1 Schematic illustration of MOF formation. 20

Figure 2.2 MOFs formed with various metal nods and organic linkers 21

Figure 2.3 MOFs with different pore sizes constructed with linkers of different lengths 22

Figure 2.4 Different binding modes of R-COO- to metal centers. 24

Figure 2.5 (a) Basic topological diagrams for the 2D design. (b) Polygon geometric transformation of stretching and multiple-component COFs with asymmetric structure 27

Figure 2.6 Secondary growth method 33

Figure 2.7 Schematic illustration of LBL fabrication 34

Figure 2.8 Interfacial synthesis of MOF membranes 35

Figure 2.9 Fabrication of ultrathin ZIF-8 HF membrane on HF via the GVD method 36

Figure 2.10 Crystalline structure of the MOFs 38

Figure 2.11 Oriented growth of MOF membrane by seeding regulation 40

Figure 2.12 Fabrication of a continuous COF membrane 50

Figure 2.13 Different methods for preparing mixed suspensions 60

Figure 2.14 Fabrication of the framework-GO composite membrane 68

Figure 3.1 Sintering program for alumina HF 102

Figure 4.1 Schematic illustration of MOF-303 membranes synthesized by a DS method 117

Figure 4.2 Schematic illustration of MOF-303 membranes synthesized by RS and in-situ growth methods. 119

Figure 4.3 SEM images of MOF-303 membranes fabricated by DS method 119

Figure 4.4 XRD patterns and sketchy view of the cross-section of membrane fabricated by DS method 121

Figure 4.5 SEM images and XRD patterns of MOF-303 membranes fabricated by RS method 122

Figure 4.6 SEM images and XRD patterns of MOF-303 membranes fabricated by conventional one-

step method ..... 123
Figure 4.7 XRD patterns and BET analysis of MOF-303 ..... 124
Figure 4.8 The schematic illustration of MOF-303 membranes synthesized by the liquid contact and the secondary growth of vacuum-coated seeding layer method ..... 125
Figure 4.9 Pervaporative water/alcohol separation of the MOF-303 membranes ..... 128
Figure 4.10 Water/ethanol contact behaviour of MOF-303 membranes ..... 128
Figure 4.11 Schematic illustration of the transport of water/ethanol and water/1-butanol mixture in MOF-303 membrane. ..... 129
Figure 4.12 Dye nanofiltration performance of MOF-303 membranes ..... 130
Figure 4.13 Stability of MOF-303 membranes fabricated by one-step RS and DS methods in nanofiltration. ..... 132
Figure 4.14 Samples fabricated with increased scale. ..... 133
Figure 5.1 Preparation strategies of PES in-situ COF and COF blend COF casting solutions. ..... 147
Figure 5.2 Schematic illustration of membrane casting with NIPS and NIPS-CCD method. ..... 148
Figure 5.3 Schematic illustration of NIPS-CCD Eva THF method using PES in-situ COF solution. 148
Figure 5.4 SEM images and SEM-EDX results of PES in-situ COF membranes ..... 150
Figure 5.5 Morphology of membrane surfaces and flake size distribution of DABA-TFP nanosheets ..... 152
Figure 5.6 SEM-EDX images of the NIPS-CCD Eva membrane with the elemental map of C, O, S, and N. ..... 153
Figure 5.7 Surface roughness of membranes ..... 154
Figure 5.8 Surface chemistry and wettability of the membranes ..... 154
Figure 5.9 Zeta potential and pore size analyses of the membranes ..... 156
Figure 5.10 Pure water permeance of membranes ..... 158
Figure 5.11 Antifouling and dye/salt separation performance of membranes ..... 161

Figure 5.12 Mechanical performance of membranes ..... 164
Figure 6.1 Schematic illustration of the membrane fabrication process ..... 175
Figure 6.2 Illustration of the pervaporation setup ..... 177
Figure 6.3 Illustration of water carrier pervaporation ..... 178
Figure 6.4 Morphology of the PGO membranes ..... 180
Figure 6.5 Morphology of the membranes and the flake size of the bPGO nanosheet ..... 182
Figure 6.6 Surface and cross-sectional EDX mapping analysis ..... 183
Figure 6.7 Inner microstructure of the CuBDC@sPGO40s membrane ..... 184
Figure 6.8 Full-rang XPS spectra of the membrane ..... 185
Figure 6.9 High-resolution XPS and Raman spectra ..... 186
Figure 6.10 XRD and FTIR patterns of the membrane ..... 187
Figure 6.11 Surface roughness of the membranes ..... 189
Figure 6.12 Water contact angles of the membranes. ..... 190
Figure 6.13 Thermal properties of the membranes ..... 190
Figure 6.14 Desalination performance of the membranes tested by RO. ..... 192
Figure 6.15 Pervaporation performance of membranes ..... 193
Figure 6.16 Desalination performance of the water carrier pervaporation system. ..... 195
Figure 6.17 Desalination performance of the membranes tested for an extended duration ..... 197
Figure 6.18 Stability test of the CuBDC@sPGO40s composite membrane operated in water carrier pervaporation mode. ..... 198

## List of Tables

Table 2.1 Summary of MOFs with high stability ..... 41

Table 2.2 Continuous MOF membrane for liquid separation ..... 46

Table 2.3 Summary of continuous COF membranes in liquid separation ..... 54

Table 2.4 COF/MOF based MMMs in liquid separation ..... 64

Table 2.5 Composite membranes constructed from MOF/COF with 2D materials for liquid separation ..... 72

Table 3.1 Composition of the ceramic suspension ..... 101

Table 3.2 Surface energy components of liquid probes ..... 110

Table 3.3 Dyes used in Chapter 5 ..... 112

Table 4.1 Comparison of nanofiltration performance of state-of-the-art MOFs-based membranes ..... 134

Table 5.1. The composition of casting solutions. ..... 147

Table 5.2 Manufacturing conditions for as-prepared membranes. ..... 149

Table 5.3 Static contact angle data of three liquid probes of different membranes fabricated by NIPS-CCD Eva method ..... 155

Table 5.4 Surface energy components of different membranes fabricated by NIPS-CCD Eva method. ..... 156

Table 5.5 Comparison with the performance of commercially available LNF membranes ..... 161

Table 5.6 Summary of previously reported LNF/TUF membranes ..... 162

Table 5.7 Mechanical strength of membranes ..... 165

Table 6.1 Comparison of membrane thickness before and after the growth of CuBDC ..... 180

Table 6.2 Atomic percentages of C, O, and Cu elements in the fabricated membranes. ..... 185

Table 6.3 Parameters used for calculating the thermal conductivity of the fabricated membranes ..... 191

Table 6.4 Comparison of state-of-the-art desalination membranes via PV ..... 193

Table 6.5 Comparison of WCPV membranes with state-of-the-art desalination membranes via direct contact membrane distillation ..... 195

## List of Equations

Equation (3-1) ..... 108

Equation (3-2) ..... 108

Equation (3-3) ..... 108

Equation (3-4) ..... 109

Equation (3-5) ..... 109

Equation (3-6) ..... 109

Equation (3-7) ..... 109

Equation (3-8) ..... 110

Equation (3-9) ..... 110

Equation (3-10) ..... 110

Equation (3-11) ..... 111

Equation (3-12) ..... 111

Equation (3-13) ..... 111

Equation (3-14) ..... 111

Equation (3-15) ..... 111

# Chapter 1: Introduction

## 1.1 Background

Membrane-based separation traces its origins to the mid-18th century when Abbé Jean Antoine Nollet observed the spontaneous diffusion of water into alcohol-filled pigskin bladders. In 1854, Sir Thomas Graham described the concept of dialysis, demonstrating the selective diffusion of solutes through a vegetable parchment membrane [1]. Inspired by these natural materials, the first synthetic membrane was developed in 1944 to mimic biological processes; however, it lacked practicality due to its low flux and poor selectivity [2]. A breakthrough came in 1962 when Loeb and Sourirajan introduced the phase inversion method to fabricate reverse osmosis (RO) membranes [3]. This process produces asymmetric membranes with a thin and dense separation layer integrated on porous support for mechanical strength, leading to the widespread commercial success since 1970s for polymer membranes in applications such as microfiltration, ultrafiltration, reverse osmosis, gas separation, dialysis, nanofiltration (NF), and pervaporation (PV). [4-7] for their affordability and processability.

However, several challenges remain in the application of polymeric membranes in fluid separation. First, their separation performance is constrained by the Robeson upper bound, which highlights the inherent trade-off between permeability and selectivity [8]. Second, issues such as concentration polarization and severe fouling further diminish their effectiveness in liquid separation. Additionally, the poor stability of polymeric materials under harsh chemical conditions and high temperatures constrains their practical applications. As a result, novel materials are urgently needed to produce high-performance membranes.

As promising candidates, crystalline frameworks, including metal organic frameworks (MOFs) and covalent organic frameworks (COFs), offer remarkable potential. These crystalline materials are synthesized via reticular chemistry under mild conditions, ensuring the preservation of their structural integrity and reactivity through robust bonding [9]. Their highly porous architectures and customizable chemistries of these materials further underscore their suitability for constructing high-performance membranes in advanced fluid separation applications.

Framework-based membranes can function either as discontinuous materials in composite membranes or as continuous membranes. Continuous framework membranes, in particular, offer high permeance owing to their exceptional porosity and precise molecular sieving capabilities, enabled by their uniform and designable pore sizes. Additionally, their versatile chemistry allows tailoring for specific separation needs [10, 11]. While various strategies have been developed to fabricate defect-free membranes with promising selectivity, challenges remain. The limited availability of chemically stable frameworks and the lack of controllable fabrication methods hinder the progress of continuous framework membranes

in liquid separation. Current membranes often suffer from poor integrity, insufficient long-term stability, and compromised permeance and selectivity due to random crystal growth.

Composite membranes incorporating frameworks in polymeric matrices have shown significant potential for commercialization by combining the structural flexibility of polymers with the functionality of embedded frameworks. However, the agglomeration of nanofillers poses a major challenge. The limited affinity between frameworks and other components, along with their poor suspensibility in precursors, often results in heterogeneous mixtures. This can lead to surface defects, pore blockage, and membrane cracking, ultimately reducing separation efficiency and causing variability between samples.

The integration of frameworks with advanced two-dimensional materials offers a promising approach for developing ultrathin membranes with well-regulated mass transport channels. Achieving high stability in these composite membranes requires an in-depth understanding of the coordination potential between the components. Furthermore, controllable synthesis processes are essential to ensure the precise regulation of mass transport channels.

## 1.2 Thesis Objectives

With a comprehensive understanding of the current limitations in the design and fabrication of framework-based membranes for liquid separation, this thesis focuses on (1) fabrication of a MOF-303 membrane through a novel dual-source seeding (DS) method for recovery of low-molecular-weight organic pollutants, (2) preparation of a COF-incorporated loose nanofiltration (LNF) membrane for ultrafast dye/salt fractionation, allowing for the secondary treatment or recovery of individual components and (3) development of a well-regulated two-dimensional (2D) membrane by a confined growth of a 2D MOF within the interlayers of a graphene oxide (GO) membrane for seawater desalination.

The specific objectives are summarized below:

### 1.2.1 Facile fabrication of MOF-303 hollow fibre membranes with controlled orientation for nanofiltration

To increase the performance of pure crystalline framework membranes for nanofiltration applications, improvements are needed in several key areas: (a) minimizing the number of intercrystalline defects, (b) enhancing the interfacial compatibility between the organic framework layer and the substrate, and (c) controlling the orientation of the permeation channels. In this study, a dual-source (DS) method is proposed to fabricate MOF-303 [Al(OH)(PZDC), PZDC = 1H-pyrazole-3,5-dicarboxylate] membranes on an alumina hollow fibre substrate. The alumina substrate serves as a metal source, reacting with

organic linkers to generate seeds, which are expected to strengthen interfacial interactions between MOF crystals and the substrate. A secondary metal source from the synthesis solution enables precise adjustment of the seed density. Secondary crystal growth with a controlled orientation aims to eliminate intercrystalline defects caused by random nucleation during the seeding process. The crystal growth and preferred orientation of the MOF-303 membranes are systematically studied using X-ray diffraction (XRD) and scanning electron microscopy (SEM), with detailed insights provided into the underlying formation mechanisms.

### 1.2.2 Loose nanofiltration PES/DABA-TFP membrane fabricated by NIPS-CCD method with ultrapermeable selectivity for dye/salt separation

This study aims to develop an effective strategy to incorporate framework nanosheets into a polymeric matrix. This approach addresses three key challenges commonly encountered in LNF membrane fabrication: (a) the formation of non-uniform membranes due to the inhomogeneous distribution of nanofillers, (b) the reduced water flux observed in most reported LNF membranes, and (c) the intrinsic fouling susceptibility of polymeric matrices. Specifically, a negatively charged COF, DABA-TFP, is integrated using an innovative approach in which polyethersulfone (PES) pellets are dissolved directly in a single solution COF precursor, mitigating COF aggregation commonly encountered in conventional physical blending. The negative charge of the COF is expected to enhance the Donnan effect, improving the membrane's repulsion of negatively charged pollutants. The membrane is fabricated using a novel method combining nonsolvent-induced phase separation (NIPS) and combined crystallization and phase inversion (CCD). This technique aims to achieve high molecular sieving capability through a dense skin layer while ensuring excellent permeance via highly interconnected pores in the support layer. The structure and physicochemical properties of the resulting membrane are systematically characterized, followed by comprehensive evaluations of its dye/salt separation performance.

### 1.2.3 Confined growth of 2D MOF nanosheets within porous graphene oxide membranes for long-term stable desalination

This study explores the precise construction of crystalline frameworks within advanced 2D materials to fully leverage the advantages of both components. Specifically, a well-structured 2D composite membrane is developed through the confined growth of 2D MOF nanosheets within the laminar architecture of porous graphene oxide (PGO) membranes. This approach aims to achieve a highly regulated membrane structure with enhanced stability and optimized performance for desalination applications. The in-situ growth of a water-stable MOF, CuBDC (copper 1,4-benzene dicarboxylate) in a vacuum-coated PGO hollow fibre membrane to patch the defects and to stabilise the interlayers of the PGO is achieved using a contra-diffusion technique. Coordination interactions are expected to occur between the oxygen-containing functional groups of the PGO nanosheets and the metal cluster of the

MOF. The confined growth of MOF nanosheets is achieved by carefully designing reactive sites, spatial constraints and controlling the diffusion of precursors. MOF loading can be adjusted by controlling the density of reactive sites on PGO via decreasing the PGO flake size by using a tip sonication technique. The resulting laminar structure of the composite membrane with well-defined microchannels as well as its superhydrophilic nature is expected to exhibit ultrahigh capillary pressure for aqueous solutions, enhancing mass transfer during the pervaporation process. Comprehensive characterizations are conducted to monitor the changes in the physicochemical properties of the membrane at various fabrication stages. The desalination performance of the resulting membrane is systematically evaluated.

## 1.3 Thesis structure and presentation

This thesis will be presented in 7 chapters:

***Chapter 1***

Comprehensive exposition of the research context and delineates the primary objectives, establishing the foundation for the work presented in this thesis.

***Chapter 2***

This chapter presents an in-depth review of organic framework-based separation membranes, encompassing their fundamental properties, including composition, synthesis principles, structural characteristics and chemical attributes. It further explores membrane fabrication techniques, practical applications, and the prevailing challenges in this field, concluding with a summary of key insights.

***Chapter 3***

The materials utilized throughout this study, along with an in-depth description of the characterization techniques and experimental protocols employed in the research, are detailed.

***Chapter 4***

Detailed analysis and discussion of the results obtained in the facile fabrication of MOF-303 hollow fibre membranes with controlled orientation for nanofiltration (1.2.1).

***Chapter 5***

Detailed analysis and discussion of the results of the loose nanofiltration PES/DABA-TFP membrane fabricated by NIPS-CCD method with ultrapermeable selectivity for dye/salt separation (1.2.2).

***Chapter 6***

Confined growth of 2D MOF nanosheets within porous graphene oxide membranes for long-term stable desalination (1.2.3).

***Chapter 7***

Conclusion and future plan.

## References

[1] T. Graham, On the absorption and dialytic separation of gases by colloid septa Part I.--Action of a septum of caoutchouc, Journal of Membrane Science 1(100) (1995) 27-31.
[2] W. Kolff, H. Berk, The artificial kidneys : a dialyser with a great area, Acta Medica Scandinavica 117 (1944) 121–134.
[3] S. Loeb, S. Sourirajan, High-flow semipermeable membranes for separation of water from saline solutions, Adv Chem Ser 38(1) (1962) 117-132.
[4] S. Loeb, S. Sourirajan, Sea Water Demineralization by Means of an Osmotic Membrane, Saline Water Conversion—II, AMERICAN CHEMICAL SOCIETY1963, pp. 117-132. https://doi.org/doi:10.1021/ba-1963-0038.ch009
10.1021/ba-1963-0038.ch009.
[5] H. Nassrullah, S.F. Anis, R. Hashaikeh, N. Hilal, Energy for desalination: A state-of-the-art review, Desalination 491 (2020) 114569. https://doi.org/https://doi.org/10.1016/j.desal.2020.114569.
[6] H. Zhou, X. Li, Y. Li, R. Dai, Z. Wang, Tuning of nanofiltration membrane by multifunctionalized nanovesicles to enable an ultrahigh dye/salt separation at high salinity, Journal of Membrane Science 644 (2022) 120094. https://doi.org/https://doi.org/10.1016/j.memsci.2021.120094.
[7] R. Xu, J. Wang, D. Chen, T. Liu, Z. Zheng, F. Yang, J. Chen, J. Kang, Y. Cao, M. Xiang, Preparation and performance of a charge-mosaic nanofiltration membrane with novel salt concentration sensitivity for the separation of salts and dyes, Journal of Membrane Science 595 (2020) 117472. https://doi.org/https://doi.org/10.1016/j.memsci.2019.117472.
[8] L.M. Robeson, Correlation of separation factor versus permeability for polymeric membranes, Journal of membrane science 62(2) (1991) 165-185.
[9] S. Wuttke, Introduction to Reticular Chemistry. Metal–Organic Frameworks and Covalent Organic Frameworks Von Omar M. Yaghi, Markus J. Kalmutzki und Christian S. Diercks, Angewandte Chemie 131(40) (2019).
[10] D.W. Burke, Z. Jiang, A.G. Livingston, W.R. Dichtel, 2D Covalent Organic Framework Membranes for Liquid-Phase Molecular Separations: State of the Field, Common Pitfalls, and Future Opportunities, Advanced Materials 36(1) (2024) 2300525. https://doi.org/https://doi.org/10.1002/adma.202300525.
[11] M.S. Denny, J.C. Moreton, L. Benz, S.M. Cohen, Metal–organic frameworks for membrane-based separations, Nature Reviews Materials 1(12) (2016) 16078. https://doi.org/10.1038/natrevmats.2016.78.

# Chapter 2: Literature Review

## 2.1 Reticular Chemistry

The synthesis of crystalline frameworks with porous structures, despite being highly desirable, remained unattainable three decades ago due to the lack of integration between organic and inorganic synthetic methodologies [1]. During that era, only discrete molecules or one-dimensional polymeric structures could be synthesized. Additionally, the precise synthesis of inorganic compounds, particularly metal complexes, was even more challenging and unpredictable owing to the variable coordination possibilities that metal ions could adopt, often leading to uncertain synthetic outcomes. These challenges remained till the concept of reticular chemistry was elaborated.

Reticular chemistry emerged from the concept of designing molecules with precise geometries and tailored atomic arrangements by systematically controlling the dimensions of building units. This approach enables the creation of crystalline, porous, and extended solid structures through a rational and structured methodology [2]. This breakthrough was first achieved by linking charged carboxylate linkers with metal centers in the synthesis of MOF-2 and MOF-5 [3, 4]. In these frameworks, zinc pyramids derived from zinc (II) ions serve as the secondary building units, facilitating crystallization. Moreover, the robust organic linkers promoted structural openness and endowed the frameworks with high porosity [5]. Unlike earlier metal complexes, MOFs feature both organic and inorganic components interconnected by robust (charged metal-carboxylate in this case) and directional (guided by designed interactions) bonds. This advancement marked a significant breakthrough in this field, leading to the development of permanently porous crystals characterized with exceptional surface areas and structural stability. Moreover, the ability to tailor the structure of secondary building units (SBUs) from a given metal source by modifying synthesis conditions allows for diverse coordination modes, even when same organic linker is used. This versatility is further enhanced by the extensive range of inorganic clusters that can be paired with compatible organic linkers. As a result, these frameworks have become the most adaptable class of extended crystalline materials, with over 120,000 unique structures reported in the Cambridge Structural Database (CSD) [6].

Inspired by the advancements in MOFs, researchers have expanded the principle of reticular chemistry to COFs through the covalent linkage of organic building units. The first breakthrough in COF synthesis was achieved with COF-1 in 2005, which was produced using a self-condensation technique inspired by the formation of $Br_3O_3$ rings via boronic acids. This marked the first successful demonstration of a crystalline extended structure, overcoming the limitations of conventional organic chemistry [7]. Benefiting from the foundational principles of reticular chemistry, COFs are characterized by permanent porosity and exceptional structural stability. Since then, the number of COFs reported in the

literature has increased, with thousands now documented in less than two decades [8].

The rapid development of MOFs and COFs highlights their great capacity for customization with tailored properties. A systematic and deeper understanding of MOFs and COFs on their building units and synthetic chemistry is essential to fully harness their potential in membrane separation.

## 2.2 Metal Organic Frameworks

An intriguing feature of MOFs is its designable structures and chemistry. To develop a desirable MOF, careful selection of SBUs and organic ligands as well as delicate design the number of coordination points are crucial. This chapter explores the structural diversity of MOFs, emphasizing the fundamental building units that significantly influence their properties. Additionally, it delves into the synthesis principles, highlighting the pre-designing and monitoring in achieving MOFs with desirable structures.

### 2.2.1 Topology of the MOFs

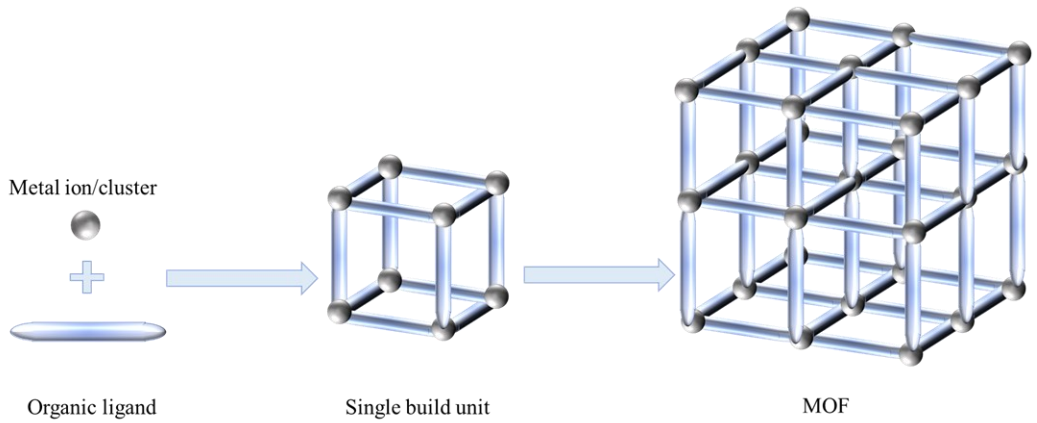



Figure 2.1 Schematic illustration of MOF formation.

MOFs are constructed through the periodic coordination of metal clusters and organic linkers (Figure 2.1). The geometry of a single build unit is collaboratively governed by the coordination preferences of the metal clusters, their spatial arrangement, and the characteristics of the organic linkers. This leads to diverse structural motifs, including triangular units with three connecting points, square paddlewheel shapes with four points, trigonal prisms units, octahedrons units with six points (Figure 2.2). These structural variants of fundamental geometric units underlie the topology and represent only the shape and connectivity of these units rather than chemical information. The underlying topological structure of MOFs is classified by their networks assigned with lowercase bold three-letter symbols, such as **dia**, **qtz**, **soc**, **pts**, and **tht**. These topology codes are often derived from the names of natural minerals that share similar topological features (e.g., **dia** is inspired by diamond, and **qtz** is derived from quartz) [2]. The comprehensive details of these topological nets, which encapsulate the geometric characteristics of

crystal structures, are catalogued in the Reticular Chemistry Structure Resource (RCSR). It includes over 3,000 entries and has been considered as an invaluable resource for designing MOF networks with tailored geometries and pore distributions [9]. The construction of these diverse topologies is predominantly governed by the coordination number and physicochemical properties of the building blocks.

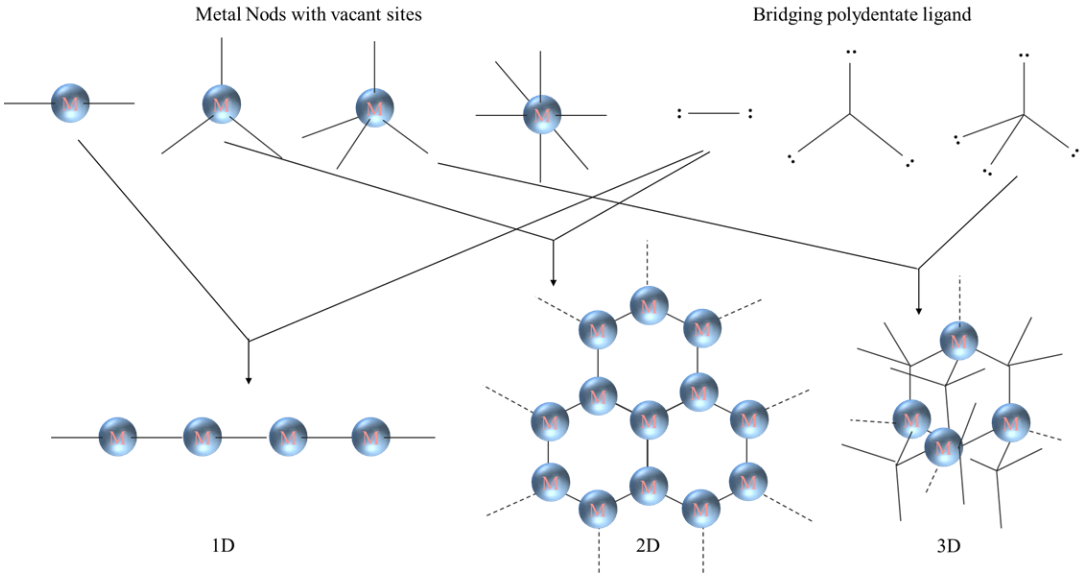



Figure 2.2 MOFs formed with various metal nods and organic linkers, adapted from [10].

### 2.2.2 Building units of MOFs

MOFs are composed of metal ions or clusters and organic linkers, often referred to the "joints" and "struts" of the MOF structure, respectively. These components define MOF's framework and physicochemical properties [11].

#### 2.2.2.1 Organic linkers

Organic linkers are composed of three fundamental components: the "core unit," the "binding groups," and the "extension units." The core unit defines the overall geometry of the linker backbone. "Binding groups" are functional moieties that play a pivotal role in anchoring the linker to SBUs. These functional groups include carboxylates, phosphates, imidazolates, catecholates, and pyrazolates [12]. These groups significantly influence the assembly and stability of MOF structures by facilitating robust coordination with SBUs. The "extension units" within MOFs can be broadly divided into three main categories: (i) linear units that increase connectivity, (ii) angled or offset units that alter symmetry while maintaining connectivity, and (iii) branched units that modify both the geometric structure and connectivity of the framework. The number of extension points plays an important role in determining the framework's connectivity. Accordingly, organic linkers are commonly classified based on their connectivity into

two-point, three-point, four-point, six-point, eight-point, and twelve-point categories.

The variation in ligand length significantly influences the final pore size and porosity of the synthesized MOFs. Longer ligands yield MOFs with larger pores and increased porosity, indicating applications in molecular sieving, gas storage, and catalysis. Conversely, shorter ligands result in more compact frameworks with smaller pore dimensions, which are advantageous for applications requiring selective adsorption or separation. Indeed, adjustment of the MOFs microstructure has been achieved by tailoring the ligand length. For example, substituting the benzene dicarboxylic acid (BDC) linker with other ditopic carboxylate linkers leads to the progressive increase in the periodic aperture size from 12 to 23.6 angstroms (Figure 2.3 a) [12, 13]. Inspired by this, the lattice dimensions and pore sizes of mixed-linker MOFs can be continuously tuned to produce MOFs with hierarchical pore structures (Figure 2.3 b) [14].

Modifying the dimensionality of linkers significantly influences the pore structures of MOFs. Three-dimensional rigid linkers surpass their two-dimensional counterparts in enhancing structural robustness and achieving precise control over pore sizes. This is particularly advantageous in applications where maintaining consistent pore dimensions is critical [15].

In addition to tuning the geometry, tuning and optimizing MOF chemistry can also be achieved by functionalizing organic linkers with functional groups. Organic functional groups, including carbonyl-based groups, nitrogen-based groups, oxygen-based groups, sulfur-based groups, phosphonate groups, and fluorine groups, have been utilized to tailor the chemistry of MOFs to obtain specific chemical properties [16].

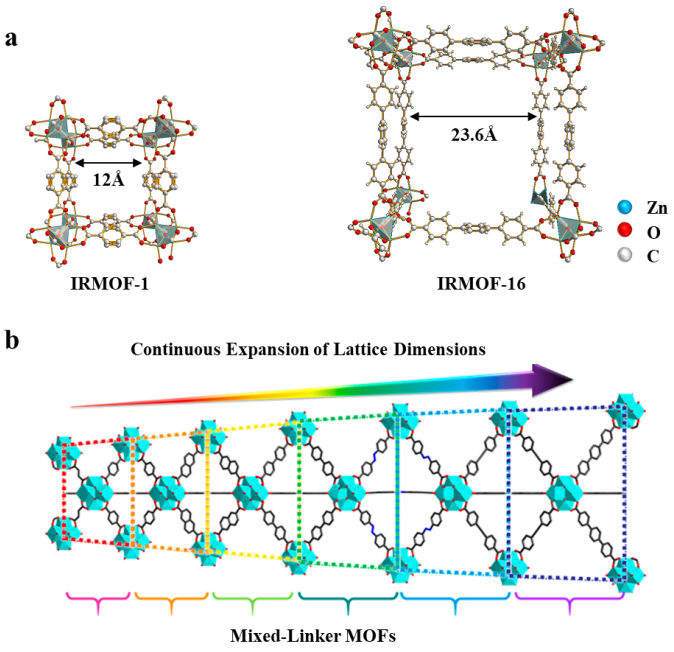



Figure 2.3 MOFs with different pore sizes constructed with linkers of different lengths. (a) Molecular

structures of IRMOF-1 and IRMOF-16. (b) Continuous variation in the lattice metric in MOFs fabricated by mixed-linkers, adapted from [14], Copyright © 2020, American Chemical Society.

#### 2.2.2.2 Metal cluster

The "joint units" refer to either individual metal ions or metal clusters, the latter often designated SBUs. These SBUs consist of clusters of metal ions interconnected via non-metallic bonds, such as oxo (M–O–M) or carboxylate (M–O–C–O–M) linkages, which contribute to the formation of three-dimensional periodic networks [17]. The development of innovative SBUs is critical for advancing MOF topology. Compared with single metal nodes, SBUs offer greater connectivity and more diverse geometries, which are crucial for expanding the range of framework structures.

A variety of metals and metalloids, including copper, zinc, cobalt, iron, aluminum, zirconium, titanium and samarium. have been integrated into MOF structures, with many incorporated into SBUs. Like organic linkers, SBUs exhibit varying connectivity, ranging from three- to twenty-two-point configurations [18]. The most highly connected SBU reported to date is a manganese-based structure, featuring a ring of 84 manganese atoms interconnected via edge- and corner-sharing octahedra, linked by 72 oxygen atoms and capped by 66 carboxylates [19]. Compared with ligand engineering, SBU modifications are less extensively explored and typically focus on four main strategies: (1) substituting the cations in the metal nodes, (2) altering the valence state of the cations, (3) introducing structural vacancies, and (4) incorporating additional species into the framework [20].

### 2.2.3 Metal-linker binding

Understanding the coordination principle between the metal cluster and linkers is vital to achieve rational design and controllable synthesis of MOFs. Taking carboxylate-based MOFs as example, carboxylate groups can interact with metal centers through various bonding modes (Figure 2.4), coordinating the formations in ionic (e.g., in sodium format), unidentate (e.g., in lithium acetate), chelating (e.g., indium acetate), or bridging (e.g., copper acetate) modes. The nature of the R–COO–M bond spans a spectrum from purely ionic to partially covalent. Chelating and bridging modes are particularly important, as they facilitate the formation of polynuclear clusters. However, the preferred binding mode for each metal ion is highly dependent on its specific properties and oxidation state [21]. We will thoroughly examine three distinct synthetic paradigms for metals bearing two, three, or four positive charges as they coordinate with typical carboxylate linkers here.

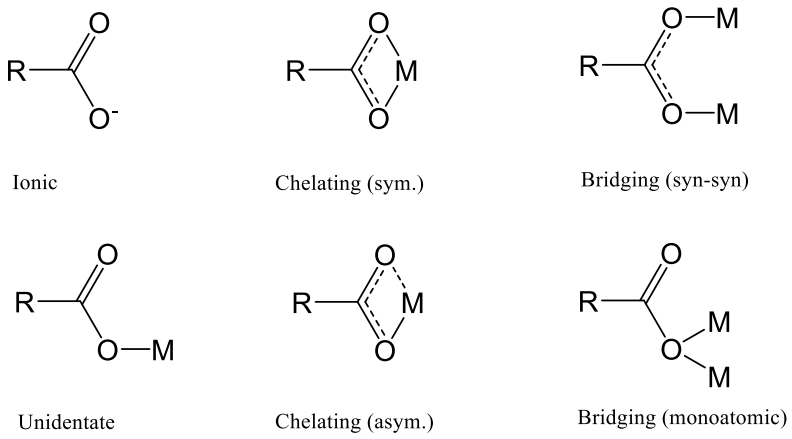



Figure 2.4 Different binding modes of R-COO- to metal centers.

For divalent metals, bonding occurs in three common hydration states: monodentate bridging, syn–syn bridging, and anti-syn bridging. A lower ionization energy in the metal reduces the covalent nature of the metal–carboxylate bond, enhancing its reversibility. This increased flexibility allows easier adjustment of the reaction conditions, thereby facilitating the formation of highly crystalline materials.

The solution chemistries of the trivalent metals, Al(III), Ga(III) and In(III) differ significantly, as aluminum and gallium hydroxides are amphoteric, whereas indium hydroxide is basic [22]. Consequently, the synthesis conditions for MOFs built from these metals vary widely. Aluminum hydrolysis in aqueous solutions results in the formation of condensed clusters such as polyoxoaluminates $[(AlO_4)_{12}[Al_{12}(OH)_{24}(H_2O)_{12}]^{7+}$ and $[Al_2O_8Al_{28}(OH)_{56}(H_2O)_{26}]^{18+}$ [23]. In contrast, gallium and indium predominantly form smaller clusters or isolated hexaquo-complexes [24, 25]. Increasing the ionic radius from $Al^{3+}$ (0.675 Å) to $Ga^{3+}$ (0.760 Å) and $In^{3+}$ (0.940 Å) reduces the surface charge, significantly increasing the ligand exchange rates from aluminum to indium by up to sixfold [26, 27]. This greater lability facilitates the growth of larger indium MOF crystals than Al- or Ga-MOFs do. The M–O bond length decreases, and the bond strength increases from In to Al, which is consistent with the greater stability of Al- and Ga-MOFs. While In-MOFs are typically synthesized in organic solvents (e.g., DMF, DMA, NMP) at low temperatures (<150 °C), Al- and Ga- MOFs require basic aqueous solutions under solvothermal conditions at relatively higher temperatures (120–220 °C).

Zirconium, titanium, and hafnium are all tetravalent metals with $d^0$ electron configurations and nearly identical ionic radii due to lanthanide contraction [28]. Polynuclear metal carboxylate clusters of zirconium, particularly $Zr_6(OH)_4O_4(R–COO)_{12}$, are well established in inorganic chemistry, but synthesizing crystalline MOFs from these clusters is challenging. This difficulty arises from the high charge of the metal ions, the strength of the R-COO-$M^{4+}$ bonds, and the strong oxophilicity of zirconium. To address these challenges, reversibility in metal-carboxylate bond formation is introduced, similar to strategies described previously. Zirconium and hafnium MOFs are typically synthesized by

reacting metal sources such as $MOCl_2$, $M(SO_4)_2$, or $MX_4$ (X = Cl, Br, I; M = $Zr^{4+}$ or $Hf^{4+}$) with carboxylate-based linkers in amide solvents, using modulators such as monocarboxylic acids (e.g., formic, acetic, or benzoic acid) at temperatures of 50–140 °C [29]. The synthesis of Ti-MOFs presents even greater challenges because of the higher charge-to-radius ratio of titanium, which results in stronger, less reversible bonds. Furthermore, the symmetry and connectivity of most titanium clusters are not conducive to forming well-ordered crystalline frameworks, a limitation discussed in subsequent chapters. Ti-MOFs are generally synthesized by reacting organic linkers with reactive titanium precursors (e.g., $Ti(OR)_4$, where R = Me, Et, iPr, Bu) in organic solvents such as DMF at elevated temperatures (100–160 °C) over extended durations (2–7 days) [30].

### 2.2.4 MOF synthesis

#### 2.2.4.1 Rational design of synthesis

Despite the relatively short history of MOFs, researchers have shown significant interest in exploring their synthesis, aiming to achieve structures with diverse architectures and chemistries. However, the synthesis techniques remain largely rooted in solvothermal methods, which have been adapted from conventional solid-state chemistry and zeolite synthesis. As previously discussed, MOF syntheses typically occur in a solvent under controlled thermal conditions with temperatures ranging from ambient levels to approximately 250 °C [31]. The exact temperature along with other parameters, including the molar ratio of each component, pH, reaction time, and pressure, should be carefully controlled, given that minimal changes may considerably influence the resulting product. Our primary goal here is to introduce MOF synthesis to systematically explore its formation, focusing on two key aspects: (1) identifying the compositional and procedural parameters, and (2) elucidating the underlying mechanisms driving the synthesis process.

High-throughput synthesis has emerged as a potent method for investigating the formation conditions of MOFs as well as for subsequent procedures optimization [32, 33]. This approach entails conducting a series of synthesis processes to gather extensive data, enabling a systematic exploration of synthesis parameters. Although these tests can be time-intensive, they offer valuable insights into the influence of individual reaction parameters on product formation.

Time-resolved investigation of MOF formation enables the identification of crystalline intermediates, providing critical insights into individual reaction parameters, such as reaction rate constants and activation energies, and offers a basis for understanding the crystallization process. The time-resolved investigations employ both in-situ and ex-situ methodologies to monitor crystallization and reaction dynamics. Ex-situ techniques are practical, accessible, and compatible with standard laboratory conditions. In ex-situ approaches, samples are collected at predetermined intervals for subsequent analysis. However, handling and processing the samples would inevitably lead to post-reaction,

potentially compromising the accuracy of the results [31]. In contrast, in-situ studies enable continuous reaction monitoring and often achieve superior temporal resolution. These studies necessitate sophisticated instrumentation. Advancements in analytical technologies can significantly bolster the capabilities of in-situ study efficiency. Recent advancement of characterization in-situ nuclear magnetic resonance (NMR), electron paramagnetic resonance (EPR), various optical spectroscopies, X-ray and neutron diffraction, and high-resolution transmission electron microscopy (HRTEM) have been successfully adopted for elucidating time-resolved structural dynamics of MOF synthesis [34].

#### 2.2.4.2 Innovative synthesis methods

Although the solvothermal method remains the predominant approach for MOF synthesis, alternative techniques have garnered increasing attention to address key challenges in the field. These challenges include (a) achieving precise synthesis of target MOFs, (b) enabling scalable processes for future commercialization, (c) expanding the diversity of MOF families, and (d) developing efficient and environmentally friendly methods. To meet these demands, innovative strategies, including electrochemical synthesis, microwave-assisted synthesis, mechanochemical methods and spray-drying techniques, have been actively explored. Each of these approaches offers unique advantages [31]. For example, electrochemical synthesis facilitates the direct growth of MOFs on conductive surfaces [35], whereas microwave synthesis accelerates reaction times and enhances product uniformity [36]. Mechanochemical methods eliminate the need for solvents, aligning with green chemistry principles [37]. Flow chemistry enables continuous production with high reproducibility and scalability [38]. These advancements collectively expand the repertoire of synthesis techniques, opening new avenues for more efficient, sustainable, and commercially viable MOF production.

## 2.3 Covalent Organic Frameworks

This subsection addresses the topology, design principles, and synthetic strategies underpinning the creation of COFs.

### 2.3.1 Structure of COFs

The topology design diagramme serves as a guiding framework for directing covalent bond formation and controlling the orderly growth of polymer backbones. This construction relies on building blocks with reactive sites arranged in rigid and well-defined geometries, forming both 2D and 3D structure [2].

#### 2.3.1.1 Topology of 2D COFs

The majority of COFs are two-dimensional owing to the widespread availability of planar monomers. These monomers, characterized by their rigid backbones, inherently constrain the polymer growth to

two dimensions. This restriction results in polygonal topologies with well-defined structures [39]. This design concept can be illustrated with a block model [40, 41], as shown in Figure 2.5 a, where each monomer is simplified as a geometry. The geometries labelled on the basis of the reactive numbers $C_2$, $C_3$, $C_4$ and $C_6$ indicate ditopic, tritopic, tetratopic and hexatopic building block, respectively. Variants of the monomer combination endows the resulting 2D COF with diverse structures. Generally, the covalent combination of $C_4$+$C_2$ and $C_4$+$C_4$ generates tetragonal COFs (**sql**), whereas $C_3$+$C_2$ and $C_2$+$C_2$+$C_2$ result in hexagonal 2D COFs (**hcb**). Additionally, 2D COFs with Kagome (**kgm**), triangle (**hxl**) and rhomboid (**kgd**) pores formed with different monomer groups are shown in Figure 2.5 a.

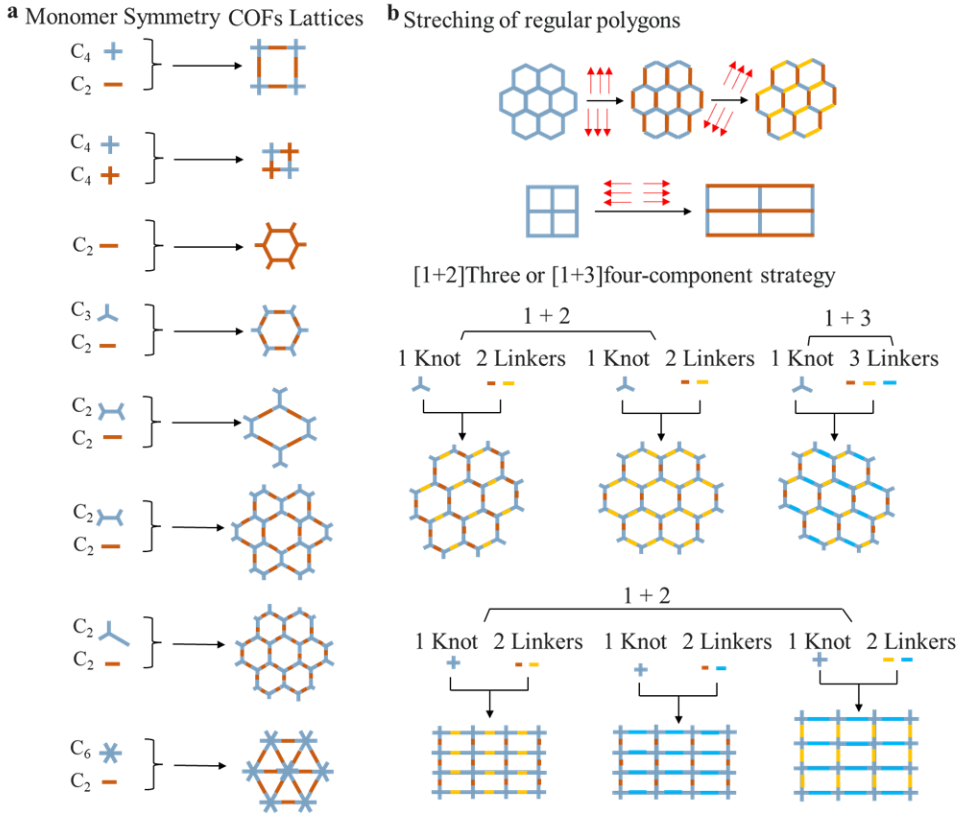



Figure 2.5 (a) Basic topological diagrams for the 2D design. (b) Polygon geometric transformation of stretching and multiple-component COFs with asymmetric structure, adapted from [42].

The abovementioned 2D COFs are all composed of two-component or single-component systems where one knot is proportionally linked to one linker, forming regular polygons and isotropic structures. Indeed, the large diversity of COFs also lies in the multiple-component concept (Figure 2.5 b) [42]. This concept leverages the integration of two or more linkers or knots within a single framework to introduce monomers with distinct geometries, lengths, or functional groups. For example, combining tetragonal and hexagonal linkers within the same COF framework can produce hybrid tiling patterns and anisotropic pore shapes that diverge from the uniformity of traditional isotropic designs. Similarly, using multiple knots with varied connectivity (e.g., three-connected and four-connected nodes) enables

the construction of frameworks with mixed coordination environments. By carefully tuning the interactions and matching the geometries of these building blocks, the multiple-component approach allows for the rational synthesis of highly ordered and structurally diverse COFs, overcoming limitations of conventional single-component systems.

Regardless of whether the topology of a 2D COF is symmetric or asymmetric, open channels, reflecting its planar structure, are typically observed. This characteristic arises from the highly ordered pack of 2D covalent polymers along the z-axis during the assembly of 2D COFs. These covalent polymers, which are defined by their rigid backbones, often incorporate π-systems [40]. The strategic positioning and orientation of π-conjugated units within two-dimensional covalent polymers favour the formation of layered assemblies, in which the alignment and spacing of adjacent layers are governed primarily by interlayer forces. To maximize attractive forces within these layered arrangements, 2D covalent polymers stack in an overlapping manner, ensuring that each monomer unit is aligned. This unique stacking behaviour enables 2D COFs to simultaneously establish fully ordered π-arrays and one-dimensional open channels [43]. Consequently, both the channel size and the density of π-units in 2D COFs are dictated by the fundamental lattice topology (Figure 2.5). For example, topologies formed by $C_2 + C_2 + C_2$ or $C_4 + C_4$ nodes typically produce microporous COFs, whereas combinations such as $C_3 + C_2$, $C_3 + C_3$, or $C_4 + C_2$ tend to form mesoporous structures. The development of the $C_6 + C_2$ topology represents a breakthrough in designing microporous COFs with the highest π-density and the smallest pore sizes, making trigonal COFs highly promising for applications such as molecular separation and semiconducting functionalities [44].

#### 2.3.1.2 Topology of 3D COFs

The building units used to construct 3D COF must possess both rigid covalent backbones to maintain structural integrity and nonplanar struts to enable the formation of 3D networks [45]. Thus, despite the extensive range of 3D topologies catalogued in the Reticular Chemistry Structure Resource (RCSR), the development of 3D COFs has been significantly constrained by the limited availability of qualified building blocks. Currently, reported 3D COFs are mostly with **ctn**, **bor**, **dia**, **srs**, **rra**, and **pts** topologies. These structures are constructed by building units with $T_d$ or orthogonal geometries, resulting in polymer backbones that interpenetrate in multiple folds to create 1D polygonal channels [46].

The majority of 3D COFs are categorized as microporous materials, yet their actual porosity is often significantly lower than expected because interpenetration occupies a significant portion of the internal space. Interpenetration is driven primarily by non-covalent interactions between adjacent networks. This phenomenon leads to a reduction in both surface area and pore size, while also complicating the prediction of their exact structures [47]. Therefore, addressing the issues of interpenetration and folding is critical for advancing the rational design and synthesis of 3D COFs.

### 2.3.2 Building blocks of COFs

In addition to geometric considerations, monomers exhibit a diverse array of structures, incorporating variations in size, docking sites, reactive functionalities, chiral centers, and properties such as redox activity, catalytic behaviour, and photoactivity. The structural versatility of monomers establishes a strong chemical foundation for achieving precise control over the primary-order structure.

The building blocks of COFs consist of π-backbones and functional sites. The core backbones span a broad spectrum, ranging from benzene derivatives to more complex aromatic systems, such as arenes, heterocyclic and macrocyclic structures. These backbones can be engineered to different configurations, including $C_2$, $C_3$, $C_4$, $C_6$, and $T_d$ geometries [48]. This structural versatility has enabled the development and investigation of hundreds of distinct monomers. The wide availability of functional groups, including aldehydes, amines, boronic acids, catechols, squaric acids, quinones, methyls, anhydrides, silanol, hydrazine, benzyl nitriles and tetros, further contributes to the diversity of building blocks [49].

### 2.3.3 Synthesis of COFs

The synthesis of COFs is fundamentally dictated by their linkage chemistry, which has now expanded to include a diverse range of bond types, enabling greater structural and functional versatility.

#### 2.3.3.1 Linkages in COFs

Boron-containing COFs, represented by the earliest reported structures, such as 2D COF-1 and COF-5, are synthesized by the self-condensation of boronic acids into boroxine rings or the co-condensation of catechols with boronic acids into boronic esters [7]. The dynamic nature of boron-based bond formation is essential for promoting error correction during synthesis and achieving high crystallinity. However, the reversibility also makes them unstable and prone to decomposition [50]. Subsequent studies have shown that boron-containing COFs are less stable in water, acids and alcohols which are broken down by more than 50% in 11s in excess water, and the hydrolysis occurs even in air. Borosilicate linkages (B–O–Si) exhibited enhanced stability at high temperatures and in general organic solvents, including tetrahydrofuran, N,N-dimethylformamide, alkanes, acetone and alcohols [51].

Schiff-based chemistry produces a large proportion of COFs. Its mechanism is generally initiated by protonation of a carbonyl group (i.e. aldehyde, ketone) to render the carbonyl carbon more electrophilic. Subsequent nucleophilic attack by an amine group as well as intramolecular proton transfer yield a hemiaminal intermediate that forms a Schiff-base upon elimination of water [52]. The advantage of these reactions is that reversibility in bond formation is achieved by employing acid as a catalyst. Consequently, the obtained bonds exhibit considerable stability under neutral pH conditions, even in aqueous environments. Depending on the substituent on the amine moiety, this chemistry can yield imines, hydrazones, azines, β-ketoenamies, phenazines, or benzoxazoles.

Imine-based COFs are quite stable and have high crystallinity because of the intramolecular hydrogen bonding between the hydroxyl and imine functional groups. These interactions help lock the phenyl rings into a planar conformation, thereby enhancing π–π stacking between adjacent COF layers and contributing to the overall framework order [53]. Compared with imines, hydrazones are generally more resistant to hydrolysis. They are commonly synthesized via a reversible condensation reaction between hydrazine derivatives and aldehyde-based building blocks [54]. Azine-linked COFs are formed through a thermodynamically controlled condensation between hydrazine and aldehyde-containing monomers, producing azine linkages with water as a by-product. These frameworks are notable for their high crystallinity, large surface areas, and robust chemical resistance [55]. β-Ketoenamine or keto–enol linked COFs are generally synthesized through a two-step mechanism. The initial stage involves reversible Schiff base condensation, resulting in the formation of a crystalline intermediate. This is followed by irreversible enol-to-keto tautomerization, which significantly improves chemical stability. Importantly, this transformation maintains the framework's crystallinity, as it involves only the migration of hydrogen and double bonds without altering the atomic positions. Despite their excellent stability, some β-ketoenamine COFs have been observed to undergo partial loss of crystallinity under strongly alkaline conditions, likely due to the reversal of the tautomeric shift [56]. Benzoxazoles are formed by the reaction of 2-hydroxy anilines with aldehydes.

COFs constructed from imide linkages are formed from acid anhydride and amine building units. Unlike the previously reported carbonyl chemistry, imide bond formation is generally irreversible under acidic conditions, although it can exhibit partial reversibility under basic environments. The resultant COF can achieve high crystallinity after a long self-correction process [21].

Covalent triazine-based frameworks (CTFs), are a novel type of porous organic material synthesized by aromatic nitrile trimerization [57]. The strong aromatic covalent linkages in CTFs make them extremely chemically stable. It also has many N atoms and high electron transport properties. It also features a high surface area and porosity, which are similar in performance to those of MOFs, zeolites or boron oxide-based COFs.

Carbon bond-based COFs that utilize $sp^2$ hybridized carbon-based conjugated bonds, can create materials with outstanding magnetic and electronic properties [58]. The structures and physicochemical properties of $sp^2$-COFs remain constant under extreme pH conditions and for most organic reagents [59].

#### 2.3.3.2 Crystallinity of COFs

For each newly developed linkage in COF chemistry, the challenge of achieving crystallization should be addressed. The formation of linkages between molecular building blocks is expected to be reversible under the selected reaction conditions to allow for sufficient error correction, ensuring the resolution of

defects via a self-healing process [21]. Covalent bonds, despite offering robust structural stability, present particular difficulties in this regard owing to their inherent tendency to form irreversibly under mild conditions. Therefore, it is essential to establish conditions that promote reversibility in bond formation without requiring extreme temperatures or pressures that could degrade organic monomers. A mixture of polar solvent and nonpolar solvent is usually employed as a reaction medium to facilitate the reversible formation of covalent linkages [60].

These reversible reactions endow the resulting frameworks with self-healing capabilities, allowing the system to undergo iterative error-checking and defect correction. This is especially critical in reactions involving multiple reactive sites, where structural precision is necessary to construct defect-free frameworks [61]. Moreover, the topology diagram requires the covalent connection of organic units in a deliberate and highly ordered fashion. This underscores the importance of employing reversible covalent reactions in the synthesis of crystalline COFs [43]. In rare cases, irreversible reactions, including phanazine linkage, dioxin linkage, and C═C linkage, are synthesized through irreversible nucleophilic aromatic substitution reactions and formed COFs [60].

#### 2.3.3.3 Synthesis methods

COF synthesis methods have diversified, each tailored to specific features of chemistry. Since we address the synthesis of COF membrane, here, we provide only a general comparison of the synthesis methods of bulk COFs.

Solvothermal synthesis [62], the most common method, produces highly crystalline and porous COFs but is time-intensive and requires precise conditions. Microwave synthesis accelerates reaction times and improves porosity but is limited to specific systems [63]. Ionothermal methods use molten salts as solvents and catalysts, enabling unique frameworks but at high energy costs [64]. Mechanochemical synthesis offers a simple, eco-friendly approach with minimal solvent use, although the crystallinity may be reduced [65]. Ambient-condition synthesis enables energy-efficient COF production at room temperature, which is ideal for fragile monomers but often compromises crystallinity [66]. These methods collectively expand the range of achievable COFs, enabling tailored properties for diverse applications.

## 2.4 Continuous Frameworks Membranes

Owing to their extensive porosity, periodic network, and versatile chemistry, continuous framework membranes are poised to achieve heightened permeability and selectivity concurrently, thereby challenging the conventional trade-off equilibrium observed in polymer membranes.

### 2.4.1 MOF membrane

An optimal continuous and ultrathin MOF membrane is proposed for broad separation applications. Achieving such a membrane hinges on developing a scalable and versatile fabrication method. This section provides a summary of approaches to fabricate continuous MOF membrane, including in-situ growth, secondary growth, interfacial synthesis, layer-by-layer (LBL), vapour deposition, and electrodeposition, which are elucidated with typical examples. Subsequently, primary concerns related to MOF membranes in liquid separation scenarios, including substrate properties, crystallinity, orientation, thickness, stability, and scalability are discussed. An overview of the application of these MOF membranes in liquid-based separation is presented at the end of this section.

#### 2.4.1.1 Fabrication methods of MOF membrane

a) In-situ growth method

The in-situ method, also known as direct growth, is a facile technique. This involves immersing a porous substrate into precursor solutions, where nucleation, crystal growth, and membrane deposition occur in one step [67].

Lai et al. first reported the synthesis of a continuous MOF membrane using in-situ growth [68]. They meticulously controlled the heating duration, composition, and temperature of the synthetic solution to achieve a thick MOF-5 membrane (25 μm) on porous α-alumina discs as substrates. The versatility of in-situ growth has been utilized to create various MOF-based membranes for separation applications, such as UiO-66 [69] and MOF-303 [70] membranes.

Despite the convenience of in-situ growth method and the modification method developed to prompt the fabrication of continuous membranes, in-situ solvothermal growth still faces challenges, including low nucleation efficiency, difficulty in controlling film thickness and orientation, and high reagent consumption. A typical example can be found in the synthesis of a ZIF-8 membrane on a pretreated alumina support using a high concentration of precursors ($Zn^{2+}$: Hmim:methanol ratio of 1:8:75). Although the resultant continuous ZIF-8 synthesis was achieved after heating for 5 h at three different temperatures (25, 100, and 150 °C), the irregular particle shapes observed on the membrane surface and cross-section indicate uneven crystal formation, suggesting its limitations in precise control over MOF crystals.

b) Secondary growth method

The secondary growth (seeding growth) method is promising for the formation of dense, continuous, and ultrathin crystalline membranes [71]. The first step involves deposition of seeds as nuclei onto the substrate, followed by the controlled growth of these nuclei into a fully developed membrane. The seeding step plays a vital role in influencing the membrane's microstructural integrity and uniformity (Figure 2.6). Various seeding techniques have been developed, including rubbing [72], dip-coating, slip-coating [73], spin-coating [74], electrospinning [75], microwave-assisted crystallization[76], reactive seeding [77], and thermal seeding [78]. These methods can be divided into two categories:

physical seeding and chemical seeding.

Physical seeding has high potential for scalable fabrication because of its versatile seeding process (Figure 2.6 a). For example, Hu et al. introduced a novel strategy for fabricating ultrathin, defect-free molecular sieving membranes by employing two-dimensional ZIF-8/graphene oxide (GO) hybrid nanosheets as a seeding layer [74]. These hybrid nanosheets were first deposited onto a porous anodic aluminum oxide (AAO) support, creating a uniform and well-distributed seed layer. Subsequent secondary growth via a contra-diffusion process facilitated the development of a compact and continuous ZIF-8 membrane.

Chemical seeding has high potential for facilitating bonding between the membrane and substrate (Figure 2.6 b). A typical example can be found in the fabrication of MIL-53 membranes on porous alumina supports using the reactive seeding method, where the support itself provided the inorganic source for forming the seed layer [77]. The direct reaction between the alumina substrate and an organic precursor not only resulted in the formation of a uniform and well-adhered seed layer but also eliminated the need for additional seeding steps. Subsequent secondary growth in a solution containing aluminum nitrate and 1,4-benzenedicarboxylic acid led to the development of a dense, defect-free MIL-53 membrane.

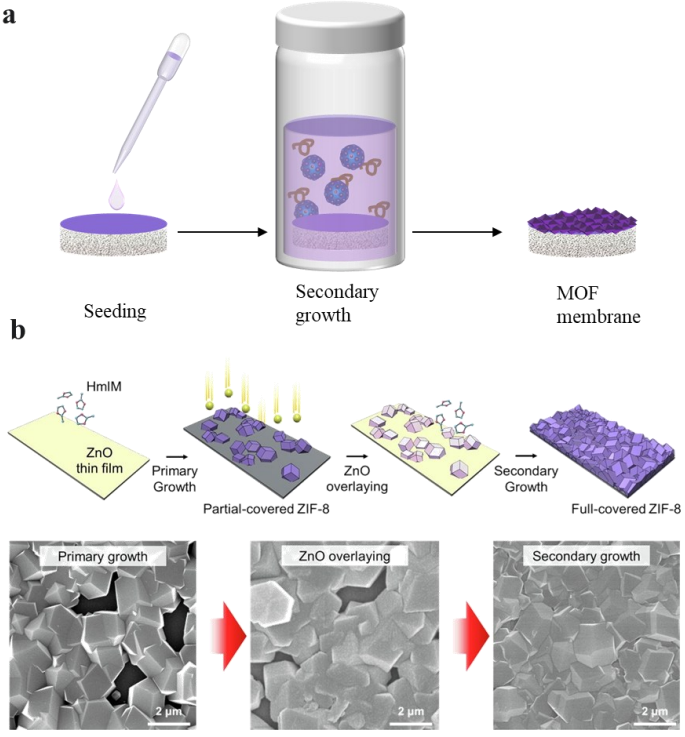



Figure 2.6 Secondary growth method. (a) Physical seeding and growth. (b) Chemical seeding and growth [79], Copyright © 2023 Elsevier B.V.

Thermal seeding has also been reported as an effective chemical seeding method. Jeong et al. [78] demonstrated the anchoring of MOF seeds on heated porous substrates. They continuously deposited a

solution of HKUST-1 crystals and precursors onto heated α-alumina supports until the surface was sufficiently covered with seed crystals. The seeded support was then placed in an autoclave filled with HKUST-1 precursor solution, yielding a continuous, crack-free HKUST-1 membrane under optimized conditions.

Despite the advantages of the seeding growth method, it is not without limitations. The first challenge is the complexity introduced by the seeding process. Furthermore, the use of a precursor solution containing metal ions and linkers in both steps leads to the formation of MOF crystals in the bulk solution potentially causing material waste.

c) Layer-by-layer method

Layer-by-layer is considered as an extension of secondary growth method. The principle is to sequentially deposit ligands and metal coupling units on the existing layer by washing the solvent, rinsing and refreshing with new precursor after the formation of each layer (Figure 2.7).

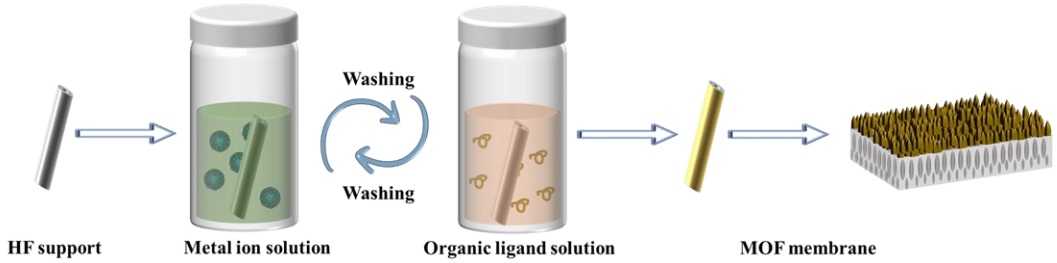



Figure 2.7 Schematic illustration of LBL fabrication

Tham et al. applied the LBL technique in an aqueous system for the fabrication of a high-performance membrane for organic solvent nanofiltration [80]. In detail, a ZnBDC MOF was grown on a modified PAN support as the selective layer, eliminating the need for organic solvents. By alternately immersing the support in metal and ligand solutions, a uniform and defect-free MOF layer was achieved. Although the process is more complicated than in-situ and secondary growth, the greatest advantage is the potential to precisely control the thickness of the membrane.

d) Interfacial synthesis method

The interfacial method involves introducing metal ion and organic ligand solutions on opposite sides, facilitating crystallization at the interface where these components diffuse and interact [81]. This technique has been further refined into two distinct approaches: static and dynamic interface synthesis. Static interfacial synthesis is usually realized by the diffusion of metals and ligands in two immiscible solvents and subsequent crystallization at the interface (Figure 2.8 a) [82]. This method produces a free-standing MOF membrane, which faces the risk of breaking during the transfer of the membrane onto the substrate. Alternatively, a porous support can be used as the interface (Figure 2.8 b) [83]. Precursors containing a metal solution and a ligand solution are introduced on two sides of the support and react to form a continuous membrane. Wang et al. successfully synthesized ZIF-8 films on flat nylon

substrates via the interfacial crystallization of a zinc nitrate methanol solution and the Hmim methanol solution method by using a porous nylon membrane with a 0.1 μm pore size as the substrate [84].

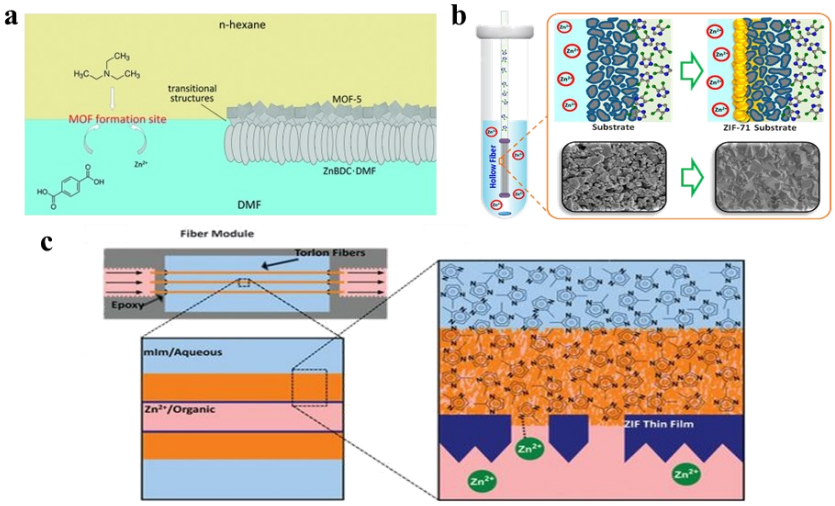



Figure 2.8 Interfacial synthesis of MOF membranes. (a) Free-standing MOF-5 fabricated at DMF/n-hexane interface [82]. (b) Static interfacial synthesis on HFs [83], Copyright © 2013 WILEY‐VCH Verlag GmbH & Co. KGaA, Weinheim. (c) Dynamic interfacial synthesis [85].

Dynamic interfacial synthesis primarily involves the microfluidic processing of membranes at the interface, where two immiscible precursors are separately introduced into the outer side and lumen of a HF/tube (Figure 2.8 c) [85]. Based on this principle, Marti et al. successfully fabricated continuous ZIF-8 thin films on the outer surface of polymeric HFs. In their approach, an aqueous solution containing $Zn^{2+}$ ions was directed through the shell, whereas a solution of 2-MeIm in water simultaneously flowed through the lumen [86].

e) Vapour deposition method

Vapour deposition typically involves three steps: 1) evaporation, 2) transport of the vaporized material, and 3) deposition of the film on the substrate. Based on whether chemical reactions occur, vapour deposition can be categorized into two types: PVD and CVD [87].

PVD relies only on physical forces to bind the deposited material. As such, MOF membranes formed via PVD often exhibit weak adhesion to the substrate and limited structural integrity. For example, ZIF-8 membranes fabricated via a pulsed-laser deposition technique can be easily detached by washing with ethanol [88]. In contrast, CVD involves chemical reactions between vapourized precursors, and the substrate leverages stronger bonding and high robustness of the membrane. Li et al. synthesized a highly crystalline ZIF-67 thin films via steam-assisted CVD [89], enabling the direct growth of ZIF-67 films at temperatures below 125 °C. This provides a scalable, cost-effective, and efficient route for film fabrication. However, challenges remain in achieving Angstrom-level thickness, enhancing reproducibility, and reducing required temperature and pressure [90-92].

In addition to PVD and CVD, an innovative gel vapour deposition (GVD) process that combines sol-gel chemistry with vapour deposition techniques has been reported for the fabrication of ZIF-8 HF membrane [93]. This process involves a sol-gel coating process to load Zn $(CH_3COO)_2$ as a metal cluster, followed by the deposition of vapour containing 2-methylinidazole. The resulting ZIF-8 membrane exhibited high uniformity and low thickness. The use of gel intermediates offers unique material properties and enhanced compatibility between MOF films and substrates. It has been successfully employed to fabricate ultrathin ZIF films (20 nm) (Figure 2.9) [93].

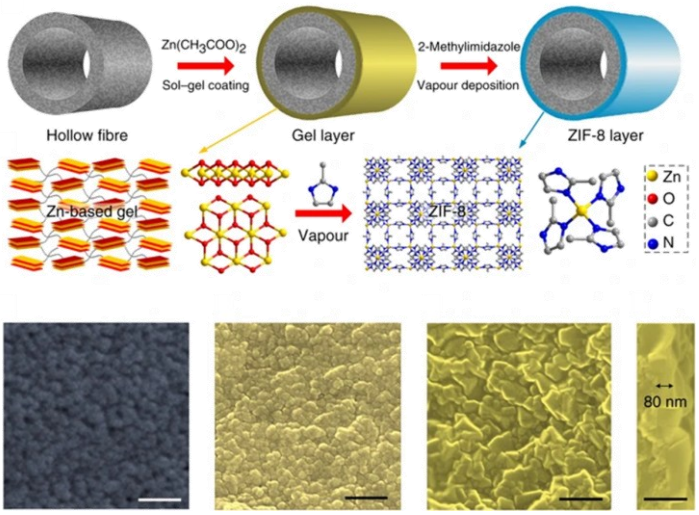



Figure 2.9 Fabrication of ultrathin ZIF-8 HF membrane on HF via the GVD method [93].

f) Electrodeposition method

The electrochemical method offers advantages including controllable synthesis, less pretreatment on the substrate, reduced growth time, and simple preparation. More importantly, this method allows for controlling the morphology and thickness by altering the current. It can be realized by anodic dissolution, cathodic deposition, and electrophoretic deposition [94]. Anodic dissolution employs a metal anode to release ions that react with organic ligands in the electrolyte to form MOF membranes [95]. Cathodic deposition fabricates MOF membranes by using electrodes as electron sources, which facilitate hydroxide generation to deprotonate ligands and promote MOF crystallization [96]. Electrophoretic deposition leverages charged MOF particles (due to missing linkers or metal nodes) to migrate under an electric field, thus forming MOF layers on the electrode [97].

The HKUST-1 membrane is the earliest MOF membrane fabricated electrochemically and was pioneered by researchers at BASF [98]. However, systematic studies are needed to understand how deposition parameters (e.g., linkers, nodes, additives, pH) influence nucleation and crystal growth in membrane fabrication. Moreover, the potential of electrodeposition for controlling the growth of MOF membranes in terms of their thickness crystal size, and microstructure features, such as defects, grain

boundaries, and channel orientation, remains underexplored [99].

#### 2.4.1.2 Key properties of MOF membrane for liquid separation

Despite extensive exploration of various fabrication methods, challenges remain in the practical application of MOF membranes. These challenges stem from both the intrinsic properties of MOF membranes, such as pore characteristics, crystallinity, defects, thickness, orientation, stability, and substrate-related limitations. As the porous feature and potential of functionality of MOs have been thoroughly discussed in Section 2.2, the following discussion will focus on other critical properties influencing MOF membrane performance in liquid separation.

a) Substrate properties

An ideal substrate is expected to offer high mechanical stability, well-regulated porosity, appropriate surface roughness, and favourable surface chemistry. Mechanical robustness is essential to ensure structural integrity under various operational conditions [100]. High porosity with a uniform pore size facilitates efficient permeance. Notably,the pore size should be less than 0.5 μm, as the large pore size of the substrate is prone to generating defects on the obtained MOF membrane [101]. The surface roughness requirements vary depending on the application. For example, increasing the roughness of a porous α-$Al_2O_3$ substrate has been shown to enhance physical interactions with ZIF-8 membranes [102]. In another case, adjusting the surface roughness by precise microstructural engineering endows the resultant MOF membrane with enhanced hydrophobicity and thus better wetting resistance in the vacuum membrane distillation (VMD) test [103].

The surface chemistry of the substrate is crucial in the successful fabrication of continuous MOF membranes, which not only dominates the interfacial adhesion between the MOF layer and the substrate but also profoundly influences the nucleation density [100]. However, the majority of conventional substrate materials present inherent limitations and often fail to meet these requirements. A diverse array of modification techniques to adapt the chemistry of substrate materials has been explored.

Organic functionalization, such as amination with APTES, introduces reactive sites that enhance MOF crystallization, improving membrane uniformity and adhesion [104-107]. Metal precursor modifications, including ZnO nanoparticle deposition or impregnation with metal ions such as $Zn^{2+}$ or $Co^{2+}$, provide a controlled nucleation environment that promotes defect-free membrane growth [108, 109]. Surface engineering techniques, such as polydopamine coatings, further strengthen interfacial interactions and mechanical stability, ensuring the formation of robust and durable membranes [110]. Additionally, polymer-based modifications, including embedding MOF precursors within polymeric matrices or integrating layered double hydroxides, increase substrate compatibility and facilitate large-scale fabrication [111]. These combined strategies enable the fabrication of high-performance MOF

membranes tailored for advanced separation applications.

b) Crystallinity

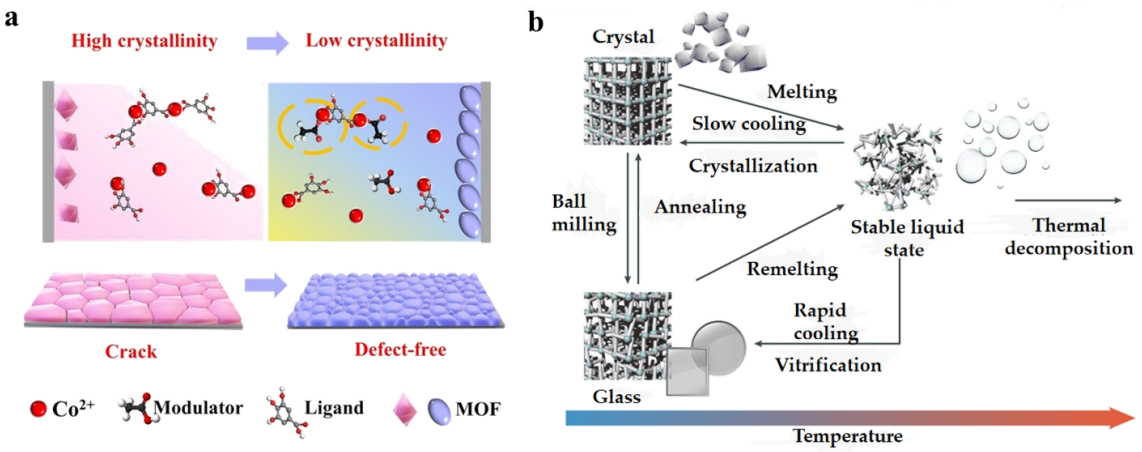



Figure 2.10 Crystalline structure of the MOFs. (a) Balance between the crystallinity and defect-free nature of the MOF membrane [112], Copyright © 2023 Wiley - VCH GmbH. (b) Transfer of MOF crystallinity state [113].

As a framework material, high crystallinity is normally pursued to fully exploit their well-ordered porous architecture and to ensure high structural uniformity and rigidity [114]. Thus, high crystallinity seems favourable for realizing precision molecular separation [115]. However, a trade-off between crystallinity and the formation of defect-free membrane was reported by Liu et al. Based on their theory, excessive crystallinity leads to intercrystalline defects due to the rigid nature of polycrystalline frameworks, which results in poor film integrity and mechanical instability. Conversely, when crystallization is excessively suppressed, the film becomes overly amorphous, leading to the loss of well-defined molecular sieving channels (Figure 2.10 a) [112]. By striking a balance between these factors, they successfully fabricated a MOF membrane with enhanced film-forming property at the expense of controlled crystallinity reduction.

Novel crystalline state of MOFs membrane also encompasses non-crystalline MOFs (Figure 2.10 b), for example amorphous Ti-MOF membrane obtained by temperature-programmed sol deposition [116], MOF glass membrane fabricated by melt-quenching crystalline ZIFs [113], and low-crystalline materials fabricated by inducing interlayer polarization [117]. Nevertheless, MOFs membranes with compromised crystallinity are limited to gas-related applications. Their amorphous structure and potential for tailored functionality could offer advantages in specific liquid separation scenarios, such as selective ion transport or organic molecule filtration. Further research is needed to fully understand their stability in liquid separation applications.

c) Defects

Two categories of defects may occur in a pure MOF membrane, which are intercrystalline defects (grain boundaries or microcracks) and intracrystalline defects (missing linkers or clusters) [67].

Intercrystalline defects result from inadequate crystal intergrowth or incomplete coverage of the substrate, creating non-selective permeation channels that compromise membrane performance [110]. Significant research efforts have been dedicated to mitigating these defects by refining synthesis parameters and optimizing fabrication conditions to increase membrane uniformity and integrity. The most commonly applied strategy is extending the synthesis time to allow the formation of a thick membrane to patch intercrystalline defects. However, this inevitably leads to a low permeance due to the inverse relationship between membrane thickness and flux. To date, intercrystalline defects remain the main concern hindering the scalable fabrication of MOF membrane.

To realize a precise molecular sieve, the elimination of intracrystalline defects has been explored. Jin et al. utilized a high-probability coordination strategy to generate the necessary chemical potential to overcome steric hindrance, which typically obstructs the full connection of ligands to metal clusters [118]. This approach enabled the successful synthesis of a series of high-connectivity MOF membranes featuring ångström-scale lattice apertures. Rather than eliminating intracrystalline defects, defect engineering exploits these structural imperfections to enhance MOF functionality, utilizing them as hierarchical pores or reactive sites for specific applications. For example, a MOF-801 membrane synthesized with a missing-linker strategy by using formic acid as a modulator successfully increased the number of water transport channels, resulting in significant water flux enhancement [119]. Notably, the diverse chemistry of linkers and SBUs offers extensive potential for tailoring intracrystalline defects in MOF membranes. Through precise design, these defects can be strategically controlled to optimize mass transport and enhance molecular selectivity to broaden the scope of MOF applications in separation and beyond.

d) Orientation

As crystalline materials, different crystallographic planes of a MOF exhibit distinct window apertures [120]. Compared with their randomly oriented counterparts, MOF membranes with a crystallographic preferred orientation (CPO) typically exhibit superior molecular sieving capabilities. This is due mainly to the alignment of specific aperture along the oriented crystallographic plane, which enables windows control and precise molecular sieving. Random growth inevitably causes partial blockage of pore openings, significantly reducing the mass transport efficiency. Additionally, this ordered structure minimizes intercrystalline defects by promoting the intergrowth (in-plane growth) of crystals, effectively lowering transport resistance. The enhanced in-plane growth also mitigates the extended synthesis time required to patch the non-selective transport in the traditional solvothermal method [121, 122]. Consequently, a thinner membrane and shorter mass transport pathway can be expected.

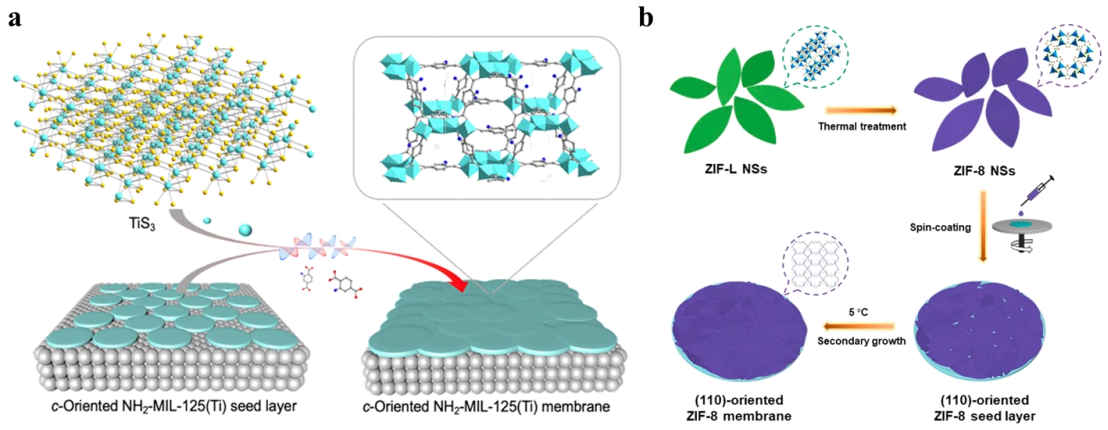



Figure 2.11 Oriented growth of MOF membrane by seeding regulation. (a) MIL-125 membrane with c-axis orientation grown from a pre-injected c-oriented seeding layer [123], Copyright © 2022, American Chemical Society. (b) (110)-Oriented ZIF-8 membrane fabricated from (110)-oriented ZIF-8 seeds [124], Copyright © 2021 Elsevier B.V. All rights reserved.

Since nucleation and crystallization occur simultaneously in all possible directions during direct in-situ growth, most reported MOF membranes with a specific CPO are obtained through secondary epitaxial growth from pre-oriented MOF seeds [120, 125, 126]. Liu et al. developed a series of oriented MOF membranes based on this principle, including an ultrathin MIL-125 membrane with *c*-axis orientation grown from a pre-injected *c*-oriented seeding layer (Figure 2.11 a) [123], a (110)-oriented ZIF-8 membrane derived from (110)-oriented ZIF-8 seeds (Figure 2.11 b) [124], and a (111)-oriented UiO-66 membrane synthesized via contra-diffusion growth from a (111)-oriented monolayer [127]. These oriented membranes have demonstrated superior molecular sieving performance.

However, achieving precise MOF orientation by introducing pre-oriented seeding layers remains highly complex and impractical for large-scale fabrication. For example, the synthesis of a (110)-oriented ZIF-8 membrane involves multiple intricate steps, including the fabrication of two-dimensional leaf-like ZIF-L, thermal conversion of ZIF-L to ZIF-8, controlled deposition of oriented seeds, and subsequent secondary growth (Figure 2.11 b) [124]. This multi-step process not only extends the overall fabrication time but also reduces reproducibility, posing significant challenges for scalable production.

The oriented growth of MOF membranes is still in its early stages, particularly when compared to other crystalline materials such as zeolites. A more comprehensive understanding of the underlying crystal growth mechanisms is essential for advancing this field. Additionally, expanding the application scope of MOF membranes with CPO is crucial to fully unlocking their potential and maximizing their impact across various separation and filtration processes.

e) Stability

The stability of MOFs, a critical factor for their practical applications, is largely governed by the composition and structure of their building chemistry [128]. Among the different stability aspects, chemical stability, defined as the ability of MOFs to resist degradation when exposed to environmental factors such as moisture, solvents, acids, bases, and aqueous solutions containing coordinating anions, is highly valued. The intrinsic chemical stability of MOFs arises from both thermodynamic and kinetic factors [129].

Thermodynamic factors refer to the coordination bond strength between a metal and a ligand, which can be predicted based on hard soft acid base (HSAB) theory. Briefly, stable MOFs are expected to be generated by coordinating high-valence metal ions ($Fe^{3+}$, $Al^{3+}$, and $Zr^{4+}$) with high p$K_a$ ligands (e.g. carboxylate-type ligands) or divalent metal ions ($Zn^{2+}$, $Cu^{2+}$, $Ni^{2+}$ and $Co^{2+}$) with low p$K_a$ linkers (imidazolate, and pyrazolates.), resulting in strong metal-linker coordination [130, 131]. The internal inertness of the metal clusters themselves can also result in high chemical stability, as witnessed by MOFs such as MIL-101(Cr) [132]. However, the chemical stability of certain MOFs, such as the UiO-66 and SUMOF-7 series, tends to decrease with longer linkers and larger pore sizes, even when the metal clusters and framework topologies remain unchanged [133].

This reduction in stability is largely influenced by kinetic factors, including the flexibility of the linker, the coordination number and surface hydrophobicity [128]. Dense, rigid frameworks composed of highly connected and robust building units, such as metal ions/clusters and ligands, generally exhibit superior stability because of their resilience against partial lattice collapse [134]. Surface hydrophobicity significantly enhances stability in aqueous environments by reducing water adsorption within the pores and preventing water condensation around metal clusters [129]. Guided by thermodynamic and kinetic factors, various stable MOFs have been reported. Some examples are listed here in Table 2.1.

Table 2.1 Summary of MOFs with high stability *(The selected literature represents key studies identified through a Web of Science search using keywords such as "stability of MOFs", "stability of COFs", "water-stable MOFs" and "water-stable COFs")*

| *MOFs* | Metal ions/SBUs | Ligands | Stability description | Ref. |
|---|---|---|---|---|
| *MAF-41* | Cu (I) | fbdim | Boiling water 7 days<br>pH = 3-14 3 days | [135] |
| *CuTBPZ* | Cu (I) | TBPZ | Water 24 h<br>pH = 3, 12 | [136] |
| *FJi-H14* | Cu (II) | BTTA | pH = 2-13 1 week | [137] |
| *CuBDC* | Cu (II) | BDC | Stable at 350-400 °C | [138] |

| | | | | |
|---|---|---|---|---|
| | | | Stable in water | |
| *Cu-BTTri* | Cu (II) | BTTri | Boiling water 3 days<br>pH = 3 1 day | [139] |
| *ZIF-8* | $[ZnN_4]$ | mIM | Boiling water 7 days | [140] |
| *ZIF-11* | $[ZnN_4]$ | bIM | Water 7 days | [141] |
| *ZIF-61* | $[ZnN_4]$ | IM, MeIM | Boiling water 7 days | [142] |
| *ZIF-68* | $[ZnN_4]$ | bIm, nIM | Boiling water 7 days | [142] |
| *ZIF-69* | $[ZnN_4]$ | cbIM, nIM | Boiling water 7 days | [142] |
| *ZIF-70* | $[ZnN_4]$ | IM, nIM | Boiling water 7 days | [142] |
| *ZIF-90* | $[ZnN_4]$ | ICA | Water 7 days | [142] |
| *Zn(1,4-BDP)* | $[Zn(PZ)_2]n$ | 1,4-BDP | Water 40 °C | [143] |
| *Zn(1,3-BDP)* | $[Zn(PZ)_2]n$ | 1,3-BDP | Boiling water 7 days | [143] |
| *MAF-23* | Zn (II) | btm | Water 7 days | [144] |
| *ZIF-67* | $[CoN_4]$ | mIM | Boiling water 7 days | [142] |
| *MFU-1* | Co (II) | bdpb | Water 180 days | [145] |
| *PCN-601* | $[Ni_8(OH)_4(H_2O)_2(PZ)_{12}]$ | TPP | Stable at 100 °C NaOH aqueous solution (5M) | [146] |
| *Ni3(BTP)2* | $[Ni_4(PZ)_8]$ | BTP | Heating in air to 430 °C<br>pH 2 to 14<br>Boiling water two weeks | [147] |
| *BUT-32* | $[Ni_4(PZ)_8]$ | TPTA | Boiling water 24 h<br>Aqueous solution (pH = 3)<br>NaOH aqueous solution (4 M) | [148] |
| *BUT-33* | $[Ni_4(PZ)_8]$ | TPTA | Boiling water 24 h<br>Aqueous solution (pH = 3)<br>NaOH aqueous solution (4 M) | [148] |
| *MIL-53(Al)* | *Al (III)* | BDC | Stable in boiling water Stable at pH = 2 and 7 | [149] |
| *Al-FUM* | *Al (III)* | FUM | Stable at 430 °C<br>Long-term water stability > 43days | [150] |
| *MIL-69* | $[Al(OH)(COO)_2]_n$ | 2,6-NDC | Stable at 430 °C<br>Long-term water stability | [151] |

| | | | | |
|---|---|---|---|---|
| *MIL-96(Al)* | $[Al(OH)(COO)_2]_n$ | BTC | Stable at pH < 8<br>Stable in liquid water up to 3 months | [152] |
| *MIL-100(Al)* | *Al (III)* | BTC | Stable in water | [153] |
| *MIL-101(Al)* | *Al (III)* | BDC-NH2 | Stable at 380 °C<br>Water stability | [154] |
| *MIL-110* | $[Al_8(OH)_{15}(COO)_9]$ | BTC | Kinetically stable in water | [155] |
| *MIL-118* | $[Al(OH)(COO)_2(COOH)_2]_n$ | BTEC | Stable at 400 °C<br>Long-term water stability | [156] |
| *MIL-120* | $[Al(OH)(COO)_2]_n$ | BTEC | Stable at 280 °C<br>High water stability | [157] |
| *MIL-121* | $[Al(OH)(COO)_2]_n$ | BTEC | Stable at 380 °C<br>High water stability | [158] |
| *MIL-122* | $[Al(OH)(COO)_2]_n$ | NTC | Stable at 440 °C<br>Water stable | [159] |
| *467-MOF* | *Al (III)* | BTTB | 30 days at room temperature<br>Boiling water 7days<br>36 h at pH = 1<br>~hours at pH 11 | [160] |
| *CAU-10* | $[Al(OH)(COO)_2]_n$ | 1,3-BDC | Stable at boiling water | [161] |
| *Al-PMOF* | $[Al(OH)(COO)_2]_n$ | TCPP | Water stable | [162] |
| *PCN-333* | Al (III) | TATB | Highly water stable | [163] |
| *MOF-303* | Al (III) | PDC | Highly water stable for more than 7 days | [164] |
| *MIL-53(Cr)* | $[Cr(OH)(COO)_2]_n$ | BDC | Stable in water<br>Stable in acidic | [165] |
| *MIL-96(Cr)* | Cr (III) | BTC | Stable in water | [166] |
| *MIL-101(Cr)* | Cr (III) | BDC | Stable in water > 14 days<br>Stable at pH 5-11 | [165] |
| *PCN-333(Cr)* | Cr (III) | TATB | Highly water stable<br>Stable at pH 3-9 | [163] |
| *PCN-333(Fe)* | Fe (III) | TATB | Highly water stable<br>Stable at pH 3-9 | [163] |

| | | | | |
|---|---|---|---|---|
| *PCN-600(Fe)* | Fe (III) | TCPP | Highly water stable<br>Stable at pH 2-11 | [167] |
| *MIL-125* | $[Ti_8O_8(OH)_4(COO)_{12}]$ | BDC | Stable in water > 1 day | [168] |
| *PCN-222* | $[Ti_7O_6(COO)_{12}]$ | TCPP | Stable in boiling water<br>Stable HCl solution > 24 h | [169] |
| *UiO-66* | Zr (IV) | BDC | Stable at pH = 0-12<br>Stable in water > 60 days | [133] |
| *UiO-67* | Zr (IV) | BPDC | Stable in water > 60 days<br>Stable at pH = 4 | [133] |
| *PCN-223* | Zr (IV) | TCPP | Stable at pH (0-10) | [170] |
| *PCN-225* | Zr (IV) | TCPP | Boiling water 12 h<br>Stable at pH (0-12) | [171] |
| *PCN-228* | Zr (IV) | TCP-1 | Stable in water 1 day Stable at pH = 0-12 | [172] |
| *PCN-229* | Zr (IV) | TCP-2 | Stable in water 1 day Stable at pH = 0-12 | [172] |
| *PCN-230* | Zr (IV) | TCP-3 | Aqueous solution (pH = 0-12) 1 day | [172] |
| *MOF-801* | Zr (IV) | FUM | Stable in boiling water and HCl | [173] |
| *MOF-802* | Zr (IV) | PZDC | Stable in water and HCl | [174] |
| *MOF-808* | Zr (IV) | BTC | Boiling water > 24h | [175] |
| *MOF-812* | Zr (IV) | MTB | Stable in water | [176] |
| *MOF-841* | Zr (IV) | MTB | Stable in water | [176] |
| *DUT-51* | Zr (IV) | DTTDC | Stable in water > 12h | [177] |
| *DUT-52* | Zr (IV) | 2,6-NDC | Stable in 0.1M NaOH<br>Stable in 0.1 M HCl<br>Stable in water | [178] |
| *DUT-67* | Zr (IV) | 2,6-NDC | Stable in water | [179] |
| *NU-1000* | Zr (IV) | TBAPy | Excellent water stability | [180] |
| *NU-1100* | Zr (IV) | PTBA | Stable in water > 24h | [181] |
| *MIL-140s* | $[ZrO(COO)_2]_n$ | BDC, 2,6-NDC, BPDC, $Cl_2$ABDC | Stable in boiling water | [182] |
| *BUT-12* | Zr (IV) | CTTA | Aqueous solution (pH = 11) 7 days<br>Boiling water 24 h | [183] |

| | | | | |
|---|---|---|---|---|
| *BUT-13,14,15* | Zr (IV) | TTNA, BCQD, PBPTT | HCl solutions (2 M, 6 M)<br>Aqueous solution (pH = 10)<br>Boiling water 24 h<br>HCl solutions (2 M, 6 M)<br>Aqueous solution (pH = 12) | [183, 184] |
| *BUT-44* | Zr (IV) | BTEB | Water 72 h<br>Aqueous solution (pH = 10) 1 Day<br>HCl aqueous solutions (1 M) 1 day | [185] |
| *BUT-66* | Zr (IV) | BDB | Water 1 month<br>Aqueous solution (pH = 1-10)<br>Water 48 h | [186] |
| *BUT-67* | Zr (IV) | NDB | Aqueous solution (pH = 1-10) | [186] |

### 2.4.1.3 Application of continuous MOF membrane in liquid separation

Continuous MOF membranes have demonstrated remarkable efficiency in various liquid separation applications, including, nanofiltration, pervaporation, and organic solvent separation (as summarized in Table 2.2).

The regularly porous structure with a well-defined pore size ensures the designable size exclusion capacity of the MOF membrane, rendering it a promising candidate for nanofiltration. A notable example is the UiO-66 membrane, synthesized via an in situ solvothermal method on an alumina HF substrate [69]. The resulting polycrystalline membrane exhibited excellent multivalent ion rejection rates, with rejection rates of 86.3% for $Ca^{2+}$, 98.0% for $Mg^{2+}$, and 99.3% for $Al^{3+}$. The robust coordination between $Zr^{4+}$ and carboxyl groups offered superior chemical stability, maintaining consistent performance over 170 hours of operation. Owing to their promising molecular-sieving capacity, continuous MOF membranes have been explored for emerging applications such as $Li^{+}/Mg^{2+}$ separation [187] and chiral molecule filtration [188].

A recently developed Co-gallate MOF membrane by Pan et al. exhibited outstanding pervaporation (PV) performance in methanol/methyl tert-butyl ether (MTBE) separation [189]. The membrane was synthesized via a secondary growth process, where a uniform Co-gallate seed layer was deposited onto a porous α-$Al_2O_3$ support by dip-coating, followed by controlled secondary crystallization to form a continuous and defect-free layer. The resultant membrane demonstrated a methanol flux of 0.565 kg $m^{-2}$ $h^{-1}$ with a separation factor of 721, outperforming most polymeric and zeolite membranes [190, 191].

The exceptional separation efficiency of MOF membranes in PVs can be attributed to their highly structured micropores and chemical functionality, which enable selective interaction with target molecules, enhancing both flux and selectivity.

In addition to NFs and PVs, continuous MOF membranes have been explored for organic solvent nanofiltration (OSN) [192], membrane distillation (MD) [110], and ultrafiltration, such as like oil-water separation [193]. Despite these advancements, their full potential remains largely untapped. Currently, most research efforts are still limited to gas separation, necessitating further exploration of chemical-resistant MOF membranes for liquid-phase applications. Exploiting advantageous microstructures and designable chemistry is also vital to their application. Continuous membrane membranes still suffer from one or more concerns mentioned in Section 2.4.1.2, which greatly compromise their performance. Further research into precise synthesis approaches and versatile modifications, for example, customizing the orientations of MOFs crystals and the targeted functionalization of continuous membranes, would be beneficial for advancing MOF membranes toward widespread industrial adoption. Finally, expanding their application scope to address emerging challenges, such as the removal of pharmaceutical contaminants and per- and polyfluoroalkyl substances (PFAS), could provide a transformative solution to conventional membrane limitations.

Table 2.2 Continuous MOF membrane for liquid separation (The selected literature represents key studies identified through a Web of Science search using keywords such as “MOF membrane for liquid separaion”, “MOF membrane for nanofiltration separation”, “MOF membrane for desalination”, “MOF membrane for organic solvent separation” and “MOF membranes for pervaporation”)

| *MOFs* | Substrate | Fabrication method | Application | Permeance/flux | Selectivity | Ref. |
|---|---|---|---|---|---|---|
| *ZIF-300* | Alumina disc | Secondary growth | NF | 36.2 L $m^{-2}$ $h^{-1}$ $bar^{-1}$ | $CuSO_4$ 99.5% | [194] |
| *ZIF-8* | PES | Interfacial synthesis | NF | 6-38 L $m^{-2}$ $h^{-1}$ $bar^{-1}$ | Rose Bengal 98% | [195] |
| *ZIF-8* | PSf | In-situ growth | NF | 130 L $m^{-2}$ $h^{-1}$ $bar^{-1}$ | Proanthocyanidin 98.5% | [196] |
| *ZIF-8* | PES | LBL | NF | 5.1 L $m^{-2}$ $h^{-1}$ $bar^{-1}$ | NaCl 55.2%<br>$Na_2SO_4$ 93.6% | [197] |
| *MOF-303* | Alumina disc | In-situ growth | NF | 0.7 L $m^{-2}$ $h^{-1}$ $bar^{-1}$ | $MgCl_2$ 93.5%<br>$Na_2SO_4$ 96.0% | [198] |
| *UiO-66* | Alumina HF | In-situ growth | NF | 0.14 L $m^{-2}$ $h^{-1}$ $bar^{-1}$ | $Ca^{2+}$ 86.3%<br>$Mg^{2+}$ 98.0% | [69] |

| | | | | | | |
|---|---|---|---|---|---|---|
| | | | | | $Al^{3+}$ 99.3% | |
| *UiO-67* | AAO | Secondary growth | NF | $Li^+$ 27 mol $m^{-2}$ $h^{-1}$ | $Li^+/Mg^{2+}$ 159.4 | [199] |
| *Zn-BLD* | ZnO disc | Reactive seeding | NF | 0.15 mmol $m^{-2}$ $h^{-1}$ | ee value 33% | [200] |
| *CuTCPP* | Nylon | Secondary growth | NF | 87 L $m^{-2}$ $h^{-1}$ $bar^{-1}$ | Rose Bengal 93.8% | [201] |
| *CuBTC* | PI-paper | Cathodic electrodepositio n | NF | 8.4 L $m^{-2}$ $h^{-1}$ $bar^{-1}$ | Rose Bengal 99 % | [202] |
| *CAU-10-H* | Stainless steel mesh | Secondary growth | UF | $1.85 \times 10^5$ L $m^{-2}$ $h^{-1}$ | Oil > 99.9% | [203] |
| *MOF-303* | Stainless steel mesh | In-situ growth | UF | 12308 L $m^{-2}$ $h^{-1}$ | Oil > 99.35% | [193] |
| *UiO-66* | YSZ HF | In-situ growth | PV (Desalinatio n) | 29.8 L $m^{-2}$ $h^{-1}$ | NaCl 100% | [204] |
| *UiO-66* | Mullite | Secondary growth | PV (Desalinatio n) | 29.8 L $m^{-2}$ $h^{-1}$ | NaCl 99.9% | [205] |
| *Sm-DOBDC* | Alumina HF | Secondary growth | PV (Ethanol dehydration) | 0.6 kg $m^{-2}$ $h^{-1}$ | Separation factor 997 | [206] |
| *ZIF-71* | ZnO | Secondary growth | PV (Ethanol dehydration) | 0.32 kg $m^{-2}$ $h^{-1}$ | Separation factor 6 | [207] |
| *ZIF-71* | Alumina HF | Contra diffusion | PV (Ethanol dehydration) | 0.7 kg $m^{-2}$ $h^{-1}$ | Separation factor 5 | [83] |
| *CAU-10-H* | Alumina disc | Secondary growth | PV (Alcohol dehydration) | 0.6 kg $m^{-2}$ $h^{-1}$ | Separation factor 148 | [208] |
| *UiO-66* | Alumina HF | In-situ growth | PV (Ethanol dehydration) | 3.7 kg $m^{-2}$ $h^{-1}$ | Separation factor 55 | [209] |
| *UiO-66* | Alumina HF | In-situ growth | PV (Ethanol dehydration) | 1.5 kg $m^{-2}$ $h^{-1}$ | Separation factor 4.9 | [210] |
| *$Ni_2$(L-asp)$_2$bipy* | $SiO_2$ disc | Secondary growth | PV (Ethanol dehydration) | 0.6 kg $m^{-2}$ $h^{-1}$ | Separation factor 148 | [211] |
| *MOF-303-Urea* | Alumina HF | Contra diffusion | PV (Ethanol dehydration) | 0.07 kg $m^{-2}$ $h^{-1}$ | Separation factor 5371 | [212] |

| | | | | | | |
|---|---|---|---|---|---|---|
| *MOF-303 PDC-TDC* | Alumina disc | Secondary growth | PV (Ethanol dehydration) | 0.1 kg $m^{-2}$ $h^{-1}$ | Separation factor 8500 | [213] |
| *SIM-1* | Porous glass | Post-synthesis modification | PV (Ethanol dehydration) | 0.5 kg $m^{-2}$ $h^{-1}$ | Separation factor ∞ | [214] |
| *NU-906* | $SiO_2$ disc | Secondary growth | PV (Ethanol dehydration) | 0.1 kg $m^{-2}$ $h^{-1}$ | Separation factor 244 | [215] |
| *ZIF-71* | ZnO | Secondary growth | PV (Methanol dehydration) | 0.4 kg $m^{-2}$ $h^{-1}$ | Separation factor 21.4 | [207] |
| *ZIF-71* | ZnO | Secondary growth | PV (DMC/methanol) | 0.27 kg $m^{-2}$ $h^{-1}$ | Separation factor 5.3 | [207] |
| *MIL-53* | Alumina disc | Secondary growth | PV (Ethyl acetate dehydration) | 0.5 kg $m^{-2}$ $h^{-1}$ | Separation factor 1317 | [77] |
| *UiO-66* | YSZ HF | In-situ growth | PV (Butanol dehydration) | 2.96 kg $m^{-2}$ $h^{-1}$ | Separation factor >1000 | [216] |
| *UiO-66* | Alumina HF | In-situ growth | PV (Butanol dehydration) | 5.4 kg $m^{-2}$ $h^{-1}$ | Separation factor 4280 | [209] |
| *fum-Zr-MOF* | Alumina disc | In-situ growth | PV (Butanol dehydration) | 3.6 kg $m^{-2}$ $h^{-1}$ | Separation factor 1653 | [217] |
| *NU-906* | $SiO_2$ disc | Secondary growth | PV (Butanol dehydration) | 1.6 kg $m^{-2}$ $h^{-1}$ | Separation factor 2630 | [215] |
| *Ni-MOF-74* | Alumina tube | Self-conversion | PV (Butanol dehydration) | 1.8 kg $m^{-2}$ $h^{-1}$ | Separation factor 1094 | [218] |
| *MOF-303-Urea* | Alumina HF | Contra diffusion | PV (IPA dehydration) | 0.1 kg $m^{-2}$ $h^{-1}$ | Separation factor 500 | [212] |
| *Co-gallate MOF* | Co-NWA | In-situ growth | PV (Methanol/MTBE) | 2.03 kg $m^{-2}$ $h^{-1}$ | Separation factor 6711 | [219] |
| *UiO-66* | Alumina disc | Secondary growth | PV (Methanol/Toluene/MTBE) | Methanol 1.18 kg $m^{-2}$ $h^{-1}$<br>Methanol 1.03 kg $m^{-2}$ $h^{-1}$ | Separation factor 3220<br>Separation factor 28000 | [220] |

| | | | | | | |
|---|---|---|---|---|---|---|
| *MIL-160* | Alumina disc | In-situ growth | PV (Xylene isomers separation) | 0.1 kg $m^{-2}$ $h^{-1}$ | *p*-/*o*-xylene selectivity 38.5 | [221] |
| *Ni-MOF* | / | Vacuum filtration | OSN | Acetone 1253.98 L $m^{-2}$ $h^{-1}$ $bar^{-1}$ | Congo red 99.69% | [222] |
| *PCN-250* | Alumina disc | Secondary growth | OSN | 2.6 L $m^{-2}$ $h^{-1}$ $bar^{-1}$ | Methyl blue 93.7% | [223] |
| *UiO-66* | Nylon | Vacuum filtration | OSN | Methanol 175 ± 10 L $m^{-2}$ $h^{-1}$ | Rose Bengal 98% | [224] |
| *ZIF-8* | PES | In-situ growth | OSN | Ethanol 1.1 kg $m^{-2}$ $h^{-1}$ $bar^{-1}$<br>IPA 0.3 kg $m^{-2}$ $h^{-1}$ $bar^{-1}$ | Rose Bengal 84-94% | [225] |
| *Zr-MOF* | Alumina disc | In-situ growth | OSN (Methanol/DCM) | 17.71 kg $m^{-2}$ $h^{-1}$ | Methanol 70% to 99.5 wt% | [118] |
| *UiO-66(Zr)-$NH_2$* | Carbon cloth | In-situ growth | OSN | DCM 0.17 kg $m^{-2}$ $h^{-1}$ $bar^{-1}$<br>Methanol 0.24 kg $m^{-2}$ $h^{-1}$ $bar^{-1}$ | Methylene blue 99.9%<br>Oil red O 99.95%<br>Nile red 99.85% | [226] |
| *ZnBDC* | PAN | LBL | OSN | IPA 3.4 L $m^{-2}$ $h^{-1}$ $bar^{-1}$ | Brilliant Blue R 86% | [227] |
| *ZIF-8* | Alumina disc | In-situ growth | MD | 17.71 kg $m^{-2}$ $h^{-1}$ | NaCl 99.8% | [110] |

### 2.4.2 COF membrane

This section provides an overview of the synthesis techniques employed in continuous COF membranes, followed by a summary of their applications across diverse liquid separation fields.

### 2.4.2.1 Fabrication of a continuous COF membrane

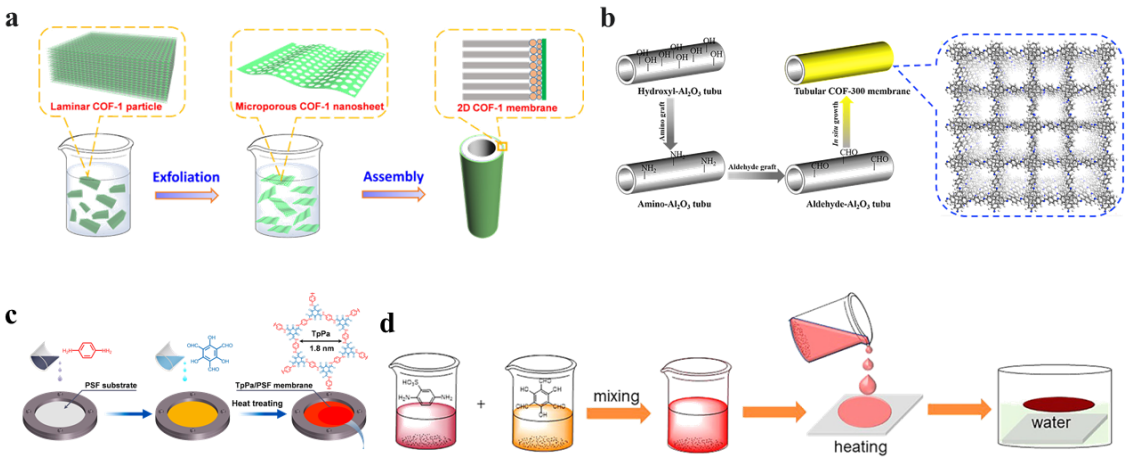



Figure 2.12 Fabrication of a continuous COF membrane. (a) Layer-by-layer stacking [228], Copyright © 2021 Elsevier B.V. All rights reserved. (b) In-situ growth method [229], Copyright © 2015 Elsevier B.V. All rights reserved. (c) Interfacial synthesis on a liquid-solid interface [230], Copyright © 2014 WILEY‐VCH Verlag GmbH & Co. KGaA, Weinheim. (d) Casting strategy [231], Copyright © 2014 WILEY‐VCH Verlag GmbH & Co. KGaA, Weinheim.

a) Layer-by-layer assembling strategy

According to the skeleton of COFs (Section 2.3), the majority of COFs display a 2D structure. Inspired by other 2D membranes, including GO, MXene and $MoS_2$ [232], the fabrication of continuous COF membranes through an LBL stacking strategy is considered feasible. Delamination of bulk COFs is needed to obtain isolated COF nanosheets. Obtaining isolated nanosheets requires breaking the van der Waals force between monolayers which are then dispersed in a solvent and subsequently deposited onto a porous substrate [233]. Available techniques for stacking included pressure-assistant filtration, spray coating and spin coating. For instance, COF-1 nanosheets, obtained via ultrasonication, were used to fabricate a continuous membrane through dip-coating on an alumina tube (Figure 2.12 a) [228]. The membrane thickness can be readily controlled by adjusting the density of COF nanosheets dispersed in the solvent and stacking circles. However, the inadequate developed delamination technique has caused major concerns. Currently, the exfoliation of bulk COFs is primarily performed via mechanical or ultrasonic methods, neither of which yields enough quantity nor consistently high-quality nanosheets for subsequent membrane assembly. Additionally, owing to the lack of bonding between the stacked COF layers and the substrate, the integrity of the resulting membrane is not satisfactory, and cracking usually occurs after drying. Therefore, pre-modification of the substrate is usually necessary for the LBL stacking process.

Like the LBL strategy employed for MOF membrane fabrication, LBL assembly has also been applied

to COFs by sequentially depositing COF layers onto a porous substrate. Wang et al. successfully fabricated two types of COF membranes, TpPa-9 and TpBD-5, on hydrolyzed polyacrylonitrile (PAN) substrates using a straightforward LBL synthesis method. By varying the number of synthesis cycles, membrane thicknesses ranging from 6 to 60 μm were achieved [234]. The concern of LBL growth is related to the relatively large thickness of the membranes, which, in turn, reduces permeance and limits overall performance.

b) In-situ growth

In-situ growth is recognized as a feasible method to produce high-crystalline COF membranes on substrate. This method was firstly applied in the fabrication of a COF-5 membrane on an $\alpha$-$Al_2O_3$ porous support with the assistance of microwave irradiation [235]. The alumina support provided both loading sites and the robustness of the resultant membrane. However, with respect to the support used for the in-situ growth of MOF membrane, the modification of the inorganic substrate is necessary to ensure high integrity. The $\alpha$-$Al_2O_3$ support utilized for COF-5 membrane fabrication was subsequently modified with APTES (3-aminopropyltriethoxysilane) and FPBA (4-formylphenylboronic acid) to functionalize $Al_2O_3$ support with $BO_3^{3-}$based APTES, facilitating the covalent anchoring between COF-5 and substrate. A similar strategy was also applied in the APTES-TPA grafted alumina for the fabrication of COF-300 (Figure 2.12 b) [229].

Polymer membranes have also been regarded as potential substrates for the in-situ growth of COF membranes. Wang et al. utilized an anion exchange membrane (AEM) by fixing it on a petri dish as the substrate for the growth of a sulfonated DABA-TFP COF [236]. During the growth process, the AEM substrate provided amine groups to covalently coordinate with the aldehyde groups of TFP, enabling the continuous growth of the COF membrane. This method demonstrated its versatility by successfully synthesizing COF membranes on three different commercial AEMs, highlighting its practicality and scalability.

The successful fabrication of a continuous COF membrane via an in-situ growth method heavily depends on the chemistry and microstructure of the chosen substrate. Complex modifications are often required when inorganic substrates are used to facilitate COF membrane growth. While polymeric substrates offer advantages such as low cost and high processability, their stability under solvothermal conditions remains a significant challenge. Most polymeric membranes swell or even degrade in harsh chemical environments and at elevated temperature, which are are typically necessary to achieve the crystallinity required for COF membranes.

c) Interfacial polymerization

Interfacial polymerization (IP) is a method used to synthesize a free-standing COF membrane after the

reaction of monomers at the interface. The fabricated membrane can be transferred to a substrate, mitigating the impact of the substrate on membrane formation [237]. The basic principle of this method is to confine the reaction to a constructed interface to eliminate secondary reactions in one phase [238]. Interfaces can be constructed between two immiscible liquids, gas-solid, gas-liquid and solid-liquid.

The liquid-liquid interface formed between two liquid phases with different polarities is the most widely used. It was first reported by Banerjee et al. in 2017 when they fabricated continuous $\beta$-ketoenamine-linked COFs membranes [239]. To achieve this, a DCM solution containing the aldehyde monomer was introduced into a beaker, followed by the addition of a water layer as buffer. An aqueous solution of PTSA was then carefully added to the top of the buffer layer. After 72 hours, the COF membrane was collected at the interface after the upper solution was removed. Precise control over the reaction rate was crucial for promoting crystallization in the IP process. In addition to the water-DCM interface, a range of liquid-liquid phase interfaces, including water-chloroform, water-ethyl acetate, and water-n-hexane systems [240] have been explored.

The gas-liquid mixture outperforms the liquid-liquid mixture by offering a more stable interface and a controllable reaction rate. Jiang et al. demonstrated the gas (vapour)-liquid IP method for the first time in the synthesis of the TFP-PDA COF on $Si/SiO_2$ disk [241]. The solid phase was obtained from an APTES-modified disk after it was coated with TFP containing an octanoic acid solution. The solid phase was place on top of the autoclave and react with the PDA vapour generated at 150 °C. Owing to the elevated temperature applied, a highly crystalline COF membrane was obtained. The formation of COF membranes at the gas-solid interface relies on highly controlled conditions, including a uniform interfacial environment, precise and continuous delivery of solid and gaseous monomers, and the stabilization of monomers at elevated temperatures.

Gas-liquid interface polymerization was developed by Lai et al. who synthesized the imine-based COF membranes at the air/water interface [242]. A solution containing amine and aldehyde monomers, dissolved in chloroform, was gradually introduced onto the water surface, followed by solvent evaporation. By precisely regulating the pressure at the polymerization interface, dense COF membranes with thickness of approximately 2~3 molecular layers were successfully formed.

Owing to the low thickness of free-standing membrane obtained on the liquid-liquid, liquid-gas, and solid-gas interface, inadequate mechanical strength can be expected in direct use. COFs are usually transferred to substrates to prepare COF composite membranes with desirable mechanical properties. However, the transfer process to a substrate inevitably results in different degrees of damage to the membranes. The IP process, which is based on liquid-solid interface by using the substrate as the sold surface, provides a potential solution (Figure 2.12c) [230]. The substrate should be saturated with one monomer solution, followed by contact with the liquid containing another monomer. Upon contact, the

reaction can be initiated on the membrane surface under suitable condition. Owing to its high processibility, this method has been applied for the scalable fabrication of COFs membranes based on PAN HFs [243].

d) Casting

The development of self-standing COF membranes with enhanced mechanical strength remains a key research focus. In recent years, various solvent-assisted polymerization techniques have been explored for their direct fabrication (Figure 2.12 d) [231]. Hou et al. synthesized highly charged COF membranes with one-dimensional nanochannels using a solvent casting approach [244]. They separately dissolved Tp and DABA monomers in N-methylpyrrolidone (NMP) and DMSO, and then mixed and sonicated them to create a homogeneous casting solution. This solution was cast onto a glass plate and dried in an oven, yielding a flexible, high-strength (Young's modulus: 2557 MPa) self-standing sulfonic acid-functionalized COF membrane (TpPa-$SO_3H$).

Despite advancements, the fabrication of continuous COF membranes remains challenging. First, their synthesis typically occurs under mild conditions, making it difficult to achieve both structural integrity and high crystallinity. A deeper understanding of reticular chemistry could enable the identification of optimal catalysts and solvents to regulate reaction rates. Second, most reported 2D COF membranes are claimed to have high crystallinity but suffer from low permeance due to disordered stacking. Moreover, the relationship between the performance and theoretical pore size of COF membranes does not align well, suggesting that molecular sieving is not achieved through the designed pores [245]. Third, while substrates provide necessary mechanical strength, they also limit scalability, highlighting the need for alternative fabrication strategies to enable large-scale production with robust self-standing COF membranes.

#### 2.4.2.2 Applications of continuous COF membrane in liquid separation.

Owing to their high porosity, structural stability, and tunable chemical functionality, COF membranes have high potential for both water treatment and organic solvent separation (Table 2.3).

a) Nanofiltration for water treatment

COF membranes have shown great potential in NF applications, particularly in dye removal and dye-salt fractionation, where their high porosity enhances permeability while maintaining efficient molecular sieving. Additionally, the versatile functional groups of COFs also increase the selectivity via the Donnan effect. The ability of these materials to selectively reject pollutants has also been extended to address emerging organic contaminants. Notably, COF membranes have been investigated for removing PFAS, which are persistent and challenging to eliminate through conventional NF membranes. A recent study introduced an anionic TpPa-$SO_3$ COF membrane fabricated via interfacial polymerization, achieving a promising water permeance of 19.9~37.5 L $m^{-2}$ $h^{-1}$ $bar^{-1}$ with over 99% rejection of short-chain PFAS and

high selectivity against salts [246].

b) Pervaporation

COF membranes have demonstrated superior PV performance in applications such as alcohol dehydration, azeotropic separation, and desalination. Unlike zeolite membranes, which often suffer from brittleness, COFs offer improved flexibility without compromising separation efficiency. A study successfully fabricated a COF membrane for alcohol dehydration, achieving superior selectivity with a high separation factor at 3620 and flux reaching 11.35 kg $m^{-2}$ $h^{-1}$ [247]. The ordered pore network of COFs enables rapid water transport while rejecting organic components, enhancing separation performance. Additionally, the tuneable chemistry of COFs allows for tailored hydrophilic or hydrophobic modifications, further optimizing selectivity.

c) Organic solvent nanofiltration

COF membranes have also been applied in OSNs, where their high chemical resistance and ultrahigh permeability offer substantial advantages. A COF membrane synthesized via solid–vapour interfacial polymerization exhibited an exceptional solvent flux exceeding 400 L $m^{-2}$ $h^{-1}$ $bar^{-1}$, significantly outperforming many polymeric OSN membranes [241]. Their rigid yet porous framework allows precise molecular sieving, making them highly effective for applications such as pharmaceutical purification and solvent recovery.

While continuous COF membranes have shown considerable promise in liquid separation, further development is needed to fully exploit their potential. Enhancing their water resistance will be essential for broader adoption in water treatment applications, particularly for emerging pollutants such as pharmaceutical residues and PFAS. Additionally, the structural integrity of COFs under harsh organic conditions suggests their potential for advanced separations, including crude oil fractionation and selective organic compound extraction.

Table 2.3 Summary of continuous COF membranes in liquid separation (The selected literature represents key studies identified through a Web of Science search using keywords such as “COF membrane for liquid separaion”, “COF membrane for nanofiltration separation”, “COF membrane for desalination”, “COF membrane for organic solvent separation” and “COF membranes for pervaporation”)

| *COFs* | Substrate | Fabrication method | Application | Permeance/flux | Selectivity | Ref. |
|---|---|---|---|---|---|---|
| $TpPa_9$ | PAN | LBL | NF | 265 L $m^{-2}$ $h^{-1}$ $bar^{-1}$ | Congo red 99% | [234] |
| $TpBD_5$ | PAN | LBL | NF | 339 L $m^{-2}$ $h^{-1}$ $bar^{-1}$ | Congo red 99% | [234] |
| *COF-300* | Alumina tube | In-situ growth | NF | 79 L $m^{-2}$ $h^{-1}$ $bar^{-1}$ | Rose Bengal 99.5 %<br>Methyl blue 99 % | [229] |

| | | | | | | |
|---|---|---|---|---|---|---|
| | | | | | Congo red 98.7 %<br>Acid blue 25 91.7 | |
| *COF-300* | Alumina tube | In-suit growth | NF | 152.5 L $m^{-2}$ $h^{-1}$ $bar^{-1}$ | Chrome black T 97.4%<br>$Na_2SO_4$ 96.0% | [229] |
| *COF-LZU-1* | Alumina tube | In-situ growth | NF | 76 L $m^{-2}$ $h^{-1}$ $bar^{-1}$ | Methyl blue 99%<br>Congo red 98.6%<br>Rose Bengal 99.1%<br>Acid fuchsin 99.4% | [248] |
| *TpPaBr* | Alumina tube | In-situ growth | NF | 23.5 L $m^{-2}$ $h^{-1}$ $bar^{-1}$ | NaCl 99.9% | [249] |
| *TpPa* | Alumina tube | In-situ growth | NF | 24 L $m^{-2}$ $h^{-1}$ $bar^{-1}$ | NaCl 98.2% | [249] |
| *TpHz* | PES | Secondary growth | NF | 4.5 L $m^{-2}$ $h^{-1}$ $bar^{-1}$ | $Na_2SO_4$ 58.3% | [250] |
| *IISERP-COF1 m* | Alumina tube | Secondary growth | NF | 0.5 L $m^{-2}$ $h^{-1}$ $bar^{-1}$ | NaCl 82.9%<br>$MgCl_2$ 90.6 %<br>$Na_2SO_4$ 96.3 % | [251] |
| *ACOF-1* | PAN | IP | NF | 141 L $m^{-2}$ $h^{-1}$ $bar^{-1}$ | Congo red 99.2%<br>Methyl blue 96.3% | [252] |
| *COF-LZU-1* | PSf | IP | NF | 6.57 L $m^{-2}$ $h^{-1}$ | $Na_2SO_4$ 90.9% | [253] |
| *TpPa* | PSf | IP | NF | 50 L $m^{-2}$ $h^{-1}$ $bar^{-1}$ | Congo red 99.5% | [230] |
| *TpPa* | PSf | IP | NF | 3.74 L $m^{-2}$ $h^{-1}$ $bar^{-1}$ | $Na_2SO_4$ 90.4% | [254] |
| *TaPa-II* | PMIA | IP | NF | 106 L $m^{-2}$ $h^{-1}$ $bar^{-1}$ | Congo red 99.2% | [255] |
| *TpPa-1* | PES | IP | NF | 300 L $m^{-2}$ $h^{-1}$ $bar^{-1}$ | Methyl blue 99%<br>Congo red 99% | [256] |
| *TpDAB* | PSf | IP | NF | 61 L $m^{-2}$ $h^{-1}$ $bar^{-1}$ | Congo red 97.7% | [257] |
| *TpDAB* | PSf | IP | NF | 15 L $m^{-2}$ $h^{-1}$ $bar^{-1}$ | Congo red 98% | [257] |
| *TpDAB-SBC* | PSf | IP | NF | 15 L $m^{-2}$ $h^{-1}$ $bar^{-1}$ | Allura red 95%<br>$Na_2SO_4$ 10% | [257] |
| *TpPa-$SO_3H$* | PES | IP | NF | 19.9–37.5 L $m^{-2}$ $h^{-1}$ $bar^{-1}$ | PFOS 99%<br>PFOA 95%<br>salt/PFAS | [246] |

| | | | | | | |
|---|---|---|---|---|---|---|
| | | | | | selectivity > 100 | |
| *3D-COF-1* | PVDF | IP | NF | / | $Na^+/Al^{3+}$ 345.3<br>$Na^+/Cu^{2+}$ 35.3<br>$K^+/Al^{3+}$ 823.5<br>$K^+/Cu^{2+}$ 84.3 | [258] |
| *DhTG$_{Cl}$* | | IP | RO | 1.7-3.7 L $m^{-2}$ $h^{-1}$ $bar^{-1}$ | NaCl 93.0 % | [259] |
| *TpPa* | AAO | In-situ growth | UF | 1173 L $m^{-2}$ $h^{-1}$ | Acid formic 93.5%<br>Ovalbumin 88.2%<br>BSA 88.6<br>God nanoparticles (10 nm) 95.2% | [260] |
| *DbTa-1* | / | IP | UF | 1536 L $m^{-2}$ $h^{-1}$ | / | [240] |
| *TpBd* | Sodium alginate | In-situ growth | PV (Ethanol dehydration) | 2.17 L $m^{-2}$ $h^{-1}$ | Separation factor 2099 | [261] |
| *COF-LZU-1* | YSZ HF | In-situ growth | PV | Acetone/Hexane 12.3 kg $m^{-2}$ $h^{-1}$<br>Acetone/cyclohexane 19 kg $m^{-2}$ $h^{-1}$ | Separation factor 4.7<br>Separation factor 2.4 | [262] |
| *COF-300* | YSZ HF | In-situ growth | PV (Acetone /Hexane) | Acetone/Hexane 2.5 kg $m^{-2}$ $h^{-1}$<br>Acetone/cyclohexane 3.7 kg $m^{-2}$ $h^{-1}$<br>Methanol/benzene 0.85 kg $m^{-2}$ $h^{-1}$ | Separation factor 30<br>Separation factor 13.4<br>Separation factor 4.3 | [262] |
| *TpPa* | PAN | IP | PV (Butanol dehydration) | 11.35 kg $m^{-2}$ $h^{-1}$ | Separation factor 3620 | [247] |
| *COF-1* | Alumina tube | LBL | PV (Desalination) | 22 kg $m^{-2}$ $h^{-1}$ | $MgSO_4$ 99.69%<br>$MgCl_2$ 99.96% | [263] |

| | | | | | | |
|---|---|---|---|---|---|---|
| *3D-OH-COF* | PI | In-situ growth | NF | Methanol 24.5 L $m^{-2}$ $h^{-1}$ $bar^{-1}$ | Acid fuchsin 97.7% | [264] |
| *M-TpTD* | / | Casting | OSN | Acetonitrile 27.8 L $m^{-2}$ $h^{-1}$ $bar^{-1}$<br>Water 11.8 L $m^{-2}$ $h^{-1}$ $bar^{-1}$ | Rose Bengal 84 %<br>Methylene blue 83%<br>Congo red 80 % | [265] |
| *M-TpBD* | / | Casting | OSN | Acetonitrile 18 L $m^{-2}$ $h^{-1}$ $bar^{-1}$<br>Water 9.2 L $m^{-2}$ $h^{-1}$ $bar^{-1}$ | Rose Bengal 99%<br>Methylene blue 94%<br>Congo red 96% | [265] |
| *CTP* | PAN | IP | OSN | Methanol 10.6 L $m^{-2}$ $h^{-1}$ $bar^{-1}$ | Reactive black 96.7%<br>Methyl orange 47.1%<br>Naphthalene blue black 83% | [266] |
| *TpPa-II* | $Si/SiO_2$ | IP | OSN | Water 211 L $m^{-2}$ $h^{-1}$ $bar^{-1}$<br>Acetonitrile 411 L $m^{-2}$ $h^{-1}$ $bar^{-1}$ | Congo red 98.9%<br>Methylene blue 98.1% | [241] |
| *Tp-DHF* | AAO | IP | OSN | Hexane 125 L $m^{-2}$ $h^{-1}$ $bar^{-1}$<br>Acetonitrile 100 L $m^{-2}$ $h^{-1}$ $bar^{-1}$<br>Water 60 L $m^{-2}$ $h^{-1}$ $bar^{-1}$<br>Ethanol 40 L $m^{-2}$ $h^{-1}$ $bar^{-1}$<br>Isopropanol 25 L $m^{-2}$ $h^{-1}$ $bar^{-1}$ | Reactive green 100% | [242] |
| *TpEt* | PAN HF | IP | OSN | Methanol 10 L $m^{-2}$ $h^{-1}$ $bar^{-1}$ | Direct red-80 99% | [243] |
| *TFPM-FP* | PAN | IP | OSN | Methanol 40 L $m^{-2}$ $h^{-1}$ $bar^{-1}$ | Acid fuchsin 100% | [267] |
| *Tp-Bpy* | Polyester | IP | OSN | Acetonitrile 339 L $m^{-2}$ $h^{-1}$ $bar^{-1}$<br>Water 211 L $m^{-2}$ $h^{-1}$ | Brilliant blue-G 94%<br>Acid fuchsin 97%<br>Cono red 80 | [239] |

| | | | | | | |
|---|---|---|---|---|---|---|
| | | | | $bar^{-1}$<br>Ethanol 174 L $m^{-2}$ $h^{-1}$ $bar^{-1}$<br>Methanol 108 L $m^{-2}$ $h^{-1}$ $bar^{-1}$ | | |
| *Tp-Azo* | Polyester | IP | OSN | Methanol 188 L $m^{-2}$ $h^{-1}$ $bar^{-1}$<br>Ethanol 261 L $m^{-2}$ $h^{-1}$ $bar^{-1}$ | Congo red 79%<br>Rhodamine B 99%<br>Reactive green 90% | [239] |
| *TraHz* | PAN | IP | OSN | Toluene 47 L $m^{-2}$ $h^{-1}$ $bar^{-1}$ | Congo red 98% | [268] |
| *TpaHz* | PAN | IP | OSN | Toluene 38 L $m^{-2}$ $h^{-1}$ $bar^{-1}$ | Congo red 98% | [268] |

## 2.5 Discontinuous Framework Membranes

Given the challenges in eliminating non-selective defects caused by poor intergrowth during the fabrication of continuous polycrystalline membranes, scaling of a continuous MOF or COF membrane has yet to be realized in industry. As such, integrating functional frameworks into other materials has emerged as a practical alternative for forming defect-free membranes. In this approach, crystalline frameworks are discontinuously incorporated into another component, resulting in composite membranes. When these frameworks are embedded into polymeric matrices, the resulting structures are referred to as mixed matrix membranes (MMMs). Owing to their chemical versatility, MOFs and COFs also have great potential in combination with other advanced materials, 2D materials specifically used to form composite materials. This section delves into framework-contained composite materials, focusing on their design principle, challenges, and potentials strategies to address these challenges. Furthermore, the discussion will extend to their applications in liquid separation.

### 2.5.1 Crystalline frameworks-contained mixed matrix membranes

#### 2.5.1.1 Roles of crystalline frameworks in mixed matrix membranes

The integration of frameworks into MMMs is often intended to enhance the properties of polymer membranes, rather than harness a particular property of the MOF particles. Owing to their easy processibility and low cost, polymeric membranes constitute the majority of the commercial membrane market. However, their applicability is greatly constrained by two limits. First, the intrinsic trade-off between permeability and selectivity, as defined by the Robeson upper bounds, poses a challenge to the concurrent enhancement of these properties [269]. Additionally, most polymers are prone to fouling

when used in liquid separation, leading to increased foulant adhesion of foulants, cake layer formation, and pore blockage, which compromise water transport and reduce membrane lifespan and fouling [270]. These can be effectively remediated by incorporating nanofillers. Diverse fillers, such as metals, metal oxides, carbon-based nanomaterials, and crystalline frameworks, have been extensively explored [271, 272].Compared with other nanofillers, frameworks are expected to provide better combinations for the presence of organic part. Indeed, both MOFs and COFs have been explored for constructing MMMs with high permeance and promising antifouling performance.

In MOFs/COFs incorporated MMMs, the intrinsic high-stability porosity plays an important role in improving the permeability of the membrane. The stable structure provides extra rigidity to the membrane by inhibiting polymer swelling or provide enhanced flux [273]. The intrinsic porosity of frameworks can promote the overall porosity of the MMMs membrane, leading to enhanced selective permeance. For example, the increased porosity resulting from the addition of 1.5 wt% loading of Cu-BTC in PES membrane was confirmed by porosity measurement, leading to a remarkable increase (207%) in pure water permeance from pristine 264.2 $L\,m^{-2}\,h^{-1}\,bar^{-1}$ of PES membrane to 546.4 $L\,m^{-2}\,h^{-1}\,bar^{-1}$ [274]. Similarly, a significant increase of gas permeance reaching 300% was found in COF-LZU1-containing PVA film because of the extra gas transport channels provided [275].

The enhanced antifouling performance of frameworks-contained MMMs is attributed to altered surface charge and hydrophilicity [276]. Surface charge significantly impacts antifouling performance by modulating interactions between the surface and fouling agents, such as proteins, bacteria, and other microorganisms. Negatively charged surfaces generally repel microorganisms with similarly charged cell walls, reducing adhesion. Conversely, positively charged surfaces tend to attract such organisms, leading to greater fouling due to electrostatic attraction. This effect is particularly evident in the reduced attachment of proteins and bacterial cells to surfaces with negative charges, as the repulsion between like charges creates an antifouling barrier [277]. As such, incorporating desirable MOFs/COFs to fine-tune the surface charge of MMMs is a promising strategy to minimize unwanted adhesion and optimize performance under specific operational conditions. Surface hydrophilicity enhances antifouling performance by forming a hydration layer on MMMs, which inhibits the adhesion of pollutants [278]. As observed in MIL-101/PVDF MMMs, adding 0.5 wt% MIL-101 caused a 30-degree decrease in the pure water contact angle and a flux recovery ratio greater than 50 % in a bovine serum albumin fouling test [279].

Unlike the positive role of MOFs/COFs in permeance and fouling restriction, their influence on the selectivity is under debate. Cases showing increased selectivity after the addition of frameworks have been reported and mostly explained by the increased viscosity [279] or introduced Donnan effect [280] by the framework fillers. The increased viscosity of solution leads to a slower solvent-nonsolvent exchange, diminishing the formation of macrovoids [281]. However, some believe that the selectivity

of resulting MMMs is governed by the original polymeric matrix [273, 282]. This is due to the complexity arising from the multifaceted influence of COFs and MOFs as additives on selectivity, which is governed by various factors, including their content, intrinsic chemistry, and compatibility with the polymer matrix.

The incorporation of MOFs and COFs into MMMs significantly enhances their mechanical strength and thermal stability due to the intrinsic properties of these frameworks. MOFs, form strong interfacial bonds with polymer matrices, reducing polymer chain flexibility and increasing tensile strength, while their high decomposition temperatures ranging from 500~550°C ensure structural integrity under extreme thermal conditions [283]. Similarly, COFs contribute to the mechanical robustness of MMMs through their rigid and porous structures, minimizing defects and improving membrane uniformity [284]. Their covalently bonded frameworks further increase the thermal resistance, enabling the membranes to maintain functionality at elevated temperatures.

### 2.5.1.2 Fabrication of framework-contained MMMs

a) Fabrication method

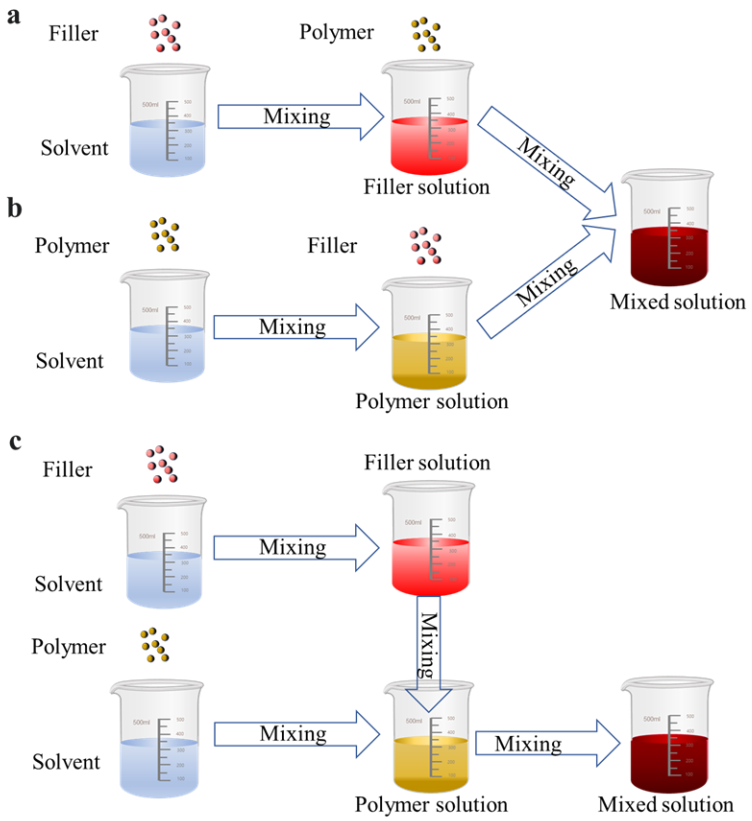



Figure 2.13 Different methods for preparing mixed suspensions. (a) and (b), filler and polymer added to the same solution in different orders. (c) The filler and polymer were dissolved/dispersed separately and then mixed together. Adapted from [285].

Generally, MMM fabrication involves the preparation of a mixed suspension, casting on a plate/substrate or spinning via spin coating, and eliminating the solvent via phase inversion or evaporation. The distinction from pure polymeric membrane fabrication is evident from the very first step when preparing the framework/polymer mixture. As shown in Figure 2.13, mixed suspensions can be prepared through three main methods: (A) dispersing filler particles into the solvent before introducing the polymer (Figure 2.13 a) [286], (B) dissolving the polymer into the solvent first and then adding the filler particles to the polymer solution (Figure 2.13 b) [287], and (C) dissolving the polymer and dispersing the filler particles in separate solvent systems, followed by combining the two suspensions (Figure 2.13 c) [288]. Among these routes, A and C are more frequently adopted for MOF and COF incorporation because of the lower viscosity of the initial filler/solvent suspension, which facilitates uniform dispersion. In contrast, route B, although applied in the preparation of MMMs with nanoparticles such as carbon nanotubes, silica, and zirconia, often leads to filler aggregation. This issue arises from the difficulty of achieving adequate dispersion in highly viscous polymer solutions. In addition to the blending method, several other factors should be carefully evaluated when fabricating MMMs.

b) Chemistry of filler/polymer pair

Among these challenges, pair-wise selection, which is directly associated with the morphology and separation performance of MMMs, is fundamentally important for MMM fabrication. The chemical compatibility between nanofillers and polymers is critical. In the case of MOFs, functional groups, such as amino groups, have been shown to improve interactions with polymer matrices. For example, $NH_2$-functionalized UiO-66 [289] and MIL [290] significantly enhanced $CO_2$ permeability and selectivity in polyimide-based MMMs. Similarly, the use of ZIF-7 and ZIF-8, owing to their structural compatibility with polybenzimidazole, has led to improved dispersion and gas separation performance [291]. The surface functionalization of MOFs, such as the introduction of amino or carboxyl groups, further enhances interfacial adhesion and prevents filler aggregation, resulting in defect-free membranes with increased permeability and selectivity.

Unlike MOFs, COFs are composed of covalent linkages of lighter elements (such as C, O, N, and B), thus exhibiting a fully organic nature and enhanced chemical compatibility with polymers [292, 293]. The functionalization of COFs enhances interfacial adhesion and reduces defects in MMMs. For example, COFs such as NUS-2 and NUS-3, when exfoliated into nanosheets and combined with polymers such as polybenzimidazole, demonstrated enhanced mechanical properties, gas permeability, and selectivity [294]. Similarly, incorporating COF-5 nanosheets into Pebax-1657 membranes improved $CO_2$ permeability and selectivity while maintaining long-term stability [284].

c) Contents

When porous framework fillers are incorporated into MMMs, increasing the loading of MOFs generally increases permeability because more nanoporous pathways are introduced for gas or liquid transport. For example, integrating up to 40 wt% of amino-functionalized ZIF-94 in a polyimide host substantially increases $CO_2$ permeability and retains selectivity, indicating that a judicious filler content maximizes both dispersion and performance [295]. However, exceeding the optimum filler fraction often induces aggregation, creating voids that reduce selectivity. Similarly, COF-based MMMs, such as COF-5 embedded in Pebax-1657, initially revealed a striking rise in $CO_2$ permeation at low or moderate filler contents, which was attributed to increased free volume and strong filler–matrix interactions [296]. Past a certain threshold, particle agglomeration undermines the membrane's uniformity and diminishes separation benefits. Thus, each MMM requires a carefully tailored filler loading that balances improved permeability with a defect-free, homogeneous morphology.

d) Physical properties of MOFs/COFs

The geometry of fillers, including their size and shape, significantly affects the performance of MMMs by influencing their dispersion, interfacial interactions, and transport properties. For MOFs, smaller particle sizes, such as nanoscale ZIF-8, enhance compatibility with polymer matrices by minimizing aggregation and ensuring uniform distribution, which improves gas selectivity and permeability [285]. However, overly large MOF particles can lead to non-selective voids at the polymer-filler interface, reducing the overall membrane performance. The shape of nanofiller also plays a role, for example, rod-like MOF particles can align with polymer chains, creating anisotropic pathways for selective transport [284]. The inherently crystalline and layered structures of COFs offer unique opportunities to tune their membrane properties. Exfoliated nanosheets of COFs, such as COF-5, enhance compatibility with polymer matrices, reducing resistance to gas or liquid transport. The nanosheet morphology creates extended interfacial contact with the polymer, resulting in improved mechanical stability and separation efficiency [280]. In contrast, bulky particles may disrupt the polymer matrix, introducing defects that compromise performance. Therefore, optimizing the filler geometry is crucial for achieving high-performing MMMs, with nanoscale fillers and tailored shapes that provide the best balance of compatibility, dispersion, and selectivity [285].

2.5.1.3 Framework-based MMMs in liquid separation.

As numerous MOF/COF incorporated MMMs have been utilized in gas separation, their application in liquid separation (Table 2.4), despite showing significant promise, has not yet been widely adopted because of the limited availability of stable MOFs and COFs.

Theoretically, the high surface area, tuneable pore sizes, and exceptional adsorption properties of crystalline frameworks can enhance permeability and possibly selectivity by improving water transport and hydrophilicity. This is beneficial for strengthening the antifouling effect of the water-based

filtration process and enhancing the ability to remove contaminants such as heavy metals and organic compounds [297-315]. For example, the integration of Co-MOF in polysulfone (PSf) increased membrane porosity, improved hydrophilicity, reduced surface hydrophobicity, and resulted in a more negative surface zeta potential. These changes led to a 360% improvement in water permeability while maintaining selectivity. Additionally, owing to reduced hydrophobic interactions and stronger electrostatic repulsion, the modified membranes exhibited superior resistance to natural organic matter fouling [299]. A similar conclusion was reached by Xia and colleagues during the fabrication of a PVDF-LUZ1 MMM. The PVDF-COF membrane, with a reduced pore size of 0.1038 μm, demonstrated ultrahigh water permeance at approximately 200 $L\,m^{-2}\,h^{-1}\,bar^{-1}$, which was double that of the unmodified PVDF membrane. Additionally, the PVDF-COF membrane significantly improved the rejection of water-soluble dyes, with RhB rejection increasing from 76.2% to 89.7%. Similarly, the rejection rates for larger dyes, such as Direct Red 80 and Congo Red, reached 99%.

Mass transport in pervaporation is highly reliant on their interactions between feed components and the surface of the confined space [316]. As such, additives with desirable physiochemical properties have been adopted in pervaporation membranes [317-320]. A typical example is the enhanced separation performance of COF-300 in COF-300-PDMS membrane [320]. This increase is attributed to the introduction of active hydrogen bonding sites (from amino and aldehyde groups) within the membrane, which selectively restrict water diffusion by increasing mass transfer resistance. Moreover, the high adsorption capacity and π-π interactions between COF-300 and aromatic compounds promote organic permeation. As a result, the 8 wt% COF-300/PDMS MMM achieved a 14.1% increase in furfural permeability and a 20% reduction in water permeability, leading to a 42.7% improvement in selectivity for furfural.

Like the PV process, crystalline framework containing MMMs have also been utilized in MD for the desalination and removal of persistent contaminants, resulting in improvements of performance and durability. For example, membranes modified with AlFu MOF have demonstrated significant improvements in flux and wetting resistance, maintaining high salt rejection during desalination [321]. COF-based membranes, such as those incorporating COF-LZU1 [322], have shown potential in treating emerging organic contaminants via the membrane distillation process, offering better ibuprofen rejection and stability under various operating conditions. COFs and MOFs offer high porosity, tuneable pore sizes, and thermal stability in the membrane distillation process, preventing the polymeric matrix from fouling and wetting. Therefore, the promising energy efficiency of the resulting membrane can be expected.

The promising stability of some MOFs and COFs renders them ideal additives in organic solvent-based separation [323-326]. Gyorgy Szekely and co-workers employed a multizoning method, realizing the target incorporation of MOFs on the membrane surface. The fabricated membranes with zirconium-

based MOFs (Zr-BI-fcu-MOF) achieved acetone permeance of 7.07 L $m^{-2}$ $h^{-1}$ $bar^{-1}$, significantly surpassing the 1.42 L $m^{-2}$ $h^{-1}$ $bar^{-1}$ observed for MMMs fabricated via direct mixing, while maintaining similar molecular weight cut-off (MWCO) values (~200 g $mol^{-1}$). This enhancement was attributed to the high porosity and tailored pore apertures of the MOFs, which facilitated efficient solvent transport while preventing the passage of larger solutes.

Table 2.4 COF/MOF based MMMs in liquid separation (The selected literature represents key studies identified through a Web of Science search using keywords such as "MOF/COF MMMs for liquid separaion", "MOF/COF MMMs for nanofiltration separation", "MOF/COF MMMs for desalination", "MOF/COF MMMs for organic solvent separation" and "MOF/COF MMMs in pervaporation")

| *Frameworks* | Loading (wt%) | Polymer matrix | Application | Permeance/flux | Selectivity | Ref |
|---|---|---|---|---|---|---|
| *CuBTC* | 3 | PPSU | NF | 135 L $m^{-2}$ $h^{-1}$ | MWCO (dye) 898 | [327] |
| *CuBTC* | 0.5 | PES | UF | 121 L $m^{-2}$ $h^{-1}$ | Chemical oxygen demand 66% | [328] |
| *CuBTC* | 0.5 | PVDF | FO | 58 L $m^{-2}$ $h^{-1}$ | Dextrose 90%<br>Urea 90%<br>$Na_2CO_3$ 90% | [329] |
| *MOF-5* | 0.75 | PES | NF | 77.1 $Lm^{-2}h^{-1}$ | Methylene blue 97%<br>Indigo carmine 89% | [297] |
| *MOF-801* | 4.8 | CS | PV (Ethanol/water) | 1.9 $Kgm^{-2}h^{-1}$ | Separation factor 2156 | [316] |
| *MOF-C300* | 1 | Pan | UF | 260 $Lm^{-2}h^{-1}bar^{-1}$ | Dextran 97% | [298] |
| *MOF-Co* | 4 | PSf | UF | 524 $Lm^{-2}h^{-1}bar^{-1}$ | PEG (400KDa) 97% | [299] |
| *MIL-53(Al)* | 5 | PVDF | UF | 44 $Lm^{-2}h^{-1}bar^{-1}$ | BSA 80% | [300] |
| *MIL-101* | 0.2 | PVDF | UF | 352 $Lm^{-2}h^{-1}$ | BSA 86% | [301] |
| *UiO-66* | 0.5 | PSf | NF | 225 $Lm^{-2}h^{-1}bar^{-1}$ | $As^{3+}$ 87.5% | [302] |
| *UiO-66* | 0.5 | PSf | NF | 5 $Lm^{-2}h^{-1}$ | HA 97% | [303] |
| *UiO-66* | 0.2 | CA/PVDF | RO | 6 $Lm^{-2}h^{-1}$ | NaCl 90.2% | [304] |
| *ZIF-8* | 20 | PDMS | NFt | 4 $Lm^{-2}h^{-1}$ | Congo red 87% | [305] |
| *ZIF-8* | 0.45 | PMIA | NF | 1.4 $Lm^{-2}h^{-1}$ | Congo red 98% | [306] |
| *ZIF-8* | 3 | CA | NF | 135 $Lm^{-2}h^{-1}$ | Methylene blue 93% | [307] |
| *ZIF-67* | 0.5 | PSf | NF | 82 $Lm^{-2}h^{-1}$ | BSA 96% | [308] |

| | | | | | | |
|---|---|---|---|---|---|---|
| *ZIF-8* | 0.5 | PVDF | PV(Methanol/water) | 380 $Kgm^{-2}h^{-1}$ | 1.6 (Water/methanol) | [330] |
| *ZIF-67* | 0.5 | PVDF | PV(Methanol/water) | 425 $Kgm^{-2}h^{-1}$ | 2 (Water/methanol) | [330] |
| *ZIF-L* | 30 | PDMS | PV (Ethanol recovery) | 0.6 $Kgm^{-2}h^{-1}$ | Separation factor 14 | [317] |
| *ZIF-8* | 10 | PDMS | PV (Ethanol recovery) | 1.8 $Kgm^{-2}h^{-1}$ | Separation factor 12 | [318] |
| *ZIF-91* | 20 | PDMS | PV (Ethanol recovery) | 0.8 $Kgm^{-2}h^{-1}$ | Separation factor 15 | [331] |
| *MIL-53* | 40 | PDMS | PV (Ethanol recovery) | 5.5 $Kgm^{-2}h^{-1}$ | Separation factor 11 | [332] |
| *ZIF-L* | 30 | PDMS | PV (Butanol recovery) | 0.4 $Kgm^{-2}h^{-1}$ | Separation factor 58 | [317] |
| *ZIF-8* | 10 | PDMS | PV (Butanol recovery) | 1.1 $Kgm^{-2}h^{-1}$ | Separation factor 21 | [288] |
| *ZIF-8* | 40 | PDMS | PV (Butanol recovery) | 4.8 $Kgm^{-2}h^{-1}$ | Separation factor 82 | [333] |
| *MOF-5* | 5 | PVC | PV (Toluene recovery) | 23 $Kgm^{-2}h^{-1}$ | Separation factor 10 | [319] |
| *AlFu MOF* | 1 | PVDF | DCMD | 12 $Kgm^{-2}h^{-1}$ | NaCl 99.9% | [334] |
| *AlFu MOF* | 1 | PVA | DCMD | 45 $Kgm^{-2}h^{-1}$ | NaCl 99.9% | [321] |
| *CuBTC* | 3 | PVDF | DCMD | 13.2 $Kgm^{-2}h^{-1}$ | PFAS 80% | [335] |
| *ZIF-8* | 0.8 | POTS | DCMD | 10.7 $Kgm^{-2}h^{-1}$ | NaCl 99.9% | [336] |
| *UiO-66-$NH_2$* | 2 | PVDF | DCMD | 21.3 $Kgm^{-2}h^{-1}$ | NaCl 99.9% | [337] |
| *CuBTC* | 20 | PDMS | OSN (Isopropanol) | 0.8 $Lm^{-2}h^{-1}bar^{-1}$ | Rose bengal 93% | [323] |
| *Cu-TCPP* | 1.5 | PI | OSN (Ethanol) | 1 $Lm^{-2}h^{-1}bar^{-1}$ | Brilliant blue R 96% | [324] |
| *MIL-47* | 20 | PDMS | OSN (Isopropanol) | 0.6 $Lm^{-2}h^{-1}bar^{-1}$ | Rose bengal 95% | [323] |
| *MIL-53 (Al)* | 0.5 | PMIA | OSN (Methanol) | 3 $Lm^{-2}h^{-1}bar^{-1}$ | nitroso R salt 94% | [325] |
| *t-Cu-TCPP* | 1.5 | PI | OSN (Ethanol) | 1.8 $Lm^{-2}h^{-1}bar^{-1}$ | Brilliant blue R 93% | [324] |
| *Zr–BI–**fcu**-MOF* | 5 | PBI | OSN (Toluene) | 7 $Lm^{-2}h^{-1}bar^{-1}$ | Methyl orange 99% | [326] |
| *Zn-TCPP* | 1.5 | PI | OSN (Ethanol) | 2.8 $Lm^{-2}h^{-1}bar^{-1}$ | Brilliant blue R 95% | [324] |

| | | | | | | |
|---|---|---|---|---|---|---|
| *ZIF-8* | 10 | PI | OSN (Isopropanol) | 2.1 $Lm^{-2}h^{-1}bar^{-1}$ | Congo red 95% | [338] |
| *ZIF-8* | 10 | PI | OSN (Ethanol) | 4.3 $Lm^{-2}h^{-1}bar^{-1}$ | Congo red 94% | [338] |
| *ZIF-8* | 20 | PDMS | OSN (Isopropanol) | 0.8 $Lm^{-2}h^{-1}bar^{-1}$ | Rose bengal 90% | [323] |
| *COF-300* | 8 | PDMS | PV (Furfural/water) | 2.1 $Kgm^{-2}h^{-1}$ | Separation factor 40 | [320] |
| *COF−$SO^{3-}$* | 12 | PES | NF | / | Uranium 92 % | [309] |
| *COF-LZU1* | / | PVDF | UF | 200 $Lm^{-2}h^{-1}bar^{-1}$ | Rhodamine blue 90%<br>Direct Red 80 99%<br>Congo red 99% | [310] |
| *COOH-COF* | 0.8 | PAN | UF | 940 $Lm^{-2}h^{-1}bar^{-1}$ | BSA 82 %<br>γ-globulin 99 % | [311] |
| *TamDbta* | 0.8 | CA | NF | 40 $Lm^{-2}h^{-1}$ | Phenol 90% | [312] |
| *TaPa-2* | 2 | PSf | UF | 200 $Lm^{-2}h^{-1}$ | HA 92% | [313] |
| *TbBd* | / | PVDF | NF | 123 $Lm^{-2}h^{-1}$ | Pb2þ 92% | [314] |
| *TpEB* | / | PAN | UF | 380 $Lm^{-2}h^{-1}bar^{-1}$ | BSA 93% | [315] |
| *SNW* | 1 | PES | NF | 116 $Lm^{-2}h^{-1}$ | Reactive green 97% | [276] |
| *COF-LZU1* | 1 | PVDF | DCMD | 56 $Lm^{-2}h^{-1}$ | Ibuprofen 100% | [322] |

### 2.5.1.4 Remaining challenges and potential solutions

For MOF-based MMMs, a primary issue lies in achieving seamless integration between the MOF fillers and the polymer matrix. Poor compatibility often results in filler aggregation and interfacial voids, which can compromise the mechanical strength and selectivity of the membrane. The inherent hydrolytic instability of certain MOFs and COFs further restricts their applicability, especially in water-based separations and harsh chemical environments.

Additionally, most reported MMMs are fabricated by directly blending fillers into a polymer solution. This approach often limits the effective utilization of the fillers' porous structures, as they are uniformly distributed throughout the membrane's cross-section. As a result, the majority of MOF or COF particles are embedded within the bulk of the membrane rather than concentrated on its surface. Since the separation performance of MMMs is predominantly governed by the properties of the top layer, the embedded MOF nanoparticles contribute minimally to the overall separation efficiency.

To mitigate these issues, various strategies can be utilized, including post functionalization with

hydrophilic or polymer-compatible groups, pre-modifications to increase stability, the introduction of other binders, and the use of novel synthetic routes. Post-synthetic modifications targeting metal centers or organic linkers have demonstrated efficacy in enhancing the chemical robustness of MOFs in MMMs, while offering superior chemical and thermal stability because their covalent frameworks present unique challenges.

In general, COFs are better nanofillers in polymeric matrices because of their good compatibility. However, the inherently brittle nature of COF powders and their tendency to form aggregation-prone structures complicate their processing into defect-free membranes. Ensuring uniform dispersion and strong interfacial adhesion with the polymer matrix is critical but challenging. Advances in functionalizing COFs with specific chemical groups, such as imine, hydroxyl, or carboxyl moieties, can be potential solutions for addressing these limitations to improve compatibility and minimize aggregation [280]. Leveraging the inherent modularity of COFs to design hybrid systems combine COFs can expand the functional and structural versatility of MMMs.

Advanced fabrication techniques can also offer additional pathways to create membranes with fewer defects and improved performance. MOF- and COF-based MMMs rely on a deeper understanding of filler-polymer interactions, enhanced functionalization strategies, and the adoption of innovative fabrication techniques [275]. The most promising approach involves the in-situ synthesis of nanofillers directly within the solvent used to dissolve the polymer matrix, which is promising to mitigate void formation and preventing aggregation [315]. By addressing these core challenges, unlocking the full potential of MMMs for a wide range of liquid separations would be possible.

### 2.5.2 Other framework-contained composite membranes

Composite membranes that integrate MOFs or COFs with other state-of-the-art materials, particularly 2D material, have also garnered significant attention in the field of separation.

#### 2.5.2.1 Framework-graphene oxide (GO) composite membrane

GO, a prominent oxidized derivative of graphene, has significant potential for various membrane separation processes, including nanofiltration, forward osmosis, and pervaporation [339]. A single GO nanosheet is characterized by the coexistence of $sp^3$ domains functionalized with oxygen-containing groups and $sp^2$ regions derived from graphene [340, 341]. The self-assembly of GO nanosheets occurs by stacking, resulting in the formation of GO membrane structures. Theoretically, the abundant functional groups distributed on the lamellar planes and edges of the nanolayers confer high hydrophilicity, facilitating the preferential adsorption of water molecules [342, 343]. These oxygen-containing functionalities readily hydrate, imparting negative charges that induce strong electrostatic repulsion between adjacent layers. This repulsion can increase the interlayer spacing, compromise

selectivity, and even lead to delamination of the GO membrane [344]. To address these challenges, the development of GO-based composite membranes through intercalation with MOFs or COFs has been proposed as a promising strategy.

Two primary fabrication methods have been developed for MOF/GO and COF/GO composite membranes: pressure-assisted self-assembly (PASA) and in-situ growth (Figure 2.14). The PASA technique, introduced by Ying *et al.* [345], involves the initial synthesis of crystalline frameworks and GO with desirable properties, followed by pressure-assisted filtration to form compact structures. This method is noted for its simplicity and the precise control it offers over the dimensions of the MOFs/COFs within the composite (Figure 2.14 a). For example, CuBDC nanosheets co-assembled with GO have been used to fabricate 2D membranes with high-aspect ratios, achieving effective molecular sieving for $H_2$ purification from $CO_2$ due to kinetic effects. The PASA approach has also been extended to a variety of MOFs, such as Al-, Cu-, Zn-, and Ni-based frameworks [345-348], as well as COFs such as TAPB-BTCA and TFP-PDA [349, 350], showing notable improvements in both gas and liquid separations. However, although the potential for the formation of π-π stacking and coordination between the MOF and GO has been reported [351], it is still widely accepted that there is only a physical combination of frameworks and GO nanosheet in physically assembled composite membrane, discounting the structural integrity of composite membrane under harsh conditions.

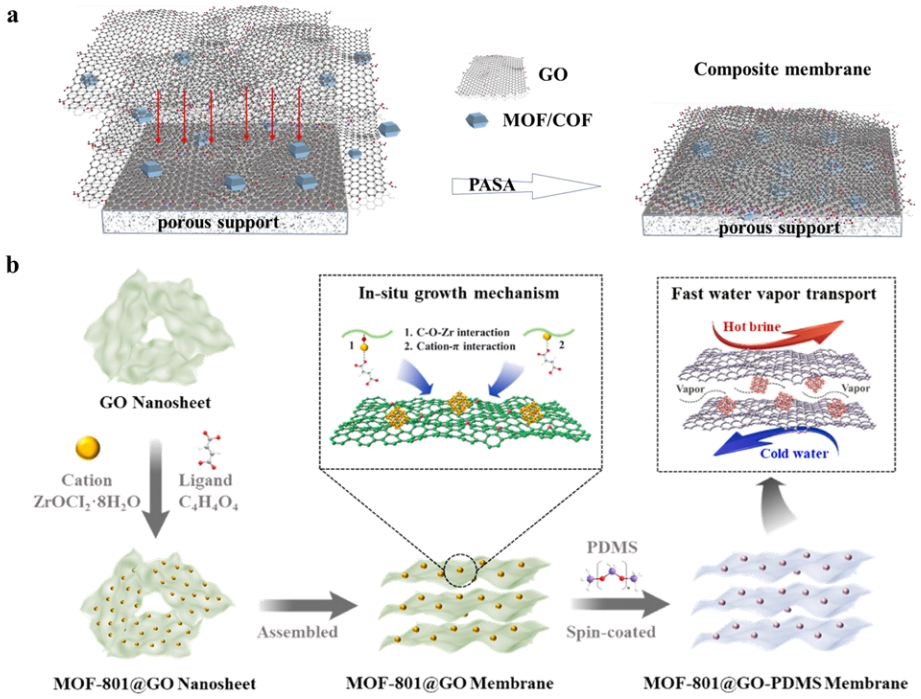



Figure 2.14 Fabrication of the framework-GO composite membrane. (a) Composite membrane prepared via the PASA method. (b) Composite membrane fabricated via the in-situ growth method [352].

The in-situ growth method has emerged as a promising approach for fabricating MOF/GO and COF/GO composite membranes because of its ability to establish strong chemical coordination between MOFs or COFs and the oxygen-containing functional groups of GO. This method ensures uniform integration of MOFs or COFs within the GO matrix, leveraging their inherent porosity and structural tunability [353]. Fabrication involves the fabrication of GO membranes, mostly via vacuum coating, followed by growth through MOF or COF through a one-step or a seeding-growth technique to form well-integrated composite membranes. The resulting composite membranes exhibit enhanced structural stability because the coordination bonds mitigate swelling and improve the interlayer interaction of GO. Beyond stability, the synergistic interaction between MOFs/COFs and GO introduces new functionalities, such as improved molecular sieving and selective permeability, making these membranes highly effective for separation applications.

A detailed example of the benefits of in-situ growth can be seen in work involving ZIF-8 nanocrystals grown on porous GO membranes [354]. The ZIF-8 crystals were precisely localized to patch microdefects in the oxygen-containing groups of the GO nanosheets. The robust interaction between the oxygen-based functional groups of GO and the ZIF-8 precursor ensured the membrane's stability under prolonged operational conditions, marking a substantial advance in water treatment and industrial applications. Additionally, this targeted coordination allowed for reduced interlayer spacing variability and maintained water permeance. The resulting membrane achieved significant improvements in solute rejection performance without compromising flux.

In addition to stabilizing the GO structure, the integration of MOFs or COFs can significantly enhance permeance by introducing additional mass transport channels through their intrinsic pores and increasing the number of effective transport pathways within the GO matrix. For example, MOF-801 nanoparticles were intercalated within GO layers, creating intrinsic pores that facilitated water transport (Figure 2.14 b) [352]. A similar enhancement was observed in COF/GO membranes, where vertically grown COF nanosheets expanded the interlayer spacing to 42.2 nm, resulting in a 157-fold increase in permeance [355]. These examples highlight how crystalline frameworks effectively complement the transport and sieving properties of GO.

Owing to the comprehensive enhancement of membrane stability, permeability and selectivity after combining frameworks with GO, other advanced techniques such as hot pressing and crystalline substrate integration, have also been developed [356]. A hot-pressed COF-GO membrane exhibited excellent structural integrity and performance in nanofiltration, combining high flux and dye rejection efficiency. Similarly, sandwich structures using crystalline substrates stabilized COF-GO composites, addressing challenges such as chlorine tolerance and fouling resistance. These innovations underscore the growing interest in the use of crystalline and interlocked structures to further expand the applications of MOF/COF-GO membranes in challenging environments.

2.5.2.2 Framework-MXene composite membrane

MXene, a family of two-dimensional materials composed of transition metal carbides, nitrides, or carbonitrides, offers exceptional potential in membrane separation due to their unique attributes [357]. These include atomic-level thickness, high aspect ratio, adjustable interlayer spacing, and abundant surface functional groups, which together enable efficient molecular sieving and selectivity [358]. Despite these advantages, MXene membranes face two major obstacles that hinder their practical applications. First, their permeance is often low because of the densely stacked structure of the MXene nanosheets, which restricts the formation of efficient mass transport channels. Second, the membranes exhibit poor stability, as they are prone to swelling, oxidation, and delamination, particularly in aqueous or oxidative environments [359]. These challenges necessitate innovative strategies, such as the incorporation of functional frameworks such as MOFs and COFs, to increase both the permeability and structural robustness of MXene-based membranes. These hybrid designs aim to leverage the distinct advantages of MOFs and COFs, such as their intrinsic porosity and tuneable chemistry, to complement and stabilize the MXene structure.

The fabrication of MXene-based composite membranes with MOFs or COFs typically involves strategies designed to ensure robust interactions and uniform dispersion. A common approach includes in-situ growth or electrostatic self-assembly, where frameworks are introduced to modify the MXene surface or intercalate between layers. For example, a $Ti_3C_2T_x$/TpTAPB membrane with an adjusted ratio is created by covalently bridging MXene with a COF followed by a vacuum filtration method, resulting in a hybrid material with a border interlayer space. This structure significantly enhanced water permeance, reaching 300 $Lm^{-2}h^{-1}bar^{-1}$ and dye rejection capabilities while maintaining stability over long-term nanofiltration test [360]. In another instance, ZIF-8 is integrated into MXenes to enhance oil/water separation. The resulting membrane achieves a significant improvement in water flux, surpassing 5000 $Lm^{-2}h^{-1}bar^{-1}$, and demonstrates excellent selectivity, with oil rejection rates exceeding 98%. This design addresses key challenges such as fouling and poor hydrophilicity by introducing larger transport channels and hydrophilic functional groups [361]. These examples underscore the potential of MOF and COF integration to transform MXene membranes into high-performance materials suitable for challenging separation tasks.

2.5.2.3 MOF-COF, MOF-MOF, COF-COF composite membranes

The complementary chemistries of MOFs and COFs provide an exciting avenue for the development of MOF-COF composite materials, offering a combination of desirable features and innovative functionalities. This is because although MOFs have high crystallinity and exceptional surface areas, they often suffer from poor stability in aqueous or acidic environments. COFs exhibit lower crystallinity and mass density but generally possess superior chemical and thermal stability [362]. Fortunately, the

versatile chemistry of both MOFs and COFs provides a viable opportunity for designing and manipulating innovative COF-MOF composites with many features and novel functionalities.

The integration of MOFs and COFs can be achieved through two main approaches: growing a MOF onto a COF (MOF-on-COF) or growing a COF onto a MOF (COF-on-MOF). The unit cell dimensions of MOFs, typically within the nanometer range (e.g., ZIF-8 and ZIF-67 with cubic cell parameters of approximately 1.7 nm), are comparable to the pore sizes of COFs [140, 363]. This structural compatibility allows COF pores to accommodate MOF units in configurations such as cages or chains. The MOF-on-COF strategy is particularly promising for creating porous structures with well-defined hierarchical channels, which are expected to deliver both high molecular sieving performance and enhanced mass transport efficiency. MOFs and COFs can be reinforced by strong covalent bonds formed through chemical reactions such as Schiff base condensation between aldehyde and amine groups, amino-carboxyl group condensation, or irreversible enol-to-keto tautomerization [364, 365]. Additionally, hybrid MOF-COF frameworks can also be stabilized by weaker interactions, including coordination bonds, hydrogen bonding, and π–π stacking [366, 367].

Fu et al. developed continuous and uniform [COF-300]-[ZIF-8] and [COF-300]-[$Zn_2(BDC)_2(DABCO)$] composite membranes by leveraging hydrogen-bonding interactions between terephthalic acid and imide groups in COF-300, as well as coordination interactions with $Zn^{2+}$ ions [368]. Similarly, defect-free composite membranes of [COF-300]-[UiO-66] and [$H_2$P-DHPh COF]-[UiO-66] were fabricated on COF-300 surfaces via strong ligation between $Zr^{4+}$ ions in UiO-66 and amine groups in the COF layer [369, 370]. Pu et al. further advanced this strategy by designing negatively charged TpPa-$SO_3$H COF nanosheets as a porous support for secondary growth, facilitating the formation of ultrathin and uniform ZIF-8, ZIF-67, and UiO-66 layers through robust electrostatic interactions with MOF precursors [371].

A MOF-on-COF composite membrane has also demonstrated potential in nanofiltration for removing organic pollutants from water. This was achieved by confining the growth of ZIF-8 on TaPa-1 nanofibers fabricated by electrospinning. These flexible nanofibers, which serve as porous supports, offer a unique alternative to conventional substrates such as inorganic discs, metal meshes, and polymer membranes. Additionally, their intrinsic nanoscale pores enhance the permeability and selectivity for organic dyes. The resulting composite membrane exhibited outstanding performance, achieving a pure water permeance of 29.3 L $m^{-2}$ $h^{-1}$ $bar^{-1}$ and a methylene blue rejection rate of 96%. This innovative design highlights the synergistic benefits of combining the precise molecular sieving capabilities of MOFs with the flexibility and stability of COFs [372].

The development of MOF-MOF and COF-COF hybrid membranes has broadened the scope of advanced separation materials, complementing the progress in MOF-COF composites. MOF-MOF membranes address challenges such as noncrystalline pores while enabling hierarchical structures and the

diversification of MOF-based membranes [373, 374]. Two key approaches for constructing MOF-MOF hybrids include epitaxial growth, where well-matched lattice parameters facilitate the seamless growth of one MOF on another, and postsynthetic modification, which involves altering the metal nodes or linkers of the initial MOF to incorporate secondary MOFs [375]. For example, functionalizing the surface of a preformed MOF can anchor metal ions from a secondary MOF, reducing energy barriers and promoting growth [376]. The UiO-66-$(COOH)_2$/UiO-66-$NH_2$ membrane exemplifies this strategy, achieving excellent $Mg^{2+}/Li^{+}$ separation by combining the advantages of dual functional groups and porous architectures [373]. Similarly, the double-layered UiO-66-$NH_2$@ZIF-8 membrane provides multidimensional pores, enhancing water flux (36.7 L $m^{-2}$ $h^{-1}$ $bar^{-1}$) while maintaining dye rejection rates above 97% [374].

Although less explored, COF-COF membranes show significant potential in liquid separation applications. A notable example is a 3D-/2D-COF composite membrane formed by in-situ growth of COF-300 on COF/LZU1, resulting in a heterogeneous crystalline structure with a pore size distribution centered at ~0.63 nm. This membrane achieved superior nanofiltration performance, with molecular weight cutoffs (MWCOs) of ~350 and ~400 g $mol^{-1}$ in water and ethanol, respectively, and solvent permeances of 21.2 and 12.2 L $m^{-2}$ $h^{-1}$ $bar^{-1}$. Furthermore, its remarkable robustness under high transmembrane pressures, acid and alkali resistance, and prolonged operation for over 650 hours highlights the potential of COF-COF membranes [377]. Despite being in the early stages of development, COF-COF composites hold promises for fabricating highly stable membranes tailored for challenging liquid separation processes.

Table 2.5 Composite membranes constructed from MOF/COF with 2D materials for liquid separation (The selected literature represents key studies identified through a Web of Science search using keywords such as “MOF/GO composite membrane for liquid separaion”, “COF/GO composite membrane for liquid separation”, “MOF/MXene membrane for liquid separation”, “COFs composite membrane for liquid separation” and “MOFs compositemembranes for liquid separation”)

| *Membranes* | Fabrication method | Support | Application | Permeance/Flux | Selectivity | Ref. |
|---|---|---|---|---|---|---|
| *Al-MOF/GO* | PASA | Nylon | NF | 51.6 $Lm^{-2}h^{-1}bar^{-1}$ | Congo red 100% | [378] |
| *Cu-TCPP/GO* | PASA | Nylon | NF | 165 $Lm^{-2}h^{-1}bar^{-1}$ | Congo red 99%<br>Rhodamine B 95%<br>Direct red 96%<br>$Na_2SO_4$ 25% | [353] |
| *Co/Ni-MOF/GO* | PASA | CA | NF | 56.9 $Lm^{-2}h^{-1}bar^{-1}$ | Methylene blue | [379] |

| | | | | | | |
|---|---|---|---|---|---|---|
| | | | | | 100% | |
| | | | | | Methyl orange 99% | |
| *Cu-BTC/GO* | PASA | PVDF | NF | 15.5 $Lm^{-2}h^{-1}bar^{-1}$ | $Cs^{+}/Th^{4+}$ 305 | [380] |
| | | | | | $Cs^{+}/UO_2^{2+}$ 40 | |
| *Zn-BTC/GO* | PASA | PVDF | NF | 1.4 $Lm^{-2}h^{-1}bar^{-1}$ | $Cs^{+}/Th^{4+}$ 341 | [380] |
| | | | | | $Cs^{+}/UO_2^{2+}$ 105 | |
| | | | | | $Cs^{+}/Sc^{3+}$ 38 | |
| *Ni-BTC/GO* | PASA | PVDF | NF | 1 $Lm^{-2}h^{-1}bar^{-1}$ | $Cs^{+}/Th^{4+}$ 527 | [380] |
| | | | | | $Sr^{2+}/Th^{4+}$ 50 | |
| | | | | | $Ce^{3+}/Th^{4+}$ 38 | |
| *ZIF-8/GO* | PASA | PSf | NF | 16.4 $Lm^{-2}h^{-1}bar^{-1}$ | $Na_2SO_4$ 86% | [381] |
| | | | | 45.4 $Lm^{-2}h^{-1}bar^{-1}$ | Congo red 99% | |
| *MOF-303/GO* | PASA | Alumina | PV (ethanol dehydration) | 3.2 $Kgm^{-2}h^{-1}$ | Separation actor 320 | [346] |
| *Sm-MOF/GO* | In-suit growth | / | NF | 26 $Lm^{-2}h^{-1}bar^{-1}$ | Rhodamine B 91% | [382] |
| | | | | | Methylene blue 91% | |
| *ZIF-8/GO* | In-suit growth | Tubular ceramic | OSN | 6 $Lm^{-2}h^{-1}bar^{-1}$ | Dye 99% | [383] |
| *ZIF-8/GO* | In-situ growth | Alumina | NF | 4 $Lm^{-2}h^{-1}bar^{-1}$ | Methyl orange 86% | [354] |
| | | | | | Crystal violet 85% | |
| *UiO-66/GO* | PASA | PAN | PV (Ethanol dehydration) | 4 $Kgm^{-2}h^{-1}$ | Separation factor 6,076 | [345] |
| *UiO-66/rGO* | PASA | PC | | 15 $Lm^{-2}h^{-1}bar^{-1}$ | Rhodamine B 85% | [384] |
| *MIL-40A/GO* | PASA | PC | NF | 15 $Lm^{-2}h^{-1}bar^{-1}$ | Methylene blue 95% | [385] |

| | | | | | | |
|---|---|---|---|---|---|---|
| *UiO-66/rGO* | PASA | PC | NF | 15 $Lm^{-2}h^{-1}bar^{-1}$ | / | [385] |
| *MOF-801/GO* | In-situ growth + PASA | PVDF | DCMD | 29 $Kgm^{-2}h^{-1}$ | NaCl 100% | [352] |
| *MOF-101(Al)/MXene* | In-situ growth | PVDF | NF | 17 $Lm^{-2}h^{-1}bar^{-1}$ | $Na_2SO_4$ 99%<br>$MgSO_4$ 97%<br>$MgCl_2$ 85%<br>NaCl 83% | [386] |
| *ZIF-8/MXene* | Vaccum filtration | CA | UF | 4000 $Lm^{-2}h^{-1}$ | Oil rejection 97% | [361] |
| *MIL-53(Fe)/MXene* | Vaccum filtration | PAN | UF | 1075 $Lm^{-2}h^{-1}$ | Oil rejection 99% | [387] |
| *COF-1/GO* | PASA | PAN | NF | 310 $Lm^{-2}h^{-1}MPa^{-1}$ | Methylene blue 99%<br>Congo red 99%<br>Reactive black 99%<br>Direct red 99% | [388] |
| *TFB-PDA/GO* | PASA | Nylon | OSN | Ethanol 51 $Lm^{-2}h^{-1}bar^{-1}$<br>Methanol 60 $Lm^{-2}h^{-1}bar^{-1}$ | Methylene blue 99%<br>Congo red 100% | [350] |
| *CTF/GO* | PASA | PC | NF | 226 $Lm^{-2}h^{-1}bar^{-1}$ | Chrome black T 99%, Congo red 93%<br>Methyl blue 93%<br>Alcian black 93% | [389] |
| *COF/GOx* | In-situ growth + spray coating | Filtration paper | UF | 26,000 $Lm^{-1}h^{-1}$ $bar^{-1}$ | DCM/Water separation efficiency 98.3% | [390] |
| *v-COF/GO* | In-situ growth + PASA | MCE | UF | 12 100 001765 $Lm^{-2}h^{-1}bar^{-1}$ | Oil rejection 100% | [355] |
| *COF-TaPa/GO* | PASA+Hot | Nylon | NF | 167 $Lm^{-2}h^{-1}bar^{-1}$ | Crystal violet | [356] |

| | | | | | | |
|---|---|---|---|---|---|---|
| | pressing | | | | 98%<br>Methylene blue 97%<br>Acid chrome blue K 68%<br>$MgCl_2$ 9%<br>NaCl 3% | |
| *TpPa-$SO_3H$/MXene* | Vacuum filtration | PES | NF | 376 $Lm^{-2}h^{-1}bar^{-1}$ | Methyl orange 43%<br>Basic fuchsin 67%<br>Methyl blue 96% | [391] |
| *TpPa/MXene* | Vacuum filtration | PES | OSN | 300 $Lm^{-2}h^{-1}bar^{-1}$ | Congo red 98%<br>Methyl blue 96%<br>Methyl orange 97% | [360] |
| *COF-LZU-1/MXene* | Vacuum filtration | PVDF | UF | 450 $Lm^{-2}h^{-1}bar^{-1}$ | Oil rejection 99% | [392] |
| *3D-S-COF/MXene* | Interficial polymerization+vacuum coating | Nylon | UF | 240 $Lm^{-2}h^{-1}bar^{-1}$ | Oil rejection 98% | [393] |
| *TpBD/MXene* | Vacuum filtration | PES | UF | 4093 $Lm^{-2}h^{-1}bar^{-1}$ | Oil rejection 100% | [394] |
| *UiO-66/ZIF-8* | In-situ growth | PVDF | NF | 37.6 $Lm^{-2}h^{-1}bar^{-1}$ | Direct red 100%<br>Acid orange 100%<br>Methyl orange 99%<br>Methylene blue 97% | [374] |
| *UiO-66-$(COOH)_2$/UiO-66-NH* | In-situ growth | Alumina | NF | / | $Mg^{2+}/Li^+$ selectivity 6.7 | [373] |
| *TaPa-1/ZIF-67* | Interficial | / | NF | 109 $Lm^{-2}h^{-1}bar^{-1}$ | Methyl blue 97% | [368] |

| | | | | | | |
|---|---|---|---|---|---|---|
| | polymerization + In-situ growth | | | | | |
| *TaPa-1/ZIF-8* | In-situ growth | PAN | NF | 29.3 $Lm^{-2}h^{-1}bar^{-1}$ | Methylene blue 96% | [372] |
| *TaPa-1/ZIF-8* | Interficial polymerization + In-situ growth | PVDF | NF | 58.1 $Lm^{-2}h^{-1}bar^{-1}$ | Direct red 97%<br>Acid orange 99%<br>Methyl orange 100%<br>Methylene blue 100% | [395] |
| *MATPA/Zr-MOF* | In-situ growth + Vacuum filtration | PVDF | UF | 162 $Lm^{-2}h^{-1}bar^{-1}$ | Oil 100% | [362] |
| *COF-LZU1/COF-300* | Vacuum filtration + in-situ growth | PAN | NF<br>OSN (Ethanol) | 21.2 $Lm^{-2}h^{-1}bar^{-1}$<br>12.2 $Lm^{-2}h^{-1}bar^{-1}$ | MWCO(dye) 350$gmol^{-1}$<br>MWCO(dye) 400$gmol^{-1}$ | [377] |

### 2.5.2.4 Summary and perspectives

MOF/COF composite membranes have shown remarkable potential in a wide range of separation applications, leveraging the intrinsic chemical functionality and structural advantages of porous frameworks while effectively mitigating intercrystalline defect-related issues. When integrated with advanced 2D materials, such as GO and MXene, the resulting membranes benefit from enhanced structural stability through strong interfacial interactions, while their porosity and functional properties further contribute to improved separation performance. Despite these promising advancements, several critical challenges remain: i) the long-term stability of interfacial coordination between the frameworks and 2D nanosheets under operational conditions requires further investigation; ii) the precise and targeted growth of MOF/COF structures on nanosheet microdefects or edges, which would fully leverage their intrinsic properties, remains underexplored; and iii) the mechanisms driving the enhanced separation performance of these composite membranes need to be comprehensively elucidated.

To address these issues, novel and innovative construction methods for composite membranes are imperative to achieve precise structural control and reliable performance. For example, strategies involving advanced in-situ growth techniques, electrochemical deposition, or tailored surface functionalization could facilitate more uniform integration of MOFs/COFs with 2D nanosheets,

minimizing defects and optimizing interface stability. Moreover, a broader exploration of the application scope of GO-MOF/COF composite membranes is essential. Expanding their use beyond traditional water purification could include areas such as organic solvent nanofiltration, pharmaceutical separations via nanofiltration, and desalination via membrane distillation. Additionally, investigating the performance of these hybrid membranes under harsh conditions, such as extreme pH, high pressures, or oxidative environments, could unlock their potential for industrial-scale applications. Future research should prioritize scalable and environmentally friendly fabrication methods, ensuring that these advanced membranes can transition from the laboratory to practical implementation while maintaining sustainability and cost-effectiveness.

The development of hybrid materials such as MOF-COF, MOF-MOF, and COF-COF remains in its infancy, with significant potential yet to be realized. While current research highlights that these hybrid materials generally outperform their single-component counterparts, their full capabilities remain untapped. Several critical challenges must be addressed to advance the design and application of multi-component crystalline frameworks. i) Constructing atomically precise structural models for these hybrids is a major challenge. Although combining small and large pore frameworks has been reported to increase both permeance and selectivity, the lack of detailed mechanistic explanations raises questions, particularly since the current understanding suggests that large pores primarily dictate a membrane's MWCO. ii) The chemical design of hybrid membranes offers considerable potential. Covalently linking robust COFs with MOFs could broaden the operational scope of membranes for water and organic solvent separations. Furthermore, optimizing the functional groups within different components for specific applications could unlock new performance capabilities. iii) In terms of synthesis, methods for fabricating MOF-COF hybrids remain limited and require significant refinement. Establishing a universal integration strategy that minimizes individual drawbacks while increasing the strengths of each component is crucial for further progress. For example, creating strong conjugated linkages, such as C=C or C≡C bonds, could simultaneously enhance stability and crystallinity. In addition to covalent bonding, exploring other interaction types, such as metal coordination, hydrogen bonding, or physical interactions, could provide diverse pathways for constructing robust hybrid frameworks. Advancing these approaches would enable the creation of multifunctional membranes with superior properties, paving the way for broader applications in advanced separation technologies.

## 2.6 Conclusion

Crystalline frameworks have demonstrated significant potential in a wide range of liquid separations, both as continuous framework membranes and as components in composite membranes. The outstanding performance of these materials is attributed to their regularly porous structures and versatile chemistry. Guided by reticular chemistry, the synthesis of pure crystalline frameworks and framework-

based membranes has been extensively explored. However, challenges persist in the fabrication and practical application of framework membranes for liquid separation.

The fabrication of continuous MOF membranes is primarily hindered by several challenges, including: a) poor membrane integrity due to weak binding with the substrate, b) low nucleation density in conventional solvothermal processes, c) non-selective defects caused by intercrystalline gaps, d) blocked crystal openings resulting from insufficient orientation control, e) excessive membrane thickness, and f) limited exploration of more stable MOF materials. Despite these challenges, continuous MOF membranes have been widely applied in various liquid separation processes, such as nanofiltration for the removal of pollutants from water or organic solvents, solvent/solvent separation via pervaporation, and desalination. To explore advanced applications and extend their use to commercial scales, addressing the aforementioned fabrication challenges systematically is essential.

The fabrication of continuous COF membranes faces significant challenges in achieving both structural integrity and high crystallinity. Although most reported COF membranes are claimed to exhibit high crystallinity, their permeance is often severely compromised by disordered stacking. Furthermore, the relationship between membrane performance and theoretical pore size is frequently inconsistent, suggesting that molecular sieving may not occur through the designed pores as intended.

Currently, incorporating COFs into a polymer matrix appears to be a more promising approach for scalable applications owing to their intrinsic organic nature and enhanced chemical compatibility with polymers. However, the inherently brittle nature of COF powders and their tendency to form aggregation-prone structures complicate their homogeneous incorporation into the polymer matrix. Ensuring uniform dispersion and strong interfacial adhesion with the polymer matrix is critical yet challenging. Pairing COFs with suitable polymeric matrices by leveraging their chemical compatibility is essential to optimize the integrity and performance of the resulting membrane. Additionally, advanced mixing techniques and feasible membrane fabrication processes must be developed to address these challenges.

Combining crystalline frameworks with advanced 2D materials, such as GO, MXene, and other 2D frameworks, has shown potential in achieving enhanced stability and functionality. Despite this progress, the long-term stability of the interfacial coordination between crystalline frameworks and 2D nanosheets under operational conditions requires further investigation. Moreover, the fabrication of composite membranes with precise structural control is necessary to fully leverage the intrinsic properties of both components. A deeper understanding of the mass transport mechanisms within these composite membranes also needs to be comprehensively elucidated to guide future developments in this field.

With the aim of addressing the major concerns in the literature review section, key objectives in the

author's research presented in the following chapters are listed here:

- A defect-free MOF membrane with high structural integrity will be fabricated on a porous support.
- The oriented growth of MOFs during membrane synthesis is expected to be achieved to regulate permeation channels.
- The influence of the MOF orientation on the membrane permeance and selectivity will be investigated.
- A feasible method for the homogeneous incorporation of COF nanosheets into a polymeric matrix will be explored.
- A high-performance COF-incorporated MMM with high permeance and competitive selectivity is expected to be developed.
- A 2D composite membrane will be constructed by confining the growth of the MOFs within the 2D interlayers of GO.
- The potential of stabilized GO/MOF composite membranes for membrane desalination will be investigated.

## References

[1] R. Freund, S. Canossa, S.M. Cohen, W. Yan, H. Deng, V. Guillerm, M. Eddaoudi, D.G. Madden, D. Fairen-Jimenez, H. Lyu, L.K. Macreadie, Z. Ji, Y. Zhang, B. Wang, F. Haase, C. Wöll, O. Zaremba, J. Andreo, S. Wuttke, C.S. Diercks, 25 Years of Reticular Chemistry, Angewandte Chemie International Edition 60(45) (2021) 23946-23974. https://doi.org/https://doi.org/10.1002/anie.202101644.
[2] O.M. Yaghi, Reticular Chemistry in All Dimensions, ACS Central Science 5(8) (2019) 1295-1300. https://doi.org/10.1021/acscentsci.9b00750.
[3] H. Li, M. Eddaoudi, T.L. Groy, O. Yaghi, Establishing microporosity in open metal− organic frameworks: gas sorption isotherms for Zn (BDC)(BDC= 1, 4-benzenedicarboxylate), Journal of the American Chemical Society 120(33) (1998) 8571-8572.
[4] H. Li, M. Eddaoudi, M. O'Keeffe, O.M. Yaghi, Design and synthesis of an exceptionally stable and highly porous metal-organic framework, nature 402(6759) (1999) 276-279.
[5] M. Fujita, J. Yazaki, K. Ogura, Preparation of a macrocyclic polynuclear complex,[(en) Pd (4, 4'-bpy)] 4 (NO3) 8 (en= ethylenediamine, bpy= bipyridine), which recognizes an organic molecule in aqueous media, Journal of the American Chemical Society 112(14) (1990) 5645-5647.
[6] D. Ongari, L. Talirz, B. Smit, Too Many Materials and Too Many Applications: An Experimental Problem Waiting for a Computational Solution, ACS Central Science 6(11) (2020) 1890-1900. https://doi.org/10.1021/acscentsci.0c00988.
[7] A.P. Cote, A.I. Benin, N.W. Ockwig, M. O'Keeffe, A.J. Matzger, O.M. Yaghi, Porous, crystalline, covalent organic frameworks, science 310(5751) (2005) 1166-1170.
[8] R.K. Sharma, P. Yadav, M. Yadav, R. Gupta, P. Rana, A. Srivastava, R. Zbořil, R.S. Varma, M. Antonietti, M.B. Gawande, Recent development of covalent organic frameworks (COFs): synthesis and catalytic (organic-electro-photo) applications, Materials Horizons 7(2) (2020) 411-454. https://doi.org/10.1039/C9MH00856J.

[9] M. O'Keeffe, M.A. Peskov, S.J. Ramsden, O.M. Yaghi, The Reticular Chemistry Structure Resource (RCSR) Database of, and Symbols for, Crystal Nets, Accounts of Chemical Research 41(12) (2008) 1782-1789. https://doi.org/10.1021/ar800124u.
[10] V.F. Yusuf, N.I. Malek, S.K. Kailasa, Review on Metal–Organic Framework Classification, Synthetic Approaches, and Influencing Factors: Applications in Energy, Drug Delivery, and Wastewater Treatment, ACS Omega 7(49) (2022) 44507-44531. https://doi.org/10.1021/acsomega.2c05310.
[11] J. Ha, J. Lee, H. Moon, Alterations to secondary building units of metal-organic frameworks for the development of new functions, Inorganic Chemistry Frontiers 7 (2019). https://doi.org/10.1039/C9QI01119F.
[12] W. Lu, Z. Wei, Z.-Y. Gu, T.-F. Liu, J. Park, J. Park, J. Tian, M. Zhang, Q. Zhang, T. Gentle Iii, M. Bosch, H.-C. Zhou, Tuning the structure and function of metal–organic frameworks via linker design, Chemical Society Reviews 43(16) (2014) 5561-5593. https://doi.org/10.1039/C4CS00003J.
[13] D. Britt, D. Tranchemontagne, O.M. Yaghi, Metal-organic frameworks with high capacity and selectivity for harmful gases, Proceedings of the National Academy of Sciences 105(33) (2008) 11623-11627. https://doi.org/doi:10.1073/pnas.0804900105.
[14] S. Yuan, L. Huang, Z. Huang, D. Sun, J.-S. Qin, L. Feng, J. Li, X. Zou, T. Cagin, H.-C. Zhou, Continuous Variation of Lattice Dimensions and Pore Sizes in Metal–Organic Frameworks, Journal of the American Chemical Society 142(10) (2020) 4732-4738. https://doi.org/10.1021/jacs.9b13072.
[15] L.K. Macreadie, K.B. Idrees, C.S. Smoljan, O.K. Farha, Expanding Linker Dimensionality in Metal-organic Frameworks for sub-Ångstrom Pore Control for Separation Applications, Angewandte Chemie 135(28) (2023) e202304094.
[16] S. Ali Akbar Razavi, A. Morsali, Linker functionalized metal-organic frameworks, Coordination Chemistry Reviews 399 (2019) 213023. https://doi.org/https://doi.org/10.1016/j.ccr.2019.213023.
[17] A. Schoedel, M. Li, D. Li, M. O'Keeffe, O.M. Yaghi, Structures of Metal–Organic Frameworks with Rod Secondary Building Units, Chemical Reviews 116(19) (2016) 12466-12535. https://doi.org/10.1021/acs.chemrev.6b00346.
[18] D.J. Tranchemontagne, J.L. Mendoza-Cortés, M. O'Keeffe, O.M. Yaghi, Secondary building units, nets and bonding in the chemistry of metal–organic frameworks, Chemical Society Reviews 38(5) (2009) 1257-1283. https://doi.org/10.1039/B817735J.
[19] A.J. Tasiopoulos, A. Vinslava, W. Wernsdorfer, K.A. Abboud, G. Christou, Giant Single-Molecule Magnets: A {Mn84} Torus and Its Supramolecular Nanotubes, Angewandte Chemie International Edition 43(16) (2004) 2117-2121. https://doi.org/https://doi.org/10.1002/anie.200353352.
[20] J. Ha, J.H. Lee, H.R. Moon, Alterations to secondary building units of metal–organic frameworks for the development of new functions, Inorganic Chemistry Frontiers 7(1) (2020) 12-27. https://doi.org/10.1039/C9QI01119F.
[21] S. Wuttke, Introduction to Reticular Chemistry. Metal–Organic Frameworks and Covalent Organic Frameworks Von Omar M. Yaghi, Markus J. Kalmutzki und Christian S. Diercks, Angewandte Chemie 131(40) (2019).
[22] C.F. Baes, R.E. Mesmer, The Hydrolysis of Cations, Wiley1976.
[23] S.E. Smart, J. Vaughn, I. Pappas, L. Pan, Controlled step-wise isomerization of the Keggin-type Al13 and determination of the γ-Al13 structure, Chemical Communications 49(97) (2013) 11352-11354. https://doi.org/10.1039/C3CC44844D.
[24] W.R. Harris, A.E. Martell, Aqueous complexes of gallium (III), Inorganic Chemistry 15(3) (1976) 713-720.
[25] S. Petrosyants, A. Ilyukhin, Indium (III) coordination compounds, Russian Journal of Inorganic Chemistry 56 (2011) 2047-2069.
[26] D.T. Richens, Ligand substitution reactions at inorganic centers, Chemical reviews 105(6) (2005) 1961-2002.
[27] H. Taube, Rates and Mechanisms of Substitution in Inorganic Complexes in Solution, Chemical Reviews 50(1) (1952) 69-126.
[28] G. Kickelbick, U. Schubert, Oxozirconium methacrylate clusters: Zr6 (OH) 4O4 (OMC) 12 and Zr4O2 (OMC) 12 (OMC= methacrylate), Chemische Berichte 130(4) (1997) 473-478.
[29] Y. Bai, Y. Dou, L.-H. Xie, W. Rutledge, J.-R. Li, H.-C. Zhou, Zr-based metal–organic frameworks: design, synthesis, structure, and applications, Chemical Society Reviews 45(8) (2016) 2327-2367.
[30] L. Li, X.-S. Wang, T.-F. Liu, J. Ye, Titanium-Based MOF Materials: From Crystal Engineering to Photocatalysis, Small Methods 4(12) (2020) 2000486. https://doi.org/https://doi.org/10.1002/smtd.202000486.
[31] N. Stock, S. Biswas, Synthesis of Metal-Organic Frameworks (MOFs): Routes to Various MOF Topologies, Morphologies, and Composites, Chemical Reviews 112(2) (2012) 933-969.

https://doi.org/10.1021/cr200304e.
[32] E. Biemmi, S. Christian, N. Stock, T. Bein, High-throughput screening of synthesis parameters in the formation of the metal-organic frameworks MOF-5 and HKUST-1, Microporous and Mesoporous Materials 117(1-2) (2009) 111-117.
[33] I.G. Clayson, D. Hewitt, M. Hutereau, T. Pope, B. Slater, High throughput methods in the synthesis, characterization, and optimization of porous materials, Advanced Materials 32(44) (2020) 2002780.
[34] V. Bon, E. Brunner, A. Pöppl, S. Kaskel, Unraveling Structure and Dynamics in Porous Frameworks via Advanced In Situ Characterization Techniques, Advanced Functional Materials 30(41) (2020) 1907847. https://doi.org/https://doi.org/10.1002/adfm.201907847.
[35] N. Campagnol, E.R. Souza, D.E. De Vos, K. Binnemans, J. Fransaer, Luminescent terbium-containing metal–organic framework films: new approaches for the electrochemical synthesis and application as detectors for explosives, Chemical Communications 50(83) (2014) 12545-12547. https://doi.org/10.1039/C4CC05742B.
[36] J.-S. Choi, W.-J. Son, J. Kim, W.-S. Ahn, Metal–organic framework MOF-5 prepared by microwave heating: Factors to be considered, Microporous and Mesoporous Materials 116(1) (2008) 727-731. https://doi.org/https://doi.org/10.1016/j.micromeso.2008.04.033.
[37] D. Braga, M. Curzi, A. Johansson, M. Polito, K. Rubini, F. Grepioni, Simple and Quantitative Mechanochemical Preparation of a Porous Crystalline Material Based on a 1D Coordination Network for Uptake of Small Molecules, Angewandte Chemie International Edition 45(1) (2006) 142-146. https://doi.org/https://doi.org/10.1002/anie.200502597.
[38] C. McKinstry, R.J. Cathcart, E.J. Cussen, A.J. Fletcher, S.V. Patwardhan, J. Sefcik, Scalable continuous solvothermal synthesis of metal organic framework (MOF-5) crystals, Chemical Engineering Journal 285 (2016) 718-725. https://doi.org/https://doi.org/10.1016/j.cej.2015.10.023.
[39] J.W. Colson, W.R. Dichtel, Rationally synthesized two-dimensional polymers, Nature chemistry 5(6) (2013) 453-465.
[40] K. Geng, T. He, R. Liu, S. Dalapati, K.T. Tan, Z. Li, S. Tao, Y. Gong, Q. Jiang, D. Jiang, Covalent Organic Frameworks: Design, Synthesis, and Functions, Chemical Reviews 120(16) (2020) 8814-8933. https://doi.org/10.1021/acs.chemrev.9b00550.
[41] N. Huang, P. Wang, D. Jiang, Covalent organic frameworks: a materials platform for structural and functional designs, Nature Reviews Materials 1(10) (2016) 16068. https://doi.org/10.1038/natrevmats.2016.68.
[42] N. Huang, L. Zhai, D.E. Coupry, M.A. Addicoat, K. Okushita, K. Nishimura, T. Heine, D. Jiang, Multiple-component covalent organic frameworks, Nature Communications 7(1) (2016) 12325. https://doi.org/10.1038/ncomms12325.
[43] X. Feng, X. Ding, D. Jiang, Covalent organic frameworks, Chemical Society Reviews 41(18) (2012) 6010-6022. https://doi.org/10.1039/C2CS35157A.
[44] S. Dalapati, M. Addicoat, S. Jin, T. Sakurai, J. Gao, H. Xu, S. Irle, S. Seki, D. Jiang, Rational design of crystalline supermicroporous covalent organic frameworks with triangular topologies, Nature Communications 6(1) (2015) 7786. https://doi.org/10.1038/ncomms8786.
[45] B. Gui, G. Lin, H. Ding, C. Gao, A. Mal, C. Wang, Three-Dimensional Covalent Organic Frameworks: From Topology Design to Applications, Accounts of Chemical Research 53(10) (2020) 2225-2234. https://doi.org/10.1021/acs.accounts.0c00357.
[46] O. Yahiaoui, A.N. Fitch, F. Hoffmann, M. Fröba, A. Thomas, J. Roeser, 3D Anionic Silicate Covalent Organic Framework with srs Topology, Journal of the American Chemical Society 140(16) (2018) 5330-5333. https://doi.org/10.1021/jacs.8b01774.
[47] Y.-X. Ma, Z.-J. Li, L. Wei, S.-Y. Ding, Y.-B. Zhang, W. Wang, A dynamic three-dimensional covalent organic framework, Journal of the American Chemical Society 139(14) (2017) 4995-4998.
[48] X. Chen, K. Geng, R. Liu, K.T. Tan, Y. Gong, Z. Li, S. Tao, Q. Jiang, D. Jiang, Covalent Organic Frameworks: Chemical Approaches to Designer Structures and Built-In Functions, Angewandte Chemie International Edition 59(13) (2020) 5050-5091. https://doi.org/https://doi.org/10.1002/anie.201904291.
[49] P.J. Waller, F. Gándara, O.M. Yaghi, Chemistry of Covalent Organic Frameworks, Accounts of Chemical Research 48(12) (2015) 3053-3063. https://doi.org/10.1021/acs.accounts.5b00369.
[50] E. Hamzehpoor, A. Jonderian, E. McCalla, D.F. Perepichka, Synthesis of Boroxine and Dioxaborole Covalent Organic Frameworks via Transesterification and Metathesis of Pinacol Boronates, Journal of the American Chemical Society 143(33) (2021) 13274-13280. https://doi.org/10.1021/jacs.1c05987.
[51] J.R. Hunt, C.J. Doonan, J.D. LeVangie, A.P. Côté, O.M. Yaghi, Reticular synthesis of covalent organic borosilicate frameworks, Journal of the American Chemical Society 130(36) (2008) 11872-11873.
[52] K.P.C. Vollhardt, N.E. Schore, Organic Chemistry: Structure and Function, W. H. Freeman2014.

[53] S. Kandambeth, V. Venkatesh, D.B. Shinde, S. Kumari, A. Halder, S. Verma, R. Banerjee, Self-templated chemically stable hollow spherical covalent organic framework, Nature Communications 6(1) (2015) 6786. https://doi.org/10.1038/ncomms7786.
[54] F.J. Uribe-Romo, C.J. Doonan, H. Furukawa, K. Oisaki, O.M. Yaghi, Crystalline Covalent Organic Frameworks with Hydrazone Linkages, Journal of the American Chemical Society 133(30) (2011) 11478-11481. https://doi.org/10.1021/ja204728y.
[55] S. Dalapati, S. Jin, J. Gao, Y. Xu, A. Nagai, D. Jiang, An Azine-Linked Covalent Organic Framework, Journal of the American Chemical Society 135(46) (2013) 17310-17313. https://doi.org/10.1021/ja4103293.
[56] C.R. DeBlase, K.E. Silberstein, T.-T. Truong, H.D. Abruña, W.R. Dichtel, β-Ketoenamine-linked covalent organic frameworks capable of pseudocapacitive energy storage, Journal of the American Chemical Society 135(45) (2013) 16821-16824.
[57] P. Kuhn, M. Antonietti, A. Thomas, Porous, Covalent Triazine-Based Frameworks Prepared by Ionothermal Synthesis, Angewandte Chemie International Edition 47(18) (2008) 3450-3453. https://doi.org/https://doi.org/10.1002/anie.200705710.
[58] T. Jadhav, Y. Fang, C.-H. Liu, A. Dadvand, E. Hamzehpoor, W. Patterson, A. Jonderian, R.S. Stein, D.F. Perepichka, Transformation between 2D and 3D Covalent Organic Frameworks via Reversible [2 + 2] Cycloaddition, Journal of the American Chemical Society 142(19) (2020) 8862-8870. https://doi.org/10.1021/jacs.0c01990.
[59] Y. Qin, X. Zhu, R. Huang, Covalent organic frameworks: linkage types, synthetic methods and bio-related applications, Biomaterials Science 11(21) (2023) 6942-6976. https://doi.org/10.1039/D3BM01247F.
[60] L. Bourda, C. Krishnaraj, P. Van Der Voort, K. Van Hecke, Conquering the crystallinity conundrum: efforts to increase quality of covalent organic frameworks, Materials Advances 2(9) (2021) 2811-2845. https://doi.org/https://doi.org/10.1039/d1ma00008j.
[61] T. Katoh, T. Suzuki, Y. Ohta, T. Yokozawa, Importance of a reversible reaction for the synthesis of telechelic polymers by means of polycondensation using an excess of one monomer, Polymer Chemistry 13(6) (2022) 794-800. https://doi.org/10.1039/D1PY01498F.
[62] B.J. Smith, A.C. Overholts, N. Hwang, W.R. Dichtel, Insight into the crystallization of amorphous imine-linked polymer networks to 2D covalent organic frameworks, Chemical Communications 52(18) (2016) 3690-3693.
[63] N.L. Campbell, R. Clowes, L.K. Ritchie, A.I. Cooper, Rapid microwave synthesis and purification of porous covalent organic frameworks, Chemistry of Materials 21(2) (2009) 204-206.
[64] X. Guan, Y. Ma, H. Li, Y. Yusran, M. Xue, Q. Fang, Y. Yan, V. Valtchev, S. Qiu, Fast, ambient temperature and pressure ionothermal synthesis of three-dimensional covalent organic frameworks, Journal of the American Chemical Society 140(13) (2018) 4494-4498.
[65] N. Brown, Z. Alsudairy, R. Behera, F. Akram, K. Chen, K. Smith-Petty, B. Motley, S. Williams, W. Huang, C. Ingram, X. Li, Green mechanochemical synthesis of imine-linked covalent organic frameworks for high iodine capture, Green Chemistry 25(16) (2023) 6287-6296. https://doi.org/10.1039/D3GC01927F.
[66] Y. Liu, Y. Wang, H. Li, X. Guan, L. Zhu, M. Xue, Y. Yan, V. Valtchev, S. Qiu, Q. Fang, Ambient aqueous-phase synthesis of covalent organic frameworks for degradation of organic pollutants, Chemical Science 10(46) (2019) 10815-10820. https://doi.org/10.1039/C9SC03725J.
[67] S. Qiu, M. Xue, G. Zhu, Metal–organic framework membranes: from synthesis to separation application, Chemical Society Reviews 43(16) (2014) 6116-6140. https://doi.org/10.1039/C4CS00159A.
[68] Y. Liu, Z. Ng, E.A. Khan, H.-K. Jeong, C.-b. Ching, Z. Lai, Synthesis of continuous MOF-5 membranes on porous α-alumina substrates, Microporous and Mesoporous Materials 118(1-3) (2009) 296-301.
[69] X. Liu, N.K. Demir, Z. Wu, K. Li, Highly Water-Stable Zirconium Metal–Organic Framework UiO-66 Membranes Supported on Alumina Hollow Fibers for Desalination, Journal of the American Chemical Society 137(22) (2015) 6999-7002. https://doi.org/10.1021/jacs.5b02276.
[70] S. Cong, Y. Yuan, J. Wang, Z. Wang, F. Kapteijn, X. Liu, Highly Water-Permeable Metal–Organic Framework MOF-303 Membranes for Desalination, Journal of the American Chemical Society 143(48) (2021) 20055-20058. https://doi.org/10.1021/jacs.1c10192.
[71] C. Algieri, G. Golemme, S. Kallus, J.D.F. Ramsay, Preparation of thin supported MFI membranes by in situ nucleation and secondary growth, Microporous and Mesoporous Materials 47(2) (2001) 127-134. https://doi.org/https://doi.org/10.1016/S1387-1811(01)00393-6.
[72] J.A. Bohrman, M.A. Carreon, Synthesis and CO 2/CH 4 separation performance of Bio-MOF-1 membranes, Chemical Communications 48(42) (2012) 5130-5132.
[73] Y. Pan, T. Li, G. Lestari, Z. Lai, Effective separation of propylene/propane binary mixtures by ZIF-8 membranes, Journal of Membrane Science 390 (2012) 93-98.

[74] Y. Hu, J. Wei, Y. Liang, H. Zhang, X. Zhang, W. Shen, H. Wang, Zeolitic imidazolate framework/graphene oxide hybrid nanosheets as seeds for the growth of ultrathin molecular sieving membranes, Angewandte Chemie 128(6) (2016) 2088-2092.
[75] Y.-n. Wu, F. Li, H. Liu, W. Zhu, M. Teng, Y. Jiang, W. Li, D. Xu, D. He, P. Hannam, Electrospun fibrous mats as skeletons to produce free-standing MOF membranes, Journal of Materials Chemistry 22(33) (2012) 16971-16978.
[76] Y. Yoo, Z. Lai, H.-K. Jeong, Fabrication of MOF-5 membranes using microwave-induced rapid seeding and solvothermal secondary growth, Microporous and mesoporous materials 123(1-3) (2009) 100-106.
[77] Y. Hu, X. Dong, J. Nan, W. Jin, X. Ren, N. Xu, Y.M. Lee, Metal–organic framework membranes fabricated via reactive seeding, Chemical communications 47(2) (2011) 737-739.
[78] V.V. Guerrero, Y. Yoo, M.C. McCarthy, H.-K. Jeong, HKUST-1 membranes on porous supports using secondary growth, Journal of Materials Chemistry 20(19) (2010) 3938-3943.
[79] H. Yoo, N. Shin, Fabrication of well-intergrown ZIF-8 films via sequential ZnO seed layer overlaying, Applied Surface Science 625 (2023) 157211. https://doi.org/https://doi.org/10.1016/j.apsusc.2023.157211.
[80] H.M. Tham, S. Japip, D. Hua, T.-S. Chung, Green Layer-by-Layer Method for the Preparation of Polyacrylonitrile-Supported Zinc Benzene-1,4-dicarboxylic Acid Membranes, ChemSusChem 11(15) (2018) 2612-2619. https://doi.org/https://doi.org/10.1002/cssc.201800740.
[81] Y. Liu, Y. Ban, W. Yang, Microstructural Engineering and Architectural Design of Metal–Organic Framework Membranes, Advanced Materials 29(31) (2017) 1606949. https://doi.org/https://doi.org/10.1002/adma.201606949.
[82] H. Lu, S. Zhu, Interfacial Synthesis of Free-Standing Metal–Organic Framework Membranes, European Journal of Inorganic Chemistry 2013(8) (2013) 1294-1300.
[83] K. Huang, Q. Li, G. Liu, J. Shen, K. Guan, W. Jin, A ZIF-71 Hollow Fiber Membrane Fabricated by Contra-Diffusion, ACS Applied Materials & Interfaces 7(30) (2015) 16157-16160. https://doi.org/10.1021/acsami.5b04991.
[84] J. Yao, D. Dong, D. Li, L. He, G. Xu, H. Wang, Contra-diffusion synthesis of ZIF-8 films on a polymer substrate, Chemical Communications 47(9) (2011) 2559-2561.
[85] A.J. Brown, N.A. Brunelli, K. Eum, F. Rashidi, J.R. Johnson, W.J. Koros, C.W. Jones, S. Nair, Interfacial microfluidic processing of metal-organic framework hollow fiber membranes, Science 345(6192) (2014) 72-75. https://doi.org/doi:10.1126/science.1251181.
[86] A.M. Marti, W. Wickramanayake, G. Dahe, A. Sekizkardes, T.L. Bank, D.P. Hopkinson, S.R. Venna, Continuous flow processing of ZIF-8 membranes on polymeric porous hollow fiber supports for CO2 capture, ACS Applied Materials & Interfaces 9(7) (2017) 5678-5682.
[87] M. Fu, Y. Liu, Q. Lyu, S. Zhang, Y. Liu, B. Li, S.-Q. Wang, Y. Dong, Sustainable vapor-phase deposition and applications of MOF films and membranes: A critical review, Separation and Purification Technology 356 (2025) 129883. https://doi.org/https://doi.org/10.1016/j.seppur.2024.129883.
[88] D. Fischer, A. von Mankowski, A. Ranft, S.K. Vasa, R. Linser, J. Mannhart, B.V. Lotsch, ZIF-8 films prepared by femtosecond pulsed-laser deposition, Chemistry of Materials 29(12) (2017) 5148-5155.
[89] J.-K. Huang, N. Saito, Y. Cai, Y. Wan, C.-C. Cheng, M. Li, J. Shi, K. Tamada, V.C. Tung, S. Li, Steam-assisted chemical vapor deposition of zeolitic imidazolate framework, ACS Materials Letters 2(5) (2020) 485-491.
[90] Z. Gao, B. Li, Z. Li, T. Yu, S. Wang, Q. Fang, S. Qiu, M. Xue, Free-Standing Metal–Organic Framework Membranes Made by Solvent-Free Space-Confined Conversion for Efficient H2/CO2 Separation, ACS Applied Materials & Interfaces 15(15) (2023) 19241-19249.
[91] L. Sun, G. Yuan, L. Gao, J. Yang, M. Chhowalla, M.H. Gharahcheshmeh, K.K. Gleason, Y.S. Choi, B.H. Hong, Z. Liu, Chemical vapour deposition, Nature Reviews Methods Primers 1(1) (2021) 5.
[92] R. Medishetty, Z. Zhang, A. Sadlo, S. Cwik, D. Peeters, S. Henke, N. Mangayarkarasi, A. Devi, Fabrication of zinc-dicarboxylate-and zinc-pyrazolate-carboxylate-framework thin films through vapour–solid deposition, Dalton Transactions 47(40) (2018) 14179-14183.
[93] W. Li, P. Su, Z. Li, Z. Xu, F. Wang, H. Ou, J. Zhang, G. Zhang, E. Zeng, Ultrathin metal–organic framework membrane production by gel–vapour deposition, Nature communications 8(1) (2017) 406.
[94] X. Zhang, K. Wan, P. Subramanian, M. Xu, J. Luo, J. Fransaer, Electrochemical deposition of metal–organic framework films and their applications, Journal of Materials Chemistry A 8(16) (2020) 7569-7587. https://doi.org/10.1039/D0TA00406E.
[95] B. Van de Voorde, R. Ameloot, I. Stassen, M. Everaert, D. De Vos, J.-C. Tan, Mechanical properties of electrochemically synthesised metal–organic framework thin films, Journal of Materials Chemistry C 1(46) (2013) 7716-7724.

[96] M. Li, M. Dincă, Selective formation of biphasic thin films of metal–organic frameworks by potential-controlled cathodic electrodeposition, Chemical Science 5(1) (2014) 107-111.
[97] I. Hod, W. Bury, D.M. Karlin, P. Deria, C.W. Kung, M.J. Katz, M. So, B. Klahr, D. Jin, Y.W. Chung, Directed growth of electroactive metal-organic framework thin films using electrophoretic deposition, Advanced materials 26(36) (2014) 6295-6300.
[98] A.U. Czaja, N. Trukhan, U. Müller, Industrial applications of metal–organic frameworks, Chemical Society Reviews 38(5) (2009) 1284-1293.
[99] Q. Xing, X. Xu, H. Li, Z. Cui, B. Chu, N. Xie, Z. Wang, P. Bai, X. Guo, J. Lyu, Fabrication Methods of Continuous Pure Metal–Organic Framework Membranes and Films: A Review, Molecules 29(16) (2024) 3885.
[100] W. Wu, X. Hong, J. Fan, Y. Wei, H. Wang, Research progress on the substrate for metal–organic framework (MOF) membrane growth for separation, Chinese Journal of Chemical Engineering 56 (2023) 299-313. https://doi.org/https://doi.org/10.1016/j.cjche.2022.08.008.
[101] A.J. Burggraaf, L. Cot, Fundamentals of inorganic membrane science and technology, Elsevier1996.
[102] Y. Liu, N. Wang, L. Diestel, F. Steinbach, J. Caro, MOF membrane synthesis in the confined space of a vertically aligned LDH network, Chemical communications 50(32) (2014) 4225-4227.
[103] J. Zuo, T.-S. Chung, Metal–Organic Framework-Functionalized Alumina Membranes for Vacuum Membrane Distillation, Water 8(12) (2016) 586.
[104] A. Huang, W. Dou, J.r. Caro, Steam-stable zeolitic imidazolate framework ZIF-90 membrane with hydrogen selectivity through covalent functionalization, Journal of the American Chemical Society 132(44) (2010) 15562-15564.
[105] J. Hou, P.D. Sutrisna, Y. Zhang, V. Chen, Formation of ultrathin, continuous metal–organic framework membranes on flexible polymer substrates, Angewandte Chemie International Edition 55(12) (2016) 3947-3951.
[106] A. Huang, H. Bux, F. Steinbach, J. Caro, Molecular-sieve membrane with hydrogen permselectivity: ZIF-22 in LTA topology prepared with 3-aminopropyltriethoxysilane as covalent linker, Angewandte Chemie International Edition 29(49) (2010) 4958-4961.
[107] A. Huang, Y. Chen, N. Wang, Z. Hu, J. Jiang, J. Caro, A highly permeable and selective zeolitic imidazolate framework ZIF-95 membrane for H 2/CO 2 separation, Chemical Communications 48(89) (2012) 10981-10983.
[108] R. Wu, Y. Li, A. Huang, Synthesis of high-performance Co-based ZIF-67 membrane for H2 separation by using cobalt ions chelated PIM-1 as interface layer, Journal of Membrane Science 620 (2021) 118841.
[109] Y. Liu, Y. Peng, N. Wang, Y. Li, J.H. Pan, W. Yang, J. Caro, Significantly enhanced separation using ZIF-8 membranes by partial conversion of calcined layered double hydroxide precursors, ChemSusChem 8(21) (2015) 3582-3586.
[110] Y. Zhu, K.M. Gupta, Q. Liu, J. Jiang, J. Caro, A. Huang, Synthesis and seawater desalination of molecular sieving zeolitic imidazolate framework membranes, Desalination 385 (2016) 75-82. https://doi.org/https://doi.org/10.1016/j.desal.2016.02.005.
[111] Y. Liu, J.H. Pan, N. Wang, F. Steinbach, X. Liu, J. Caro, Remarkably Enhanced Gas Separation by Partial Self-Conversion of a Laminated Membrane to Metal–Organic Frameworks, Angewandte Chemie 127(10) (2015) 3071-3075.
[112] Y. Liu, H. Chen, T. Li, Y. Ren, H. Wang, Z. Song, J. Li, Q. Zhao, J. Li, L. Li, Balancing the Crystallinity and Film Formation of Metal–Organic Framework Membranes through In Situ Modulation for Efficient Gas Separation, Angewandte Chemie International Edition 62(37) (2023) e202309095. https://doi.org/https://doi.org/10.1002/anie.202309095.
[113] Z. Li, Y. Wang, J. Zhang, S. Cheng, Y. Sun, A Short Review of Advances in MOF Glass Membranes for Gas Adsorption and Separation, Membranes 14(5) (2024) 99.
[114] W. Bi, L. Han, Y. Liu, L. Li, The Key to MOF Membrane Fabrication and Application: the Trade-off between Crystallization and Film Formation, Chemistry – A European Journal 30(64) (2024) e202401868. https://doi.org/https://doi.org/10.1002/chem.202401868.
[115] J.Y. Lin, Molecular sieves for gas separation, Science 353(6295) (2016) 121-122.
[116] J. Hu, B. Cai, Y. Wang, Z. Bian, T. Hou, Y. Sun, Amorphous Ti-MOF membrane for selective molecular sieving, Journal of Membrane Science 717 (2025) 123635. https://doi.org/https://doi.org/10.1016/j.memsci.2024.123635.
[117] Z. Qiao, Y. Liang, Z. Zhang, D. Mei, Z. Wang, M.D. Guiver, C. Zhong, Ultrathin Low-Crystallinity MOF Membranes Fabricated by Interface Layer Polarization Induction, Advanced Materials 32(34) (2020) 2002165. https://doi.org/https://doi.org/10.1002/adma.202002165.
[118] G. Liu, Y. Guo, C. Chen, Y. Lu, G. Chen, G. Liu, Y. Han, W. Jin, N. Xu, Eliminating lattice defects in

metal–organic framework molecular-sieving membranes, Nature Materials 22(6) (2023) 769-776. https://doi.org/10.1038/s41563-023-01541-0.
[119] F. Yan, J. Yan, Y. Sun, T. Ji, Y. He, X. Guo, Y. Liu, Fabrication of Defect-Engineered MOF-801 Membrane for Efficient Dye Rejection, European Journal of Inorganic Chemistry 26(10) (2023) e202200679. https://doi.org/https://doi.org/10.1002/ejic.202200679.
[120] T.C.T. Pham, H.S. Kim, K.B. Yoon, Growth of Uniformly Oriented Silica MFI and BEA Zeolite Films on Substrates, Science 334(6062) (2011) 1533-1538. https://doi.org/doi:10.1126/science.1212472.
[121] H.W. Kim, H.W. Yoon, S.-M. Yoon, B.M. Yoo, B.K. Ahn, Y.H. Cho, H.J. Shin, H. Yang, U. Paik, S. Kwon, Selective gas transport through few-layered graphene and graphene oxide membranes, Science 342(6154) (2013) 91-95.
[122] Q. Liu, H.-Y. Chi, S. Song, R. Goswami, K.V. Agrawal, Towards ultrathin metal-organic frameworks membranes for high-performance separation, APL Materials 11(10) (2023). https://doi.org/10.1063/5.0169507.
[123] Y. Sun, D. Yan, Y. Wu, F.-Y. Shih, C. Zhang, H. Luo, S.-H. Lin, Y. Liu, Fabrication of Twin-Free Ultrathin NH2-MIL-125(Ti) Membrane with c-Preferred Orientation Using Transition-Metal Trichalcogenides as Titanium Source, ACS Materials Letters 4(1) (2022) 55-60. https://doi.org/10.1021/acsmaterialslett.1c00452.
[124] C. Zhang, J. Yan, T. Ji, D. Du, Y. Sun, L. Liu, X. Zhang, Y. Liu, Fabrication of highly (110)-Oriented ZIF-8 membrane at low temperature using nanosheet seed layer, Journal of Membrane Science 641 (2022) 119915. https://doi.org/https://doi.org/10.1016/j.memsci.2021.119915.
[125] A. Van der Drift, Evolutionary selection, a principle governing growth orientation in vapour-deposited layers, Philips Res. Rep 22(3) (1967) 267.
[126] Y. Sun, Y. Liu, Oriented Metal-Organic Framework Membranes for Molecular Separations, Chemistry – A European Journal 30(37) (2024) e202304162. https://doi.org/https://doi.org/10.1002/chem.202304162.
[127] Y. Sun, J. Yan, Y. Gao, T. Ji, S. Chen, C. Wang, P. Lu, Y. Li, Y. Liu, Fabrication of Highly Oriented Ultrathin Zirconium Metal-Organic Framework Membrane from Nanosheets towards Unprecedented Gas Separation, Angewandte Chemie International Edition 62(15) (2023) e202216697. https://doi.org/https://doi.org/10.1002/anie.202216697.
[128] S. Yuan, L. Feng, K. Wang, J. Pang, M. Bosch, C. Lollar, Y. Sun, J. Qin, X. Yang, P. Zhang, Q. Wang, L. Zou, Y. Zhang, L. Zhang, Y. Fang, J. Li, H.-C. Zhou, Stable Metal–Organic Frameworks: Design, Synthesis, and Applications, Advanced Materials 30(37) (2018) 1704303. https://doi.org/https://doi.org/10.1002/adma.201704303.
[129] N.C. Burtch, H. Jasuja, K.S. Walton, Water Stability and Adsorption in Metal–Organic Frameworks, Chemical Reviews 114(20) (2014) 10575-10612. https://doi.org/10.1021/cr5002589.
[130] C. Wang, X. Liu, N. Keser Demir, J.P. Chen, K. Li, Applications of water stable metal–organic frameworks, Chemical Society Reviews 45(18) (2016) 5107-5134. https://doi.org/10.1039/C6CS00362A.
[131] X. Liu, X. Wang, F. Kapteijn, Water and Metal–Organic Frameworks: From Interaction toward Utilization, Chemical Reviews 120(16) (2020) 8303-8377. https://doi.org/10.1021/acs.chemrev.9b00746.
[132] L. Jiao, Y. Wang, H.-L. Jiang, Q. Xu, Metal–Organic Frameworks as Platforms for Catalytic Applications, Advanced Materials 30(37) (2018) 1703663. https://doi.org/https://doi.org/10.1002/adma.201703663.
[133] J.H. Cavka, S. Jakobsen, U. Olsbye, N. Guillou, C. Lamberti, S. Bordiga, K.P. Lillerud, A New Zirconium Inorganic Building Brick Forming Metal Organic Frameworks with Exceptional Stability, Journal of the American Chemical Society 130(42) (2008) 13850-13851. https://doi.org/10.1021/ja8057953.
[134] X.-L. Lv, S. Yuan, L.-H. Xie, H.F. Darke, Y. Chen, T. He, C. Dong, B. Wang, Y.-Z. Zhang, J.-R. Li, H.-C. Zhou, Ligand Rigidification for Enhancing the Stability of Metal–Organic Frameworks, Journal of the American Chemical Society 141(26) (2019) 10283-10293. https://doi.org/10.1021/jacs.9b02947.
[135] D.-D. Zhou, P. Chen, C. Wang, S.-S. Wang, Y. Du, H. Yan, Z.-M. Ye, C.-T. He, R.-K. Huang, Z.-W. Mo, N.-Y. Huang, J.-P. Zhang, Intermediate-sized molecular sieving of styrene from larger and smaller analogues, Nature Materials 18(9) (2019) 994-998. https://doi.org/10.1038/s41563-019-0427-z.
[136] J.-H. Wang, M. Li, D. Li, An Exceptionally Stable and Water-Resistant Metal–Organic Framework with Hydrophobic Nanospaces for Extracting Aromatic Pollutants from Water, Chemistry – A European Journal 20(38) (2014) 12004-12008. https://doi.org/https://doi.org/10.1002/chem.201403501.
[137] L. Liang, C. Liu, F. Jiang, Q. Chen, L. Zhang, H. Xue, H.-L. Jiang, J. Qian, D. Yuan, M. Hong, Carbon dioxide capture and conversion by an acid-base resistant metal-organic framework, Nature Communications 8(1) (2017) 1233. https://doi.org/10.1038/s41467-017-01166-3.
[138] R. Dai, X. Zhang, M. Liu, Z. Wu, Z. Wang, Porous metal organic framework CuBDC nanosheet

incorporated thin-film nanocomposite membrane for high-performance forward osmosis, Journal of Membrane Science 573 (2019) 46-54. https://doi.org/https://doi.org/10.1016/j.memsci.2018.11.075.
[139] A. Demessence, D.M. D'Alessandro, M.L. Foo, J.R. Long, Strong CO2 Binding in a Water-Stable, Triazolate-Bridged Metal−Organic Framework Functionalized with Ethylenediamine, Journal of the American Chemical Society 131(25) (2009) 8784-8786. https://doi.org/10.1021/ja903411w.
[140] K.S. Park, Z. Ni, A.P. Côté, J.Y. Choi, R. Huang, F.J. Uribe-Romo, H.K. Chae, M. O'Keeffe, O.M. Yaghi, Exceptional chemical and thermal stability of zeolitic imidazolate frameworks, Proceedings of the National Academy of Sciences 103(27) (2006) 10186-10191. https://doi.org/doi:10.1073/pnas.0602439103.
[141] A. Phan, C.J. Doonan, F.J. Uribe-Romo, C.B. Knobler, M. O'Keeffe, O.M. Yaghi, Synthesis, Structure, and Carbon Dioxide Capture Properties of Zeolitic Imidazolate Frameworks, Accounts of Chemical Research 43(1) (2010) 58-67. https://doi.org/10.1021/ar900116g.
[142] R. Banerjee, A. Phan, B. Wang, C. Knobler, H. Furukawa, M. O'Keeffe, O.M. Yaghi, High-Throughput Synthesis of Zeolitic Imidazolate Frameworks and Application to CO<sub>2</sub> Capture, Science 319(5865) (2008) 939-943. https://doi.org/doi:10.1126/science.1152516.
[143] H.J. Choi, M. Dincă, A. Dailly, J.R. Long, Hydrogen storage in water-stable metal–organic frameworks incorporating 1,3- and 1,4-benzenedipyrazolate, Energy & Environmental Science 3(1) (2010) 117-123. https://doi.org/10.1039/B917512A.
[144] Y. Wang, N.-Y. Huang, X.-W. Zhang, H. He, R.-K. Huang, Z.-M. Ye, Y. Li, D.-D. Zhou, P.-Q. Liao, X.-M. Chen, J.-P. Zhang, Selective Aerobic Oxidation of a Metal–Organic Framework Boosts Thermodynamic and Kinetic Propylene/Propane Selectivity, Angewandte Chemie International Edition 58(23) (2019) 7692-7696. https://doi.org/https://doi.org/10.1002/anie.201902209.
[145] M. Tonigold, Y. Lu, B. Bredenkötter, B. Rieger, S. Bahnmüller, J. Hitzbleck, G. Langstein, D. Volkmer, Heterogeneous Catalytic Oxidation by MFU-1: A Cobalt(II)-Containing Metal–Organic Framework, Angewandte Chemie International Edition 48(41) (2009) 7546-7550. https://doi.org/https://doi.org/10.1002/anie.200901241.
[146] K. Wang, X.-L. Lv, D. Feng, J. Li, S. Chen, J. Sun, L. Song, Y. Xie, J.-R. Li, H.-C. Zhou, Pyrazolate-based porphyrinic metal–organic framework with extraordinary base-resistance, Journal of the American Chemical Society 138(3) (2016) 914-919.
[147] V. Colombo, S. Galli, H. Choi, G. Han, A, Maspero, G. Palmisano, N. Masciocchi and JR Long, Chem. Sci 2 (2011) 1311.
[148] T. He, Z. Huang, S. Yuan, X.-L. Lv, X.-J. Kong, X. Zou, H.-C. Zhou, J.-R. Li, Kinetically Controlled Reticular Assembly of a Chemically Stable Mesoporous Ni(II)-Pyrazolate Metal–Organic Framework, Journal of the American Chemical Society 142(31) (2020) 13491-13499. https://doi.org/10.1021/jacs.0c05074.
[149] X. Qian, B. Yadian, R. Wu, Y. Long, K. Zhou, B. Zhu, Y. Huang, Structure stability of metal-organic framework MIL-53 (Al) in aqueous solutions, International Journal of Hydrogen Energy 38(36) (2013) 16710-16715. https://doi.org/https://doi.org/10.1016/j.ijhydene.2013.07.054.
[150] F. Jeremias, D. Fröhlich, C. Janiak, S.K. Henninger, Advancement of sorption-based heat transformation by a metal coating of highly-stable, hydrophilic aluminium fumarate MOF, RSC Advances 4(46) (2014) 24073-24082. https://doi.org/10.1039/C4RA03794D.
[151] T. Loiseau, C. Mellot-Draznieks, H. Muguerra, G. Ferey, M. graphic Computing System, 2006. Haouas, F. Taulelle, CR Chim 8 (2005) 765-772.
[152] T. Loiseau, L. Lecroq, C. Volkringer, J. Marrot, G. Férey, M. Haouas, F. Taulelle, S. Bourrelly, P.L. Llewellyn, M. Latroche, MIL-96, a Porous Aluminum Trimesate 3D Structure Constructed from a Hexagonal Network of 18-Membered Rings and μ3-Oxo-Centered Trinuclear Units, Journal of the American Chemical Society 128(31) (2006) 10223-10230. https://doi.org/10.1021/ja0621086.
[153] P. Serra-Crespo, E.V. Ramos-Fernandez, J. Gascon, F. Kapteijn, Synthesis and Characterization of an Amino Functionalized MIL-101(Al): Separation and Catalytic Properties, Chemistry of Materials 23(10) (2011) 2565-2572. https://doi.org/10.1021/cm103644b.
[154] F. Jeremias, A. Khutia, S.K. Henninger, C. Janiak, MIL-100(Al, Fe) as water adsorbents for heat transformation purposes—a promising application, Journal of Materials Chemistry 22(20) (2012) 10148-10151. https://doi.org/10.1039/C2JM15615F.
[155] T.B. Čelič, M. Mazaj, G. Mali, V. Kaučič, N.Z. Logar, Hydrothermal stability as an important characteristics of metal-organic framework materials, Proceedings of the 5th Serbian-Croatian-Slovenian Symposium on Zeolites, 2013, pp. 72-75.
[156] C. Volkringer, T. Loiseau, N. Guillou, G. Férey, M. Haouas, F. Taulelle, N. Audebrand, I. Margiolaki, D. Popov, M. Burghammer, C. Riekel, Structural Transitions and Flexibility during Dehydration−Rehydration Process in the MOF-type Aluminum Pyromellitate Al2(OH)2[C10O8H2] (MIL-118), Crystal Growth &

Design 9(6) (2009) 2927-2936. https://doi.org/10.1021/cg900276g.
[157] C. Volkringer, T. Loiseau, M. Haouas, F. Taulelle, D. Popov, M. Burghammer, C. Riekel, C. Zlotea, F. Cuevas, M. Latroche, Occurrence of uncommon infinite chains consisting of edge-sharing octahedra in a porous metal organic framework-type aluminum pyromellitate Al4 (OH) 8 [C10O8H2](MIL-120): synthesis, structure, and gas sorption properties, Chemistry of Materials 21(24) (2009) 5783-5791.
[158] C. Volkringer, T. Loiseau, N. Guillou, G. Férey, M. Haouas, F. Taulelle, E. Elkaim, N. Stock, High-Throughput Aided Synthesis of the Porous Metal−Organic Framework-Type Aluminum Pyromellitate, MIL-121, with Extra Carboxylic Acid Functionalization, Inorganic Chemistry 49(21) (2010) 9852-9862. https://doi.org/10.1021/ic101128w.
[159] C. Volkringer, T. Loiseau, N. Guillou, G. Férey, E. Elkaïm, Syntheses and structures of the MOF-type series of metal 1,4,5,8,-naphthalenetetracarboxylates M2(OH)2[C14O8H4] (Al, Ga, In) with infinite trans-connected M–OH–M chains (MIL-122), Solid State Sciences 11(8) (2009) 1507-1512. https://doi.org/https://doi.org/10.1016/j.solidstatesciences.2009.05.017.
[160] Z.-W. Wang, M. Chen, C.-S. Liu, X. Wang, H. Zhao, M. Du, A Versatile AlIII-Based Metal–Organic Framework with High Physicochemical Stability, Chemistry – A European Journal 21(48) (2015) 17215-17219. https://doi.org/https://doi.org/10.1002/chem.201502615.
[161] H. Reinsch, M.A. van der Veen, B. Gil, B. Marszalek, T. Verbiest, D. De Vos, N. Stock, Structures, sorption characteristics, and nonlinear optical properties of a new series of highly stable aluminum MOFs, Chemistry of Materials 25(1) (2013) 17-26.
[162] S. Shang, C. Yang, M. Sun, Z. Tao, A. Hanif, Q. Gu, J. Shang, CO2 capture from wet flue gas using transition metal inserted porphyrin-based metal-organic frameworks as efficient adsorbents, Separation and Purification Technology 301 (2022) 122058. https://doi.org/https://doi.org/10.1016/j.seppur.2022.122058.
[163] D. Feng, T.-F. Liu, J. Su, M. Bosch, Z. Wei, W. Wan, D. Yuan, Y.-P. Chen, X. Wang, K. Wang, X. Lian, Z.-Y. Gu, J. Park, X. Zou, H.-C. Zhou, Stable metal-organic frameworks containing single-molecule traps for enzyme encapsulation, Nature Communications 6(1) (2015) 5979. https://doi.org/10.1038/ncomms6979.
[164] M. Zhai, F. Moghadam, T. Gosiamemang, J.Y.Y. Heng, K. Li, Facile orientation control of MOF-303 hollow fiber membranes by a dual-source seeding method, Nature Communications 15(1) (2024) 10264. https://doi.org/10.1038/s41467-024-54730-z.
[165] H. Zhang, X. Hu, T. Li, Y. Zhang, H. Xu, Y. Sun, X. Gu, C. Gu, J. Luo, B. Gao, MIL series of metal organic frameworks (MOFs) as novel adsorbents for heavy metals in water: A review, Journal of Hazardous Materials 429 (2022) 128271. https://doi.org/https://doi.org/10.1016/j.jhazmat.2022.128271.
[166] P. Long, H. Wu, Q. Zhao, Y. Wang, J. Dong, J. Li, Solvent effect on the synthesis of MIL-96(Cr) and MIL-100(Cr), Microporous and Mesoporous Materials 142(2) (2011) 489-493. https://doi.org/https://doi.org/10.1016/j.micromeso.2010.12.036.
[167] K. Wang, D. Feng, T.-F. Liu, J. Su, S. Yuan, Y.-P. Chen, M. Bosch, X. Zou, H.-C. Zhou, A series of highly stable mesoporous metalloporphyrin Fe-MOFs, Journal of the American Chemical Society 136(40) (2014) 13983-13986.
[168] N.S. Abdul Mubarak, K.Y. Foo, R. Schneider, R.M. Abdelhameed, S. Sabar, The chemistry of MIL-125 based materials: Structure, synthesis, modification strategies and photocatalytic applications, Journal of Environmental Chemical Engineering 10(1) (2022) 106883. https://doi.org/https://doi.org/10.1016/j.jece.2021.106883.
[169] L.-J. Chen, X. Zhao, X.-P. Yan, Porphyrinic metal-organic frameworks for biological applications, Advanced Sensor and Energy Materials 2(1) (2023) 100045. https://doi.org/https://doi.org/10.1016/j.asems.2022.100045.
[170] D. Feng, Z.-Y. Gu, Y.-P. Chen, J. Park, Z. Wei, Y. Sun, M. Bosch, S. Yuan, H.-C. Zhou, A Highly Stable Porphyrinic Zirconium Metal–Organic Framework with shp-a Topology, Journal of the American Chemical Society 136(51) (2014) 17714-17717. https://doi.org/10.1021/ja510525s.
[171] H.-L. Jiang, D. Feng, K. Wang, Z.-Y. Gu, Z. Wei, Y.-P. Chen, H.-C. Zhou, An Exceptionally Stable, Porphyrinic Zr Metal–Organic Framework Exhibiting pH-Dependent Fluorescence, Journal of the American Chemical Society 135(37) (2013) 13934-13938. https://doi.org/10.1021/ja406844r.
[172] T.-F. Liu, D. Feng, Y.-P. Chen, L. Zou, M. Bosch, S. Yuan, Z. Wei, S. Fordham, K. Wang, H.-C. Zhou, Topology-Guided Design and Syntheses of Highly Stable Mesoporous Porphyrinic Zirconium Metal–Organic Frameworks with High Surface Area, Journal of the American Chemical Society 137(1) (2015) 413-419. https://doi.org/10.1021/ja5111317.
[173] J. Zhang, H.-J. Bai, Q. Ren, H.-B. Luo, X.-M. Ren, Z.-F. Tian, S. Lu, Extra Water- and Acid-Stable MOF-801 with High Proton Conductivity and Its Composite Membrane for Proton-Exchange Membrane,

ACS Applied Materials & Interfaces 10(34) (2018) 28656-28663. https://doi.org/10.1021/acsami.8b09070.
[174] F.-R. Lin, Z.-Y. Liu, G.-Q. Zhang, J. Zhang, X.-M. Ren, Understanding proton conduction enhancement of MOF-802 through in situ incorporation of imidazole into its channels, Inorganic Chemistry Communications 157 (2023) 111340. https://doi.org/https://doi.org/10.1016/j.inoche.2023.111340.
[175] W. Liang, H. Chevreau, F. Ragon, P.D. Southon, V.K. Peterson, D.M. D'Alessandro, Tuning pore size in a zirconium–tricarboxylate metal–organic framework, CrystEngComm 16(29) (2014) 6530-6533. https://doi.org/10.1039/C4CE01031K.
[176] H. Furukawa, F. Gándara, Y.-B. Zhang, J. Jiang, W.L. Queen, M.R. Hudson, O.M. Yaghi, Water adsorption in porous metal–organic frameworks and related materials, Journal of the American Chemical Society 136(11) (2014) 4369-4381.
[177] V. Bon, V. Senkovskyy, I. Senkovska, S. Kaskel, Zr(iv) and Hf(iv) based metal–organic frameworks with reo-topology, Chemical Communications 48(67) (2012) 8407-8409. https://doi.org/10.1039/C2CC34246D.
[178] Y. Shen, R. Duan, J. Qian, Q. Li, Preparation of Highly Stable DUT-52 Materials and Adsorption of Dichromate Ions in Aqueous Solution, ACS Omega 7(19) (2022) 16414-16421. https://doi.org/10.1021/acsomega.2c00373.
[179] Y. Wang, H. Chen, Z. Liu, J. Li, Z. Tu, S. Li, Improved adsorption desalination performance of DUT-67 by incorporating Graphene Oxide (GO), Microporous and Mesoporous Materials 354 (2023) 112554. https://doi.org/https://doi.org/10.1016/j.micromeso.2023.112554.
[180] J. Liu, R. Anderson, K.M. Schmalbach, T.R. Sheridan, Z. Wang, N.M. Schweitzer, A. Stein, N.A. Mara, D. Gomez-Gualdron, J.T. Hupp, Insights into dual-functional modification for water stability enhancement of mesoporous zirconium metal–organic frameworks, Journal of Materials Chemistry A 10(33) (2022) 17307-17316. https://doi.org/10.1039/D2TA03851J.
[181] O.V. Gutov, W. Bury, D.A. Gomez-Gualdron, V. Krungleviciute, D. Fairen-Jimenez, J.E. Mondloch, A.A. Sarjeant, S.S. Al-Juaid, R.Q. Snurr, J.T. Hupp, T. Yildirim, O.K. Farha, Water-Stable Zirconium-Based Metal–Organic Framework Material with High-Surface Area and Gas-Storage Capacities, Chemistry – A European Journal 20(39) (2014) 12389-12393. https://doi.org/https://doi.org/10.1002/chem.201402895.
[182] V. Guillerm, F. Ragon, M. Dan-Hardi, T. Devic, M. Vishnuvarthan, B. Campo, A. Vimont, G. Clet, Q. Yang, G. Maurin, A series of isoreticular, highly stable, porous zirconium oxide based metal–organic frameworks, Angewandte Chemie-International Edition 51(37) (2012) 9267.
[183] B. Wang, X.-L. Lv, D. Feng, L.-H. Xie, J. Zhang, M. Li, Y. Xie, J.-R. Li, H.-C. Zhou, Highly Stable Zr(IV)-Based Metal–Organic Frameworks for the Detection and Removal of Antibiotics and Organic Explosives in Water, Journal of the American Chemical Society 138(19) (2016) 6204-6216. https://doi.org/10.1021/jacs.6b01663.
[184] B. Wang, Q. Yang, C. Guo, Y. Sun, L.-H. Xie, J.-R. Li, Stable Zr(IV)-Based Metal–Organic Frameworks with Predesigned Functionalized Ligands for Highly Selective Detection of Fe(III) Ions in Water, ACS Applied Materials & Interfaces 9(11) (2017) 10286-10295. https://doi.org/10.1021/acsami.7b00918.
[185] X.-J. Kong, Y.-Z. Zhang, T. He, X.-Q. Wu, M.-M. Xu, S.-N. Wang, L.-H. Xie, J.-R. Li, Two interpenetrated metal–organic frameworks with a slim ethynyl-based ligand: designed for selective gas adsorption and structural tuning, CrystEngComm 20(39) (2018) 6018-6025. https://doi.org/10.1039/C8CE00779A.
[186] L.-H. Xie, X.-M. Liu, T. He, J.-R. Li, Metal-Organic Frameworks for the Capture of Trace Aromatic Volatile Organic Compounds, Chem 4(8) (2018) 1911-1927. https://doi.org/10.1016/j.chempr.2018.05.017.
[187] R. Xu, Y. Kang, W. Zhang, X. Zhang, B. Pan, Oriented UiO-67 Metal–Organic Framework Membrane with Fast and Selective Lithium-Ion Transport, Angewandte Chemie International Edition 61(3) (2022) e202115443. https://doi.org/https://doi.org/10.1002/anie.202115443.
[188] W. Wang, X. Dong, J. Nan, W. Jin, Z. Hu, Y. Chen, J. Jiang, A homochiral metal–organic framework membrane for enantioselective separation, Chemical Communications 48(56) (2012) 7022-7024. https://doi.org/10.1039/C2CC32595K.
[189] Q. Wang, C. Zhou, L. Shen, E. Song, Y. Yang, H. Lian, R. Hou, Y. Pan, Co-gallate MOF Membrane for Efficient Pervaporation Separation of MeOH from MTBE, Journal of Membrane Science 698 (2024) 122621. https://doi.org/https://doi.org/10.1016/j.memsci.2024.122621.
[190] L.C. Wang, Y. Wang, L.Y. Wu, G. Wei, Fabrication, Properties, Performances, and Separation Application of Polymeric Pervaporation Membranes: A Review, Polymers 12(7) (2020). https://doi.org/10.3390/polym12071466.
[191] N.A.A. Razak, M.S.M. Shayuti, N.H. Othman, F. Marpani, N.H. Alias, M.Z. Shahruddin, N. Abd Rahman, S.L. Heng, S.O. Lai, A.F. Ismail, W.K. Soh, F. Kadirkhan, A mini review on the potential of zeolite

membrane for pervaporation, Chemical Engineering Communications (2024). https://doi.org/10.1080/00986445.2024.2432670.
[192] X. Yu, W.D. Fan, V. Wee, D.C. Shi, H.Y. Yuan, Y.P. Ying, Y.D. Yuan, Z.Q. Yang, Y. Feng, D.F. Sun, D. Zhao, Polycrystalline Iron(III) metal-organic framework membranes for organic solvent nanofiltration with high permeance, Journal of Membrane Science 644 (2022). https://doi.org/10.1016/j.memsci.2021.120130.
[193] X. Yin, Y. He, T. He, H. Li, J. Wu, L. Zhou, S. Li, C. Li, A durable MOF-303-coated stainless steel mesh with robust anti-oil-fouling performance for multifunctional oil/water separation, Colloids and Surfaces A: Physicochemical and Engineering Aspects 657 (2023) 130515. https://doi.org/https://doi.org/10.1016/j.colsurfa.2022.130515.
[194] J. Yuan, W.-S. Hung, H. Zhu, K. Guan, Y. Ji, Y. Mao, G. Liu, K.-R. Lee, W. Jin, Fabrication of ZIF-300 membrane and its application for efficient removal of heavy metal ions from wastewater, Journal of Membrane Science 572 (2019) 20-27. https://doi.org/https://doi.org/10.1016/j.memsci.2018.10.080.
[195] Y. Li, L.H. Wee, J.A. Martens, I.F.J. Vankelecom, Interfacial synthesis of ZIF-8 membranes with improved nanofiltration performance, Journal of Membrane Science 523 (2017) 561-566. https://doi.org/https://doi.org/10.1016/j.memsci.2016.09.065.
[196] Y.-L. Ji, B.-X. Gu, H.-Q. Huo, S.-J. Xie, H. Peng, W.-H. Zhang, M.-J. Yin, B. Xiong, H. Lu, L.F. Villalobos, Q. Zhao, C.-J. Gao, M. Elimelech, Q.-F. An, Roll-to-roll fabrication of large-area metal–organic framework-based membranes for high-performance aqueous separations, Nature Water 2(2) (2024) 183-192. https://doi.org/10.1038/s44221-023-00184-4.
[197] Y. Xiao, W. Zhang, Y. Jiao, Y. Xu, H. Lin, Metal-phenolic network as precursor for fabrication of metal-organic framework (MOF) nanofiltration membrane for efficient desalination, Journal of Membrane Science 624 (2021) 119101. https://doi.org/https://doi.org/10.1016/j.memsci.2021.119101.
[198] S. Cong, Y. Yuan, J. Wang, Z. Wang, F. Kapteijn, X.J.J.o.t.A.C.S. Liu, Highly Water-Permeable Metal–Organic Framework MOF-303 Membranes for Desalination, 143(48) (2021) 20055-20058.
[199] R. Xu, Y. Kang, W. Zhang, X. Zhang, B. Pan, Oriented UiO-67 Metal–Organic Framework Membrane with Fast and Selective Lithium-Ion Transport, 61(3) (2022) e202115443. https://doi.org/https://doi.org/10.1002/anie.202115443.
[200] W. Wang, X. Dong, J. Nan, W. Jin, Z. Hu, Y. Chen, J.J.C.c. Jiang, A homochiral metal–organic framework membrane for enantioselective separation, 48(56) (2012) 7022-7024.
[201] J. Chen, X. Wu, C. Chen, Y. Chen, W. Li, J. Wang, Secondary-assembled defect-free MOF membrane via triple-needle electrostatic atomization for highly stable and selective organics permeation, Journal of Membrane Science 648 (2022) 120382. https://doi.org/https://doi.org/10.1016/j.memsci.2022.120382.
[202] S. Xie, W. Monnens, K. Wan, W. Zhang, W. Guo, M. Xu, I.F.J. Vankelecom, X. Zhang, J. Fransaer, Cathodic Electrodeposition of MOF Films Using Hydrogen Peroxide, Angewandte Chemie International Edition 60(47) (2021) 24950-24957. https://doi.org/https://doi.org/10.1002/anie.202108485.
[203] P. Nian, X. Wang, S. Li, Z. Wang, Y. Wei, Switchable CAU-10-H mesh membrane for on-demand separation of immiscible oil/water mixtures and emulsions, Journal of Environmental Chemical Engineering 11(3) (2023) 109656. https://doi.org/https://doi.org/10.1016/j.jece.2023.109656.
[204] X. Wang, Q. Lyu, T. Tong, K. Sun, L.-C. Lin, C.Y. Tang, F. Yang, M.D. Guiver, X. Quan, Y. Dong, Robust ultrathin nanoporous MOF membrane with intra-crystalline defects for fast water transport, Nature Communications 13(1) (2022) 266. https://doi.org/10.1038/s41467-021-27873-6.
[205] H. Li, M. Fu, S.-Q. Wang, X. Zheng, M. Zhao, F. Yang, C.Y. Tang, Y. Dong, Stable Zr-Based Metal–Organic Framework Nanoporous Membrane for Efficient Desalination of Hypersaline Water, Environmental Science & Technology 55(21) (2021) 14917-14927. https://doi.org/10.1021/acs.est.1c06105.
[206] L. Zhai, X. Yu, Y. Wang, J. Zhang, Y. Ying, Y. Cheng, S.B. Peh, G. Liu, X. Wang, Y. Cai, D. Zhao, Polycrystalline rare-earth metal-organic framework membranes with in-situ healing ability for efficient alcohol dehydration, Journal of Membrane Science 610 (2020) 118239. https://doi.org/https://doi.org/10.1016/j.memsci.2020.118239.
[207] X. Dong, Y.S. Lin, Synthesis of an organophilic ZIF-71 membrane for pervaporation solvent separation, Chemical Communications 49(12) (2013) 1196-1198. https://doi.org/10.1039/C2CC38512K.
[208] H. Jin, K. Mo, F. Wen, Y. Li, Preparation and pervaporation performance of CAU-10-H MOF membranes, Journal of Membrane Science 577 (2019) 129-136.
[209] X. Liu, C. Wang, B. Wang, K. Li, Novel Organic-Dehydration Membranes Prepared from Zirconium Metal-Organic Frameworks, Advanced Functional Materials 27(3) (2017) 1604311. https://doi.org/https://doi.org/10.1002/adfm.201604311.
[210] M. Miyamoto, K. Hori, T. Goshima, N. Takaya, Y. Oumi, S. Uemiya, An Organoselective Zirconium-Based Metal–Organic-Framework UiO-66 Membrane for Pervaporation, European Journal of Inorganic

Chemistry 2017(14) (2017) 2094-2099. https://doi.org/https://doi.org/10.1002/ejic.201700010.
[211] S. Wang, Z. Kang, B. Xu, L. Fan, G. Li, L. Wen, X. Xin, Z. Xiao, J. Pang, X. Du, D. Sun, Wettability switchable metal-organic framework membranes for pervaporation of water/ethanol mixtures, Inorganic Chemistry Communications 82 (2017) 64-67. https://doi.org/https://doi.org/10.1016/j.inoche.2017.05.016.
[212] J.-Y. Lai, T.-Y. Wang, C. Zou, J.-J. Chen, L.-C. Lin, D.-Y. Kang, Highly-selective MOF-303 membrane for alcohol dehydration, Journal of Membrane Science 661 (2022) 120879. https://doi.org/https://doi.org/10.1016/j.memsci.2022.120879.
[213] F.-H. Hu, L.-T. Chi, G.-B. Syu, T.-Y. Yu, M.-P. Lin, J.-J. Chen, W.-Y. Yu, D.-Y. Kang, Mixed-linker MOF-303 membranes for pervaporation, Journal of Membrane Science Letters 3(2) (2023) 100053. https://doi.org/https://doi.org/10.1016/j.memlet.2023.100053.
[214] A.M. Marti, D. Tran, K.J. Balkus, Fabrication of a Substituted Imidazolate Material 1 (SIM-1) membrane using post synthetic modification (PSM) for pervaporation of water/ethanol mixtures, Journal of Porous Materials 22(5) (2015) 1275-1284. https://doi.org/10.1007/s10934-015-0005-y.
[215] R. Luo, H. Fu, Y. Li, Q. Xing, G. Liang, P. Bai, X. Guo, J. Lyu, M. Tsapatsis, In Situ Fabrication of Metal–Organic Framework Thin Films with Enhanced Pervaporation Performance, Advanced Functional Materials 33(18) (2023) 2213221. https://doi.org/https://doi.org/10.1002/adfm.202213221.
[216] K. Huang, B. Wang, S. Guo, K. Li, Micropatterned Ultrathin MOF Membranes with Enhanced Molecular Sieving Property, Angewandte Chemie International Edition 57(42) (2018) 13892-13896. https://doi.org/https://doi.org/10.1002/anie.201809872.
[217] B. Mo, Y. Jin, G. Zhou, G. Liu, C. Chen, Z. Liu, G. Liu, W. Jin, Ligand-engineered Zr-MOF membranes with fast water transport channels for alcohol–water separation, AIChE Journal 70(5) (2024) e18368. https://doi.org/https://doi.org/10.1002/aic.18368.
[218] G. Gao, Y. Zhao, P. Zhu, H. Liu, Y. Guo, X. Zhang, Self-converted fabrication of a Ni-MOF-74 tubular membrane from nickel-based nanosheets for butanol dehydration by pervaporation, CrystEngComm 25(48) (2023) 6740-6747. https://doi.org/10.1039/D3CE01007D.
[219] G. Gao, Y. Zhao, P. Zhu, H. Liu, X. Zhang, Y. Guo, G. Yang, Rapid Synthesis of Defect-Free Tubular Co-Gallate MOF Membranes for MeOH/MTBE Separation by Pervaporation, Industrial & Engineering Chemistry Research 63(50) (2024) 22043-22052. https://doi.org/10.1021/acs.iecr.4c03471.
[220] L. Wu, Y. Liang, B. Zhang, S. Cong, S. Tang, K. Jiang, L. Luan, Z. Wang, X. Liu, Post-synthetic modification of MOF UiO-66-$NH_2$ membranes for efficient methanol/organic separation, Journal of Membrane Science 715 (2025) 123475. https://doi.org/https://doi.org/10.1016/j.memsci.2024.123475.
[221] X. Wu, W. Wei, J. Jiang, J. Caro, A. Huang, High-Flux High-Selectivity Metal–Organic Framework MIL-160 Membrane for Xylene Isomer Separation by Pervaporation, Angewandte Chemie International Edition 57(47) (2018) 15354-15358. https://doi.org/https://doi.org/10.1002/anie.201807935.
[222] G. Li, Y. Qi, H. Lin, N. Lu, J. Chen, J. Wang, Q. Han, F. Liu, Ni-metal-organic-framework (Ni-MOF) membranes from multiply stacked nanosheets (MSNs) for efficient molecular sieve separation in aqueous and organic solvent, Journal of Membrane Science 635 (2021) 119470. https://doi.org/https://doi.org/10.1016/j.memsci.2021.119470.
[223] X. Yu, W. Fan, V. Wee, D. Shi, H. Yuan, Y. Ying, Y.D. Yuan, Z. Yang, Y. Feng, D. Sun, D. Zhao, Polycrystalline Iron(III) metal-organic framework membranes for organic solvent nanofiltration with high permeance, Journal of Membrane Science 644 (2022) 120130. https://doi.org/https://doi.org/10.1016/j.memsci.2021.120130.
[224] I. Chandio, T.H. Banglani, D. Janwery, S. Rahujo, A.A. Memon, K.H. Thebo, A. Nadeem, S.M. Attia, Highly stable Zirconium@metal-organic framework (UiO-66)-based lamellar membranes for organic solvent nanofiltration, Journal of Physics and Chemistry of Solids 199 (2025) 112565. https://doi.org/https://doi.org/10.1016/j.jpcs.2025.112565.
[225] Y. Li, L.H. Wee, A. Volodin, J.A. Martens, I.F.J. Vankelecom, Polymer supported ZIF-8 membranes prepared via an interfacial synthesis method, Chemical Communications 51(5) (2015) 918-920. https://doi.org/10.1039/C4CC06699E.
[226] Y. Cai, D. Shi, G. Liu, Y. Ying, Y. Cheng, Y. Wang, D. Chen, J. Lu, D. Zhao, Polycrystalline zirconium metal-organic framework membranes supported on flexible carbon cloth for organic solvent nanofiltration, Journal of Membrane Science 615 (2020) 118551. https://doi.org/https://doi.org/10.1016/j.memsci.2020.118551.
[227] H.M. Tham, S. Japip, D. Hua, T.-S. Chung, Green Layer-by-Layer Method for the Preparation of Polyacrylonitrile-Supported Zinc Benzene-1,4-dicarboxylic Acid Membranes, 11(15) (2018) 2612-2619. https://doi.org/https://doi.org/10.1002/cssc.201800740.
[228] G. Li, K. Zhang, T. Tsuru, Two-Dimensional Covalent Organic Framework (COF) Membranes

Fabricated via the Assembly of Exfoliated COF Nanosheets, ACS Applied Materials & Interfaces 9(10) (2017) 8433-8436. https://doi.org/10.1021/acsami.6b15752.
[229] Z. Wang, Z. Si, D. Cai, G.L. Shufeng Li, P. Qin, Synthesis of stable COF-300 nanofiltration membrane via in-situ growth with ultrahigh flux for selective dye separation, Journal of Membrane Science 615 (2020) 118466. https://doi.org/https://doi.org/10.1016/j.memsci.2020.118466.
[230] R. Wang, X. Shi, A. Xiao, W. Zhou, Y. Wang, Interfacial polymerization of covalent organic frameworks (COFs) on polymeric substrates for molecular separations, Journal of Membrane Science 566 (2018) 197-204. https://doi.org/https://doi.org/10.1016/j.memsci.2018.08.044.
[231] S. Hou, W. Ji, J. Chen, Y. Teng, L. Wen, L. Jiang, Free-Standing Covalent Organic Framework Membrane for High-Efficiency Salinity Gradient Energy Conversion, Angewandte Chemie International Edition 60(18) (2021) 9925-9930. https://doi.org/https://doi.org/10.1002/anie.202100205.
[232] M.N. Wang, Y.J. Song, W.L. Jiang, F. Fornasiero, J.J. Urban, B.X. Mi, Layer-by-layer Assembly of Nanosheets with Matching Size and Shape for More Stable Membrane Structure than Nanosheet-Polymer Assembly, Acs Applied Materials & Interfaces 16(20) (2024) 26568-26579. https://doi.org/10.1021/acsami.4c03891.
[233] Y. Ying, M. Tong, S. Ning, S.K. Ravi, S.B. Peh, S.C. Tan, S.J. Pennycook, D. Zhao, Ultrathin two-dimensional membranes assembled by ionic covalent organic nanosheets with reduced apertures for gas separation, Journal of the American Chemical Society 142(9) (2020) 4472-4480.
[234] X. Shi, R. Wang, A. Xiao, T. Jia, S.-P. Sun, Y. Wang, Layer-by-Layer Synthesis of Covalent Organic Frameworks on Porous Substrates for Fast Molecular Separations, ACS Applied Nano Materials 1(11) (2018) 6320-6326. https://doi.org/10.1021/acsanm.8b01537.
[235] D. Hao, J. Zhang, H. Lu, W. Leng, R. Ge, X. Dai, Y. Gao, Fabrication of a COF-5 membrane on a functionalized α-Al 2 O 3 ceramic support using a microwave irradiation method, Chemical Communications 50(12) (2014) 1462-1464.
[236] Y. Wang, L. Ren, J. Wang, J. Zhao, Q.-B. Chen, In-situ growth of anionic covalent organic frameworks efficaciously enhanced the monovalent selectivity of anion exchange membranes, Journal of Membrane Science 659 (2022) 120818. https://doi.org/https://doi.org/10.1016/j.memsci.2022.120818.
[237] M.Q. Seah, W.J. Lau, P.S. Goh, H.H. Tseng, R.A. Wahab, A.F. Ismail, Progress of Interfacial Polymerization Techniques for Polyamide Thin Film (Nano)Composite Membrane Fabrication: A Comprehensive Review, Polymers (Basel) 12(12) (2020). https://doi.org/10.3390/polym12122817.
[238] H. Wang, Z. Zeng, P. Xu, L. Li, G. Zeng, R. Xiao, Z. Tang, D. Huang, L. Tang, C. Lai, Recent progress in covalent organic framework thin films: fabrications, applications and perspectives, Chemical Society Reviews 48(2) (2019) 488-516.
[239] K. Dey, M. Pal, K.C. Rout, S. Kunjattu H, A. Das, R. Mukherjee, U.K. Kharul, R. Banerjee, Selective Molecular Separation by Interfacially Crystallized Covalent Organic Framework Thin Films, Journal of the American Chemical Society 139(37) (2017) 13083-13091. https://doi.org/10.1021/jacs.7b06640.
[240] A.K. Mohammed, A.A. Al Khoori, M.A. Addicoat, S. Varghese, I. Othman, M.A. Jaoude, K. Polychronopoulou, M. Baias, M.A. Haija, D. Shetty, Solvent-influenced fragmentations in free-standing three-dimensional covalent organic framework membranes for hydrophobicity switching, Angewandte Chemie 134(13) (2022) e202200905.
[241] N.A. Khan, R. Zhang, H. Wu, J. Shen, J. Yuan, C. Fan, L. Cao, M.A. Olson, Z. Jiang, Solid–Vapor Interface Engineered Covalent Organic Framework Membranes for Molecular Separation, Journal of the American Chemical Society 142(31) (2020) 13450-13458. https://doi.org/10.1021/jacs.0c04589.
[242] D.B. Shinde, G. Sheng, X. Li, M. Ostwal, A.-H. Emwas, K.-W. Huang, Z. Lai, Crystalline 2D Covalent Organic Framework Membranes for High-Flux Organic Solvent Nanofiltration, Journal of the American Chemical Society 140(43) (2018) 14342-14349. https://doi.org/10.1021/jacs.8b08788.
[243] S. Kunjattu H, N.M. Thorat, S. Gawas, U.K. Kharul, Scalable, Interfacially Synthesized, Covalent–Organic Framework (COF)-Based Thin-Film Composite (TFC) Hollow Fiber Membranes for Organic Solvent Nanofiltration (OSN), ACS Applied Materials & Interfaces 16(15) (2024) 19463-19471. https://doi.org/10.1021/acsami.4c00305.
[244] S. Hou, W. Ji, J. Chen, Y. Teng, L. Wen, L. Jiang, Free-standing covalent organic framework membrane for high-efficiency salinity gradient energy conversion, Angewandte Chemie 133(18) (2021) 10013-10018.
[245] D.W. Burke, Z. Jiang, A.G. Livingston, W.R. Dichtel, 2D Covalent Organic Framework Membranes for Liquid-Phase Molecular Separations: State of the Field, Common Pitfalls, and Future Opportunities, Advanced Materials 36(1) (2024) 2300525. https://doi.org/https://doi.org/10.1002/adma.202300525.
[246] T.-T. Nguyen, X. Min, W. Xia, Z. Qiang, R.S. Khandge, H.-K. Yu, J.-W. Wang, Y. Wang, X. Ma, Anionic covalent organic framework membranes for the removal of per- and polyfluoroalkyl substances with

enhanced selectivity, Journal of Membrane Science 705 (2024) 122925. https://doi.org/https://doi.org/10.1016/j.memsci.2024.122925.
[247] C. Cao, H. Wang, M. Wang, Y. Liu, Z. Zhang, S. Liang, W. Yuhan, F. Pan, Z. Jiang, Conferring efficient alcohol dehydration to covalent organic framework membranes via post-synthetic linker exchange, Journal of Membrane Science 630 (2021) 119319. https://doi.org/https://doi.org/10.1016/j.memsci.2021.119319.
[248] H. Fan, J. Gu, H. Meng, A. Knebel, J. Caro, High-Flux Membranes Based on the Covalent Organic Framework COF-LZU1 for Selective Dye Separation by Nanofiltration, Angewandte Chemie International Edition 57(15) (2018) 4083-4087. https://doi.org/https://doi.org/10.1002/anie.201712816.
[249] G. Yang, J. Fan, H. Chen, L. Wang, Z. Li, L. Guo, G. Liu, C. Yu, S. Zou, G. Zeng, Covalent organic framework composite membranes with skeleton charge for efficient desalination, Journal of Membrane Science 701 (2024) 122700. https://doi.org/https://doi.org/10.1016/j.memsci.2024.122700.
[250] R. Wang, M. Wei, Y. Wang, Secondary growth of covalent organic frameworks (COFs) on porous substrates for fast desalination, Journal of Membrane Science 604 (2020) 118090. https://doi.org/https://doi.org/10.1016/j.memsci.2020.118090.
[251] C. Liu, Y. Jiang, A. Nalaparaju, J. Jiang, A. Huang, Post-synthesis of a covalent organic framework nanofiltration membrane for highly efficient water treatment, Journal of Materials Chemistry A 7(42) (2019) 24205-24210. https://doi.org/10.1039/C9TA06325K.
[252] D. Liu, K. Li, M. Li, Z. Wang, M. Shan, Y. Zhang, Moderately Crystalline Azine-Linked Covalent Organic Framework Membrane for Ultrafast Molecular Sieving, ACS Applied Materials & Interfaces 13(31) (2021) 37775-37784. https://doi.org/10.1021/acsami.1c06891.
[253] F.-x. Kong, S.-y. Zhang, D.-w. Zhang, P. Xia, J.-f. Chen, The influence of the preheated PSf substrate on COF-LZU1 layer formation and the performance for salt and pharmaceutical rejection, Desalination 579 (2024) 117514. https://doi.org/https://doi.org/10.1016/j.desal.2024.117514.
[254] L.-p. Yue, F.-x. Kong, Y. Wang, G.-d. Sun, J.-f. Chen, PTSA-mediated interfacial catalytic polymerization of crystalline dense covalent organic framework membranes for enhanced desalination, Journal of Membrane Science 685 (2023) 121877. https://doi.org/https://doi.org/10.1016/j.memsci.2023.121877.
[255] Q. Liu, P. Huang, N. Xu, Q. Wang, L. Fan, Decoupling synthesis and crystallization of covalent organic frameworks (COFs) for more crystalline layer targeting high efficiency dye separation, Separation and Purification Technology 341 (2024) 126881. https://doi.org/https://doi.org/10.1016/j.seppur.2024.126881.
[256] Y.X. Liu, J.H. Chen, N. Qin, D.L. Gao, Y.Y. Zhang, Q. Yang, Construction of covalent organic frameworks membranes in situ through nonsolvent-induce phase separation for fast and accurate nanofiltration, Journal of Membrane Science 697 (2024) 122601. https://doi.org/https://doi.org/10.1016/j.memsci.2024.122601.
[257] Z. Zha, S. Zhao, G. Ma, A.S. Pittman, Z. Wang, J. Wang, Covalent organic framework membrane reconstructed through intra-pore reaction having tunable performance for molecular separation, Separation and Purification Technology 285 (2022) 120387. https://doi.org/https://doi.org/10.1016/j.seppur.2021.120387.
[258] X. Shi, Z. Zhang, M. Wei, X. Wang, J. Wang, Y. Zhang, Y. Wang, Three-Dimensional Covalent Organic Framework Membranes: Synthesis by Oligomer Interfacial Ripening and Application in Precise Separations, Macromolecules 55(8) (2022) 3259-3266. https://doi.org/10.1021/acs.macromol.1c02333.
[259] H. Wang, J. Zhao, Y. Li, Y. Cao, Z. Zhu, M. Wang, R. Zhang, F. Pan, Z. Jiang, Aqueous two-phase interfacial assembly of COF membranes for water desalination, Nano-Micro Letters 14(1) (2022) 216.
[260] X. Shi, A. Xiao, C. Zhang, Y. Wang, Growing covalent organic frameworks on porous substrates for molecule-sieving membranes with pores tunable from ultra- to nanofiltration, Journal of Membrane Science 576 (2019) 116-122. https://doi.org/https://doi.org/10.1016/j.memsci.2019.01.034.
[261] H. Yang, X. Cheng, X. Cheng, F. Pan, H. Wu, G. Liu, Y. Song, X. Cao, Z. Jiang, Highly water-selective membranes based on hollow covalent organic frameworks with fast transport pathways, Journal of Membrane Science 565 (2018) 331-341. https://doi.org/https://doi.org/10.1016/j.memsci.2018.08.043.
[262] K. Banjerdteerakul, H. Peng, K. Li, Covalent organic frameworks based membranes for separation of azeotropic solvent mixtures by pervaporation, Journal of Membrane Science 678 (2023) 121679. https://doi.org/https://doi.org/10.1016/j.memsci.2023.121679.
[263] Z. Li, J. Fan, L. Wang, X. Yang, L. Guo, H. Chen, D. Gong, G. Yang, Q. Xu, S. Zou, G. Zeng, Two-dimensional lamellar stacking COF membrane with charge repulsion effect for ions separation, Journal of Membrane Science 699 (2024) 122645. https://doi.org/https://doi.org/10.1016/j.memsci.2024.122645.
[264] X. Shi, Z. Zhang, S. Fang, J. Wang, Y. Zhang, Y. Wang, Flexible and Robust Three-Dimensional Covalent Organic Framework Membranes for Precise Separations under Extreme Conditions, Nano Letters 21(19) (2021) 8355-8362. https://doi.org/10.1021/acs.nanolett.1c02919.

[265] S. Kandambeth, B.P. Biswal, H.D. Chaudhari, K.C. Rout, S. Kunjattu H., S. Mitra, S. Karak, A. Das, R. Mukherjee, U.K. Kharul, R. Banerjee, Selective Molecular Sieving in Self-Standing Porous Covalent-Organic-Framework Membranes, Advanced Materials 29(2) (2017) 1603945. https://doi.org/https://doi.org/10.1002/adma.201603945.
[266] S.K. Das, P. Manchanda, K.-V. Peinemann, Solvent-resistant triazine-piperazine linked porous covalent organic polymer thin-film nanofiltration membrane, Separation and Purification Technology 213 (2019) 348-358. https://doi.org/https://doi.org/10.1016/j.seppur.2018.12.046.
[267] X. Shi, Z. Zhang, C. Yin, X. Zhang, J. Long, Z. Zhang, Y. Wang, Design of Three-Dimensional Covalent Organic Framework Membranes for Fast and Robust Organic Solvent Nanofiltration, Angewandte Chemie International Edition 61(36) (2022) e202207559. https://doi.org/https://doi.org/10.1002/anie.202207559.
[268] S. Kumar, N. Alqadhi, J. Hu, G. Szekely, Swift fabrication of thin-film composite membranes with azine-linked covalent organic framework for high-temperature organic solvent nanofiltration, Journal of Membrane Science 691 (2024) 122257. https://doi.org/https://doi.org/10.1016/j.memsci.2023.122257.
[269] L.M. Robeson, The upper bound revisited, Journal of Membrane Science 320(1) (2008) 390-400. https://doi.org/https://doi.org/10.1016/j.memsci.2008.04.030.
[270] S. Zinadini, A.A. Zinatizadeh, M. Rahimi, V. Vatanpour, H. Zangeneh, Preparation of a novel antifouling mixed matrix PES membrane by embedding graphene oxide nanoplates, Journal of Membrane Science 453 (2014) 292-301. https://doi.org/10.1016/j.memsci.2013.10.070.
[271] P.T.P. Aryanti, F.A. Nugroho, I.N. Widiasa, P.D. Sutrisna, I.G.J.J.o.A.P.S. Wenten, Preparation of highly selective PSf/ZnO/PEG400 tight ultrafiltration membrane for dyes removal, Journal of Applied Polymer Science 139(33) (2022) e52779. https://doi.org/10.1002/app.52779.
[272] H. Yu, D. Cai, S. Li, C. Gao, L.J.J.o.M.S. Xue, Tight UF membranes with ultrahigh water flux prepared by in-situ growing ZIF particles in NIPS process for greatly enhanced dye removal efficiency, Journal of Membrane Science 666 (2023) 121136. https://doi.org/10.1016/j.memsci.2022.121136.
[273] M.S. Denny, J.C. Moreton, L. Benz, S.M. Cohen, Metal–organic frameworks for membrane-based separations, Nature Reviews Materials 1(12) (2016) 16078. https://doi.org/10.1038/natrevmats.2016.78.
[274] W. Gai, S. Xu, J. Pan, X. Pan, Y. Liu, Q. Li, L. Huang, Y. Ma, High dye separation performance of novel Cu-BTC/PES MMMs with water-stabilized Cu-BTC nanoparticles, Journal of Applied Polymer Science 140(40) (2023) e54506. https://doi.org/https://doi.org/10.1002/app.54506.
[275] X. Cao, H. Xu, S. Dong, J. Xu, Z. Qiao, S. Zhao, J. Wang, Z. Wang, Preparation of high-performance and pressure-resistant mixed matrix membranes for CO2/H2 separation by modifying COF surfaces with the groups or segments of the polymer matrix, Journal of Membrane Science 601 (2020) 117882. https://doi.org/https://doi.org/10.1016/j.memsci.2020.117882.
[276] V. Vatanpour, S. Paziresh, A melamine-based covalent organic framework nanomaterial as a nanofiller in polyethersulfone mixed matrix membranes to improve separation and antifouling performance, Journal of Applied Polymer Science 139(1) (2022) 51428. https://doi.org/https://doi.org/10.1002/app.51428.
[277] X. Zhu, D. Jańczewski, S. Guo, S.S.C. Lee, F.J. Parra Velandia, S.L.-M. Teo, T. He, S.R. Puniredd, G.J. Vancso, Polyion Multilayers with Precise Surface Charge Control for Antifouling, ACS Applied Materials & Interfaces 7(1) (2015) 852-861. https://doi.org/10.1021/am507371a.
[278] M. Yang, P. Hadi, X. Yin, J. Yu, X. Huang, H. Ma, H. Walker, B.S. Hsiao, Antifouling nanocellulose membranes: How subtle adjustment of surface charge lead to self-cleaning property, Journal of Membrane Science 618 (2021) 118739. https://doi.org/10.1016/j.memsci.2020.118739.
[279] M. Dehghankar, T. Mohammadi, M.T. Moghadam, M.A. Tofighy, Metal-organic framework/zeolite nanocrystal/polyvinylidene fluoride composite ultrafiltration membranes with flux/antifouling advantages, Materials Chemistry and Physics 260 (2021) 124128. https://doi.org/https://doi.org/10.1016/j.matchemphys.2020.124128.
[280] N. Elmerhi, S. Kumar, M. Abi Jaoude, D. Shetty, Covalent Organic Framework-derived Composite Membranes for Water Treatment, Chemistry – An Asian Journal 19(2) (2024) e202300944. https://doi.org/https://doi.org/10.1002/asia.202300944.
[281] G. Bakeri, A.F. Ismail, M. Shariaty-Niassar, T. Matsuura, Effect of polymer concentration on the structure and performance of polyetherimide hollow fiber membranes, Journal of Membrane Science 363(1) (2010) 103-111. https://doi.org/https://doi.org/10.1016/j.memsci.2010.07.018.
[282] H. Xu, S. Chen, Y.-F. Zhao, F. Wang, F. Guo, MOF-Based Membranes for Remediated Application of Water Pollution, ChemPlusChem 89(8) (2024) e202400027. https://doi.org/https://doi.org/10.1002/cplu.202400027.
[283] T.-Y. Liu, H.-G. Yuan, Y.-Y. Liu, D. Ren, Y.-C. Su, X. Wang, Metal–Organic Framework Nanocomposite Thin Films with Interfacial Bindings and Self-Standing Robustness for High Water Flux and

Enhanced Ion Selectivity, ACS Nano 12(9) (2018) 9253-9265. https://doi.org/10.1021/acsnano.8b03994.
[284] K. Duan, J. Wang, Y. Zhang, J. Liu, Covalent organic frameworks (COFs) functionalized mixed matrix membrane for effective CO2/N2 separation, Journal of Membrane Science 572 (2019) 588-595. https://doi.org/https://doi.org/10.1016/j.memsci.2018.11.054.
[285] R. Lin, B. Villacorta Hernandez, L. Ge, Z. Zhu, Metal organic framework based mixed matrix membranes: an overview on filler/polymer interfaces, Journal of Materials Chemistry A 6(2) (2018) 293-312. https://doi.org/10.1039/C7TA07294E.
[286] J. Shen, G. Liu, K. Huang, Q. Li, K. Guan, Y. Li, W. Jin, UiO-66-polyether block amide mixed matrix membranes for CO2 separation, Journal of Membrane Science 513 (2016) 155-165. https://doi.org/https://doi.org/10.1016/j.memsci.2016.04.045.
[287] X. Guo, H. Huang, Y. Ban, Q. Yang, Y. Xiao, Y. Li, W. Yang, C. Zhong, Mixed matrix membranes incorporated with amine-functionalized titanium-based metal-organic framework for CO2/CH4 separation, Journal of Membrane Science 478 (2015) 130-139. https://doi.org/https://doi.org/10.1016/j.memsci.2015.01.007.
[288] M. Fang, C. Wu, Z. Yang, T. Wang, Y. Xia, J. Li, ZIF-8/PDMS mixed matrix membranes for propane/nitrogen mixture separation: Experimental result and permeation model validation, Journal of Membrane Science 474 (2015) 103-113. https://doi.org/https://doi.org/10.1016/j.memsci.2014.09.040.
[289] Q. Qian, A.X. Wu, W.S. Chi, P.A. Asinger, S. Lin, A. Hypsher, Z.P. Smith, Mixed-matrix membranes formed from imide-functionalized UiO-66-NH2 for improved interfacial compatibility, ACS applied materials & interfaces 11(34) (2019) 31257-31269.
[290] A. Kuzminova, M. Dmitrenko, A. Zolotarev, A. Korniak, D. Poloneeva, A. Selyutin, A. Emeline, A. Yushkin, A. Foster, P. Budd, Novel mixed matrix membranes based on polymer of intrinsic microporosity PIM-1 modified with metal-organic frameworks for removal of heavy metal ions and food dyes by nanofiltration, Membranes 12(1) (2021) 14.
[291] M.S. Mia, B. Yan, X. Zhu, T. Xing, G. Chen, Dopamine grafted iron-loaded waste silk for Fenton-like removal of toxic water pollutants, Polymers 11(12) (2019) 2037.
[292] A.P. Cote, A.I. Benin, N.W. Ockwig, M. O'Keeffe, A.J. Matzger, O.M.J.s. Yaghi, Porous, crystalline, covalent organic frameworks, Science 310(5751) (2005) 1166-1170. https://doi.org/10.1126/science.1120411.
[293] X. Feng, D. Peng, J. Zhu, Y. Wang, Y.J.S. Zhang, P. Technology, Recent advances of loose nanofiltration membranes for dye/salt separation, Seperation and Purification Technology 285 (2022) 120228. https://doi.org/10.1016/j.seppur.2021.120228.
[294] Z. Kang, Y. Peng, Y. Qian, D. Yuan, M.A. Addicoat, T. Heine, Z. Hu, L. Tee, Z. Guo, D. Zhao, Mixed matrix membranes (MMMs) comprising exfoliated 2D covalent organic frameworks (COFs) for efficient CO2 separation, Chemistry of Materials 28(5) (2016) 1277-1285.
[295] M. Etxeberria-Benavides, O. David, T. Johnson, M.M. Łozińska, A. Orsi, P.A. Wright, S. Mastel, R. Hillenbrand, F. Kapteijn, J. Gascon, High performance mixed matrix membranes (MMMs) composed of ZIF-94 filler and 6FDA-DAM polymer, Journal of membrane science 550 (2018) 198-207.
[296] J. Deng, Z. Dai, J. Hou, L. Deng, Morphologically tunable MOF nanosheets in mixed matrix membranes for CO2 separation, Chemistry of Materials 32(10) (2020) 4174-4184.
[297] G. Gnanaselvan, B. Sasikumar, G. Arthanareeswaran, Y.S. Mok, Performance of composite PES/MOF-5 membranes for the treatment of textile wastewater, Desalin Water Treat 156 (2019) 220-228.
[298] J.-Y. Lee, C.Y. Tang, F. Huo, Fabrication of Porous Matrix Membrane (PMM) Using Metal-Organic Framework as Green Template for Water Treatment, Scientific Reports 4(1) (2014) 3740. https://doi.org/10.1038/srep03740.
[299] E. Gil, X. Huang, K. Zuo, J. Kim, S. Rincón, J.M. Rivera, K. Ranjbari, F. Perreault, P. Alvarez, A. Zepeda, Q. Li, A Polysulfone/Cobalt Metal–Organic Framework Nanocomposite Membrane with Enhanced Water Permeability and Fouling Resistance, ACS Applied Polymer Materials 4(5) (2022) 3532-3542. https://doi.org/10.1021/acsapm.2c00132.
[300] L. Cheng, Z. Zhou, L. Li, P. Xiao, Y. Ma, F. Liu, J. Li, PVDF/MOFs mixed matrix ultrafiltration membrane for efficient water treatment, Frontiers in Chemistry 10 (2022) 985750.
[301] H. Wang, H. Chen, Y. Zeng, G. Chen, M. Cui, Hydrophilic modification and anti-fouling properties of PVDF ultrafiltration membrane via blending of nano-particle MIL-101 MOFs, Digest Journal of Nanomaterials & Biostructures (DJNB) 16(2) (2021).
[302] M.H.A. Tajuddin, J. Jaafar, N.A.H.M. Nordin, A.F. Ismail, M.H.D. Othman, A. Rahman, Metal organic framework mixed-matrix membrane for arsenic removal, Malaysian Journal of Fundamental and Applied Sciences 16(3) (2020) 359-362.
[303] T. Anjum, R. Tamime, A.L. Khan, Mixed-matrix membranes comprising of polysulfone and porous

UiO-66, zeolite 4A, and their combination: Preparation, removal of humic acid, and antifouling properties, Membranes 10(12) (2020) 393.
[304] O.A. Koriem, M.S. Showman, A.H. El-Shazly, M.F. Elkady, Cellulose acetate/polyvinylidene fluoride based mixed matrix membranes impregnated with UiO-66 nano-MOF for reverse osmosis desalination, Cellulose 30(1) (2023) 413-426. https://doi.org/10.1007/s10570-022-04889-9.
[305] M. Ali, M. Aslam, A. Khan, M.A. Gilani, A.L. Khan, Mixed matrix membranes incorporated with sonication-assisted ZIF-8 nanofillers for hazardous wastewater treatment, Environmental Science and Pollution Research 26(35) (2019) 35913-35923. https://doi.org/10.1007/s11356-019-06698-3.
[306] K. Yang, X. Liu, X. Wang, T. Hao, W. Zhang, M. Chen, ZIF-8 modified poly (m-phenylene isophthalamide)(PMIA) hybrid membrane for dye wastewater treatment, Journal of Industrial Textiles 52 (2022) 15280837221139235.
[307] P.D. Sutrisna, R.P. Hadi, C. Wijaya, J. Liliani, C. Robby, Cellulose acetate–Based mixed matrix membrane for methylene blue wastewater treatment, AIP Conference Proceedings, AIP Publishing, 2023.
[308] J. Yin, H. Tang, D. Liu, T. Huang, L. Zhu, Application of ZIF-67 as a crosslinker to prepare sulfonated polysulfone mixed-matrix membranes for enhanced water permeability and separation properties, Water Science and Technology 84(1) (2021) 144-158. https://doi.org/10.2166/wst.2021.202.
[309] G. Wu, Y. Liu, Q. Zheng, Z. Yu, F. Luo, Ultrahigh uranium extraction performance of COFs/SPES mixed matrix membranes at acidic medium, Journal of Solid State Chemistry 288 (2020) 121364.
[310] C. Wu, X. Wang, T. Zhu, P. Li, S. Xia, Covalent organic frameworks embedded membrane via acetic-acid-catalyzed interfacial polymerization for dyes separation: Enhanced permeability and selectivity, Chemosphere 261 (2020) 127580. https://doi.org/https://doi.org/10.1016/j.chemosphere.2020.127580.
[311] P.H.H. Duong, V.A. Kuehl, B. Mastorovich, J.O. Hoberg, B.A. Parkinson, K.D. Li-Oakey, Carboxyl-functionalized covalent organic framework as a two-dimensional nanofiller for mixed-matrix ultrafiltration membranes, Journal of Membrane Science 574 (2019) 338-348. https://doi.org/https://doi.org/10.1016/j.memsci.2018.12.042.
[312] A.K. Mohammed, J.K. Ali, M.B.S. Kuzhimully, M.A. Addicoat, S. Varghese, M. Baias, E. Alhseinat, D. Shetty, The fragmented 3D-covalent organic framework in cellulose acetate membrane for efficient phenol removal, Chemical Engineering Journal 466 (2023) 143234.
[313] L. Xu, J. Xu, B. Shan, X. Wang, C. Gao, TpPa-2-incorporated mixed matrix membranes for efficient water purification, Journal of Membrane Science 526 (2017) 355-366.
[314] W. Xu, X. Sun, M. Huang, X. Pan, X. Huang, H. Zhuang, Novel covalent organic framework/PVDF ultrafiltration membranes with antifouling and lead removal performance, Journal of Environmental Management 269 (2020) 110758.
[315] X. Wang, X. Shi, Y. Wang, In Situ Growth of Cationic Covalent Organic Frameworks (COFs) for Mixed Matrix Membranes with Enhanced Performances, Langmuir 36(37) (2020) 10970-10978. https://doi.org/10.1021/acs.langmuir.0c01714.
[316] Q.Q. Li, Q. Liu, J. Zhao, Y.Y. Hua, J.J. Sun, J.G. Duan, W.Q. Jin, High efficient water/ethanol separation by a mixed matrix membrane incorporating MOF filler with high water adsorption capacity, Journal of Membrane Science 544 (2017) 68-78. https://doi.org/10.1016/j.memsci.2017.09.021.
[317] H. Mao, H.-G. Zhen, A. Ahmad, S.-H. Li, Y. Liang, J.-F. Ding, Y. Wu, L.-Z. Li, Z.-P. Zhao, Highly selective and robust PDMS mixed matrix membranes by embedding two-dimensional ZIF-L for alcohol permselective pervaporation, Journal of Membrane Science 582 (2019) 307-321. https://doi.org/https://doi.org/10.1016/j.memsci.2019.04.022.
[318] H. Mao, H.-G. Zhen, A. Ahmad, A.-S. Zhang, Z.-P. Zhao, In situ fabrication of MOF nanoparticles in PDMS membrane via interfacial synthesis for enhanced ethanol permselective pervaporation, Journal of Membrane Science 573 (2019) 344-358. https://doi.org/https://doi.org/10.1016/j.memsci.2018.12.017.
[319] A. Hamlil, L. Aouinti, Preparation and characterization of dense membrane based metal organic networks (MOF- 5) for separation :aromatic-aliphatic mixtures, Polymer-Plastics Technology and Materials 62(7) (2023) 909-920. https://doi.org/10.1080/25740881.2023.2172683.
[320] S. Li, P. Li, D. Cai, H. Shan, J. Zhao, Z. Wang, P. Qin, T. Tan, Boosting pervaporation performance by promoting organic permeability and simultaneously inhibiting water transport via blending PDMS with COF-300, Journal of Membrane Science 579 (2019) 141-150. https://doi.org/https://doi.org/10.1016/j.memsci.2019.02.041.
[321] Z. Huang, G. Yang, J. Zhang, S. Gray, Z. Xie, Dual-layer membranes with a thin film hydrophilic MOF/PVA nanocomposite for enhanced antiwetting property in membrane distillation, Desalination 518 (2021) 115268. https://doi.org/https://doi.org/10.1016/j.desal.2021.115268.
[322] Y. Zhao, C. Wang, L.-F. Ren, B. Zhang, J. Shao, Facile preparation of COF-LZU1 modified membrane

via electrostatic spraying for emerging contaminants treatment in direct contact membrane distillation, Separation and Purification Technology 337 (2024) 126411. https://doi.org/https://doi.org/10.1016/j.seppur.2024.126411.
[323] S. Basu, M. Maes, A. Cano-Odena, L. Alaerts, D.E. De Vos, I.F. Vankelecom, Solvent resistant nanofiltration (SRNF) membranes based on metal-organic frameworks, Journal of membrane science 344(1-2) (2009) 190-198.
[324] A. Yao, D. Hua, F. Zhao, D. Zheng, J. Pan, Y. Hong, Y. Liu, X. Rao, S. Zhou, G. Zhan, Integration of P84 and porphyrin–based 2D MOFs (M−TCPP, M = Zn, Cu, Co, Ni) for mixed matrix membranes towards enhanced performance in organic solvent nanofiltration, Separation and Purification Technology 282 (2022) 120022. https://doi.org/https://doi.org/10.1016/j.seppur.2021.120022.
[325] L. Zhu, H. Yu, H. Zhang, J. Shen, L. Xue, C. Gao, B. van der Bruggen, Mixed matrix membranes containing MIL-53(Al) for potential application in organic solvent nanofiltration, RSC Advances 5(89) (2015) 73068-73076. https://doi.org/10.1039/C5RA10259F.
[326] R. Hardian, J. Jia, A. Diaz-Marquez, S. Naskar, D. Fan, O. Shekhah, G. Maurin, M. Eddaoudi, G. Szekely, Design of Mixed-Matrix MOF Membranes with Asymmetric Filler Density and Intrinsic MOF/Polymer Compatibility for Enhanced Molecular Sieving, Advanced Materials 36(26) (2024) 2314206. https://doi.org/https://doi.org/10.1002/adma.202314206.
[327] N.A.A. Sani, W.J. Lau, A.F. Ismail, Polyphenylsulfone-based solvent resistant nanofiltration (SRNF) membrane incorporated with copper-1,3,5-benzenetricarboxylate (Cu-BTC) nanoparticles for methanol separation, RSC Advances 5(17) (2015) 13000-13010. https://doi.org/10.1039/C4RA14284E.
[328] M. Mazani, S. Aghapour Aktij, A. Rahimpour, N. Tavajohi Hassan Kiadeh, Cu-BTC Metal−Organic Framework Modified Membranes for Landfill Leachate Treatment, Water 12(1) (2020) 91.
[329] R. Lakra, M.R. Bilad, M. Balakrishnan, S. Basu, Development of high-performance CuBTC MOF-based forward osmosis (FO) membranes and their cleaning strategies, Chemical Engineering Research and Design 190 (2023) 566-579. https://doi.org/https://doi.org/10.1016/j.cherd.2023.01.005.
[330] D.D. Kachhadiya, Z.V.P. Murthy, Preparation and characterization of ZIF-8 and ZIF-67 incorporated poly(vinylidene fluoride) membranes for pervaporative separation of methanol/water mixtures, Materials Today Chemistry 22 (2021) 100591. https://doi.org/https://doi.org/10.1016/j.mtchem.2021.100591.
[331] Y. Pan, X. Yu, Preparation of Zeolitic Imidazolate Framework-91 and its modeling for pervaporation separation of water/ethanol mixtures, Separation and Purification Technology 237 (2020) 116330. https://doi.org/https://doi.org/10.1016/j.seppur.2019.116330.
[332] G. Zhang, J. Li, N. Wang, H. Fan, R. Zhang, G. Zhang, S. Ji, Enhanced flux of polydimethylsiloxane membrane for ethanol permselective pervaporation via incorporation of MIL-53 particles, Journal of Membrane Science 492 (2015) 322-330. https://doi.org/https://doi.org/10.1016/j.memsci.2015.05.070.
[333] H. Fan, Q. Shi, H. Yan, S. Ji, J. Dong, G. Zhang, Simultaneous Spray Self-Assembly of Highly Loaded ZIF-8–PDMS Nanohybrid Membranes Exhibiting Exceptionally High Biobutanol-Permselective Pervaporation, Angewandte Chemie International Edition 53(22) (2014) 5578-5582. https://doi.org/https://doi.org/10.1002/anie.201309534.
[334] D. Cheng, L. Zhao, N. Li, S.J.D. Smith, D. Wu, J. Zhang, D. Ng, C. Wu, M.R. Martinez, M.P. Batten, Z. Xie, Aluminum fumarate MOF/PVDF hollow fiber membrane for enhancement of water flux and thermal efficiency in direct contact membrane distillation, Journal of Membrane Science 588 (2019) 117204. https://doi.org/https://doi.org/10.1016/j.memsci.2019.117204.
[335] M. Prajapati, S. Kalla, A. Sivaiah, A CuBTC@PVDF-based super hydrophobic membrane for perfluoroheptanoic acid (PFHpA) rejection through membrane distillation, Process Safety and Environmental Protection 194 (2025) 152-163. https://doi.org/https://doi.org/10.1016/j.psep.2024.11.107.
[336] H. Cao, Y. Mao, W. Wang, Y. Jin, Y. Gao, M. Zhang, X. Zhao, J. Sun, Z. Song, ZIF-8 based dual scale superhydrophobic membrane for membrane distillation, Desalination 550 (2023) 116373. https://doi.org/https://doi.org/10.1016/j.desal.2023.116373.
[337] L. Chen, F. Li, L. Jiang, F. He, Y. Wei, UiO-66-NH2/PVA composite Janus membrane with a dense hydrophilic surface layer for strong resistance to fouling and wettability in membrane distillation, Journal of Water Process Engineering 48 (2022) 102887. https://doi.org/https://doi.org/10.1016/j.jwpe.2022.102887.
[338] Z. Wang, Z. Si, D. Cai, G. Li, S. Li, P. Qin, T. Tan, Improving ZIF-8 stability in the preparation process of polyimide-based organic solvent nanofiltration membrane, Separation and Purification Technology 227 (2019) 115687.
[339] C.-N. Yeh, K. Raidongia, J. Shao, Q.-H. Yang, J. Huang, On the origin of the stability of graphene oxide membranes in water, Nature Chemistry 7(2) (2015) 166-170. https://doi.org/10.1038/nchem.2145.
[340] S. Pei, H.-M. Cheng, The reduction of graphene oxide, Carbon 50(9) (2012) 3210-3228.

https://doi.org/https://doi.org/10.1016/j.carbon.2011.11.010.
[341] H.C. Schniepp, J.-L. Li, M.J. McAllister, H. Sai, M. Herrera-Alonso, D.H. Adamson, R.K. Prud'homme, R. Car, D.A. Saville, I.A. Aksay, Functionalized Single Graphene Sheets Derived from Splitting Graphite Oxide, The Journal of Physical Chemistry B 110(17) (2006) 8535-8539. https://doi.org/10.1021/jp060936f.
[342] R.K. Joshi, P. Carbone, F.C. Wang, V.G. Kravets, Y. Su, I.V. Grigorieva, H.A. Wu, A.K. Geim, R.R. Nair, Precise and Ultrafast Molecular Sieving Through Graphene Oxide Membranes, 343(6172) (2014) 752-754. https://doi.org/doi:10.1126/science.1245711.
[343] R.R. Nair, H.A. Wu, P.N. Jayaram, I.V. Grigorieva, A.K. Geim, Unimpeded Permeation of Water Through Helium-Leak–Tight Graphene-Based Membranes, 335(6067) (2012) 442-444. https://doi.org/doi:10.1126/science.1211694.
[344] F. Moghadam, M. Zhai, T. Zouaoui, K. Li, Hybrid graphene oxide membranes with regulated water and ion permeation channels via functional materials, Current Opinion in Chemical Engineering 40 (2023) 100907. https://doi.org/https://doi.org/10.1016/j.coche.2023.100907.
[345] Y. Ying, D. Liu, W. Zhang, J. Ma, H. Huang, Q. Yang, C. Zhong, High-Flux Graphene Oxide Membranes Intercalated by Metal–Organic Framework with Highly Selective Separation of Aqueous Organic Solution, ACS Applied Materials & Interfaces 9(2) (2017) 1710-1718. https://doi.org/10.1021/acsami.6b14371.
[346] L. Siahkamari, O. Bakhtiari, Preparation of post-synthetized MOF-303@ graphene oxide (GO) composite membrane for pervaporative dehydration of ethanol, Separation and Purification Technology 359 (2025) 130564. https://doi.org/https://doi.org/10.1016/j.seppur.2024.130564.
[347] Y. Li, H. Liu, H. Wang, J. Qiu, X. Zhang, GO-guided direct growth of highly oriented metal–organic framework nanosheet membranes for H 2/CO 2 separation, Chemical science 9(17) (2018) 4132-4141.
[348] J. Cheng, J. Liang, L. Dong, J. Chai, N. Zhao, S. Ullah, H. Wang, D. Zhang, S. Imtiaz, G. Shan, G. Zheng, Self-assembly of 2D-metal–organic framework/graphene oxide membranes as highly efficient adsorbents for the removal of Cs+ from aqueous solutions, RSC Advances 8(71) (2018) 40813-40822. https://doi.org/10.1039/C8RA08410F.
[349] M. Chen, M. Trubyanov, P. Zhang, D. Rodríguez-San-Miguel, F. Zamora, K.S. Novoselov, D.V. Andreeva, Control of gas selectivity and permeability through COF-GO composite membranes for sustainable decarbonization and hydrogen production, Carbon 219 (2024) 118855. https://doi.org/https://doi.org/10.1016/j.carbon.2024.118855.
[350] L. Chen, W. Wang, Q. Fang, K. Zuo, G. Hou, Q. Ai, Q. Li, L. Ci, J. Lou, High performance hierarchically nanostructured graphene oxide/covalent organic framework hybrid membranes for stable organic solvent nanofiltration, Applied Materials Today 20 (2020) 100791. https://doi.org/https://doi.org/10.1016/j.apmt.2020.100791.
[351] F. Yang, M. Wu, Y. Wang, S. Ashtiani, H. Jiang, A GO-Induced Assembly Strategy To Repair MOF Nanosheet-Based Membrane for Efficient H2/CO2 Separation, ACS Applied Materials & Interfaces 11(1) (2019) 990-997. https://doi.org/10.1021/acsami.8b19480.
[352] Y. Mao, J. Xu, H. Chen, G. Liu, Z. Liu, L. Cheng, Y. Guo, G. Liu, W. Jin, Hydrophobic metal-organic framework@graphene oxide membrane with enhanced water transport for desalination, Journal of Membrane Science 669 (2023) 121324. https://doi.org/https://doi.org/10.1016/j.memsci.2022.121324.
[353] Z. Wang, J. Zhu, S. Xu, Y. Zhang, B. Van der Bruggen, Graphene-like MOF nanosheets stabilize graphene oxide membranes enabling selective molecular sieving, Journal of Membrane Science 633 (2021) 119397. https://doi.org/https://doi.org/10.1016/j.memsci.2021.119397.
[354] F. Moghadam, C. Zhang, Z. Li, J. Li, M. Zhai, K. Li, Structurally Stable Hollow-Fiber-Based Porous Graphene Oxide Membranes with Improved Rejection Performance by Selective Patching of Framework Defects with Metal–Organic Framework Crystals, ACS Applied Materials & Interfaces 17(1) (2025) 1803-1812. https://doi.org/10.1021/acsami.4c13400.
[355] Y. Liu, J. Guan, Y. Su, R. Zhang, J. Cao, M. He, J. Yuan, F. Wang, X. You, Z. Jiang, Graphene oxide membranes with an ultra-large interlayer distance through vertically grown covalent organic framework nanosheets, Journal of Materials Chemistry A 7(44) (2019) 25458-25466. https://doi.org/10.1039/C9TA09685J.
[356] G. Kong, J. Pang, Y. Tang, L. Fan, H. Sun, R. Wang, S. Feng, Y. Feng, W. Fan, W. Kang, H. Guo, Z. Kang, D. Sun, Efficient dye nanofiltration of a graphene oxide membrane via combination with a covalent organic framework by hot pressing, Journal of Materials Chemistry A 7(42) (2019) 24301-24310. https://doi.org/10.1039/C9TA07684K.
[357] B. Anasori, M.R. Lukatskaya, Y. Gogotsi, 2D metal carbides and nitrides (MXenes) for energy storage, Nature Reviews Materials 2(2) (2017). https://doi.org/10.1038/natrevmats.2016.98.

[358] A. VahidMohammadi, J. Rosen, Y. Gogotsi, The world of two-dimensional carbides and nitrides (MXenes), Science 372(6547) (2021) eabf1581. https://doi.org/doi:10.1126/science.abf1581.
[359] Q.Q. Lin, Y.C. Liu, Z.M. Yang, Z.Z. He, H.S. Wang, L.Y. Zhang, M. Ang, G.Y. Zeng, Construction and application of two-dimensional MXene-based membranes for water treatment: A mini-review, Results in Engineering 15 (2022). https://doi.org/10.1016/j.rineng.2022.100494.
[360] Y. Zheng, H. Zhang, S. Yu, H. Zhou, W. Chen, J. Yang, Covalently bridged MXene/COF hybrid membrane toward efficient dye separation, Separation and Purification Technology 349 (2024) 127908. https://doi.org/https://doi.org/10.1016/j.seppur.2024.127908.
[361] G. Zeng, Y. Liu, Q. Lin, S. Pu, S. Zheng, M.B.M.Y. Ang, Y.-H. Chiao, Constructing composite membranes from functionalized metal organic frameworks integrated MXene intended for ultrafast oil/water emulsion separation, Separation and Purification Technology 293 (2022) 121052. https://doi.org/https://doi.org/10.1016/j.seppur.2022.121052.
[362] S. Peng, H. Ma, X. Hao, R. Han, X. Ji, L. Wang, Y. Fang, K. Pang, K. Il-Ho, X. Chen, Constructing green superhydrophilic and superoleophobic COFs-MOFs hybrid-based membrane for efficiently emulsion separation and synchronous removal of microplastics, dyes, and pesticides, Environmental Research 243 (2024) 117777. https://doi.org/https://doi.org/10.1016/j.envres.2023.117777.
[363] R. Banerjee, A. Phan, B. Wang, C. Knobler, H. Furukawa, M. O'Keeffe, O.M. Yaghi, High-throughput synthesis of zeolitic imidazolate frameworks and application to CO2 capture, Science 319(5865) (2008) 939-943.
[364] F.M. Zhang, J.L. Sheng, Z.D. Yang, X.J. Sun, H.L. Tang, M. Lu, H. Dong, F.C. Shen, J. Liu, Y.Q. Lan, Rational design of MOF/COF hybrid materials for photocatalytic H2 evolution in the presence of sacrificial electron donors, Angewandte Chemie International Edition 57(37) (2018) 12106-12110.
[365] K. Endo, S. Canossa, F. Heck, D.M. Proserpio, M.S. Istek, F. Stemmler, J. Van Slageren, S. Hartmann, A. Hartschuh, B.V. Lotsch, Crystalline porous frameworks based on double extension of metal–organic and covalent organic linkages, Nature Synthesis (2025) 1-11.
[366] W. Sun, X. Tang, Q. Yang, Y. Xu, F. Wu, S. Guo, Y. Zhang, M. Wu, Y. Wang, Coordination-induced interlinked covalent-and metal–organic-framework hybrids for enhanced lithium storage, Advanced Materials 31(37) (2019) 1903176.
[367] M.-L. Gao, M.-H. Qi, L. Liu, Z.-B. Han, An exceptionally stable core–shell MOF/COF bifunctional catalyst for a highly efficient cascade deacetalization–Knoevenagel condensation reaction, Chemical Communications 55(45) (2019) 6377-6380.
[368] B. Chen, X. Gao, X. Hou, Y. Fu, Y. Li, F. Fan, T. Wang, F. Meng, Y. Fu, J. Ma, Self-standing COF-MOF composite sandwich membranes with high permeability for dye separation, Desalination 586 (2024) 117841. https://doi.org/https://doi.org/10.1016/j.desal.2024.117841.
[369] S. Das, T. Ben, A [COF-300]-[UiO-66] composite membrane with remarkably high permeability and H 2/CO 2 separation selectivity, Dalton Transactions 47(21) (2018) 7206-7212.
[370] S. Das, T. Ben, S. Qiu, V. Valtchev, Two-dimensional COF–three-dimensional MOF dual-layer membranes with unprecedentedly high H2/CO2 selectivity and ultrahigh gas permeabilities, ACS applied materials & interfaces 12(47) (2020) 52899-52907.
[371] Y. Pu, M. Zhao, X. Liang, S. Wang, H. Wang, Z. Zhu, Y. Ren, Z. Zhang, G. He, D. Zhao, Growing ZIF-8 Seeds on Charged COF Substrates toward Efficient Propylene-Propane Separation Membranes, Angewandte Chemie International Edition 62(22) (2023) e202302355.
[372] X. Ma, N. Sun, Z. Li, M. Tong, Q. Ding, Z. Wang, L. Bai, L. Dong, Y. Liu, Highly Flexible and Self-Standing Covalent Organic Framework–Metal–Organic Framework (COF–MOF) Composite Crystalline Porous Material (CPM) Membrane for Molecular Separation, Advanced Functional Materials 34(19) (2024) 2312203. https://doi.org/https://doi.org/10.1002/adfm.202312203.
[373] H. Xiao, M. Chai, M. Abdollahzadeh, H. Ahmadi, V. Chen, D.B. Gore, M. Asadnia, A. Razmjou, A lithium ion selective membrane synthesized from a double layered Zrbased metalorganic framework (MOF-on-MOF) thin film, Desalination 532 (2022) 115733.
[374] Y. Xu, X. Zhao, R. Chang, H. Qu, J. Xu, J. Ma, Designing heterogeneous MOF-on-MOF membrane with hierarchical pores for effective water treatment, Journal of Membrane Science 658 (2022) 120737. https://doi.org/https://doi.org/10.1016/j.memsci.2022.120737.
[375] Y. Shan, L. Chen, H. Pang, Q. Xu, Metal–Organic Framework-Based Hybrid Frameworks, Small Structures 2(2) (2021) 2000078. https://doi.org/https://doi.org/10.1002/sstr.202000078.
[376] Z. Wang, S. Wannapaiboon, K. Rodewald, M. Tu, B. Rieger, R.A. Fischer, Directing the hetero-growth of lattice-mismatched surface-mounted metal–organic frameworks by functionalizing the interface, Journal of Materials Chemistry A 6(43) (2018) 21295-21303.

[377] T. Feng, X. Shi, T. Ju, J. Long, Q. Liu, M. Liu, Y. Wang, 3D-/2D-covalent organic framework (COF) bilayered membranes for efficient pharmaceutical purification, Journal of Membrane Science 709 (2024) 123144. https://doi.org/https://doi.org/10.1016/j.memsci.2024.123144.
[378] H.G. Alemayehu, C. Liu, J. Hou, J. Yang, M. Fang, Z. Tang, L. Li, Highly stable membrane comprising MOF nanosheets and graphene oxide for ultra-permeable nanofiltration, Journal of Membrane Science 652 (2022) 120479. https://doi.org/https://doi.org/10.1016/j.memsci.2022.120479.
[379] F. Jia, L. Yang, L. Sun, D. Yu, Y. Song, Y. Wang, M.J. Kipper, J. Tang, L. Huang, Efficient separation of dyes using two-dimensional heterogeneous composite membranes, Water Research 247 (2023) 120693. https://doi.org/https://doi.org/10.1016/j.watres.2023.120693.
[380] T. Liu, Z. Li, X. Zhang, H. Tan, Z. Chen, J. Wu, J. Chen, H. Qiu, Metal–Organic Framework-Intercalated Graphene Oxide Membranes for Selective Separation of Uranium, Analytical Chemistry 93(48) (2021) 16175-16183. https://doi.org/10.1021/acs.analchem.1c03982.
[381] Y. Li, X. Zhang, A. Yang, C. Jiang, G. Zhang, J. Mao, Q. Meng, Polyphenol etched ZIF-8 modified graphene oxide nanofiltration membrane for efficient removal of salts and organic molecules, Journal of Membrane Science 635 (2021) 119521. https://doi.org/https://doi.org/10.1016/j.memsci.2021.119521.
[382] G. Yang, D. Zhang, G. Zhu, T. Zhou, M. Song, L. Qu, K. Xiong, H. Li, A Sm-MOF/GO nanocomposite membrane for efficient organic dye removal from wastewater, RSC Advances 10(14) (2020) 8540-8547. https://doi.org/10.1039/D0RA01110J.
[383] H. Yang, N. Wang, L. Wang, H.-X. Liu, Q.-F. An, S. Ji, Vacuum-assisted assembly of ZIF-8@GO composite membranes on ceramic tube with enhanced organic solvent nanofiltration performance, Journal of Membrane Science 545 (2018) 158-166. https://doi.org/https://doi.org/10.1016/j.memsci.2017.09.074.
[384] K. Guan, D. Zhao, M. Zhang, J. Shen, G. Zhou, G. Liu, W. Jin, 3D nanoporous crystals enabled 2D channels in graphene membrane with enhanced water purification performance, Journal of Membrane Science 542 (2017) 41-51. https://doi.org/https://doi.org/10.1016/j.memsci.2017.07.055.
[385] X. Sui, H. Ding, Z. Yuan, C.F. Leong, K. Goh, W. Li, N. Yang, D.M. D'Alessandro, Y. Chen, The roles of metal-organic frameworks in modulating water permeability of graphene oxide-based carbon membranes, Carbon 148 (2019) 277-289. https://doi.org/https://doi.org/10.1016/j.carbon.2019.03.049.
[386] R. Ghanbari, E. Nazarzadeh Zare, A.C. Paiva-Santos, N. Rabiee, Ti3C2Tx MXene@MOF decorated polyvinylidene fluoride membrane for the remediation of heavy metals ions and desalination, Chemosphere 311 (2023) 137191. https://doi.org/https://doi.org/10.1016/j.chemosphere.2022.137191.
[387] X. Chen, Y. Zhan, W. Yang, A. Sun, H. Jia, J. Tang, B. Lin, Rod-like MIL-53(Fe) intercalated MXene nanosheets lamellar composite membrane for the purification of multi-component oily wastewater, Colloids and Surfaces A: Physicochemical and Engineering Aspects 676 (2023) 132091. https://doi.org/https://doi.org/10.1016/j.colsurfa.2023.132091.
[388] X. Zhang, H. Li, J. Wang, D. Peng, J. Liu, Y. Zhang, In-situ grown covalent organic framework nanosheets on graphene for membrane-based dye/salt separation, Journal of Membrane Science 581 (2019) 321-330. https://doi.org/https://doi.org/10.1016/j.memsci.2019.03.070.
[389] N.A. Khan, J. Yuan, H. Wu, L. Cao, R. Zhang, Y. Liu, L. Li, A.U. Rahman, R. Kasher, Z. Jiang, Mixed Nanosheet Membranes Assembled from Chemically Grafted Graphene Oxide and Covalent Organic Frameworks for Ultra-high Water Flux, ACS Applied Materials & Interfaces 11(32) (2019) 28978-28986. https://doi.org/10.1021/acsami.9b09945.
[390] H. Wang, M. Wang, Y. Wang, J. Wang, X. Men, Z. Zhang, V. Singh, Synergistic effects of COF and GO on high flux oil/water separation performance of superhydrophobic composites, Separation and Purification Technology 276 (2021) 119268. https://doi.org/https://doi.org/10.1016/j.seppur.2021.119268.
[391] Z.-H. Wu, M. Wang, Y.-X. Ren, S. Li, X.-Y. Liu, Y. Cao, X.-Q. Wu, G. Hai, Z. Jiang, D.-S. Li, MXene-intercalated covalent organic framework membranes for high-flux nanofiltration, Journal of Membrane Science 701 (2024) 122755. https://doi.org/https://doi.org/10.1016/j.memsci.2024.122755.
[392] J. Wang, X. Xu, Y. Zhou, W. Ma, F. Wang, Y. Zhou, X. Men, A robust COF@MXene membrane for ultra-high flux of water-in-oil emulsion separation, Chemical Communications 59(57) (2023) 8858-8861. https://doi.org/10.1039/D3CC01951A.
[393] Y. Qu, Y. Liu, X. Du, H. Jia, S. Xu, M. Zhang, B. Liu, Photocatalytic and fouling resistant MXene/3D-S-COF for efficient oil-water emulsion separation, Separation and Purification Technology 352 (2025) 128242. https://doi.org/https://doi.org/10.1016/j.seppur.2024.128242.
[394] Y. Li, J. Ma, H. Lin, C. Chen, S. Raza, Q. Zeng, X. Lu, L. Shen, Unique dual superlyophobic covalent organic frameworks (COF-TpBD) intercalated MXene composite membrane for efficient oil-water separation, Journal of Membrane Science 717 (2025) 123579. https://doi.org/https://doi.org/10.1016/j.memsci.2024.123579.

[395] Y. Hou, Z. Su, Y. Wu, J. Ma, Hierarchically engineered flexible COF/CNT-MOF composite membrane with interpenetrated pores for water purification, Separation and Purification Technology 358 (2025) 130310. https://doi.org/https://doi.org/10.1016/j.seppur.2024.130310.

# Chapter 3: Experimental

## 3.1 Materials

The following chemicals were used without further purification: alumina oxide powder (Inframat Advanced Materials, 99.99%, α-phase, 0.5~1μm), hydrogen peroxide ($H_2O_2$, Merck, 30%), ammonium hydroxide ($NH_4OH$, 28-30%), ethanol (VWR, 99.5%), acetone (VWR, 99.5%) anhydrous N, N-dimethylformamide (DMF, VWR, 99%), acetonitrile ($CH_3CN$, VWR, 99.9%), chloroform ($CHCl_3$, VWR, 99.9%), methanol (VWR, 98.5%), sodium chloride (NaCl, VWR, 98%). Sodium hydroxide (NaOH, VWR, ≥98%) N-methyl-2-pyrrolidone (NMP, anhydrous 99.5%), and poly(methyl methacrylate) (PMMA), Arlacel P135 (polyethyleneglycol 30-dipolyhydroxystearate) were used.

## 3.2 Preparation of The Alumina-based Substrate

### 3.2.1 Preparation of alumina hollow fibres (HFs)

The fabrication of alumina HFs was carried out using a phase-inversion process consisting of three main steps [1]: solution preparation, spinning, and sintering. The suspension was prepared by dispersing $Al_2O_3$ powder into NMP containing a dispersant. This mixture was homogenized using a ball mill for 48 hours. The PMMA pellets were subsequently added, and the mixture was further stirred on a roller for an additional 48 hours. The detailed composition of the suspension is provided in Table 3.1.

To remove entrapped air, the prepared suspension was degassed in a sealed reservoir under continuous stirring for 4 hours. It was then transferred into a 200 mL stainless-steel syringe (1/4-inch SWAGELOK, Harvard) for extrusion. Moreover, the bore liquid, consisting of a 50/50 (v/v) ethanol-water mixture, was loaded into two separate syringes. These syringes were connected to programmable syringe pumps (PHD 2000, Harvard) to ensure a consistent injection rate for both fluids. The ceramic suspension and bore liquids were simultaneously extruded through a custom-designed tube-in-orifice spinneret (OD/ID: 3 mm/1.2 mm) at injection rates of 7 mL $min^{-1}$ and 13 mL $min^{-1}$, respectively. A coagulation bath filled with DI water was positioned directly below the spinneret, maintaining a 4 cm air gap between them.

Table 3.1 Composition of the ceramic suspension

| Compositions | |
|---|---|
| Alumina powder (g) | 140 |
| NMP (g) | 100 |

| | |
|---|---|
| Arlacel P135 (g) | 1.5 |
| PMMA | 20 |

After drying and straiting overnight, the HFs were calcined in a programmable chamber furnace. The sintering program is plotted below in Figure 3.1.

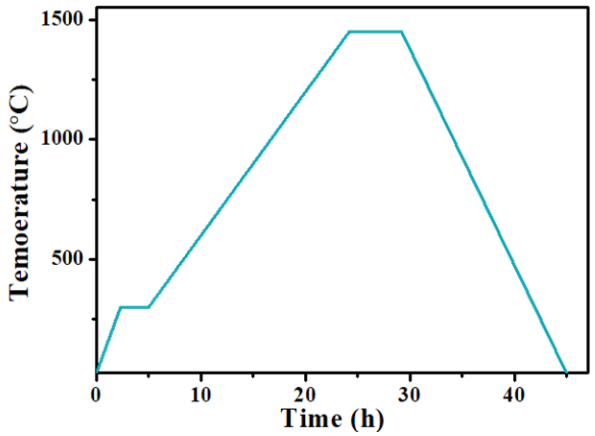



Figure 3.1 Sintering program for alumina HF

### 3.2.2 Preparation of alumina disc

Alumina discs were prepared for characterization, ensuring that the flat surface was suitable for analysis. These discs were fabricated via the same suspension and sintering program as those employed for HF fabrication. However, they were distinguished by being cast in a custom-designed mould that provided a 2.6 cm × 0.5 cm (diameter × height) cavity for shaping the casting solution.

## 3.3 Framework-based Membranes Preparation

### 3.3.1 Synthesis of MOF-303 and continuous MOF-303 membranes (Chapter 4)

#### 3.3.1.1 Synthesis of MOF-303 powder

MOF-303 powder was collected after membrane fabrication through the precipitation of one-step growth and secondary growth via the reactive seeding (RS) and dual seeding (DS) methods via centrifugation. The collected powder was then washed with methanol three times and dried at 100 °C for further characterization.

#### 3.3.1.2 Synthesis of the MOF-303 membrane via a liquid contact in-situ growth method

Briefly, 145 mg of $H_3PDC$ and 67 mg of NaOH were dissolved in 27 mL of deionized water and sonicated for 15 min. The metal solution was prepared by mixing 100 mg of $AlCl_3 \cdot 6H_2O$ in 3 mL of

deionized water in a separate container. The ligand and the metal solutions were simultaneously added to an autoclave with HFs, which were sealed and placed vertically inside. Gentle stirring was used to obtain a homogenous solution. The synthesis proceeded at 100 °C for 48 hours.

#### 3.3.1.3 Synthesis of the MOF-303 membrane by a secondary growth method with a vacuum coating process for seeding

MOF-303 seeds prepared via the solvothermal method were dispersed in DI water via sonication at a concentration of 1 mg $mL^{-1}$. The dispersed MOF-303 suspension was coated on the outer surface of HFs using a vacuum filtration system. Two types of seeding layers with different thicknesses were formed by coating times of 10 s and 60 s, respectively. To improve the attachment between the coated seeding layer and the HF substrate, the mixture was kept under vacuum for 1 minute in air after the HFs were removed from the coating suspension and then dried in a vacuum oven at 40 °C for 4 hours. The secondary growth step of the vacuum-coated MOF-303 seeds was the same as that of the RS and DS processes.

#### 3.3.1.4 Synthesis of the MOF-303 membrane via a one-step hydrothermal method

145 mg of $H_3PDC$, 200 mg of $AlCl_3 \cdot 6H_2O$, and 67 mg of NaOH were added to a Schott glass bottle with 30 mL of deionized water. The glass bottle was ultrasonicated for 15 min before being transferred to a Teflon-lined stainless-steel autoclave. Before the addition of solution, one HF was sealed at both ends with PTFE tape and positioned vertically in a custom PTFE holder, exposing an effective area of 2.1 $cm^2$. The synthesis process was carried out in an oven at 100 °C for 48 h. After cooling to room temperature, the prepared samples were removed, washed with methanol three times and activated in a vacuum oven at 100 °C overnight.

#### 3.3.1.5 Synthesis of the MOF-303 membrane via the reactive seeding method

In the seeding step, 145 mg of $H_3PDC$ and 67 mg of NaOH were dissolved in 30 mL of deionized water under ultrasonication for 15 minutes. The solution was transferred to an autoclave in which 1 piece of PTFE-sealed α-alumina HF was placed vertically using a custom PTFE holder. After the solution was added, the autoclave was promptly placed in a 100 °C oven for 2 hours. The seeded alumina HF was washed with methanol three times and dried at 100 °C under vacuum to remove unreacted precursors. The secondary growth procedure of the seeded support was performed similarly to the one-step growth method.

#### 3.3.1.6 Synthesis of the MOF-303 membrane via the dual seeding method

This method was similar to that of RS except that 100 mg of $AlCl_3 \cdot 6H_2O$ was added to the synthesis

solution for the seeding process, and the solution for the secondary growth step was the same as that for the one-step hydrothermal process.

#### 3.3.1.7 Large-scale synthesis of MOF-303 membrane via DS method

The DS method was adapted for the large-scale synthesis of MOF-303 membranes with four 4 cm HF membranes in a single autoclave, and two 8 cm HF membranes in a larger autoclave with 2.5 times the volume.

### 3.3.2 Synthesis of PES/DABA-TFP loose nanofiltration membrane (Chapter 5)

#### 3.3.2.1 Synthesis of DABA-TFP in a single solution-phase

DABA-TFP was synthesized following a single solution-phase methodology. Briefly, DABA and TFP were each dissolved in DMSO with a concentration of 2 wt% per monomer solution. The TFP/DMSO solution was subsequently added dropwise to the amino acid mixture at a stoichiometric ratio under gentle stirring. A DABA-TFP colloid was formed after keeping the mixed solution stationary at room temperature for 24 hours to complete the polymerization process. DABA-TFP nanosheets were then obtained by dialyzing the diluted colloid in deionized water (DI water) for 3 days, followed by freeze drying.

#### 3.3.2.2 Preparation of pure PES solution

A pure PES solution was prepared by dissolving 20 wt% dried PES pellets in DMSO or DMSO/THF in a rotator roller for 36 hours. The obtained solution was kept stationary at ambient temperature overnight to remove air bubbles before casting.

#### 3.3.2.3 Preparation of PES in-situ dissolving DABA-TFP solution (PES in-situ COF solution)

PES pellets at 20 wt% were dissolved in-situ in the as-synthesized DABA-TFP single-phase solution with/without further addition of 4 wt% THF and degassed at room temperature overnight (Figures 5.1 and 5.3).

#### 3.3.2.4 Physical blending of PES with the DABA-TFP solution (PES blend COF solution)

The freeze-dried DABA-TFP nanosheets (as mentioned in Section 3.3.2.1) were redispersed in DMSO or DMSO/THF under sonication for 5 minutes. After that, PES pellets with a concentration of 20 wt% were dissolved in the aforementioned DABA-TFP/DMSO colloid and degassed (Figure 5.1).

#### 3.3.2.5 Membrane fabrication via the NIPS method

The solution was cast onto a 6 mm glass plate using a 0.5 mm automatic blade at a speed of 2000 mm $min^{-1}$. The nascent film was subsequently immersed in a water bath at ambient temperature to initiate phase inversion (Figure 5.2 a).

#### 3.3.2.6 Membrane fabrication via the NIPS-CCD method

Casting was performed under identical conditions to those of the NIPS method but on a 1 mm aluminium plate. The film was immediately immersed in a -7 °C ethanol/water coagulation bath (70/30, v/v %). In this immersion step, NIPS-type phase inversion initiates at the S/NS interface (the top surface of the membrane), and CCD-type freezing initiates at the solution/casting plate interface (the bottom surface of the membrane). This simultaneous action resulted in the formation of a membrane characterized by both NIPS and CCD features in a single step. After spending 1 min in an ethanol/water bath, the membrane was transferred to a 0 °C ice water bath, where it remained overnight for solvent exchange (Figure 5.2 b).

#### 3.3.2.7 Membrane fabrication via the NIPS-CCD Eva method

Following the same initial steps as those of the NIPS-CCD method, a solvent evaporation step was introduced. This involved placing the nascent film in an 80 °C oven for 5 minutes before immersing in the ethanol/water mixture and subsequently in a 0°C ice water bath for solvent exchange.

#### 3.3.2.8 Membrane fabrication via the NIPS-CCD Eva THF method

In addition to the steps described for NIPS-CCD Eva, this method included blending 4 wt% (relative to the total solvent weight) of THF as co-solvent with DMSO to increase evaporation. The membranes were then processed using the same coagulation and solvent exchange steps as those in the NIPS-CCD Eva method.

For all methods, the water used for solvent exchange was changed three times over the subsequent 60 hours.

### 3.3.3 Confined growth of 2D MOF nanosheets within porous graphene oxide membranes for long-term stable desalination (Chapter 6)

Two types of PGO nanosheets are prepared: big-flake PGO (bPGO) and small-flake PGO (sPGO)

#### 3.3.3.1 Preparation of bPGO nanosheets

bPGO nanosheets were synthesized as described in our previous work [2-4]. Briefly, 80 mg of graphene oxide (GO), derived from graphite via a modified Hummer's method, was dispersed in 20 mL of deionized water under sonication. The resulting dispersion was gently stirred at 50 °C for 5 hours

following the addition of $NH_4OH$ (2 mL) and $H_2O_2$ (2 mL). The bPGO nanosheets were then collected by centrifugation at 12,000 rpm for 1 hour at 10 °C. To ensure the removal of residual reagents, the collected bPGO was redispersed in deionized water and dialyzed for three days.

#### 3.3.3.2 Preparation of sPGO nanosheets

sPGO nanosheets were synthesized via ultrasonication (Fisher Scientific FB505, 500 W, 20 kHz) under controlled conditions. The PGO dispersion was placed in double-wall glassware, with temperature regulation maintained via a recirculating water chiller. The flake size was precisely tuned by optimizing the sonication parameters, including duration, pulse mode, and amplitude, which were set at 2 hours, 03/01 (ON/OFF), and 30%, respectively.

#### 3.3.3.3 PGO HF membrane fabrication

The PGO membranes were fabricated using a vacuum-assisted self-assembly. The alumina substrate, with one end sealed by Araldite adhesive and the other connected to a vacuum pump, was immersed in a PGO dispersion (0.0125 mg $mL^{-1}$). The membrane thickness was controlled by varying the coating time of 40, 80, and 120 seconds, yielding PGO40s, PGO80, and PGO120, respectively. After coating, the membranes were dried in a vacuum oven at 40 °C for 3 hours.

#### 3.3.3.4 CuBDC@PGO membrane fabrication

The CuBDC@PGO membrane was synthesized via in-situ growth of CuBDC nanosheets within the laminar structure of the PGO membrane via a contra-diffusion method. The ligand and metal solutions for CuBDC synthesis were prepared separately. The ligand solution was obtained by dissolving 0.36 g of $H_2BDC$ in a mixture of 36 mL of DMF and 12 mL of acetonitrile under constant stirring. Similarly, the metal solution was prepared by dissolving 0.36 g of $Cu(NO_3)_2 \cdot 3H_2O$ in a mixture of 12 mL of DMF and 36 mL of acetonitrile. For the CuDBC patch, the PGO membrane was immersed in the ligand solution (15 mL for the 4 cm HF and 25 mL for the 13 cm HF), while the metal solution was injected into the lumen of the HF. The system was left undisturbed for 24 hours to facilitate CuBDC crystallization. Afterward, the resulting membrane was thoroughly washed in methanol (three cycles of 30 minutes each) and dried at 40 °C overnight.

## 3.4 Characterizations and Performance tests

### 3.4.1 Microstructure characterization

The morphology of membrane was examined by scanning electron microscopy (LEO Gemini 1525 FEGSEM) at an accelerating voltage of 5 kV. To achieve a better image, a conductive layer was sputter-

coated before SEM characterization (40 nm Cr for membrane s in chapter 4, 15 nm gold for membrane tested in chapter 5 and 6).

The flake size of nanosheets and surface roughness of the membranes were measured using atomic force microscopy (AFM, MFP-3D, Oxford Instrument).

The flake size distribution was also evaluated via dynamic light scattering (Litesizer DLS, Anton Paar).

The surface area, pore size, and pore volume of MOFs were determined by $N_2$ sorption isotherms measured at 77 K using a physisorption analyser (Micromeritics, 3 FLEX).

### 3.4.2 Chemistry characterization

The elemental distributions of carbon, nitrogen, sulfur, copper, and aluminum were detected via energy-dispersive X-ray spectroscopy coupled with SEM (SEM-EDX, LEO 1525, Zeiss).

The crystalline structure of the MOF/COF powder and the crystal orientation of the membranes were characterized via XRD (X'Pert PRO, Cu Kα, Panalytical) at 2θ values between 5° and 50° at 40 kV and 40 mA.

X-ray photoelectron spectroscopy (XPS, K-Alpha$^+$, Thermo Scientific) was used to measure the surface chemistry of the membranes.

The wettability of the membrane surface was assessed by recording the liquid contact behaviour via the Ramé-hart Model 590 Advanced Automated Goniometer. For each trial, 5 µl of liquid was dispensed onto the flat membrane surface.

The zeta potential was measured by an electrokinetic analyser (SurPasstm 3, AntonPaar) equipped with a clamping cell (10 mm×20 mm). KOH (1 mM) was used as the electrolyte solution, and the measurement was conducted in the pH range of 3~9.5.

The functional groups of membranes were detected via Fourier transform infrared (FTIR) spectroscopy (Spectra 100, PerkinElmer) over 400~3600 nm at a resolution of 4 $cm^{-1}$.

The Raman characterization was conducted with a SENTERRA II instrument (Bruke).

### 3.4.3 Thermal property characterization

Thermal gravimetry analysis (TGA, TGA-8000, PerkinElmer) was conducted to evaluate the thermal stability of the membrane in the temperature range between 50~1000 °C at a heating rate of 10 °C $min^{-1}$ in an $N_2$ atmosphere.

The thermal conductivity ($K$, W $m^{-1}$ $K^{-1}$) of the membranes was evaluated via the following equation (3-1):

$$K = D \times \rho \times C_p \qquad \text{Equation (3-1)}$$

Where $D$ refers to the thermal diffusivity measured using a laser flash apparatus (LFA, NETZSCH) over a temperature range from room temperature to 60 °C. The heating rate was 1°C per minute, and three measurements were recorded every 10 minutes. $\rho$ is the density of the samples, which is determined based on their dimensions and weight. The specific heat capacity $C_p$ was measured using a Pyris-1 differential scanning calorimeter (DSC, PerkinElmer) according to the method described in the ASTM E1269−11 standard.

### 3.4.4 Vapour sorption measurement (Chapter 4)

The water vapour and ethanol sorption properties of the MOF powder were measured via a DVS advantage system. A small amount of the dried powder (8~10 mg) was loaded into the sample pan and placed into a sample chamber. To conduct the analysis, vapours were introduced at P/Psat=90% at 60 °C using compressed air (200 mL $min^{-1}$) as a carrier gas. Sorption equilibrium was assumed to be reached at each stage when the rate of mass change (dm $dt^{-1}$) was less than 0.002%/min for 5 min.

### 3.4.5 Nanofiltration test by using dead-end system (Chapter 4)

The pure water permeance and dye rejection performance were investigated using a homemade dead-end test filtration device. The MOF-303 HF membrane was mounted into a stainless-steel cylinder filled with 80% deionized water. Under a constant pressure of 5 bar, pure water permeated from the membrane was collected and weighed. The pure water permeance ($J$, LMH $bar^{-1}$) was calculated with the following equation:

$$J = \frac{V}{A \times t \times P} \qquad \textit{Equation (3-2)}$$

where $V$ is the permeate volume, $t$ is the test time, $P$ is the test pressure, and $A$ refers to the effective test area of the membrane.

Three neutral dye dispersions, including azobenzene, MR and PPh-IX, at a concentration of 20 ppm in deionized water were utilized as feed to evaluate the nanofiltration performance of the membranes. To avoid the effect of dye adsorption by the membranes on the rejection performance, all the samples were immersed in the feed solution for 24 hours before the rejection test. After reaching static equilibrium, the dye rejection test was conducted with the same dead-end test system. Permeants from the membrane were collected after 1 hour of testing to avoid the influence of extra adsorption of the membrane under pressure. The dye concentrations in the feed ($C_p$) and permeate ($C_f$) were tested via an ultraviolet–visible (UV–Vis) spectrophotometer (Metller Toledo, UV5), and the rejection ($R$) of dyes was calculated using the following formula:

$$R = \left(1 - \frac{C_p}{C_f}\right) \times 100\% \qquad \textit{Equation (3-3)}$$

To determine the concentration of dyes in the permeate, a calibration curve was prepared for each individual dye. A series of dye dispersions with known concentrations (16 ppm, 12 ppm, 8 ppm, 4 ppm, 1 ppm and 0.5 ppm) were created, and the peak intensities were measured at the corresponding wavelengths. The calibration curves correlating the dye concentration with the peak intensity were subsequently used to calculate the dye concentration in the permeate.

### 3.4.6 Dehydration test by pervaporation

The ethanol and 1-butanol dehydration performances were evaluated via a custom-built pervaporation apparatus. Before the HF membranes were immersed in the feed mixture, one end of the membrane was connected to the vacuum pump, while the other end was sealed with epoxy. The feed mixture was heated and maintained at 70 °C during the measurement. On the downstream side, a trap cooled with liquid nitrogen was used to collect the permeated vapour. The collected permeate was analysed via gas chromatography (GC). The separation factor ($\beta$) of component $i$ was calculated using the following equation:

$$\beta_{i/j} = \frac{y_i(1-x_i)}{x_i(1-y_i)} \qquad \textit{Equation (3-4)}$$

where $x_i$ and $y_i$ refer to the weight fractions of component i in the feed and permeate solutions, respectively.

The flux $J$ is calculated using equation (3-5):

$$J = \frac{\Delta w}{\Delta t \times A} \qquad \textit{Equation (3-5)}$$

Where $\Delta w$ is the weight gain in the permeate, $\Delta t$ is the time interval and $A$ is the effective membrane area.

The pervaporation separation index (PSI) was quoted to evaluate the comprehensive properties of the membrane, which is calculated by equation (3-6):

$$PSI = J \times (\beta - 1) \qquad \textit{Equation (3-6)}$$

### 3.4.7 Surface free energy (Chapter 5)

The surface energy of membrane was calculated by using the van Oss–Chaudhury–Good (vOCG) theory, which extends the classical Young's equation to account for acid-base interactions in addition to Lifshitz–van der Waals (dispersive) forces (equation 3-7) [5].

$$\gamma_L(1 + cos\theta) = 2\left(\sqrt{\gamma_S^{LW} + \gamma_L^{LW}} + \sqrt{\gamma_S^{+}\gamma_L^{-}} + \sqrt{\gamma_S^{-}\gamma_L^{+}}\right) \qquad \textit{Equation (3-7)}$$

Where $\gamma_L$refers to the surface free energy (or surface tension), $S$ and $L$ are the solid/air and liquid/ air boundary, respectively, and the superscript $LW$, $+$ and $-$ indicate, respectively to the apolar Lifshita-van der Waals (non-polar), electron acceptor and, and electron donor contribute to surface energy. Three components of surface energy ($\gamma_S^{LW}, \gamma_S^{+}$ and $\gamma_S^{-}$) of the membrane ($\gamma_S$) can be calculated by the

measured contact angle value (CA), θ of three liquid probes (water, glycerol and diidomethane) with known surface tension components. The short-range polar contributions to the surface energy, $\gamma_S^{AB}$, is calculated from the $\gamma_S^+$ and $\gamma_S^-$ components by following equation (3-8):

$$\gamma_S^{AB} = 2(\gamma_S^+ \gamma_S^-)^{\frac{1}{2}} \qquad \textit{Equation (3-8)}$$

Then, the total surface energy can be calculated by following equation (3-9):

$$\gamma_S = \gamma_S^{LW} + \gamma_S^{AB} \qquad \textit{Equation (3-9)}$$

The components of liquid probes have been provided as Table 3.2

Table 3.2 Surface energy components of liquid probes

| Liquid Probe | $\gamma_L$(mJ m$^{-2}$) | $\gamma_L^{LW}$(mJ m$^{-2}$) | $\gamma_L^-$(mJ m$^{-2}$) | $\gamma_S^+$(mJ m$^{-2}$) |
|---|---|---|---|---|
| Water | 72.8 | 21.8 | 25.5 | 25.5 |
| Glycerol | 64.0 | 34.0 | 3.92 | 3.92 |
| Diiodomethane | 50.8 | 49.5 | 0.0 | 0.0 |

The measured contact angle of different samples and the calculated surface energy components of each membrane are tabulated in Table 5.3 and Table 5.4, respectively.

### 3.4.8 Mechanical property characterization (Chapter 5)

The mechanical strength of the membranes was tested according to the American Society for testing and Materials (ASTM) D882 using a tensile testing machine, Lloyed EZ 50. Protocols applied to test the mechanical strength can be found elsewhere [6].

### 3.4.9 Molecular weight cut-off (MWCO) (Chapter 5)

The molecular weight cut-off (MWCO) was determined by measuring the rejection of polyethylene glycols (PEG) with a series of molecular weights (400, 600, 1000, 2000 and 6000 g mol$^{-1}$) at a concentration of 1 g L$^{-1}$. The resultant rejection was collected and tested with high performance liquid chromatography (HPLC) equipped with evaporative light-scatting detector (ELSD). The PEG rejection can be calculated by following equation (3-3).

Then a log-normal model between PEG rejection and the Stokes radius of PEG ($d_p$) was used to obtain the pore size information of the tested membranes. The Stokes radius of the PEG solute can be calculated based on its average molecular weight [7]:

$$d_p = 33.46 \times 10^{-12} \times MW^{0.557} \qquad Equation(3-10)$$

Then the pore size distribution of the membrane can be predicated by following the following probability density function:

$$\frac{dR(d_p)}{dd_p} = \frac{1}{d_p ln\sigma_p \sqrt{2\pi}} exp\left[-\frac{(lnd_p - ln\mu_p)^2}{2(ln\sigma_p)^2}\right] \qquad Equation(3-11)$$

Where $\mu_p$ is the mean Stokers pore radius, $\sigma_p$ indicates the geometric standard deviation defined as the ratio of the radius at $R = 84.13\%$ over that at $R = 50\%$.

### 3.4.10 Pure water permeance test with a crossflow system (Chapter 5)

The filtration performance of the membranes was evaluated via a crossflow filtration mode with a constant feed pressure of 1 bar. Wet samples with an effective area of 21.24 $cm^2$ were assembled in a custom-made crossflow filtration cell. Pure water permeating through the membrane was weighed and recorded with an RsWeight (WinCT) connected with a mass balance (A&D,). The PWP ($P_{w0}$, L $m^{-2}$ $h^{-1}$ $bar^{-1}$) of the membrane was calculated according to equation (3-12),

$$J_w = \frac{v}{A \cdot \Delta t \cdot p} \qquad Equation\ (3-12)$$

where $Q$ is the volume of permeate (L), $A$ is the effective area of the test membrane ($m^2$), $\Delta t$ refers to the time difference (h), and $p$ is the applied pressure. The PWP test was carried out continuously for 200 min until a stable value was obtained.

### 3.4.11 BSA fouling (Chapter 5)

The freshly prepared BSA solution (1 g $L^{-1}$ in water) was used as feed after the pure water permeance test and compacted with DI water at a trans-membrane pressure of 1 bar for 120 min. The concentrations of the permeate and the retained solution in the feed tank were tested by using a UV-vis spectrophotometer (NanodropTM 2000, Thermofisher Scientific, UK). After a continuous test with BSA for every 45 minutes, the membrane was backwashed with DI water for 10 minutes before the next DI water permeance cycle. The test was run for three cycles to monitor the BSA fouling performance in this study. The flux recovery ratio (FRR), irreversible ratio ($R_{ir}$) and reversible ratio ($R_r$) were calculated using the following equations:

$$FRR = \frac{J_{wt}}{J_{wc}} \times 100\% \qquad Equation\ (3\text{-}13)$$

$$R_{ir}\ (\%) = \left(\frac{J_{wc} - J_{wt}}{Jwc}\right) \times 100\% \qquad Equation\ (3\text{-}14)$$

$$R_r\ (\%) = \left(\frac{J_{wt} - J_{bt}}{Jwc}\right) \times 100\% \qquad Equation\ (3\text{-}15)$$

where $J_{wc}$ refers to the PWP of membrane after compaction by DI water for a 120-minute test, $J_{wt}$ is the PWP following three cycles of BSA fouling tests and hydraulic cleaning, $J_{bt}$ is the BSA permeance after the final cycle test.

### 3.4.12 Dye/salt separation (Chapter 5)

To determine the dye/salt separation, three negatively charged dyes, Allura Red AC, Methyl Blue, and Rose Bengal, were utilized in this study (Table 3.3).

Table 3.3 Dyes used in Chapter 5

| Species | MW (g/mol) | Dimension (nm) | Valence | pH |
|---|---|---|---|---|
| Allura Red AC (AR) | 496.4 | 1.6 × 0.9 × 0.3 | -2 | 8.9 |
| Methyl Blue (MB) | 799.8 | 2.4 × 1.3 × 0.5 | -2 | 9.1 |
| Rose Bengal (RB) | 1017.6 | 1.2 × 1.1 × 0.7 | -2 | 8.7 |

Each dye was dissolved in 1 g $L^{-1}$ $MgSO_4$ aqueous mixture to prepare a feed mixture containing 50 ppm dye. The rejection of dye or salt, *R* (%), was calculated via equation (3-3).

### 3.4.13 Desalination performance test via reverse osmosis (Chapter 6)

The RO performance of all the samples was evaluated using a dead-end filtration system. The prepared HF membrane was mounted within a stainless steel cylinder containing a 35 g $L^{-1}$ NaCl aqueous solution. The permeate was collected under an applied transmembrane pressure of 10 bar. The permeance and rejection were calculated based on equations (3-2) and (3-3), respectively.

### 3.4.14 Desalination performance test via pervaporation (Chapter 6)

The PV performance of all the samples was evaluated using a custom-built setup in which a NaCl solution (3.5 wt%) was used as the feed. The flux and rejection were calculated using equations (3-5) and (3-3), respectively.

### 3.4.15 Desalination performance test via water carrier pervaporation (WCPV) (Chapter 6)

WCPV was conducted using a laboratory-made setup with a 3.5 wt% NaCl solution as the feed stream. The WCPV performance was assessed based on the change in weight and conductivity of the permeate tank, and the flux and salt rejection were calculated by following equations (3-5) and (3-3), respectively.

## References

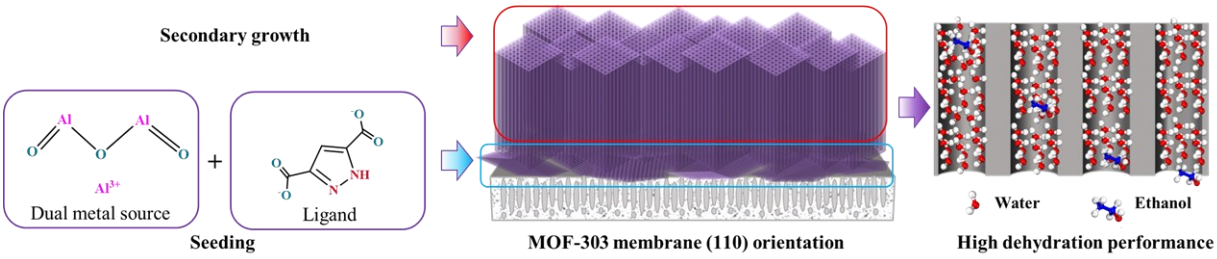
[1] B. Kingsbury, J. Stewart, Z. Wu, R. Douglas, K. Li, Advanced Ceramic Substrate with Ordered and Designed Micro-Structure for Applications in Automotive Catalysis, SAE International, 2014.
[2] T. Wu, F. Moghadam, K. Li, High-performance porous graphene oxide hollow fiber membranes with tailored pore sizes for water purification, Journal of Membrane Science 645 (2022) 120216. https://doi.org/https://doi.org/10.1016/j.memsci.2021.120216.
[3] W.S. Hummers, Jr., R.E. Offeman, Preparation of Graphitic Oxide, Journal of the American Chemical Society 80(6) (1958) 1339-1339. https://doi.org/10.1021/ja01539a017.

[4] C. Petit, T.J. Bandosz, MOF–Graphite Oxide Composites: Combining the Uniqueness of Graphene Layers and Metal–Organic Frameworks, Advanced Materials 21(46) (2009) 4753-4757. https://doi.org/https://doi.org/10.1002/adma.200901581.
[5] C. Van Oss, R. Good, Orientation of the water molecules of hydration of human serum albumin, Journal of protein chemistry 7 (1988) 179-183.
[6] H. Peng, V. Shah, K. Li, Unprecedented water permeation in nanostructured PVDF membranes prepared by unidirectional freezing and surface melting method, Journal of Membrane Science 669 (2023) 121299. https://doi.org/https://doi.org/10.1016/j.memsci.2022.121299.
[7] P. Zhong, X. Fu, T.-S. Chung, M. Weber, C. Maletzko, Development of Thin-Film Composite forward Osmosis Hollow Fiber Membranes Using Direct Sulfonated Polyphenylenesulfone (sPPSU) as Membrane Substrates, Environmental Science & Technology 47(13) (2013) 7430-7436. https://doi.org/10.1021/es4013273.

# Chapter 4: Facile Fabrication of MOF-303 Hollow Fibre Membranes with Controlled Orientation for Nanofiltration

## 4.1 Abstract

Fabrication of continuous MOF membrane with designed orientation are poised to fully exploit its advantages of extensive porosity, periodic network, and versatile chemistry in separation. However, the preparation of defect-free and water-stable MOF membranes with high permselectivity and good structural integrity remains challenging. Herein, we demonstrate a dual-source seeding (DS) approach to produce high-performance, water-stable MOF-303 membranes with hollow fibre (HF) geometry and preferentially tailored crystallographic orientation. By controlling the nucleation site density during secondary growth, MOF-303 membranes with a crystallographic preferred orientation (CPO) on the (011) plane were fabricated. The MOF-303 membrane with CPO on (011) provides straight one-dimensional permeation channels with a superior water flux of 18 kg $m^{-2}$ $h^{-1}$ in pervaporative water/ethanol separation, which is higher than that of most of the reported zeolite membranes and 1~2 orders of magnitude greater than that of previously reported MOF membranes. The straight water permeation channels also offer a promising water permeance of 15 L $m^{-2}$ $h^{-1}$ $bar^{-1}$ and a molecular weight cut-off (MWCO ≈ 269) for dye nanofiltration. These results provide a concept for developing ultrapermeable MOF membranes with good selectivity and structural integrity for pervaporation and nanofiltration.




**Keywords:** MOF-303 membrane, Dual source seeding, Crystallographic Preferred orientation, Pervaporation

## 4.2 Introduction

The chemical stability of MOFs, dictated by their composition and structural framework, is a critical factor for their application in liquid separation [1]. As detailed in Section 2.4, the design of stable MOFs aligns with the principles of hard–soft acid–base (HSAB) theory [2]. According to this framework, MOFs with high chemical stability can be synthesized by coordinating high-valence metal ions (e.g., $Fe^{3+}$, $Al^{3+}$, $Zr^{4+}$) with carboxylate-type ligands or by pairing divalent metal ions (e.g., $Zn^{2+}$, $Cu^{2+}$, $Ni^{2+}$, $Co^{2+}$) with soft azolate linkers (e.g., imidazolate, pyrazolate) [3, 4]. These coordination strategies are expected to enhance the resilience of metal–linker interactions, thereby preventing their decomposition induced by chemical attack. A wide range of water-stable MOFs has been reported, predominantly including ZIFs (-7, -8, -67, -78), UiOs (-66), PCNs (-230, -229, -228, -777, -521), MILs (-100, -101, -808, -160, -163, -121), and NUs (-1105, -1000) [5]. Despite ongoing efforts to develop water-stable MOFs, their integration into continuous membranes has remained a significant challenge due to the limited advancement in continuous MOF membrane fabrication techniques. Zr-based UiO-66 was the first MOF membrane to demonstrate good water stability and separation performance in desalination [6] and dye nanofiltration [7].

A recently reported Al-based MOF, i.e., MOF-303 [Al(OH)(PZDC), PZDC = 1H-pyrazole-3,5-dicarboxylate], in which the strong metal–linker coordination between high-valent $Al^{3+}$ and carboxylate groups confers high structural stability. Additionally, the pyrazole groups in MOF-303 serve as functional sites, providing high water sorption capacity and facilitating rapid water sorption–desorption cycles, making it a promising candidate for water harvesting applications [8-11]. MOF-303 comprises one-dimensional (1D) channels with a 0.6 nm pore size and hydrophilic characteristics due to the PZDC linker, making it a suitable nanoporous material for developing high-performance water purification membranes [12, 13]. Cong et al. [12] fabricated a MOF-303 membrane via in-situ growth of MOF-303 crystals on a flat alumina disc, which showed good divalent ion rejection but very low water permeance (< 0.8 L $m^{-2}$ $h^{-1}$ $bar^{-1}$) because the membrane was prepared with a high thickness and random orientation of MOF crystals. Lai et al. [13] used a seeding growth technique to prepare MOF-303 membranes with very high water/ethanol selectivity, but the water flux ranged from 0.1~0.2 kg $m^{-2}$ $h^{-1}$ because of the partially amorphous structure of the crystals. While these studies demonstrate good water stability, the membranes still suffer from low water permeance owing to their high thickness for patching intercrystalline defects.

A major challenge contributing to low permeance is the random orientation of MOF crystals, which considerably undermines the intrinsic features of MOFs in three-dimensional (3D) structures. Controlling the MOF crystal orientation is an effective way to fabricate MOF membranes with high permeance and good size sieving performance [14]. Additionally, when fabricating MOF-based composite membranes, the formation of interfacial defects between the MOF membrane and the substrate is another issue that is

detrimental to selectivity. This is because, in general, neither the metal component nor the organic linker provides a link to bond to the support surface, making the membranes structurally unstable. The reactive seeding (RS) technique reported by Hu et al. [15, 16] is a facile secondary growth method in which an alumina support can be used as a metal source to interact with a linker to form high-density MOF seeds, which not only mitigates interfacial defects but also considerably minimizes the formation of intercrystalline voids, thus improving MOF membrane selectivity. Therefore, to make high-performance MOF membranes, a fabrication technique that can (i) minimize intercrystalline defects, (ii) improve the interfacial compatibility between the MOF layer and substrate and (iii) control the orientation of MOF permeation channels should be developed.

In this study, we propose a DS method to achieve the above goal in the preparation of high-performance MOF-303 membranes on an alumina HF substrate. The alumina substrate acts as a metal source to react with organic linkers to form seeds, which results in better interfacial interactions between MOF crystals and the HF substrate. The second metal source provided by the synthesis solution allows the density of seeds to be preferentially adjusted. The subsequent secondary growth of crystals with a tailored orientation eliminates intercrystalline defects induced by random nucleation in the seeding step. By tailoring the orientation of the MOF-303 crystals, an unprecedented water flux, i.e., up to two orders of magnitude greater than that of previously reported MOF-based membranes with promising selectivity, was achieved for the membrane with CPO on the (011) for ethanol dehydration and dye nanofiltration applications. The crystal growth mechanism and orientation of the MOF-303 membranes were also thoroughly investigated via X-ray diffraction (XRD) and scanning electron microscopy (SEM) analyses. The proposed study provides a concept for developing ultrahigh water-permeable MOF membranes with good selectivity and structural integrity for pervaporation and nanofiltration.

## 4.3 Material and Methods

### 4.3.1 Material and membrane fabrication

1H-pyrazole-3,5-dicarboxylic acid ($H_3PDC$, ≥98%) and aluminum chloride hexahydrate ($AlCl_3 \cdot 6H_2O$, ≥99%) were purchased from Thermal Scientific and used for the synthesis of MOF303 without further purification. Details of other chemicals can be found in Section 3.1.

### 4.3.2 Preparation of alumina hollow fibre and disc as substrate

The alumina-based substrate was prepared following the methodology outlined in Section 3.2.

### 4.3.3 Synthesis of MOF-303 and MOF-303 membranes

MOF-303 was synthesized using a solvothermal method. The fabrication of MOF-303 membranes was carried out through various approaches, including a liquid-contact in-situ growth, vacuum-coating

seeding growth, a one-step hydrothermal method, a reactive seeding method, and a dual-seeding method. A detailed description of the synthesis processes is provided in Section 3.3.1.

### 4.3.4 Characterizations and performance test

Characterizations conducted in this study include SEM, XRD, BET, contact angle measurements, and TGA, with detailed descriptions provided in Section 3.4. Additionally, vapour sorption capacity, nanofiltration performance, and dehydration performance were evaluated as described in Sections 3.3.4, 3.4.5, and 3.4.6, respectively.

## 4.4 Results and Discussion

### 4.4.1 Fabrication and characterization of MOF-303 HF membranes

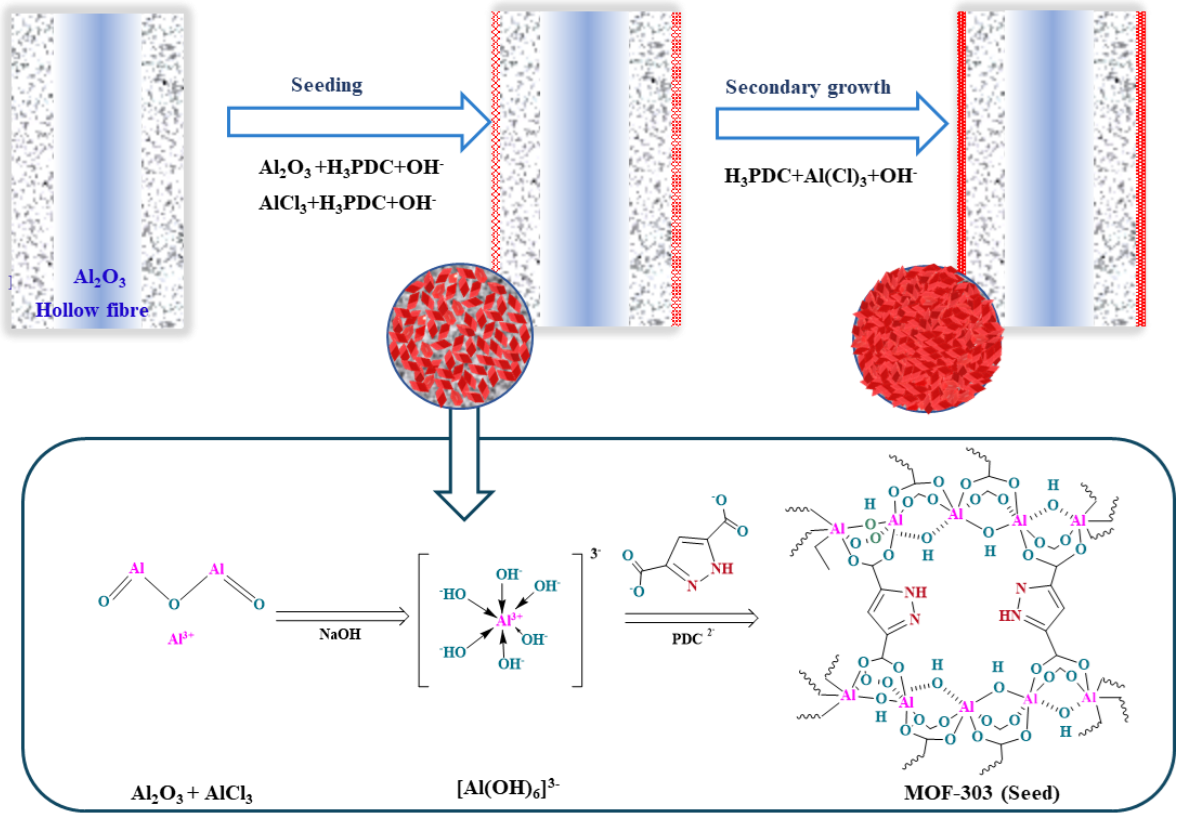



Figure 4.1 Schematic illustration of MOF-303 membranes synthesized by a DS method. The alumina HF is placed vertically in an autoclave filled with a ligand solution containing NaOH and an inadequate stoichiometric amount of aluminium chloride hexahydrate ($AlCl_3 \cdot 6H_2O$). The ligand reacts with the OH groups both on the surface of the alumina HF support and in the synthesis solution to form the seed layer (seeding step), followed by a secondary growth for the final MOF-303 membranes named as DS membrane.

A DS approach illustrated schematically in Figure 4.1 was used to fabricate the MOF-303 HF membrane.

In this method, metal sources from both the alumina HF substrate and the seeding solution, i.e., aluminum chloride hexahydrate ($AlCl_3 \cdot 6H_2O$), contribute to the formation of seeds. The alumina octahedral structure on the surface of the alumina HF substrate was first formed in an aqueous solution containing NaOH at high temperature [17] and then coordinated with ligands (1H-pyrazole-3,5-dicarboxylic acid [$H_3PDC$]) in the reaction solution to generate MOF-303 seeds on the surface of the support [15, 18], illustrated as the red dots in Figure 4.1. In the secondary growth step, the MOF-303 seeds further grew to the final MOF-303 membrane, which was named the DS membrane.

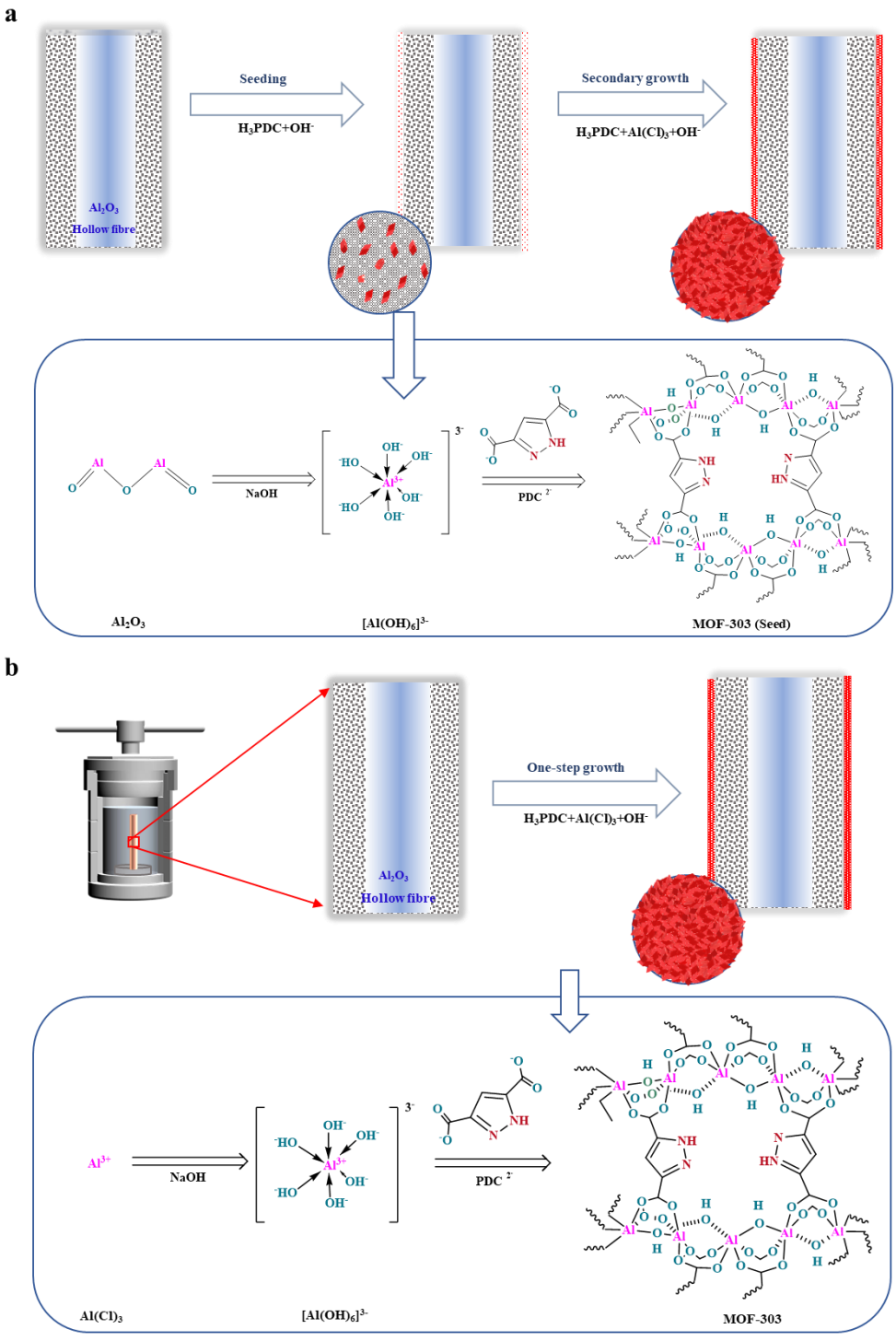


Figure 4.2 Schematic illustration of MOF-303 membranes synthesized by (a) RS and (b) in-situ growth methods.

For comparison, MOF-303 membranes were also produced using conventional RS and one-step hydrothermal methods (Figure 4.2). In RS method, the alumina HF is placed vertically in an autoclave filled with ligand solution containing NaOH. The ligand reacts with the OH group on the surface alumina HF support to form the seed layer (seeding step), followed by a secondary growth for the final MOF-303 membranes named RS membrane. The one-step method used the same set-up as those in RS and DS set-up in the solution containing ligand, metal salt and NaOH in a stochiometric ratio to ensure instantly form crystals.

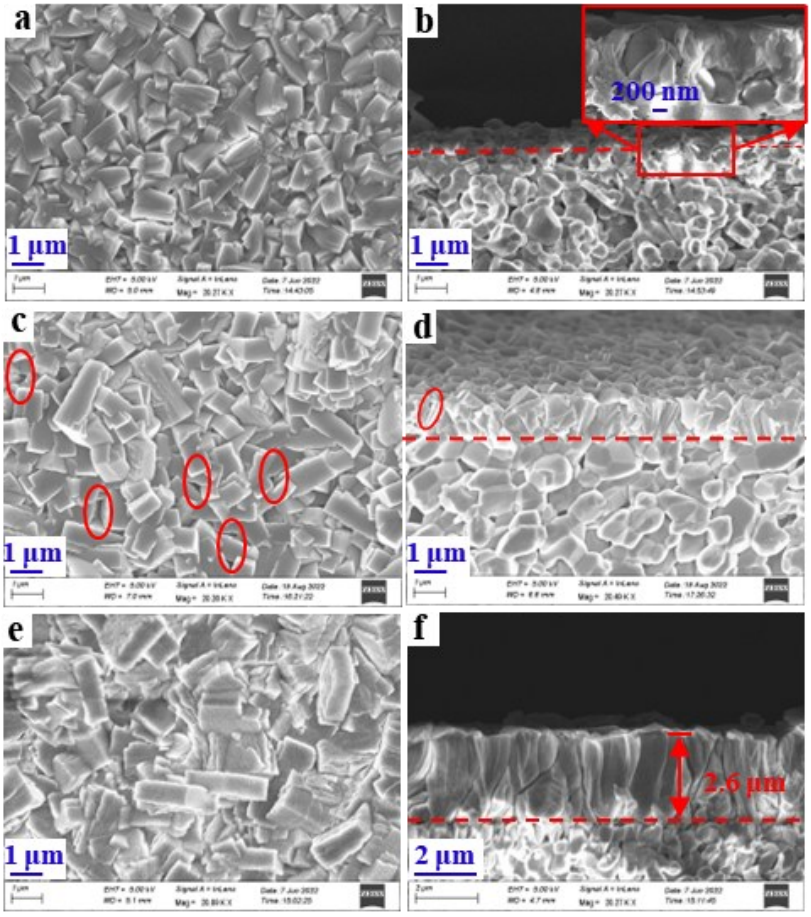
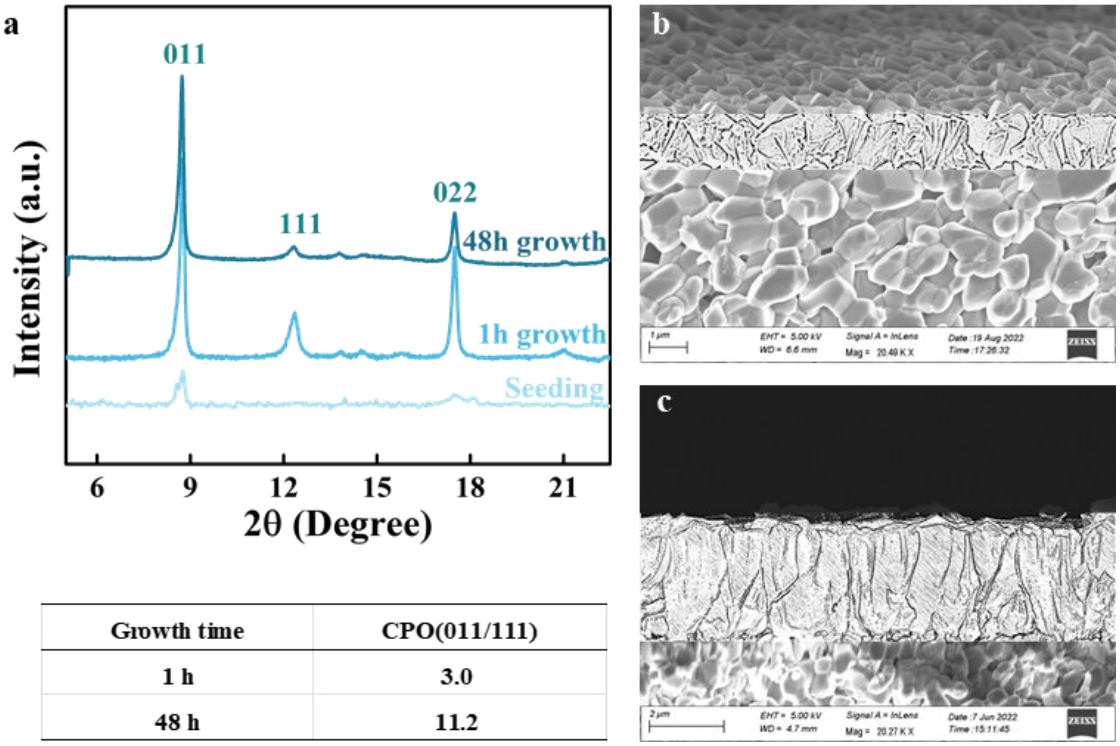



Figure 4.3 SEM images of MOF-303 membranes fabricated by DS method. (a-f) SEM images of the membrane after (a, b), seeding (the inset in b shows an enlarged view of the seeding layer covering the alumina HF substrate). (c, d) 1-hour, and (e, f) 48-hour secondary growth. (a, c, e) are surface images, and (b, d, f) are cross-sectional images of the membrane. The red circles in (c) display the intercrystalline gaps. The red dotted lines in (b, d, and f) divide the cross-sections into the HF substrate and MOF layer parts.

The morphology and crystalline structure of the MOF-303 membranes prepared by a DS approach were investigated using SEM and XRD, as shown in Figures 4.3 and 4.4. After the seeding step, the seeds formed a thin layer almost fully covering the surface of the support, as shown in Figure 4.3 a, b. In the DS method, seeds grow from the grain boundaries of the support, encapsulating the alumina particles and ultimately forming the seeding layer. This distinctive growth pattern is illustrated in Figure 4.3 a, b, and the inset in Figure 4.3 b. The metal sources provided by both the seeding solution and the alumina support account for this growth pattern. The deficiency in the stoichiometric ratio of metal in the solution allows for the participation of the metal source from the alumina support, facilitating the nucleation of the alumina grains. Promoted by the ligand and metal source in the synthesis solution, the nuclei consistently grow from the alumina grains towards the nutrient-rich side (i.e., the outer surface of the HF), leading to the formation of seeds and establishing a strong interaction between the seeding layer and the support. Simultaneously, the reaction between the metal source and ligand in the synthesis solution also contributes to seed formation, thereby increasing the density of the seeding layer.

After 1 h of secondary growth, the seeding layer formed a MOF-303 membrane. However, intercrystalline defects were observed on the surface of the membrane due to insufficient growth time (highlighted with red circles in Figure 4.3 c, d). These intercrystalline defects disappeared after 48 hours of secondary growth when a uniform membrane with a thickness of 2.6 μm formed (Figure 4.3 e, f), signifying successful intergrowth of the crystals. Notably, the crystals produced using the DS approach exhibited a preferred orientation, growing vertically from the substrate, particularly on the upper part of the membrane (Figure 4.3 f). This observation aligns well with the XRD results presented in Figure 4.4 a. The random crystal orientation of the seeding layer was confirmed by the (011), (022), and (1-2-2) peaks, with the (011) peak showing stronger intensity. During the 1-hour secondary growth, the (011) and (022) peaks became increasingly stronger and sharper due to the growth of the crystals. In particular, a peak corresponding to the (111) face appeared, suggesting that random crystal growth still occurred at this stage, resulting in the random orientation of the crystals (Figures 4.3 d and 4.4 a, and b). With the extension of the reaction time to 48 hours, the relative intensity of the (111) peak gradually decreased, and that of $CPO_{011/111}$ increased from 3 to 11, indicating preferable growth along with (011) (Figure 4.4 c).



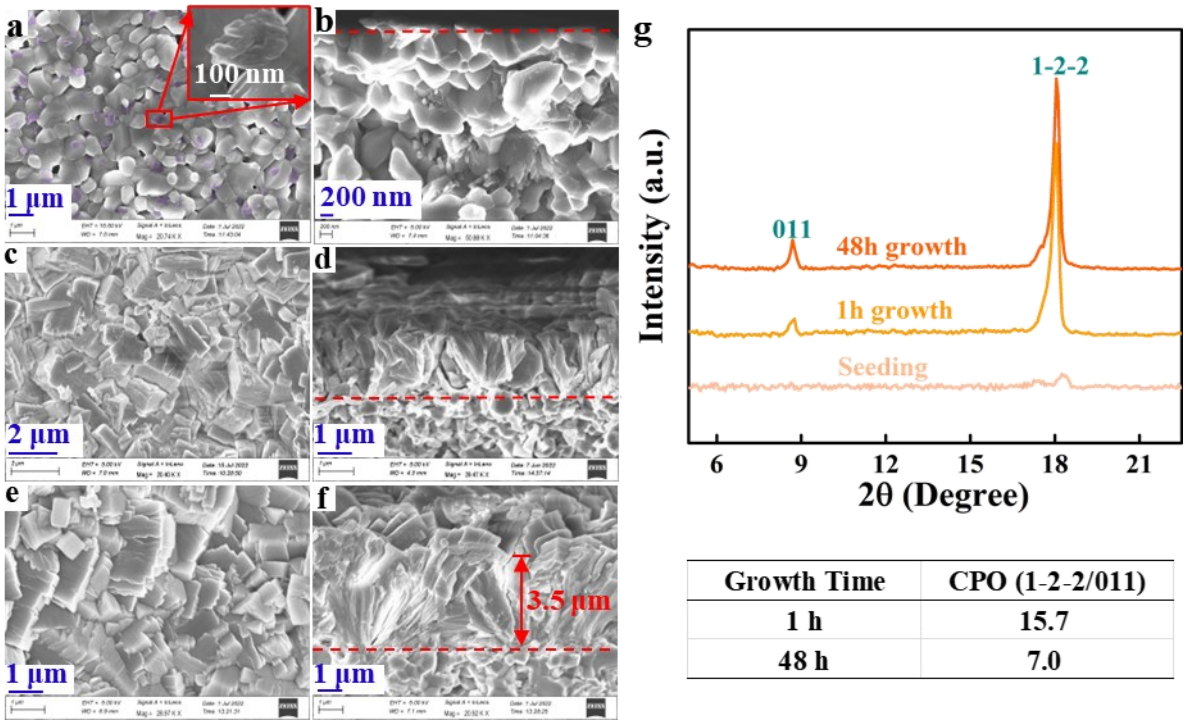

| Growth time | CPO(011/111) |
|---|---|
| 1 h | 3.0 |
| 48 h | 11.2 |

Figure 4.4 XRD patterns and sketchy view of the cross-section of membrane fabricated by DS method. (a) XRD patterns and corresponding CPO ratio of membrane, (b) sketchy view of the cross-section of 1 hour growth, (c) sketchy view of the cross-section of 48-hour growth. Sketchy views were obtained by processing the original SEM image in Photoshop to highlight the outline of the crystals.

The crystal orientation in the DS membranes can be explained based on the evolutionary selection model proposed by van der Drift. According to this model, all the seed crystals are expected to grow randomly at the same face-dependent rate in the initial stage [19]. This stage continues until the seeds meet neighboring crystals. Then, crystals with faster growth in the out-of-plane or nearly out-of-plane direction ultimately overgrow other crystals, dominating the orientation of the top membrane layer. This theory determines the crystal growth orientation if (i) the crystals follow an anisotropic growth pattern, (ii) all the crystals in the seed layer grow simultaneously, and (iii) the seed layer contains competing crystals in close contact. Given the anisotropic structure and high density of MOF-303 crystals in the seeding layer, the evolutionary selection model perfectly explains the out-of-plane orientation (vertical alignment) of the DS membrane. This is supported by the initial random orientation and the preferable orientation on the top part of the membrane (Figures 4.3 and 4.4).

To further demonstrate the DS concept, the conventional RS approach (Figure 4.2 a) was employed to fabricate the MOF-303 membrane for comparison. As shown in Figure 4.5 a, b, MOF-303 particles were seeded at the grain boundaries and grew to fill the gaps between the grains. This phenomenon aligns with

the theory that crystal growth is favoured on rough surfaces compared with smooth surfaces[20]. Since no metal salt was added in the seeding step, it can be assumed that these particles (clusters) were formed due to the reaction between the metal source from the alumina substrate and the $H_3PDC$ ligand. The formation of multiedge clusters in Figure 4.5 a, b can be attributed to either the accumulation of small crystal seeds in the rough corners of the surface or the formation of crystals due to the imperfect stoichiometric ratio. Both cases are shown to induce twinning during the growth step [21, 22]. No continuous membrane was formed after 1 h of secondary growth because the intergrowth of the crystals was not complete (Figure 4.5 c, d).



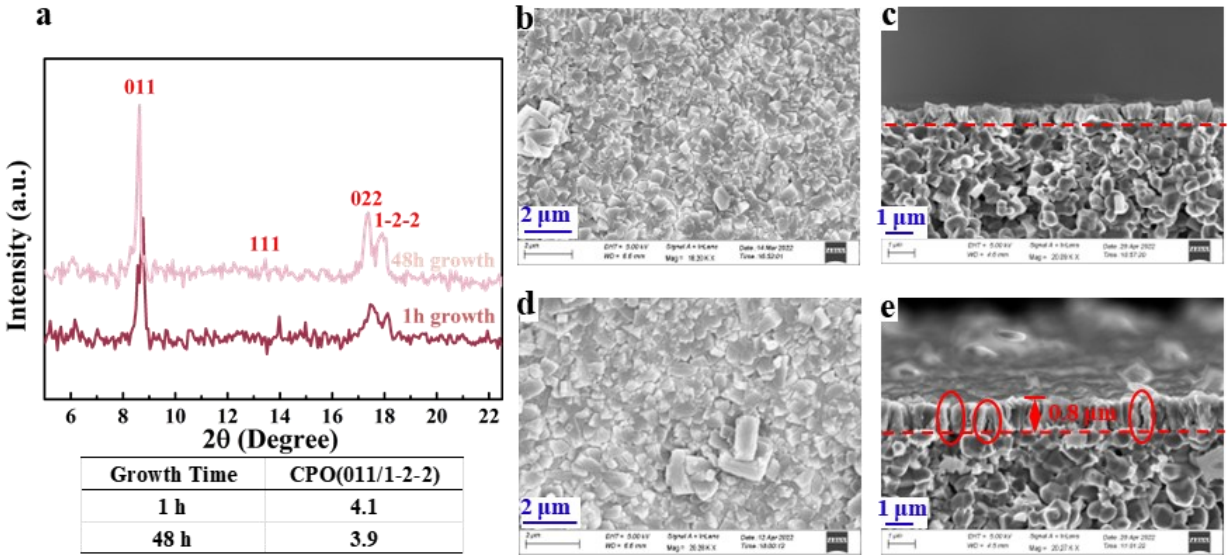

| Growth Time | CPO (1-2-2/011) |
|---|---|
| 1 h | 15.7 |
| 48 h | 7.0 |

Figure 4.5 SEM images and XRD patterns of MOF-303 membranes fabricated by RS method. (a-f) SEM images of the membrane after (a, b) seeding (the inset in a is an enlarged view of a multiedge cluster), (c, d) 1-hour, and (e, f) 48-hour secondary growth. (a, c, e) are surfaces, and (b, d, f) are cross-sections of the membrane. The red dotted lines in b, d and f divide the cross-sections into alumina substrate and MOF-303 membrane parts. (g) XRD patterns and CPO ratios of the membrane.

According to classic nucleation theory [23], subsequent growth from these seeds is favoured over the formation of new crystals because of the lower nucleation barrier. After 48 hours of secondary growth, a uniform RS membrane with well-intergrown crystals fully covering the substrate surface and a thickness of approximately 3.5 µm was formed, as shown in Figure 4.5 e, f. The RS membrane has a grass-like morphology, originating from a single root (seed) on the alumina surface and extending in all directions (Figure 4.5 d). These crystal clusters originate from stacked tiny seeds and extend from the support surface until they meet their neighboring crystals, forming a continuous membrane containing twin

crystals, as shown in Figure 4.5 f. Although the precise effect of crystal twinning on membrane properties remains complex and depends on various factors, it can lead to pore obstruction [24]. The XRD patterns of the samples after 1-hour and 48-hour secondary growth are shown in Figure 4.5 g, where the (011) and (1-2-2) planes become dominant after 1 hour of secondary growth, with a stronger intensity for the latter. By increasing the secondary growth time to 48 hours, the relative intensity of the (1-2-2) and (011) reflections, $CPO_{1\text{-}2\text{-}2/011}$, decreased to less than half of its initial value, implying that the crystals tended to grow in the (011) direction but that (1-2-2) was still the dominant growth direction of the RS membrane.

Considering the very low density of stacked metastable crystals in the RS seeding stage (Figure 4.5 a), the Bons and Bons model [25] describes the "grass-like" morphology well. Rooted in scattered small seeds, a divergent crystal structure emerged in all free directions during the secondary growth step (Figure 4.5 d) until it eventually met and connected with neighboring crystals to form the RS membrane, as shown in Figure 4.5 f. The lateral growth is ultimately confined to neighboring crystals and gradually directed toward the out-of-plane orientation, as verified by the decrease in $CPO_{1\text{-}2\text{-}2/011}$ from 15.7 to 7.




| Growth Time | CPO(011/1-2-2) |
|---|---|
| 1 h | 4.1 |
| 48 h | 3.9 |

Figure 4.6 SEM images and XRD patterns of MOF-303 membranes fabricated by conventional one-step method. (a) XRD patterns and corresponding CPO ratio of membrane. The patterns match those of MOF-303 powder. The SEM images of the membrane after (b, c) 1-hour synthesis and (d, e) 48-hour synthesis. The red circles in e display the intercrystalline gaps and interfacial voids between the substrate and MOF-303 layer. Red lines are to distinguish the MOF-303 layer from the alumina substrate.

To further demonstrate the advantages of our DS approach, the MOF-303 HF membrane was also fabricated using the conventional one-step method (Figure 4.2 b), and its SEM and XRD results are presented in Figure 4.6. As shown in Figure 4.6 a, the most significant peak reflected by the (011) peak

matches that of the MOF-303 powder (Figure 4.7 a). The CPO indices of the (1-2-2) to (011) reflections ($CPO_{1\text{-}2\text{-}2/011}$) remained constant, implying that the crystal orientations were identical over the growth time. Despite the formation of crystalline structures, intercrystalline defects were observed via SEM, as shown in Figure 4.6 b-e, especially in the cross section, as highlighted by the red circles Figure 4.6 e. The formation of these intercrystalline defects is likely due to inefficient heterogeneous nucleation on the support during one-step hydrothermal growth.

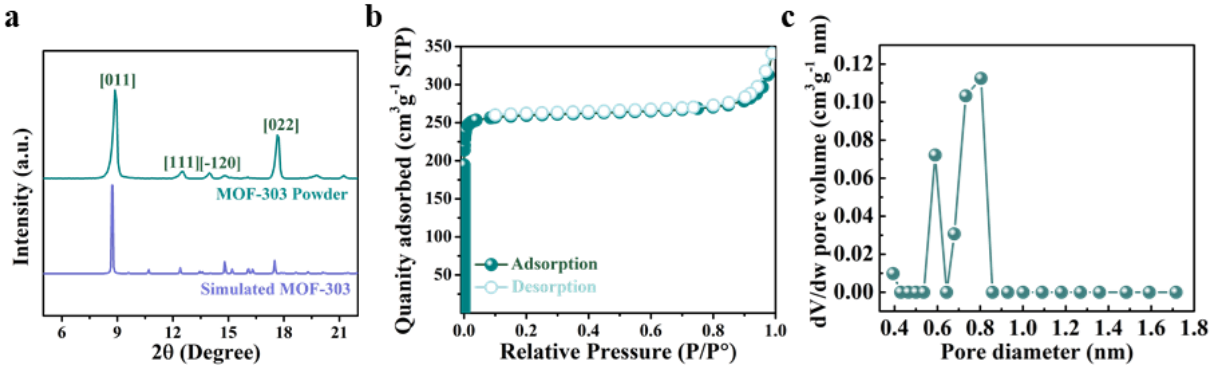



Figure 4.7 XRD patterns and BET analysis of MOF-303. (a) Simulated MOF-303 and the MOF-303 powder collected during the growth. (b) $N_2$ sorption isotherms of MOF-303 powder and (c) corresponding pore size distribution. The MOF-303 crystals contain pores with the size of 0.6~0.8 nm.

Moreover, the membrane prepared by the in-situ growth process exhibited poor attachment with the substrate. In the conventional one-step process, the metal consumption in the solution is expected to be primary since it is sufficient and readily available for reactions, resulting in the instant formation of crystals in the solution and on the surface of the support (Figure 4.6 b-e). This leads to a weak attachment between the MOF layer and the support.

This theory is further validated by the liquid contact method (Figure 4.8 a), where the rapid reaction leads to the formation of a membrane with an amorphous structure in the lower region and poor adhesion to the substrate. This is attributed to the excessively fast nucleation and accumulation of MOF-303 in the bulk solution, preventing attachment of crystals on alumina support.

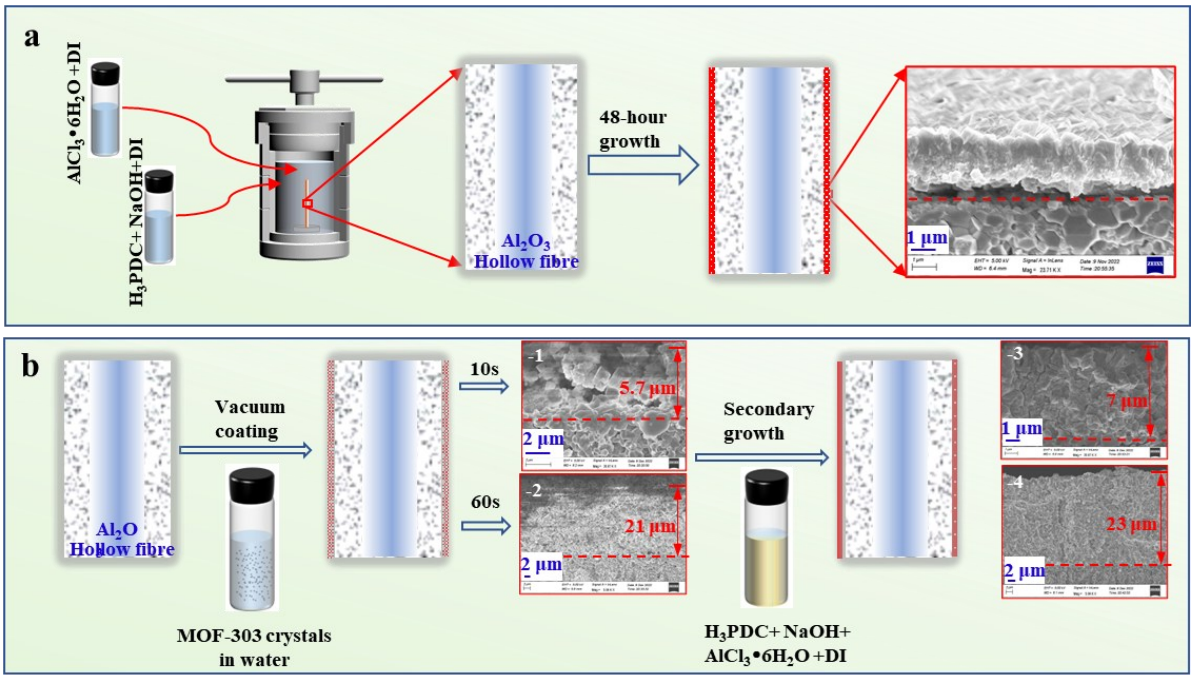



Figure 4.8 The schematic illustration of MOF-303 membranes synthesized by the liquid contact and the secondary growth of vacuum-coated seeding layer method. (a) The liquid contact method where the ligand with NaOH and metal salt dissolved separately before adding to the autoclave. (b) The secondary growth of vacuum-coated seeding layer. The MOF-303 crystals were dispersed in water and vacuum-coated onto HF substrate to form the seeding layer. The seeding layers were formed after (b-1) 10 seconds coating, and (b-2) 60 seconds coating and finally form continuous membranes, (b-3) and (b-4), respectively.

Moreover, a secondary growth method using vacuum-coated seeds was also utilized for the fabrication of the MOF-303 membrane (Figure 4.8 b), achieving strong adhesion to the substrate but failing to obtain oriented growth. Seeding layers with thicknesses of approximately 5.7 μm and 21 μm were obtained after 10 seconds and 60 seconds of coating, respectively. However, due to the random stacking of crystals and the absence of chemical bonding between them, the seeding layers exhibited a highly loosely packed structure. Following secondary growth, the membrane thickness increased slightly to 7 μm and 23 μm, respectively, while the overall structure became denser. Although this densification is expected to enhance selectivity, it may also result in reduced permeance due to the extended mass transport pathway imposed by the significant membrane thickness.

### 4.4.2 Pervaporative alcohol dehydration performance

High water sorption capacity and rapid water adsorption and desorption rates are the key features of water-stable MOF-303. These results indicate the preferential permeation of water in the dehydration of alcohol. Ethanol and 1-butanol are widely recognized as essential industrial alcohols, extensively

employed as solvents, fuel additives, and chemical intermediates. However, it is important to note that separating water/ethanol and water/1-butanol mixtures via conventional distillation remains a significant challenge due to their azeotropic behavior [26, 27]. Remarkably, both the DS and RS MOF-303 membranes demonstrated good ethanol and 1-butanol dehydration performances in a pervaporation system, as shown in Figure 4.9 a, b. For a feed containing 95 wt% ethanol, the fluxes of the DS and RS membranes were 18 and 6 kg $m^{-2}$ $h^{-1}$, respectively, which are greater than those of most of the state-of-the-art membranes and 1~2 orders of magnitude greater than those of previously reported for MOF and zeolite membranes, as shown in Figure 4.9 a [13, 28-37].

Due to the inherent trade-off between flux and selectivity, both parameters must be considered when evaluating the pervaporation performance of a membrane. To provide a comprehensive assessment, the pervaporation separation index (PSI) was calculated and is presented in Figure 4.9 c. The results confirm that both DS and RS membranes exhibit significantly higher PSI values compared to other reported MOF-based membranes for ethanol dehydration, highlighting their superior overall performance.

A comparison of the kinetic diameters of water vapour (2.9 Å) and ethanol (4.3 Å) molecules [38] with the pore size of MOF-303 crystals (6.0~8.0 Å) in Figure 4.7 b, c, implies that diffusion selectivity on the basis of pore size is not the rate-determining step in water/ethanol separation. According to a previous study, both the adsorption capacity and diffusion rate determine the water and ethanol permeation rates through MOF-303 membranes. An extraordinary water affinity was visually confirmed by observing the water contact behaviour shown in Figure 4.10 a, wherein the droplet traversed the membrane in a mere 1-second interval. This high-water affinity was further demonstrated by measuring the water vapour sorption kinetics of MOF-303 powder using a dynamic vapour sorption (DVS) system (Figure 4.9 e). The adsorption of ethanol also occurs in the pervaporation process. However, with only one hydrophilic end, ethanol exhibited a lower affinity for MOF-303, as shown in Figure 4.10 b, where penetration took more than twice as long as water. The DVS results also indicated that the ethanol sorption capacity was less than a quarter that of water (Figure 4.9 e). Due to the -OH and -NH groups in the pyrazole linker, the hydrophilic nature of the MOF-303 membrane traps the first water molecule with three hydrogen bonds, which seeds for the formation of trimeric clusters. These clusters act as the nucleus for binding other water molecules and form a water network throughout the pores [8], leading to continuous pore filling of the MOF (Figure 4.9 g) [39] and thus ultrahigh water flux.

In dynamic pore filling, water molecules are expected to dominate the pores. These water molecules can readily diffuse through the pores by sliding over those strongly attached to the pore wall (surface diffusion). The water molecules in the pores act as a significant diffusion barrier to ethanol and 1-butanol with larger kinetic diameters, thus ensuring an ample supply of water molecules for subsequent desorption [40].

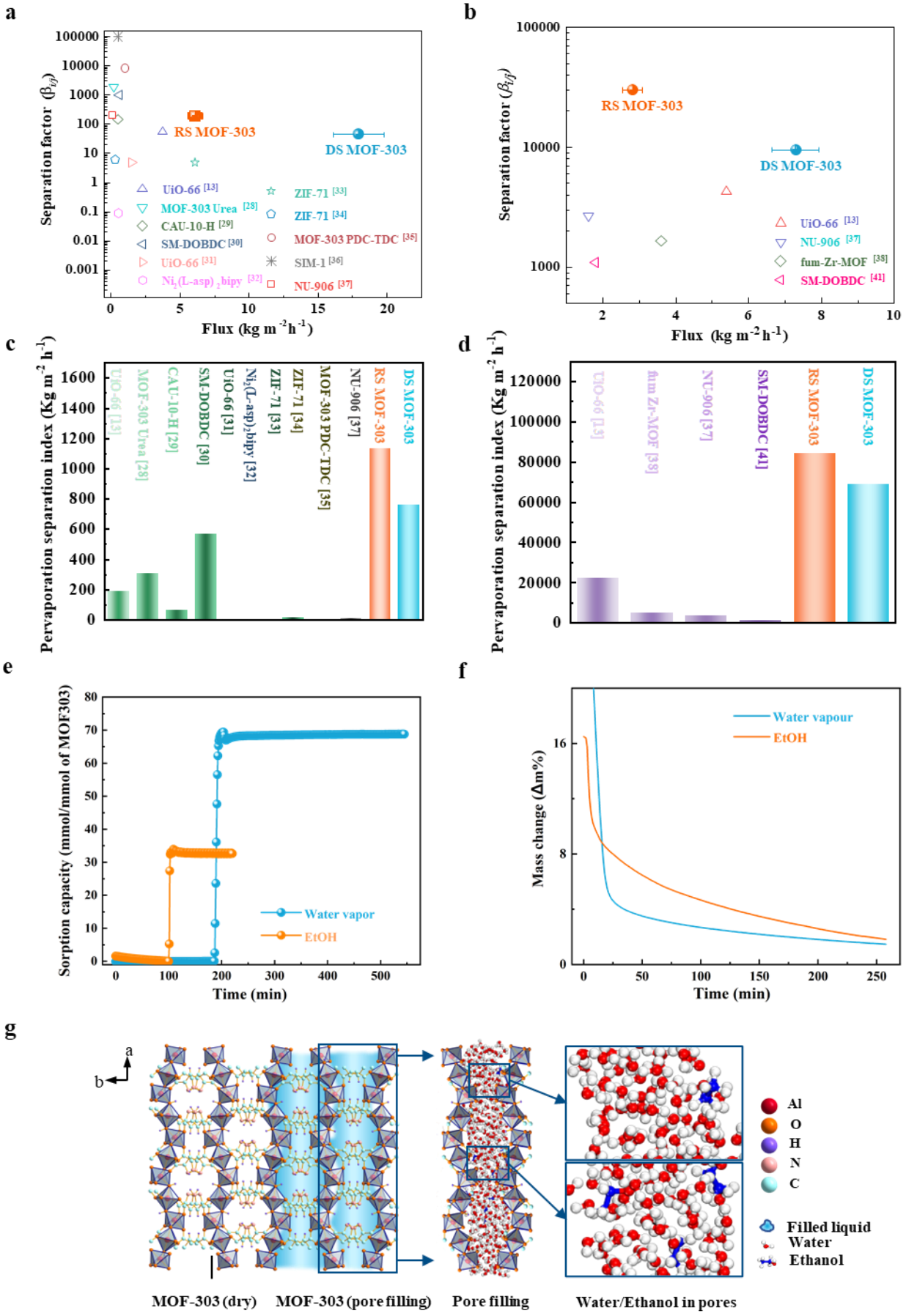

a
Separation factor ($\beta_{ij}$)
Flux (kg m$^{-2}$h$^{-1}$)
RS MOF-303
DS MOF-303
UiO-66 [13]
MOF-303 Urea [28]
CAU-10-H [29]
SM-DOBDC [30]
UiO-66 [31]
Ni$_2$(L-asp)$_2$bipy [32]
ZIF-71 [33]
ZIF-71 [34]
MOF-303 PDC-TDC [35]
SIM-1 [36]
NU-906 [37]
b
Separation factor ($\beta_{ij}$)
Flux (kg m$^{-2}$h$^{-1}$)
RS MOF-303
DS MOF-303
UiO-66 [13]
NU-906 [37]
fum-Zr-MOF [38]
SM-DOBDC [41]
c
Pervaporation separation index (Kg m$^{-2}$ h$^{-1}$)
UiO-66 [13]
MOF-303 Urea [28]
CAU-10-H [29]
SM-DOBDC [30]
UiO-66 [31]
Ni$_2$(L-asp)$_2$bipy [32]
ZIF-71 [33]
ZIF-71 [34]
MOF-303 PDC-TDC [35]
NU-906 [37]
RS MOF-303
DS MOF-303
d
Pervaporation separation index (Kg m$^{-2}$ h$^{-1}$)
UiO-66 [13]
fum-Zr-MOF [38]
NU-906 [37]
SM-DOBDC [41]
RS MOF-303
DS MOF-303
e
Sorption capacity (mmol/mmol of MOF303)
Time (min)
Water vapor
EtOH
f
Mass change (Δm%)
Time (min)
Water vapour
EtOH
g
a
b
Al
O
H
N
C
Filled liquid
Water
Ethanol
MOF-303 (dry)
MOF-303 (pore filling)
Pore filling
Water/Ethanol in pores

Figure 4.9 Pervaporative water/alcohol separation of the MOF-303 membranes. (a) Water/ethanol (5/95, wt%) and (b) water/butanol (5/95, wt%) separation performances of the RS and DS membranes compared with those of other MOF-based membranes. The feed temperature was 75 °C. Data are presented as mean standard deviation values, n = 3 or 4. (c) and (b) are the PSI of the RS and DS membranes compared with those of other MOF-based membranes. (e) Water and ethanol sorption kinetics of MOF-303 powder measured by DVS at P/Psat = 90% and T=60 °C. (f) Desorption rates of pure water and pure ethanol measured by DVS. (g) Side view of (left) the pristine MOF-303 crystal and (right) MOF-303 in terms of dynamic pore filling in the pervaporation process. The pores contain water and ethanol molecules, but they are mainly occupied by water molecules. The higher concentration of water molecules in the pores results in a diffusion barrier to ethanol molecules because of their larger kinetic diameter.

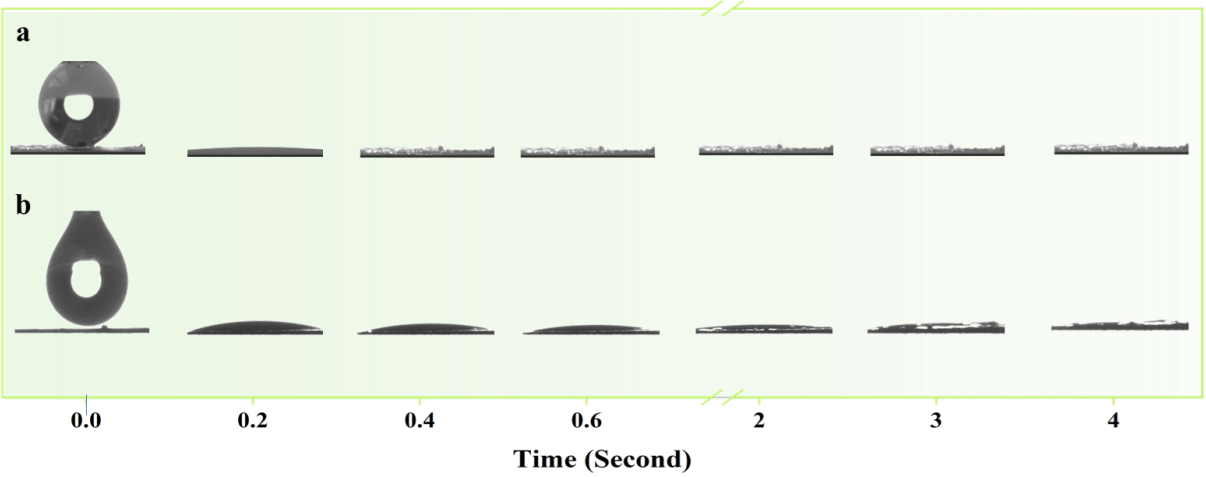



Figure 4.10 Water/ethanol contact behaviour of MOF-303 membranes. Changes of (a) water, (b) ethanol contact on MOF-303 membrane as a function of time. Pictures were captured from recorded videos.

Compared with those of ethanol, the MOF-303 membranes prepared in this study presented a greater separation factor and a much higher PSI for butanol dehydration compared to the data given in Figure 4.9 b and d [13, 37, 38, 41]. This can be ascribed to the larger kinetic diameter and more hydrophobic nature of butanol, as illustrated in Figure 4.11. Firstly, ethanol is more hydrophilic than 1-butanol due to the shorter hydrocarbon part, which provides a favourable adsorption of ethanol molecular onto the MOF-303 membrane. Owing to the superhydrophilic nature of MOF-303 membrane elucidated above, water molecules are preferably influencing the binding of subsequent molecules. As a result, the effective aperture size of the MOF-303 membrane during pervaporation is smaller than the theoretical aperture size of approximately 7.7 Å. Considering the occupancy of the first bonded water molecule (kinetic diameter, 2.9 Å), the effective pore size is reduced to less than 4.8 Å. This size, larger than the kinetic

diameter of ethanol (4.3 Å), facilitates rapid mass transport through the pores, as depicted in Figure 4.9 e. While the kinetic diameter of 1-butanol (5.1 Å) is only 0.8 Å larger, its diffusion is significantly hindered. This hindrance also restricts the transport of water molecules, resulting in reduced flux. In fact, it is well-documented that even a slight variation in molecular size can lead to large differences in diffusion coefficients, which can vary by several orders of magnitude[42].

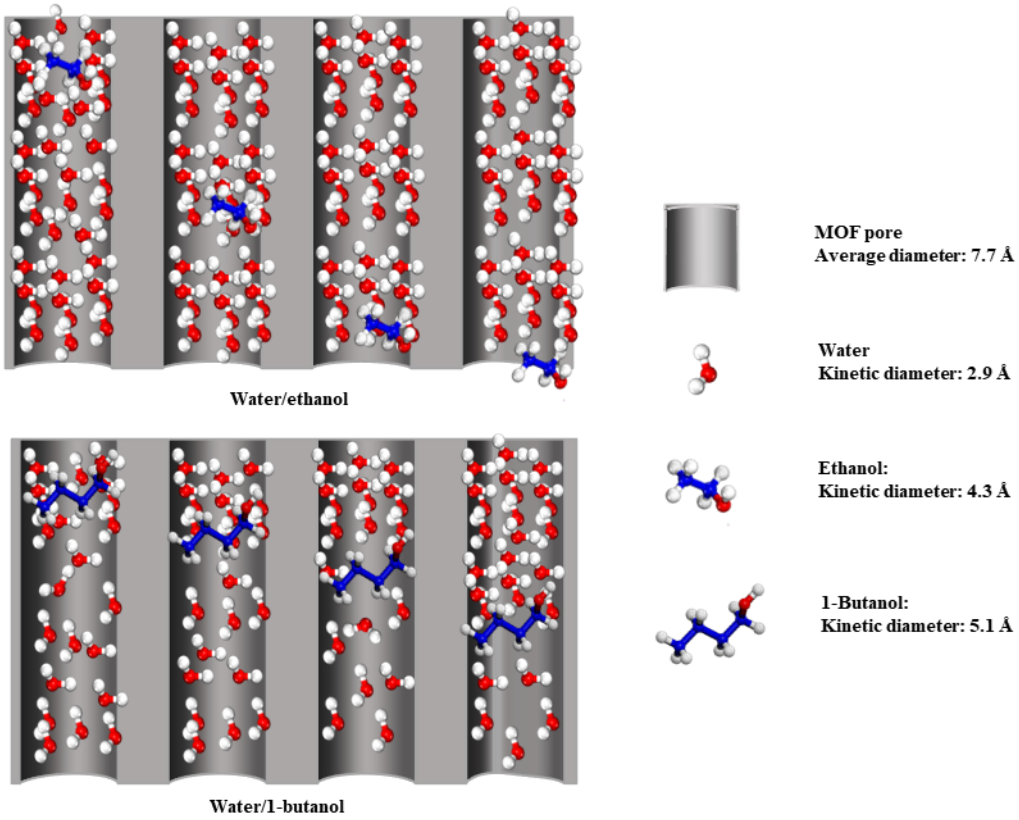



Figure 4.11 Schematic illustration of the transport of water/ethanol and water/1-butanol mixture in MOF-303 membrane.

To the best of our knowledge, the water fluxes of the DS and RS membranes are among the highest values reported thus far for state-of-the-art membranes. Interestingly, the water flux of the DS membrane is approximately 200% greater than that of the RS membrane because of the straight water permeation channels provided by the vertically aligned MOF-303 crystals. On the other hand, the RS membrane offered a slightly greater water/ethanol separation factor because the divergent MOF-303 crystals, which are partially blocked, created tortuous permeation pathways.

The desorption rates of water and ethanol can be affected by their diffusion through pores. Due to the higher concentration of water in the pores, its diffusion driving force is greater than that of ethanol, resulting in a faster desorption rate for water. In addition, the diffusion barrier to ethanol molecules with one hydrophobic end and a larger kinetic diameter is greater than that to water. This was confirmed by comparing the desorption rates of pure water and ethanol measured by DVS, in which ethanol exhibited

a slower desorption rate despite its higher vapour pressure (Figure 4.9 f).

Therefore, such good water/ethanol separation performance could be a combined effect of high-water adsorption, hindered diffusion of ethanol in the water-filled pores and higher desorption rates through the pores of MOF-303 membranes.

### 4.4.3 Performance in dye nanofiltration

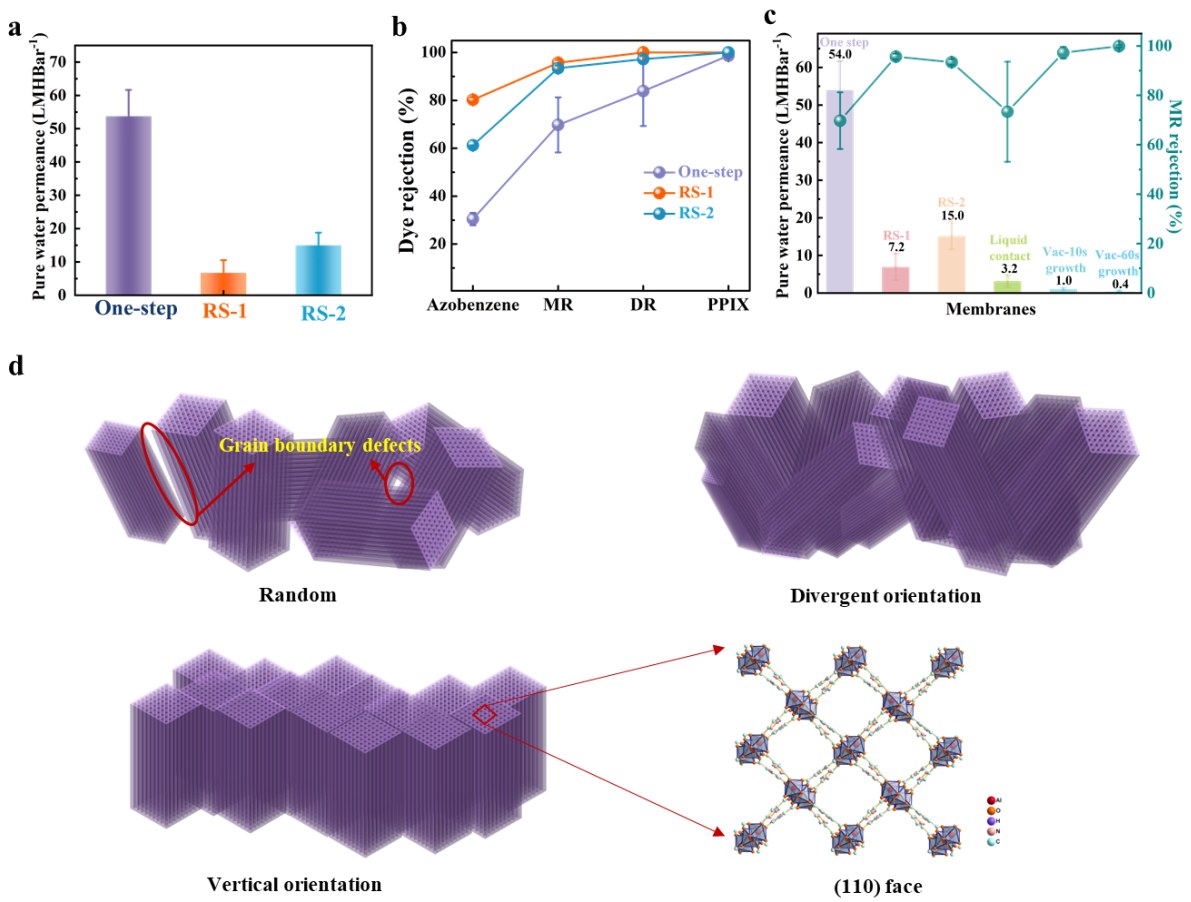



Figure 4.12 Dye nanofiltration performance of MOF-303 membranes. (a) Pure water permeance and (b) dye rejection performance of MOF-303 membranes fabricated via one-step growth, the RS method, and the DS method. (c) Pure water permeance ad MR rejection comparison of MOF-303 membranes fabricated by different methods. Neutral dyes with different molecular weights were used in this study (azobenzene: 182.22 g mol$^{-1}$, MR: 269.3 g mol$^{-1}$, DR: 324.3 g mol$^{-1}$, PPh-IX: 562.66 g mol$^{-1}$). Data are presented as mean standard deviation values, n = 3 or 6. (d) Schematic illustration of membrane formed by different crystal orientations.

The dye nanofiltration performance of the MOF-303 HF membranes was evaluated to gain further insight into their size-sieving ability. The pure water permeance of the MOF-303 HF membranes was measured using a dead-end filtration system. The membrane prepared via the one-step method demonstrated pure

water permeance up to 54 L $m^{-2}$ $h^{-1}$ $bar^{-1}$ but very poor rejection, largely due to intercrystalline defects [43] (Figure 4.12 a, b). The molecular weight cut-off (MWCO) was evaluated using four neutral dye molecules: azobenzene, methyl red (MR, 269.3 g $mol^{-1}$), disperse red (DR, 324.3 g $mol^{-1}$), and protoporphyrin IX (PPh-IX, 562.7 g $mol^{-1}$). Detailed information on the dyes' dimensions is provided in Chapter 3, Section 3.4.5. As shown, the MWCO of the RS and DS membranes was approximately 269.3 g $mol^{-1}$, whereas the membrane fabricated by the one-step approach showed poor rejection performance (MWCO≈562.7; Figure 4.12 b). The water permeances of the RS and DS membranes were 7 and 15 L $m^{-2}$ $h^{-1}$ $bar^{-1}$, respectively, remarkably surpassing those reported for MOF-303 membranes fabricated on flat alumina discs (0.8 L $m^{-2}$ $h^{-1}$ $bar^{-1}$) [12] and those prepared by direct liquid contact and vacuum coating seeded growth methods (Figure 4.12 c). This significant increase in water permeance and improved selectivity result from the thin and uniform thickness of the membrane and the controlled orientation of the permeation channels.

As schematically illustrated in Figure 4.12 d, the (011) orientation of the crystals prepared via the DS method was well-intergrown such that the number of grain boundary defects could be effectively minimized. This is in good accordance with the SEM images shown in Figure 4.3 e, f, especially compared with the one-step membrane presented in Figure 4.6, where significant gaps and pinholes tend to form at the grain boundaries in the membranes. These defects, which are larger than intracrystalline pores, create non-MOF transport pathways that enhance flux but compromise molecular sieving. Furthermore, as an anisotropic MOF with one-dimensional pores, the (011) orientation provides shorter mass transport pathways aligned perpendicular to the substrate, facilitating straight water permeation channels with reduced transport resistance (Figure 4.10 d) [8]. Conversely, while the RS membrane also demonstrated high selectivity due to well-intergrown crystals, the inclined orientation and partially blocked pores from neighboring crystals created longer, more tortuous permeation channels, resulting in significantly lower water permeance.

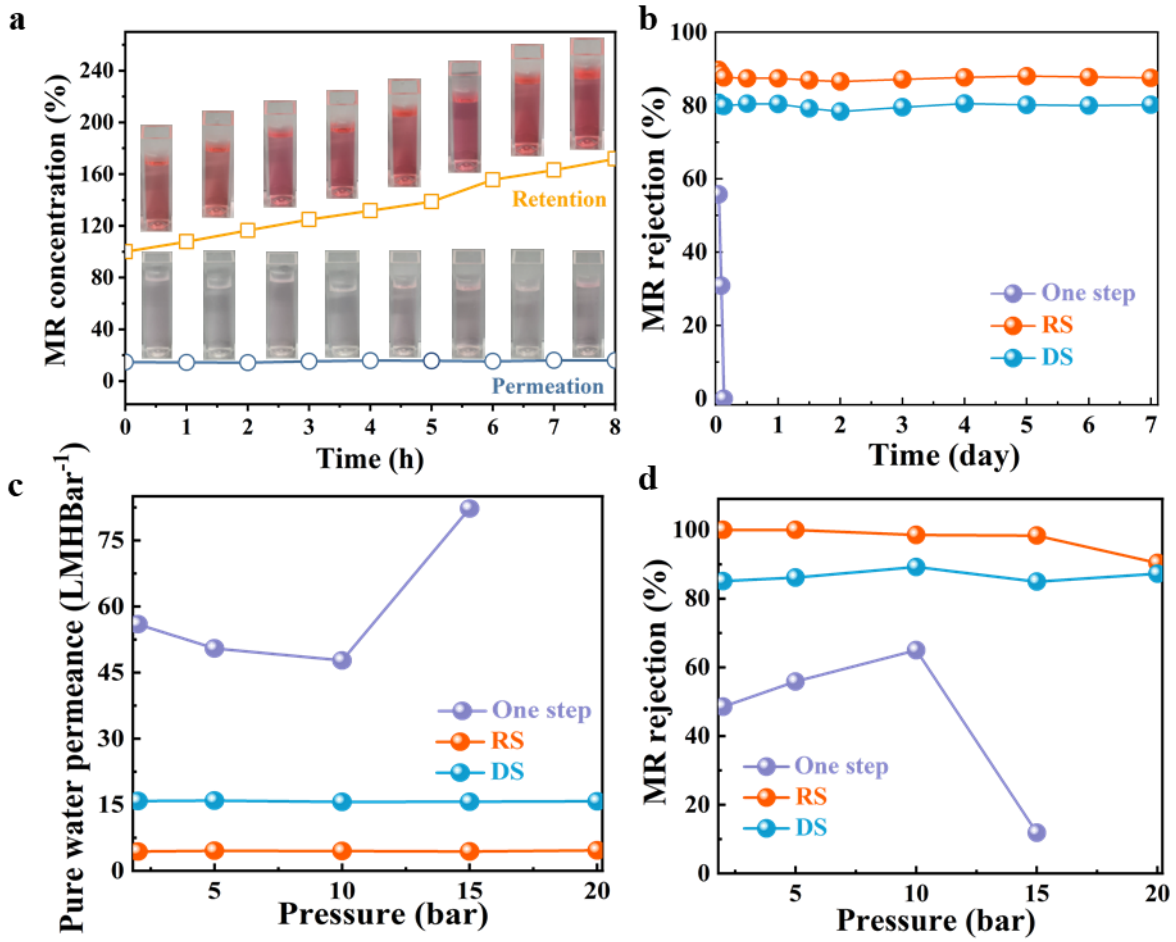



Figure 4.13 Stability of MOF-303 membranes fabricated by one-step RS and DS methods in nanofiltration. (a) Concentration changes during long-term MR rejection test of DS MOF-303 membrane. (b) Long-term stability of MOF-303 membranes at a pressure of 5 bar. (c) MR rejection and (d) pure water permeance of MOF-303 membranes at different pressures.

As shown in Figure 4.13 a, the MR rejection test was evaluated over a duration of 7 hours, when the permeate with a MR concentration was continuously collected, verifying the stable MR rejection of the fabricated membrane. Additionally, the size-sieving mechanism, rather than adsorption, was confirmed by the increased dye concentration in the retentate. In order to comprehensively investigate the durability of the obtained membranes, a prolonged test up to 7 days was conducted by one-step, RS and DS MOF-303 membranes and the results are displayed in Figure 4.13 b. Unlike the one-step fabricated membrane which lost structure integrity within 2 hours, the RS and DS MOF-303 membranes demonstrated stable performance without losing rejection. Similarly, in the varied-pressure measurement, both the RS and DS MOF-303 membranes demonstrated stable water permeance and good compaction resistance and maintained good MR dye rejection under pressures of up to 20 bar, whereas the membrane fabricated via the one-step technique could not withstand pressures greater than 10 bar (Figure 4.13 c and d). This stable

performance is attributed to (i) the better attachment of MOF-303 crystals to the support in the seeding step realized by the metal source available on the HF substrate, (ii) the higher density of MOF-303 crystals in the seeding layer, and (iii) the good growth of the crystalline structure.

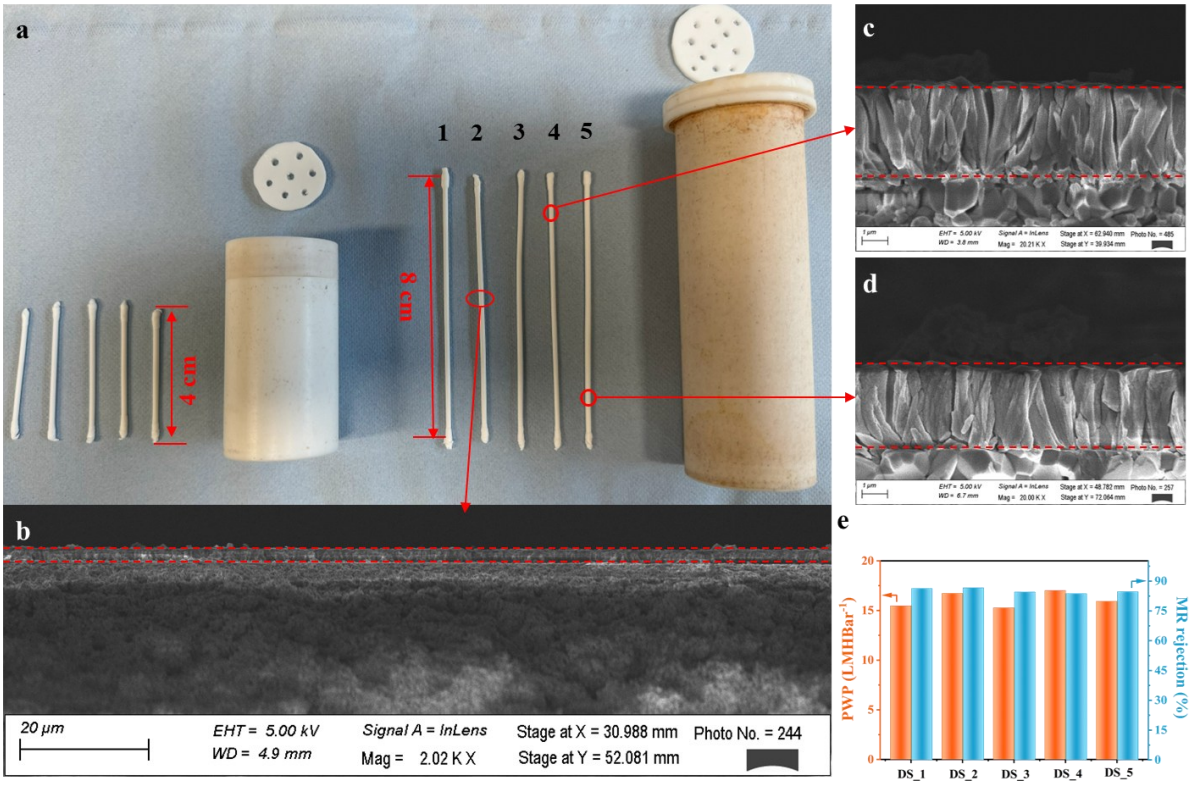



Figure 4.14 Samples fabricated with increased scale. (a) HF cut into 4 cm- and 8 cm- lengths for fabrication of DS membrane in autoclave with different sizes, two pieces of HF were put in each reactor, (b), (c) and (d) are cross-section views of DS membrane observed on the random position of samples fabricated in the big autoclave. (e) is the PWP and MR rejection of five samples in the sample autoclave.

Furthermore, the larger membrane areas were performed via the DS method. As shown in Figure 4.14 a, instead of one 4-cm long fibre substrate in the original autoclave, we increased the number of substrates to four. Also, we employed a large autoclave, which allowed us to place two 8-cm long fibre substrates. Thus, in both autoclaves, the production area increased fourfold. The cross-sectional morphologies observed from random sections of different samples synthesized by the big autoclave exhibited good repeatability and well-controlled orientation identical to DS the membrane described before (Figure 4.14 b-d). The nanofiltration result with these samples shown in Figure 4.14 e indicated that the pure water permeance and MR rejections remain almost unchanged compared with the results shown in Figure 4.10 a, b, suggesting that the proposed method holds significant potential for large-scale MOF-303 membrane fabrication. Finally, a comparative analysis of the data in Table 4.1 demonstrates that the nanofiltration

performance of the DS membranes is competitive with that of the state-of-the-art MOF membranes reported to date. This finding underscores the importance of structural optimization, particularly the alignment of one-dimensional permeation channels, in maximizing membrane performance.

Table 4.1 Comparison of nanofiltration performance of state-of-the-art MOFs-based membranes (The selected literature represents key studies identified through a Web of Science search using keyw ords such as “MOF membranes for liquid separaion”, “MOF membranes for nanofiltration” and “MOF membranes for desalination”)

| MOF | Polymer matrix | Fabrication technique | Permeance (L $m^{-2}$ $h^{-1}$ $bar^{-1}$) | Rejection | Ref. |
|---|---|---|---|---|---|
| *MOF-303* | - | RS | 7.0 | Azobenzene, 80.2%<br>Methyl red, 95.7%<br>Disperse red, 100%<br>Protoporphyrin IX, 100% | This work |
| *MOF-303* | - | DS | 15.2 | Azobenzene, 61.2%<br>Methyl red, 93.4%<br>Disperse red, 97.2%<br>Protoporphyrin IX, 100% | This work |
| *MOF-303* | - | In-situ growth | 0.7 | $MgCl_2$, 93.5%<br>$Na_2SO_4$, 96.0% | [12] |
| *ZIF-8* | - | Nanoreactor-confined crystallization | 130 | Proanthocyanidin, 98.5% | [44] |
| *ZIF-8* | - | In-situ growth on a tannic acid (TA) and $Zn^{2+}$ network | 5.1 | NaCl, 55.2%<br>$Na_2SO_4$, 93.6% | [45] |
| *ZIF-8* | Polyamide | Liquid-liquid interfacial coordination | 37.5 | Rose Bengal, >98% | [46] |
| *ZIF-8* | Polyamide | In-situ growth with substrate modification | >30 | Methyl orange, >97%<br>Isatin, >97%<br>Methyl blue, >99%<br>Congo red, >99% | [47] |
| *ZIF-8* | Polyamide | Layer-by-layer | 27 | Congo red, >99.8% | [48] |
| *ZIF-8* | Polyamide | Non-solvent induced phase inversion | 10.4 | Rode Bengal, >96.1% | [49] |

| | | | | | |
|---|---|---|---|---|---|
| *ZIF-8* | Polyamide | Interfacial polymerization | 4.8 | $SO_4^{2-}$, 89.9% | [50] |
| *ZIF-8* | Polyamide | Layer-by-layer | 5.5 | Acetaminophen, 55% | [51] |
| *ZIF-8* | Polyethylenimine | Self-assembly and interfacial reaction | 33 | Methyl blue, 99.6% | [52] |
| *ZIF-8* | Polyamide | Blending interfacial polymerization | 7.1 | NaCl, 35%<br>Xylose, 67% | [53] |
| *ZIF-300* | - | Secondary growth | 39.2 | Rhodamine B, 99.9%<br>Methyl blue, 99.6%<br>Methyl orange, 98.89% | [54] |
| *ZIF-L* | - | Heteroepitaxial growth | 51.6 | Methyl orange, 80%<br>Acid fuchsin, 90% | [55] |
| *UiO-66* | - | In-situ growth | 0.2 | $Ca^{2+}$, 86.3%<br>$Mg^{2+}$, 98. 0%<br>$Al^{3+}$, 99.3% | [6] |
| *UiO-66-$OH_2$* | - | Secondary growth | 2.4 | Methyl blue, 98.7%<br>$Na^{+}$, 26%<br>$Zn^{2+}$, 42.5%<br>$Fe^{3+}$, 54.7% | [56] |
| *$NH_2$-UiO-66@ZIF-8* | - | In-situ growth | 36.7 | Direct red 80, 100%<br>Acid orange, 100%<br>Methyl orange, 99.6%<br>Methylene blue, 97.0% | [57] |
| *UiO-66* | GO/polyacrylonitrile | Vacuum filtration after phase inversion | 31.3 | Methyl orange, 94.8%<br>Methyl blue, 100%<br>Congo red, 99.6<br>Rhodamine B, 95.5<br>Tetracycline hydrochloride, 95.5%<br>Oxytetracycline, 94.8%<br>Ciprofloxacin, 98.6% | [7] |
| *UiO-66-$NH_2$* | Polyamide | Blending interfacial polymerization | 7.2 | NaCl, 42%<br>Xylose, 65% | [53] |
| *UiO-66* | Polyamide | Dispersion and interfacial | 11.5 | $SeO_3^{2-}$, 96.5%<br>$SeO_4^{2-}$, 97.4% | [58] |

| | | | | | |
|---|---|---|---|---|---|
| | | polymerization | | $HAsO_4^{2-}$, 98.6% | |
| *UiO-66-$NH_2$* | Polyamide | Blending and interfacial polymerization | 30 | Methyl orange, 92%<br>Sunset yellow, 96%<br>Congo red, 99.6% | [59] |
| *UiO-66* | Polyelectrolytes | Blending and layer-by-layer | 14.8 | $MgSO_4$, 96.3%<br>Congo red, 99.9% | [60] |
| *UiO-66-$NH_2$* | Polyacrylonitrile | Drop coating and vacuum filtration | 14 | Congo red, 94%<br>Methyl orange, 94%<br>Rhodamine B, 94%<br>Methylene blue, 94 % | [61] |
| *UiO-66-$NH_2$* | Graphene oxide | Crosslinking and vacuum filtration | 83.5 | Methyl blue, 100%<br>Congo red, 99.9%<br>Alphazurine A, 97.8%<br>Eriochrome Black T, 99.3<br>Crystal violet, 100<br>Disperse black 9, 100% | [62] |
| *MIL-53(Al)* | Polyamide | Blending interfacial polymerization | 6.9 | NaCl, 40%<br>Xylose, 61% | [53] |
| *$NH_2$-MIL-101(Al)* | Chitosan | Blending and solvent evaporation | 4 | $MgCl_2$, 93.0%<br>$CaCl_2$, 86.5% | [63] |
| *BUT-8(A)* | Polyethylenimine | Blending and spinning coating | Up to 68.3 | Methyl blue, 98.3%<br>Congo red, 99.8%<br>Acid fuchsin, 89.3%<br>Methyl orange, 82.1% | [64] |
| *BUT-8(A)* | Polydiallyldimethylammonium chloride | Spinning coating | 16.4 | Methyl blue, 98.8% | [65] |
| *$Zn_2(bim)_4$* | Polyethylenimine | Blending and vacuum coating | 290 | Methyl red, 98%<br>Coomassie brilliant blue, 98%<br>Methylene blue, 98%<br>$Ca^{2+}$, 66.2%<br>$Mg^{2+}$, 52.7%<br>$Al^{3+}$, 74.3% | [66] |
| *MOF-1* | Chitosan | Blending and crosslinking | 20 | Metyl blue, 85%<br>Rhodamine B, 85% | [67] |

| | | | | | |
|---|---|---|---|---|---|
| | | | | Eriochrome black t, 92%<br>CR: 98 | |
| *MOF-801* | - | Epitaxial growth | >71 | Congo red, 99.8%<br>Methyl blue, 99.7%<br>Malachite green, 99.4% | [68] |
| *MOF-808* | - | In-situ growth | 3.6 | Congo red, 99.5% | [69] |
| *MIP-202* | GO | Blending and vacuum filtration | 55.3 | Crystal violet, 99.5% | [70] |
| *NUS-8* | - | Doctor-blading | ~1 | $Mg^{2+}$, 98%<br>$Al^{3+}$, 98%<br>Acide fuchsin, ~ 90%<br>Methyl blue, ~94% | [71] |
| *CuBTC* | Polyvinyl alcohol | In-situ growth and crosslinking | 12.9 | Congo red, 99.5% | [72] |
| *Cu-TCPP* | - | Vacuum filtration | 840.1 | Congo red, 99.8%<br>Chrome black T, 93.3%<br>Methyl blue, 99.7%<br>Crystal violet, 90.1% | [73] |
| *Cu-TCPP* | - | Electrophoretic deposition | 16.4 | Brilliant blue G, 97% | [74] |
| *Cu-TCPP* | - | Vacuum filtration | 9.4 | Evans blue, 97% | [74] |
| *Ag-MOF* | Polyamide | Vacuum assisted interfacial polymerization | 14.3 | Methyl orange, 95.4%<br>Methyl blue, 88.7%<br>Rhodamine B, 99.3%<br>$Na_2SO_4$, 84.1%<br>$MgSO_4$, 73.1% | [75] |
| *Ni-MOF* | - | Vacuum filtration | - | Congo red, 97.7% | [76] |
| *Prussian blue* | - | In-situ growth | 26.2 | Congo red, 99.7%<br>Calcein, 99.3%<br>Methyl blue, 99% | [77] |

## 4.5 Conclusion

In this study, we experimentally demonstrated well-crystallized MOF-303 membranes with a controlled crystal orientation on the (011) facet by proposing a DS method. The MOF-303 membrane with a one-dimensional pore structure (011) (i.e., the DS membrane) provided straight water permeation channels

with ultrahigh water flux for ethanol dehydration, twofold greater than that of the RS membrane with divergent crystal orientations (1-2-2) and 1~2 order(s) of magnitude greater than those previously reported for other water-stable MOF-based membranes.

The pure water permeance data from dye nanofiltration tests also proved the critical role of tailoring the crystal orientation in the fabrication method. The DS membrane showed much greater water permeance than the other membranes while retaining a very good MWCO (~269). The excellent durability of the DS MOF-303 membrane under pressurized conditions was realized by the better interfacial interaction between the MOF-303 crystals and the HF substrate facilitated by aluminum metal sites available on the alumina support. We believe that the findings from this study can provide valuable insights into the design and fabrication of stable, high-performance MOF-based membranes for water separation applications.

## References

[1] S. Yuan, L. Feng, K. Wang, J. Pang, M. Bosch, C. Lollar, Y. Sun, J. Qin, X. Yang, P. Zhang, Q. Wang, L. Zou, Y. Zhang, L. Zhang, Y. Fang, J. Li, H.-C. Zhou, Stable Metal–Organic Frameworks: Design, Synthesis, and Applications, Advanced Materials 30(37) (2018) 1704303. https://doi.org/https://doi.org/10.1002/adma.201704303.
[2] R.G. Pearson, Hard and Soft Acids and Bases, Journal of the American Chemical Society 85(22) (1963) 3533-3539. https://doi.org/10.1021/ja00905a001.
[3] C. Wang, X. Liu, N. Keser Demir, J.P. Chen, K. Li, Applications of water stable metal–organic frameworks, Chemical Society Reviews 45(18) (2016) 5107-5134. https://doi.org/10.1039/C6CS00362A.
[4] X. Liu, X. Wang, F. Kapteijn, Water and Metal–Organic Frameworks: From Interaction toward Utilization, Chemical Reviews 120(16) (2020) 8303-8377. https://doi.org/10.1021/acs.chemrev.9b00746.
[5] A.J. Howarth, Y.Y. Liu, P. Li, Z.Y. Li, T.C. Wang, J. Hupp, O.K. Farha, Chemical, thermal and mechanical stabilities of metal-organic frameworks, Nature Reviews Materials 1(3) (2016). https://doi.org/10.1038/natrevmats.2015.18.
[6] X. Liu, N.K. Demir, Z. Wu, K. Li, Highly Water-Stable Zirconium Metal–Organic Framework UiO-66 Membranes Supported on Alumina Hollow Fibers for Desalination, Journal of the American Chemical Society 137(22) (2015) 6999-7002. https://doi.org/10.1021/jacs.5b02276.
[7] S.-Y. Fang, P. Zhang, J.-L. Gong, L. Tang, G.-M. Zeng, B. Song, W.-C. Cao, J. Li, J. Ye, Construction of highly water-stable metal-organic framework UiO-66 thin-film composite membrane for dyes and antibiotics separation, Chemical Engineering Journal 385 (2020) 123400. https://doi.org/https://doi.org/10.1016/j.cej.2019.123400.
[8] N. Hanikel, X. Pei, S. Chheda, H. Lyu, W. Jeong, J. Sauer, L. Gagliardi, O.M. Yaghi, Evolution of water structures in metal-organic frameworks for improved atmospheric water harvesting, Science 374(6566) (2021) 454-459. https://doi.org/doi:10.1126/science.abj0890.
[9] F. Fathieh, M.J. Kalmutzki, E.A. Kapustin, P.J. Waller, J. Yang, O.M. Yaghi, Practical water production from desert air, Science Advances 4(6) (2018) 3198. https://doi.org/doi:10.1126/sciadv.aat3198.
[10] N. Hanikel, M.S. Prévot, F. Fathieh, E.A. Kapustin, H. Lyu, H. Wang, N.J. Diercks, T.G. Glover, O.M.J.A.c.s. Yaghi, Rapid cycling and exceptional yield in a metal-organic framework water harvester, ACS Central Science 5(10) (2019) 1699-1706.
[11] C. Wang, X. Yan, X. Liu, Polycrystalline Metal–Organic Framework Membranes for Pervaporation, Industrial & Engineering Chemistry Research 62(28) (2023) 10787-10799. https://doi.org/10.1021/acs.iecr.3c00795.
[12] S. Cong, Y. Yuan, J. Wang, Z. Wang, F. Kapteijn, X. Liu, Highly Water-Permeable Metal–Organic Framework MOF-303 Membranes for Desalination, Journal of the American Chemical Society 143(48) (2021)

20055-20058. https://doi.org/10.1021/jacs.1c10192.
[13] J.-Y. Lai, T.-Y. Wang, C. Zou, J.-J. Chen, L.-C. Lin, D.-Y. Kang, Highly-selective MOF-303 membrane for alcohol dehydration, Journal of Membrane Science 661 (2022) 120879. https://doi.org/https://doi.org/10.1016/j.memsci.2022.120879.
[14] I.E. Khalil, J. Fonseca, M.R. Reithofer, T. Eder, J.M. Chin, Tackling orientation of metal-organic frameworks (MOFs): The quest to enhance MOF performance, Coordination Chemistry Reviews 481 (2023) 215043. https://doi.org/https://doi.org/10.1016/j.ccr.2023.215043.
[15] Y. Hu, X. Dong, J. Nan, W. Jin, X. Ren, N. Xu, Y.M. Lee, Metal–organic framework membranes fabricated via reactive seeding, Chemical communications 47(2) (2011) 737-739.
[16] T. Wu, N. Prasetya, K. Li, Re-generable and re-synthesisable micro-structured MIL-53 Rachig Rings for ibuprofen removal, Journal of Environmental Chemical Engineering 10(3) (2022) 107432. https://doi.org/https://doi.org/10.1016/j.jece.2022.107432.
[17] L. Barcza, M. Pálfalvi-Rózsahegyi, The aluminate lye as a system of equilibria, Materials Chemistry and Physics 21(4) (1989) 345-356. https://doi.org/https://doi.org/10.1016/0254-0584(89)90136-3.
[18] D.E.J.J.o.C.P. O'reilly, NMR Chemical Shifts of Aluminum: Experimental Data and Variational Calculation, Journal of Chemical Physics 32 (1960) 1007-1012.
[19] A. Drift, Evolutionary Selection, a Principle Governing Growth Orientation in Vapour-Deposited Layers, Philips Res. Rep. 22 (1967) 267-288.
[20] I.J.Z.P.C. Stranski, The theory of crystal growth, 136 (1928) 259-278.
[21] P. Lagerlof, Crystal Dislocations: Their Impact on Physical Properties of Crystals, Crystals 8(11) (2018) 413.
[22] M.V. Klassen-Neklyudova, Mechanical twinning of crystals, Springer Science & Business Media2012.
[23] V.I. Kalikmanov, Classical nucleation theory, Nucleation theory, Springer2012, pp. 17-41.
[24] Z. Lai, M. Tsapatsis, J.P.J.A.F.M. Nicolich, Siliceous ZSM-5 membranes by secondary growth of b-oriented seed layers, Advanced Functional Materials 14(7) (2004) 716-729.
[25] A.-J. Bons, P.D. Bons, The development of oblique preferred orientations in zeolite films and membranes, Microporous and Mesoporous Materials 62(1) (2003) 9-16. https://doi.org/https://doi.org/10.1016/S1387-1811(03)00384-6.
[26] A. Kujawska, W. Kujawski, W. Capała, U. Kiełkowska, M. Plesnar, J. Kujawa, Influence of Process Parameters on the Efficiency of Pervaporation Pilot ECO-001 Plant for Raw Ethanol Dehydration, Membranes, 2024.
[27] A. Rozicka, J. Niemistö, R.L. Keiski, W. Kujawski, Apparent and intrinsic properties of commercial PDMS based membranes in pervaporative removal of acetone, butanol and ethanol from binary aqueous mixtures, Journal of Membrane Science 453 (2014) 108-118. https://doi.org/https://doi.org/10.1016/j.memsci.2013.10.065.
[28] X. Liu, C. Wang, B. Wang, K. Li, Novel Organic-Dehydration Membranes Prepared from Zirconium Metal-Organic Frameworks, Advanced Functional Materials 27(3) (2017) 1604311. https://doi.org/https://doi.org/10.1002/adfm.201604311.
[29] H. Jin, K. Mo, F. Wen, Y.J.J.o.m.s. Li, Preparation and pervaporation performance of CAU-10-H MOF membranes, Journal of membrane science 577 (2019) 129-136.
[30] L. Zhai, X. Yu, Y. Wang, J. Zhang, Y. Ying, Y. Cheng, S.B. Peh, G. Liu, X. Wang, Y.J.J.o.m.s. Cai, Polycrystalline rare-earth metal-organic framework membranes with in-situ healing ability for efficient alcohol dehydration, Journal of membrane science 610 (2020) 118239.
[31] M. Miyamoto, K. Hori, T. Goshima, N. Takaya, Y. Oumi, S.J.E.J.o.I.C. Uemiya, An organoselective zirconium-based metal–organic-framework UiO-66 membrane for pervaporation, European Journal of Inorganic Chemistry 2017(14) (2017) 2094-2099.
[32] S. Wang, Z. Kang, B. Xu, L. Fan, G. Li, L. Wen, X. Xin, Z. Xiao, J. Pang, X. Du, D. Sun, Wettability switchable metal-organic framework membranes for pervaporation of water/ethanol mixtures, Inorganic Chemistry Communications 82 (2017) 64-67. https://doi.org/https://doi.org/10.1016/j.inoche.2017.05.016.
[33] K. Huang, Q. Li, G. Liu, J. Shen, K. Guan, W. Jin, A ZIF-71 Hollow Fiber Membrane Fabricated by Contra-Diffusion, ACS Applied Materials & Interfaces 7(30) (2015) 16157-16160. https://doi.org/10.1021/acsami.5b04991.
[34] X. Dong, Y.S. Lin, Synthesis of an organophilic ZIF-71 membrane for pervaporation solvent separation, Chemical Communications 49(12) (2013) 1196-1198. https://doi.org/10.1039/C2CC38512K.
[35] F.-H. Hu, L.-T. Chi, G.-B. Syu, T.-Y. Yu, M.-P. Lin, J.-J. Chen, W.-Y. Yu, D.-Y. Kang, Mixed-linker MOF-303 membranes for pervaporation, Journal of Membrane Science Letters 3(2) (2023) 100053. https://doi.org/https://doi.org/10.1016/j.memlet.2023.100053.

[36] A. Marti, D. Tran, K. Balkus, Fabrication of a Substituted Imidazolate Material 1 (SIM-1) membrane using post synthetic modification (PSM) for pervaporation of water/ ethanol mixtures, Journal of Porous Materials (2015). https://doi.org/10.1007/s10934-015-0005-y.
[37] R. Luo, H. Fu, Y. Li, Q. Xing, G. Liang, P. Bai, X. Guo, J. Lyu, M. Tsapatsis, In Situ Fabrication of Metal–Organic Framework Thin Films with Enhanced Pervaporation Performance, 33(18) (2023) 2213221. https://doi.org/https://doi.org/10.1002/adfm.202213221.
[38] B. Mo, Y. Jin, G. Zhou, G. Liu, C. Chen, Z. Liu, G. Liu, W. Jin, Ligand-engineered Zr-MOF membranes with fast water transport channels for alcohol–water separation, 70(5) (2024) e18368. https://doi.org/https://doi.org/10.1002/aic.18368.
[39] J. Canivet, A. Fateeva, Y. Guo, B. Coasne, D. Farrusseng, Water adsorption in MOFs: fundamentals and applications, Chemical Society Reviews 43(16) (2014) 5594-5617. https://doi.org/10.1039/C4CS00078A.
[40] A. Nalaparaju, X.S. Zhao, J.J.J.o.P.C.C. Jiang, Molecular Understanding for the Adsorption of Water and Alcohols in Hydrophilic and Hydrophobic Zeolitic Metal−Organic Frameworks, Journal of Physical Chemistry C 114 (2010) 11542-11550.
[41] G. Gao, Y. Zhao, P. Zhu, H. Liu, Y. Guo, X. Zhang, Self-converted fabrication of a Ni-MOF-74 tubular membrane from nickel-based nanosheets for butanol dehydration by pervaporation, CrystEngComm 25(48) (2023) 6740-6747. https://doi.org/10.1039/D3CE01007D.
[42] K. Zhang, R.P. Lively, C. Zhang, R.R. Chance, W.J. Koros, D.S. Sholl, S. Nair, Exploring the Framework Hydrophobicity and Flexibility of ZIF-8: From Biofuel Recovery to Hydrocarbon Separations, The Journal of Physical Chemistry Letters 4(21) (2013) 3618-3622. https://doi.org/10.1021/jz402019d.
[43] Z. Xing, X. Xuan, H. Hu, M. Li, H. Gao, A. Alowasheeir, D. Jiang, L. Zhu, Z. Li, Y. Kang, J. Zhang, X. Yi, Y. Yamauchi, X. Xu, Particle size optimization of metal–organic frameworks for superior capacitive deionization in oxygenated saline water, Chemical Communications 59(30) (2023) 4515-4518. https://doi.org/10.1039/D2CC06460J.
[44] Y.-L. Ji, B.-X. Gu, H.-Q. Huo, S.-J. Xie, H. Peng, W.-H. Zhang, M.-J. Yin, B. Xiong, H. Lu, L.F. Villalobos, Q. Zhao, C.-J. Gao, M. Elimelech, Q.-F. An, Roll-to-roll fabrication of large-area metal–organic framework-based membranes for high-performance aqueous separations, Nature Water 2(2) (2024) 183-192. https://doi.org/10.1038/s44221-023-00184-4.
[45] Y. Xiao, W. Zhang, Y. Jiao, Y. Xu, H. Lin, Metal-phenolic network as precursor for fabrication of metal-organic framework (MOF) nanofiltration membrane for efficient desalination, Journal of Membrane Science 624 (2021) 119101. https://doi.org/https://doi.org/10.1016/j.memsci.2021.119101.
[46] Y. Li, L.H. Wee, J.A. Martens, I.F.J.J.o.M.S. Vankelecom, Interfacial synthesis of ZIF-8 membranes with improved nanofiltration performance, 523 (2017) 561-566.
[47] M.-y. Zhang, X.-p. Wang, R. Lin, Y. Liu, F.-s. Chen, L.-s. Cui, X.-m. Meng, J. Hou, Improving the hydrostability of ZIF-8 membrane by biomolecule towards enhanced nanofiltration performance for dye removal, Journal of Membrane Science 618 (2021) 118630. https://doi.org/https://doi.org/10.1016/j.memsci.2020.118630.
[48] L. Wang, M. Fang, J. Liu, J. He, J. Li, J.J.A.a.m. Lei, interfaces, Layer-by-layer fabrication of high-performance polyamide/ZIF-8 nanocomposite membrane for nanofiltration applications, 7(43) (2015) 24082-24093.
[49] A. Karimi, A. Khataee, M. Safarpour, V.J.S. Vatanpour, P. Technology, Development of mixed matrix ZIF-8/polyvinylidene fluoride membrane with improved performance in solvent resistant nanofiltration, 237 (2020) 116358.
[50] B. Zhao, X. Long, H. Wang, L. Wang, Y. Qian, H. Zhang, C. Yang, Z. Zhang, J. Li, C.J.C. Ma, S.A. Physicochemical, E. Aspects, Polyamide thin film nanocomposite membrane containing polydopamine modified ZIF-8 for nanofiltration, 612 (2021) 125971.
[51] S. Basu, M.J.S. Balakrishnan, P. Technology, Polyamide thin film composite membranes containing ZIF-8 for the separation of pharmaceutical compounds from aqueous streams, 179 (2017) 118-125.
[52] L. Yang, Z. Wang, J.J.J.o.m.s. Zhang, Zeolite imidazolate framework hybrid nanofiltration (NF) membranes with enhanced permselectivity for dye removal, 532 (2017) 76-86.
[53] Y.-y. Zhao, Y.-l. Liu, X.-m. Wang, X. Huang, Y.F. Xie, Impacts of Metal–Organic Frameworks on Structure and Performance of Polyamide Thin-Film Nanocomposite Membranes, ACS Applied Materials & Interfaces 11(14) (2019) 13724-13734. https://doi.org/10.1021/acsami.9b01923.
[54] J. Yuan, W.-S. Hung, H. Zhu, K. Guan, Y. Ji, Y. Mao, G. Liu, K.-R. Lee, W. Jin, Fabrication of ZIF-300 membrane and its application for efficient removal of heavy metal ions from wastewater, Journal of Membrane Science 572 (2019) 20-27. https://doi.org/https://doi.org/10.1016/j.memsci.2018.10.080.
[55] S. Wang, J. Liu, B. Pulido, Y. Li, D. Mahalingam, S.P. Nunes, Oriented Zeolitic Imidazolate Framework

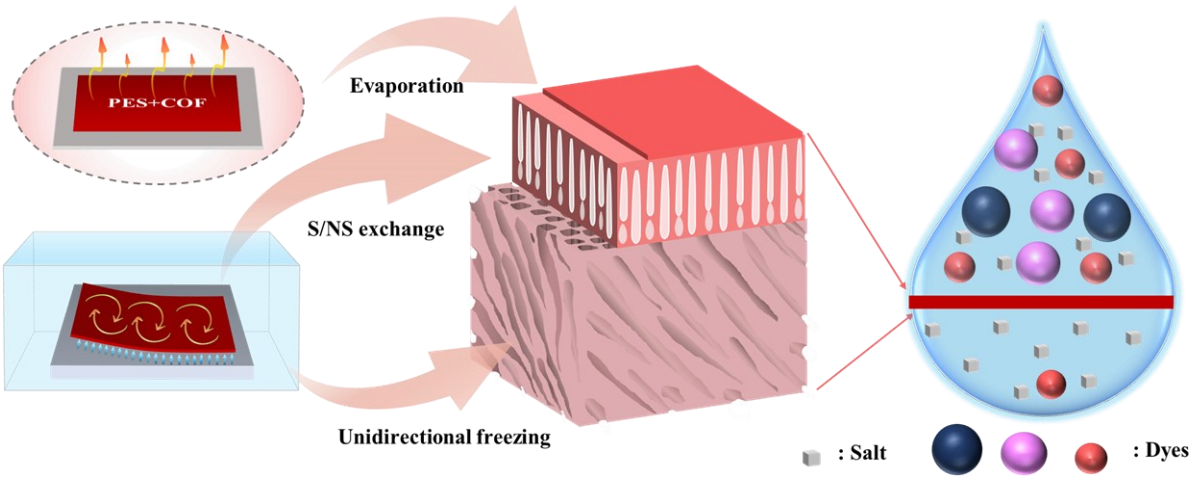
(ZIF) Nanocrystal Films for Molecular Separation Membranes, ACS Applied Nano Materials 3(4) (2020) 3839-3846. https://doi.org/10.1021/acsanm.0c00570.
[56] X. Wang, L. Zhai, Y. Wang, R. Li, X. Gu, Y.D. Yuan, Y. Qian, Z. Hu, D. Zhao, Improving Water-Treatment Performance of Zirconium Metal-Organic Framework Membranes by Postsynthetic Defect Healing, ACS Applied Materials & Interfaces 9(43) (2017) 37848-37855. https://doi.org/10.1021/acsami.7b12750.
[57] Y. Xu, X. Zhao, R. Chang, H. Qu, J. Xu, J. Ma, Designing heterogeneous MOF-on-MOF membrane with hierarchical pores for effective water treatment, Journal of Membrane Science 658 (2022) 120737. https://doi.org/https://doi.org/10.1016/j.memsci.2022.120737.
[58] Y. He, Y.P. Tang, D. Ma, T.-S. Chung, UiO-66 incorporated thin-film nanocomposite membranes for efficient selenium and arsenic removal, Journal of Membrane Science 541 (2017) 262-270. https://doi.org/https://doi.org/10.1016/j.memsci.2017.06.061.
[59] Q. Yu, Y. Zhou, C. Gao, UiO-66 regulated thin-film nanocomposite membranes for water treatment, Desalination 587 (2024) 117917. https://doi.org/https://doi.org/10.1016/j.desal.2024.117917.
[60] K. Wang, Y. Qin, S. Quan, Y. Zhang, P. Wang, H. Liang, J. Ma, X.Q. Cheng, Development of highly permeable polyelectrolytes (PEs)/UiO-66 nanofiltration membranes for dye removal, Chemical Engineering Research and Design 147 (2019) 222-231. https://doi.org/https://doi.org/10.1016/j.cherd.2019.05.014.
[61] P. Zhao, R. Li, W. Wu, J. Wang, J. Liu, Y. Zhang, In-situ growth of polyvinylpyrrolidone modified Zr-MOFs thin-film nanocomposite (TFN) for efficient dyes removal, Composites Part B: Engineering 176 (2019) 107208. https://doi.org/https://doi.org/10.1016/j.compositesb.2019.107208.
[62] F. Xiao, M. Cao, R. Chu, X. Hu, W. Shi, Y. Chen, Novel Perylene-3, 4, 9, 10-tetracarboxylic dianhydride modified Zr-MOFs/Graphene oxide membrane for dye wastewater treatment, Journal of Colloid and Interface Science 610 (2022) 671-686. https://doi.org/https://doi.org/10.1016/j.jcis.2021.11.113.
[63] X.-H. Ma, Z. Yang, Z.-K. Yao, Z.-L. Xu, C.Y. Tang, A facile preparation of novel positively charged MOF/chitosan nanofiltration membranes, Journal of Membrane Science 525 (2017) 269-276. https://doi.org/https://doi.org/10.1016/j.memsci.2016.11.015.
[64] Y.S. Meng, L. Shu, L. Liu, Y.Q. Wu, L.H. Xie, M.J. Zhao, J.R. Li, A high-flux mixed matrix nanofiltration membrane with highly water-dispersible MOF crystallites as filler, Journal of Membrane Science 591 (2019). https://doi.org/10.1016/j.memsci.2019.117360.
[65] Y. Meng, L. Shu, L.-H. Xie, M. Zhao, T. Liu, J.-R. Li, High performance nanofiltration in BUT-8(A)/PDDA mixed matrix membrane fabricated by spin-assisted layer-by-layer assembly, Journal of the Taiwan Institute of Chemical Engineers 115 (2020) 331-338. https://doi.org/https://doi.org/10.1016/j.jtice.2020.10.032.
[66] T. Li, Y. Ren, D. Wu, W. Zhang, M. Shi, C. Ji, L. Lv, M. Hua, W. Zhang, A novel water-stable two-dimensional zeolitic imidazolate frameworks thin-film composite membrane for enhancements in water permeability and nanofiltration performance, Chemosphere 261 (2020) 127717. https://doi.org/https://doi.org/10.1016/j.chemosphere.2020.127717.
[67] A. Maraddi, M. Halakarni, M. Manohara Halanur, S.K. Nataraj, Fe-MOF induced biopolymer-based sustainable self-cleaning membranes for effective selective separation and wastewater treatment, Sustainable Materials and Technologies 35 (2023) e00537. https://doi.org/https://doi.org/10.1016/j.susmat.2022.e00537.
[68] W. Dong, J. Yan, T. Ji, M. Wu, Y. Sun, Y. He, X. Li, K. Yu, B. Sun, Y. Liu, Room temperature aqueous synthesis of defect-engineered MOF-801 membrane towards efficient nanofiltration, Journal of Membrane Science 705 (2024) 122946. https://doi.org/https://doi.org/10.1016/j.memsci.2024.122946.
[69] M. Wu, Y. Sun, T. Ji, K. Yu, L. Liu, Y. He, J. Yan, S. Meng, W. Hu, X. Fan, D. Du, Y. Liu, Fabrication of water-stable MOF-808 membrane for efficient salt/dye separation, Journal of Membrane Science 686 (2023) 122023. https://doi.org/https://doi.org/10.1016/j.memsci.2023.122023.
[70] L. Fei, C. Chen, L. Shen, Y. Zhang, B. Wang, J. Xu, B. Li, S. Raza, H. Lin, Graphene oxide assisted assembly of superhydrophilic MOF-based membrane with 2D/3D hybrid nanochannels for enhanced water purification, Chemical Engineering Journal 460 (2023) 141694. https://doi.org/https://doi.org/10.1016/j.cej.2023.141694.
[71] H. Yuan, K. Li, D. Shi, H. Yang, X. Yu, W. Fan, P.J.S. Buenconsejo, D. Zhao, Large-Area Fabrication of Ultrathin Metal-Organic Framework Membranes, 35(18) (2023) 2211859. https://doi.org/https://doi.org/10.1002/adma.202211859.
[72] Y.B. Chen, H.Q. Liu, X.Y. Hu, B.W. Cheng, D.Q. Liu, Y.F. Zhang, S. Nair, PVDF/Cu-BTC Composite Membranes for Dye Separation, Fibers and Polymers 18(7) (2017) 1250-1254. https://doi.org/10.1007/s12221-017-6814-7.
[73] P. Cheng, Y. Huang, C. Wu, X. Wang, X. Fu, P. Li, Y. Liu, S. Xia, Two-dimensional metal−porphyrin framework membranes for efficient molecular sieving, Journal of Membrane Science 640 (2021) 119812.

https://doi.org/https://doi.org/10.1016/j.memsci.2021.119812.
[74] J.H. Cai, S.Z. Song, L.J. Zhu, Q.P. Lu, Z. Lu, Y.Y. Wei, H.H. Wang, Two-dimensional Cu-porphyrin nanosheet membranes for nanofiltration, Nano Research 16(5) (2023) 6290-6297. https://doi.org/10.1007/s12274-023-5447-y.
[75] Z.K. Tan, J.L. Gong, S.Y. Fang, J. Li, W.C. Cao, Z.P. Chen, Outstanding anti-bacterial thin-film composite membrane prepared by incorporating silver-based metal-organic framework (Ag-MOF) for water treatment, Applied Surface Science 590 (2022). https://doi.org/10.1016/j.apsusc.2022.153059.
[76] L. Han, J. Ma, H. Lin, C. Chen, J. Teng, B. Li, D. Zhao, Y. Xu, W. Yu, L. Shen, A novel flower-like nickel-metal-organic framework (Ni-MOF) membrane for efficient multi-component pollutants removal by gravity, Chemical Engineering Journal 470 (2023) 144311. https://doi.org/https://doi.org/10.1016/j.cej.2023.144311.
[77] Q. Bian, M. Zhang, Y. Liu, L.L. Liu, Y. Li, C. Wang, G.H. He, Layered Double Hydroxide-Assisted Fabrication of Prussian Blue Membranes for Precise Molecular Sieving, Angewandte Chemie-International Edition 61(1) (2022). https://doi.org/10.1002/anie.202113662.

# Chapter 5: Loose Nanofiltration PES/DABA-TFP Membrane Fabricated by NIPS-CCD Method with Ultrapermeable Selectivity for Dye/Salt Separation

## 5.1 Abstract

Covalent organic frameworks (COFs) have emerged as promising nanofillers for fabricating high-performance membranes when combined with polymeric matrices. However, COF-based mixed matrix membranes (MMMs) usually exhibit low permeance due to the inherent limitations of polymeric matrices produced via the conventional nonsolvent-induced phase inversion (NIPS) process. Moreover, these membranes often suffer from poor uniformity because of agglomeration. Here, we develop an ultrapermeable loose nanofiltration (LNF) membrane with excellent antifouling properties from an in-situ dissolved polyethersulfone (PES) in a colloidal COF using a recently developed approach that combines NIPS with the combined crystallisation and diffusion (CCD) technique, named NIPS-CCD. The integration of the anionic COF, DABA-TFP not only imparted a negative charge to the membrane but also enhanced the membrane hydrophilicity. Performance tests involving dye-salt separation revealed a molecular weight cut-off (MWCO) for dyes of approximately 800-1000 Da while maintaining high salt permeability. Notably, the water permeance of the COF-enhanced PES membranes was 10~100 times greater than that of commercial LNF membranes, with a fouling recovery ratio exceeding 80%. This study offers a promising approach for manufacturing COF-incorporated membranes for loose nanofiltration applications.




**Keywords:** DABA-TFP COF, Polyethersulfone; Loose nanofiltration; NIPS-CCD; Dye/salt separation

## 5.2 Introduction

The integration of crystalline frameworks into polymeric matrices has emerged as a promising strategy in fabricating defect-free MOF/COF-based membranes, effectively addressing the persistent challenge of mitigating intrinsic non-selective defects that arises during the synthesis of pure MOFs or COFs membranes [1]. In comparison to MOFs, COFs consist of covalently bonded lighter elements, such as carbon, oxygen, nitrogen, and boron, imparting them with a fully organic nature and superior chemical compatibility with polymeric matrices [2, 3]. Considering their ordered pore structures with tuneable pore sizes ranging from 0.5 to 4.7 nm, COFs hold distinctive promise for nanofiltration (NF) and loose nanofiltration applications (LNF), where their incorporation is anticipated to facilitate enhanced molecular selectivity [4]. Additionally, the construction of COF-contained NF/LNF membrane have exhibited great potential in improving the permeance, antifouling properties and structural robustness of NF membranes [5-8].

The intrinsic porosity of frameworks can promote the overall porosity of MMMs membrane, thereby improving selective permeance. For example, a significant increase of permeance reaching 300% was found in COF-LZU1-contained PVA film due to the extra mass transport channels provided [9]. Additionally, COF-containing MMMs demonstrate superior antifouling performance due to the modifications in surface charge and hydrophilicity [6]. Surface charge plays a critical role in antifouling behaviour by regulating interactions between the membrane surface and fouling agents such as proteins, bacteria, and other microorganisms. Negatively charged surfaces generally repel microorganisms with similarly charged cell walls, thereby reducing adhesion, whereas positively charged surfaces tend to attract them via electrostatic interactions, leading to increased fouling. This phenomenon is particularly evident in the reduced attachment of proteins and bacterial cells to negatively charged membranes where the electrostatic repulsion serves as a protective antifouling barrier [7]. Moreover, COFs contribute to the mechanical robustness of MMMs through their rigidity which binds polymeric matrix [8]. Their covalently bonded frameworks further enhance thermal resistance, enabling the membranes to maintain functionality at elevated temperatures and various operational conditions. Despite these advantages, several challenges remain in the development of high-performance COF-based MMMs for LNF and NF applications.

One primary limitation arises from the intrinsically low porosity of polymeric matrices, which restricts the full utilization of the high porosity offered by COFs. The industrial applicability of LNF technology is evidenced by membrane products such as ENTA 01PP, NP030, and GE, which are predominantly manufactured using the nonsolvent-induced phase inversion (NIPS) technique [10-13]. Within this domain, polyethersulfone (PES) is a primary material of choice owing to its high thermal and chemical resistance, low cost, and flexibility [14]. Typical examples include NP030 and NP010 by Microdyn

Nadir, which have molecular weight cut-off (MWCO) values of approximately 1000 and 500 Dalton, respectively. However, their relatively low permeance of these membranes at 5 and 1 $LMHBar^{-1}$ [15] , is primarily attributed to the presence of limited interconnected pores, which severely undermines the benefits conferred by COF integration.

To address this issue, we recently developed the NIPS-CCD technique, a simple, one-step membrane fabrication method that combines the strength of both NIPS and combined crystallisation and phase inversion (CCD) techniques. This innovative method leverages the superior pore connectivity from the CCD structure to replace the closed and less permeable backside of a NIPS-made PES membrane. This structural alteration leads to a 50-fold increase in the PWP to 677 $LMHBar^{-1}$ while maintaining the surface pore size in the 6~7 nm range, rendering it highly suitable for ultrafiltration applications. To adapt the NIPS-CCD technique for LNF membrane fabrication, a tighter skin layer is required to filter out dye molecules with sizes between 0.5 and 2 nm. One feasible method is through dry/wet phase inversion [16], where delayed post-casting allows the evaporation of volatile cosolvent, creating a high polymer concentration at the skin layer. The subsequent wet step in a nonsolvent bath yields a membrane with a tight skin layer and a porous supporting structure [17]. Agnieszka K. Hołda et al. investigated the influence of volatile cosolvent and evaporation time on the microstructure and separation performance of a nanofiltration membrane. They found that a 2-minute evaporation period increased Rose Bengal rejection from 47% to 76%, albeit with a significant decrease in permeance from 2.38 to 0.07 $LMHBar^{-1}$ [18]. This combined technique is promising to overcome the inherent limit of polymer matrix when constructing COF-contained MMMs.

Another concern stems from the tendency of COFs nanosheets to form aggregation-prone structures, complicating their processing into defect-free membranes. The typical fabrication process for MMMs involves several key steps, including the preparation of a mixed suspension, deposition onto a substrate via casting or spin-coating, and subsequent solvent removal through phase inversion or evaporation. COFs are generally introduced into the casting solution either before or after the polymer is fully dissolved. [19]. However, agglomeration of COFs is inevitable during the purification and collection of the synthesized COFs due to the π-π interactions and van der Waals forces [20]. Such aggregation not only hinders their redispersion in solution but also makes it exceedingly difficult to achieve a homogeneous dispersion within a viscous polymer matrix. Thus, a uniform distribution of COFs in MMMs would be obtained, significantly undermining their potential benefits by introducing defects, reducing permeance, increasing fouling susceptibility, and compromising mechanical stability.

The combination of the synthesis of COFs and the mixing with polymers provide a promising solution to obtain a homogeneous casting solution and thus a uniform MMMs. Recent advancements in COF synthesis involve a single solution-phase technique in which positively/negatively charged COFs are effectively crystallised with exceptional suspensibility and high volume yield in organic solvents [21]. A

notable example is the synthesis of DABA-TFP nanosheets, which are achieved by homogeneously polymerising anionic 2,5-diaminobenzenesulfonic acid (DABA) with 1,3,5-triformylphloroglucinol (TFP) in dimethyl sulfoxide (DMSO). The formation of the DABA-TFP nanosheets results in only a colour change rather than any precipitation, indicating excellent dispersion of the COF nanosheets in DMSO. This finding illuminates the potential of using DMSO, given its efficacy as a solvent in PES membrane preparation, for homogeneously integrating COF fillers into the membrane casting solution. Furthermore, the negatively charged pore surface of DABA-TFP is expected to enhance the rejection of charged pollutants and improve fouling resistance in the membrane.

The aim of the present study is to develop a PES-based LNF membrane that combines high PWP, exceptional dye/salt separation capacity, and robust fouling resistance. To achieve this goal, a PES-based membrane was fabricated using the innovative NIPS-CCD process with a casting suspension prepared by in situ dissolution of PES in a DABA-TFP/DMSO colloid. A dense skin layer, which is crucial for the sieving effect, was created through a dry phase separation process induced by the evaporation of tetrahydrofuran (THF) before casting. This evaporation-assisted NIPS-CCD approach not only imparted PES membrane nanofiltration selectivity but also created highly interconnected pores in the membrane cross section. Overall, a series of PES LNF membranes with a high permeance of up to 315 $LMHBar^{-1}$ were successfully fabricated. The incorporation of DABA-TFP further increased the hydrophilicity and charge density of the membrane, significantly enhancing its fouling resistance and dye rejection. The membrane exhibited a high dye/salt separation performance, as evidenced by the rejection rates of methyl blue (98.00%), rose bangle (93.41%), and $MgSO_4$ (4.90%). Furthermore, this study compared two blending strategies for preparing PES-COF membranes, and the respective membrane performances were evaluated and discussed in detail.

## 5.3 Material and Methods

### 5.3.1 Material and membrane fabrication

To synthesize COFs, 1,3,5-triformylphloroglucinol (TFP, 97%) and 2,5-diaminobenzenesulfonic acid (DABA, 99%) were purchased from Sigma-Aldrich. Polyethersulfone (PES, Radel® A300, $\rho = 1.37$ g $cm^{-3}$) was obtained from Ameco Performance, USA. Tetrahydrofuran (THF, 99%), n-hexane (99%), and dimethyl sulfoxide (DMSO, 99%) were purchased from VWR International, LLC. Details of other chemicals can be found in Section 3.1.

### 5.3.2 Synthesis of DABA-TFP in single solution-phase

The DABA-TFP was prepared following the methodology outlined in Section 3.3.2 and schematical illustration in Figure 5.1.

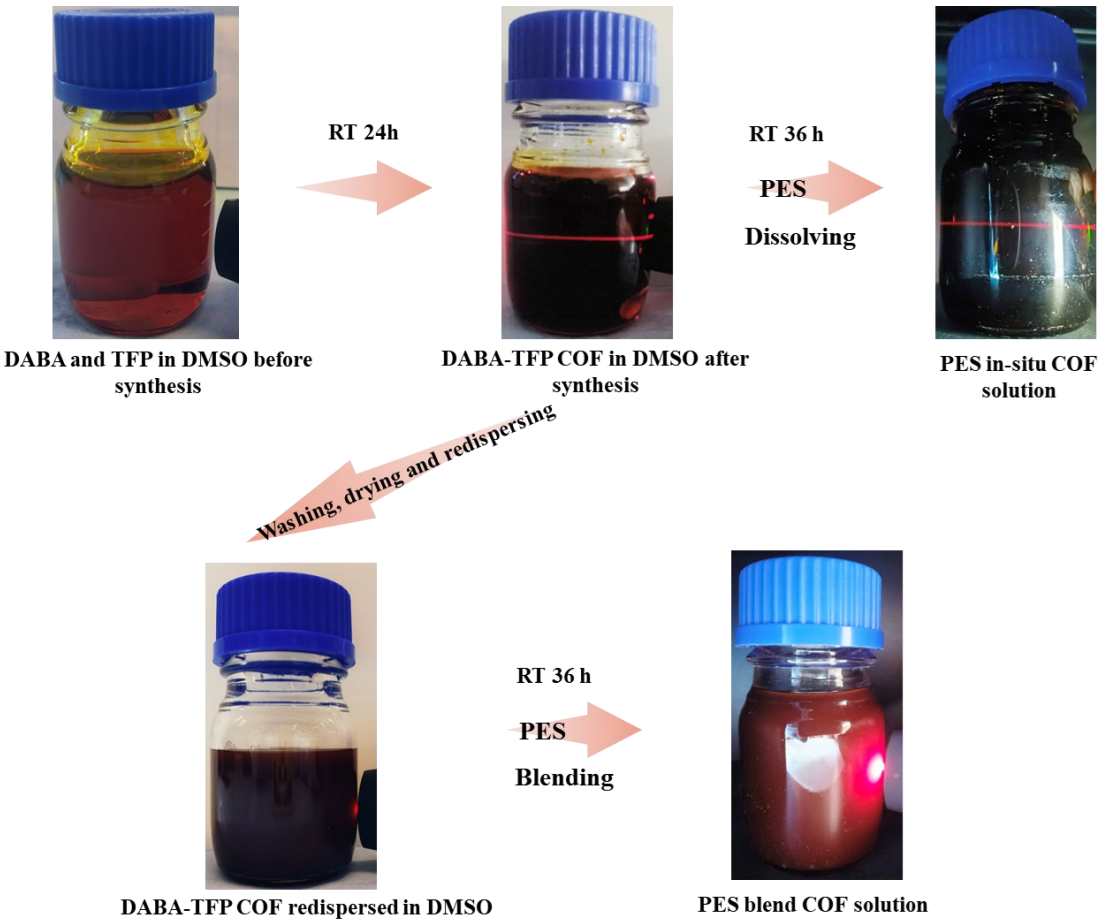



Figure 5.1 Preparation strategies of PES in-situ COF and COF blend COF casting solutions.

### 5.3.3 Preparation of casting solutions

Three solutions, the pure PES solution, PES in-situ COF solution and PES blend COF solution were utilized for membrane casting. Detailed preparation methods and compositions were introduced in Section 3.3.2 and Table 5.1. The casting solutions prepared by PES in-situ COF solution and COF blend COF casting solution are displayed in Figure 5.1.

The detailed composition of each solution is tabulated in Table 5.1:

Table 5.1. The composition of casting solutions.

| Solution | DMSO and THF (wt%) | PES (wt%) | In-situ synthesized DABA-TFP (wt%) | Physical blended DABA-TFP* (wt%) |
|---|---|---|---|---|
| Pure PES | 80 | 20 | | / |
| PES physical blending COF (PES blend COF) | 77.12 | 20 | | 2.88 |
| PES in-situ dissolving COF (PES in-situ COF) | 77.12 | 20 | / | / |

* The concentration of DABA-TFP was the same as that in the PES in-situ COF solution by calculating the yield of COF nanosheet after synthesis.

### 5.3.4 Membrane fabrication methods

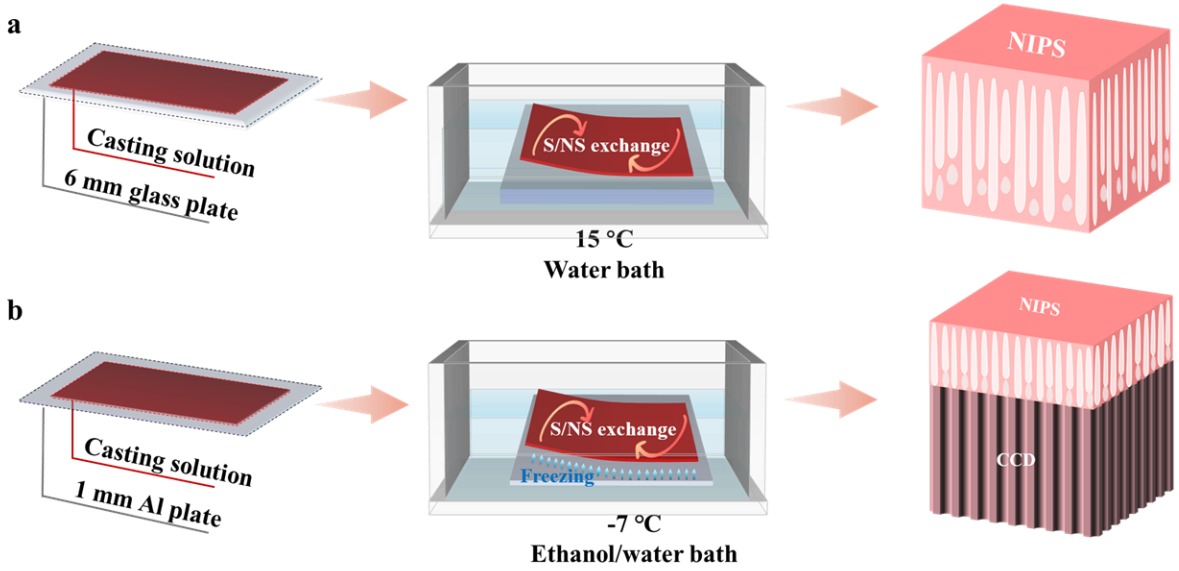



Figure 5.2 Schematic illustration of membrane casting with (a) NIPS and (b) NIPS-CCD method.

Membranes were fabricated with four methods described detailly in Section 3.3.3 and Table 5.2. These methods include NIPS method (Figure 5.2 a), NIPS-CCD method (Figure 5.2 b, NIPS-CCD Eva method, and NIPS-CCD Eva THF method (Figure 5.3).

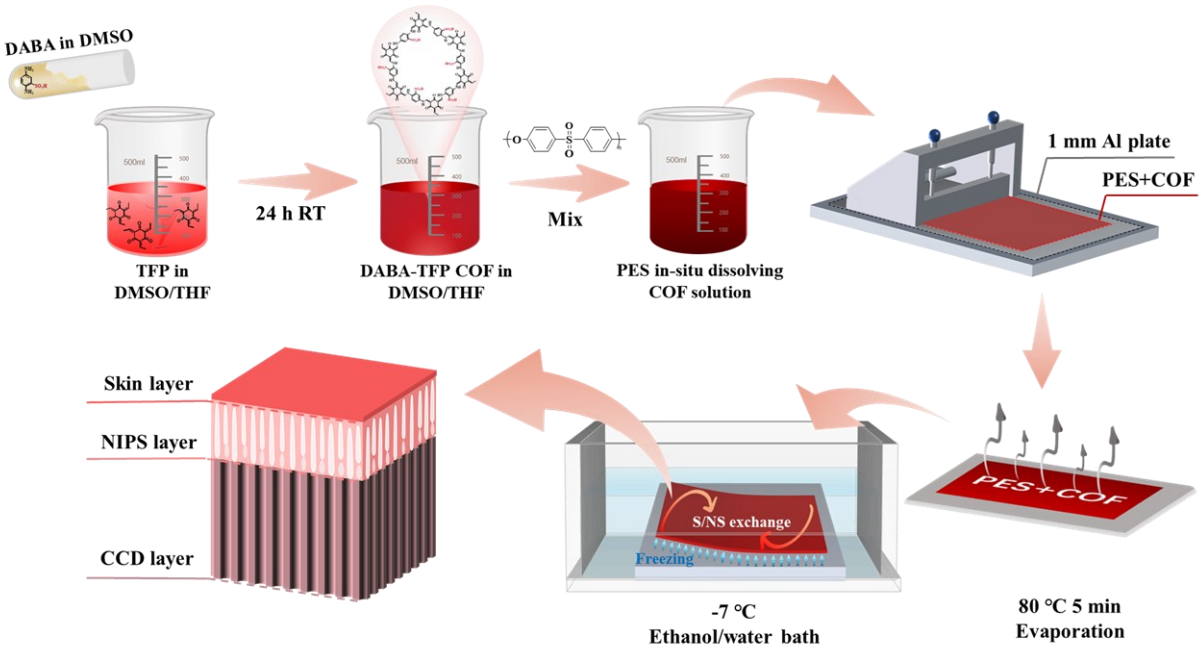



Figure 5.3 Schematic illustration of NIPS-CCD Eva THF method using PES in-situ COF solution.

The parameters for each fabrication method are detailed and listed in Table 5.2.

Table 5.2 Manufacturing conditions for as-prepared membranes.

| Name | Casting plate | Co-solvent | Evaporation time (min) | Coagulation* temperature (°C) |
|---|---|---|---|---|
| NIPS | 6 mm glass | / | / | 15 |
| NIPS-CCD | 1 mm aluminium | / | / | -7 |
| NIPS-CCD Eva | 1 mm aluminium | / | 5 | -7 |
| NIPS-CCD Eva THF | 1 mm aluminium | THF (4 wt%) | 5 | -7 |

* The coagulation bath for NIPS membrane was DI wate

### 5.3.5 Characterizations and performance test

Characterizations conducted in this chapter include SEM, EDX, FTIR, AFM, DSC, zeta potential, and XRD, with detailed descriptions available in Section 3.4. Additionally, molecular weight cut-off and pore size distribution, nanofiltration performance, BSA fouling performance, and mechanical performance were evaluated as described in Sections 3.4.9, 3.4.11, 3.4.10, and 3.4.7, respectively.

## 5.4 Results and Discussion

### 5.4.1 Membrane structure and physicochemical properties

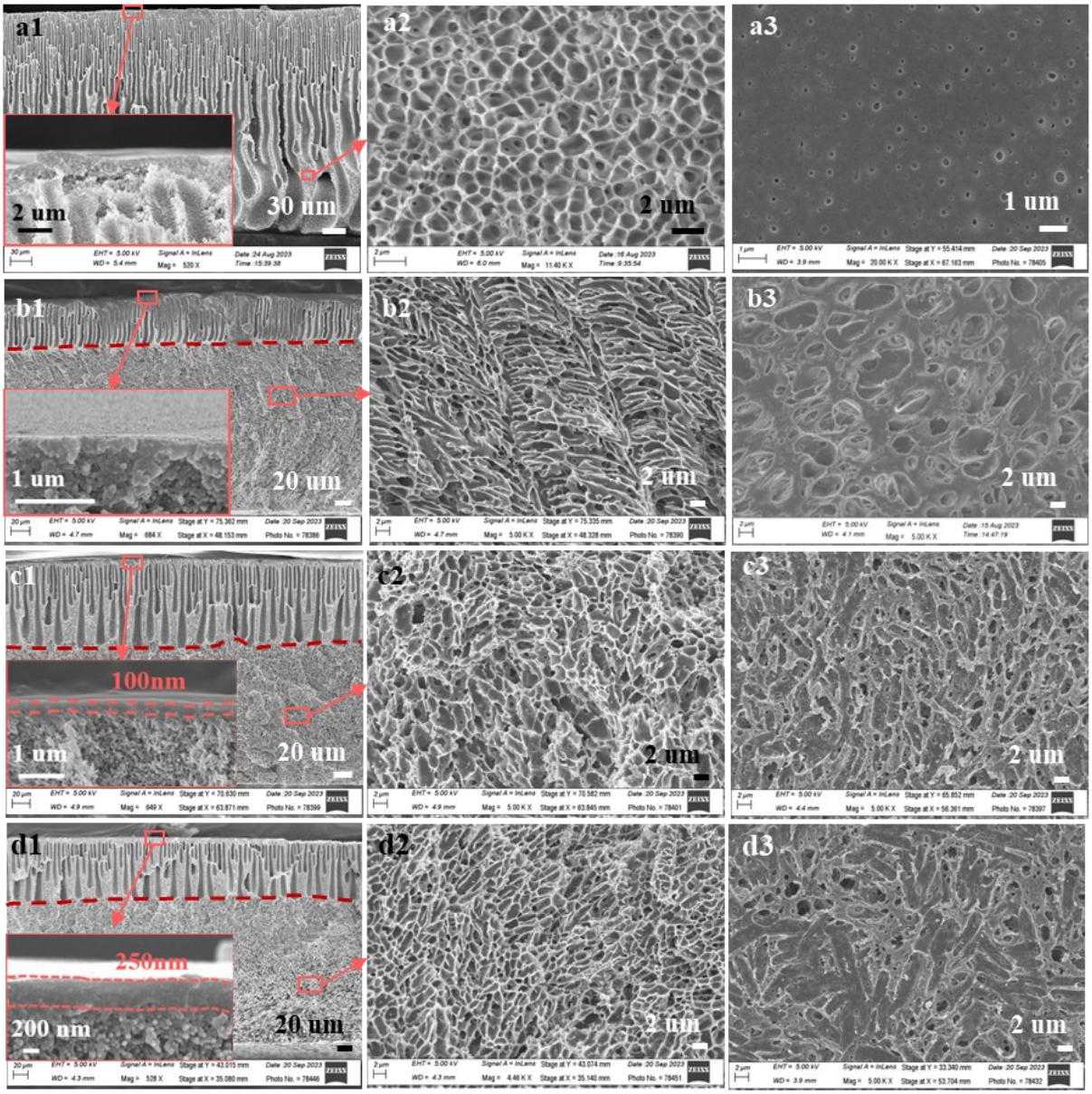



Figure 5.4 SEM images and SEM-EDX results of PES in-situ COF membranes. SEM images were taken for membranes fabricated by (a) NIPS, (b) NIPS-CCD, (c) NIPS-CCD Eva and (d) NIPS-CCD Eva THF methods. -1) The overall cross-section of the corresponding membrane; the inset shows an enlarged top section close to the NIPS side taken from the selected area; the red dotted lines divide the NIPS and CCD domains of the membrane; -2) the magnified CCD/bottom view of the selected section in -1); -3) the bottom surface morphology of the membranes.

Figure 5.4 shows the morphology of PES in-situ COF membranes fabricated under different conditions. As shown in Figure 5.4 a, the membrane cast on a glass plate and coagulated in a water bath at ambient temperature inherited a typical NIPS morphology, featuring a finger-like structure and a thick bottom layer. These finger-like pores were formed due to instantaneous phase inversion resulting from the high affinity between water and DMSO. The bottom section of the membrane was composed of discrete pores

(Figure 5.4 a2). This leads to the formation of a dense bottom layer with low surface porosity (Figure 5.4 a3), which may significantly hinder water transport. In contrast, for the NIPS-CCD membranes presented in Figure 5.4 b, the finger-like structure was connected by interconnected microchannels typical of CCD morphology (Figure 5.4 b2). These channels opened at the bottom surface of the membrane, forming macropores with high porosity (Figure 5.4 b3). The simultaneous formation of the NIPS and CCD structures occurs when the aluminium casting plate is immersed in a cold coagulation bath, such that the NIPS process initiates at the S/NS interface, while the CCD process commences from the opposite surface next to the casting plate due to the unidirectional freezing of the solvent. A detailed explanation can be found in our previous report and is schematically demonstrated here in Figure 5.3 [22].

The NIPS and CCD effects from the two sides of the membrane surface showed competitive behaviour depending on the fabrication conditions. For the NIPS-CCD method, the use of a thin aluminium casting plate and a low coagulation temperature (-7°C) initiated rapid crystallisation of DMSO from the surface of the casting plate. Consequently, the cross-section of the NIPS-CCD membrane was dominated by CCD-type microchannels (Figure 5.4 b1). In contrast, if evaporation occurred prior to the phase inversion process, as shown in Figure 5.4 c1 and d1, the whole system was heated; hence, the freezing rate of DMSO was delayed, and the subsequent growth of the CCD domain was suppressed.

As indicated by Figure 5.5 a, b, the NIPS and NIPS-CCD membranes had identical separation surface morphologies and were covered by fine nodules alongside the obvious boundaries between the nodules. Compared with the NIPS-CCD membrane, a dense skin layer of approximately 100 nm was identified after 5 min of evaporation (inset in Figure 5.4 c1), and a thicker layer of 250 nm was formed after the addition of volatile THF as a cosolvent (inset in Figure 5.4 d1). The formation of the skin layer also reduced the S/NS exchange, which is responsible for the enlargement of finger-like pores beneath the surface [23]. As observed from the top of the separation layer, as shown in Figure 5.5 c and Figure 5.5 d, continuous surfaces with finer distributed nodules were formed after the evaporation of solvents. These denser separation layers make high selectivity possible.

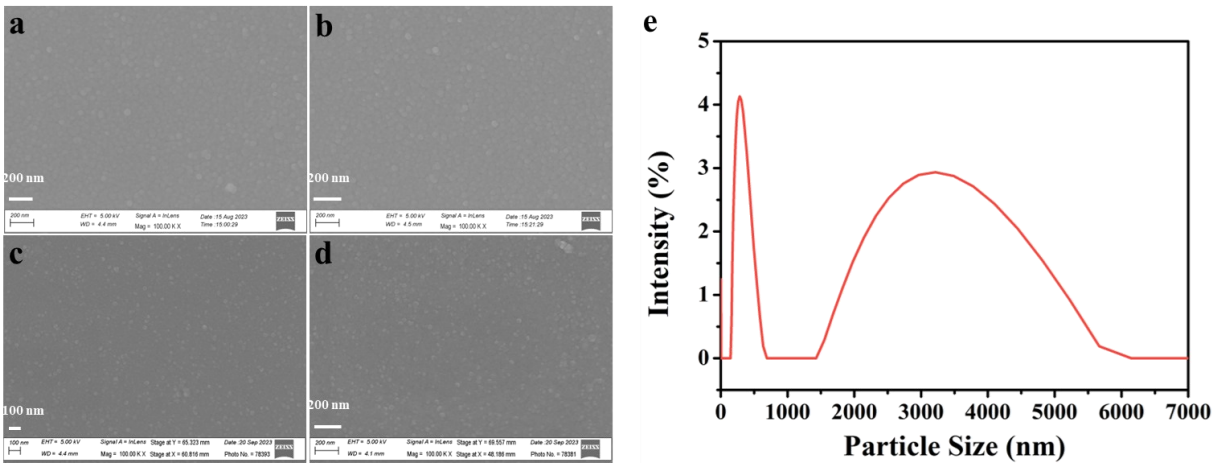


Figure 5.5 Morphology of membrane surfaces and flake size distribution of DABA-TFP nanosheets. NIPS surface morphology of PES in-situ COF membranes fabricated by (a) NIPS, (b) NIPS-CCD, (c) NIPS-CCD Eva and (d) NIPS-CCD Eva THF method. (e) Size distribution of DABA-TFP CO measured by dynamic laser scattering (DLS).

Notably, no agglomeration of DABA-TFP nanosheets was observed in membranes prepared using PES in-situ COF solution. To assess the distribution of DABA-TFP, elementary mappings were constructed, as shown in Figure 5.6 a, b. The uniform distribution of nitrogen atoms implies a homogeneous colloid of DABA-TFP nanosheets in the membrane casting solution. The DABA-TFP nanosheets, synthesised via a single solution phase, formed a dark red colloid in DMSO and exhibited a distinct Tyndall effect (Figure 5.1). The average size of these nanosheets was approximately at 3.1 μm (Figure 5.5 e). After in-situ dissolution of PES, the transparency of the colloid decreased, yet it still maintained a clear laser scattering path, indicating the high compatibility between PES and DABA-COF in DMSO (Figure 5.1). However, the behaviours of the colloids in the PES blend COF solutions were markedly different. The freeze-dried DABA-COF nanosheets could not be completely redispersed in DMSO, resulting in an opaque suspension after blending with PES (Figure 5.1).

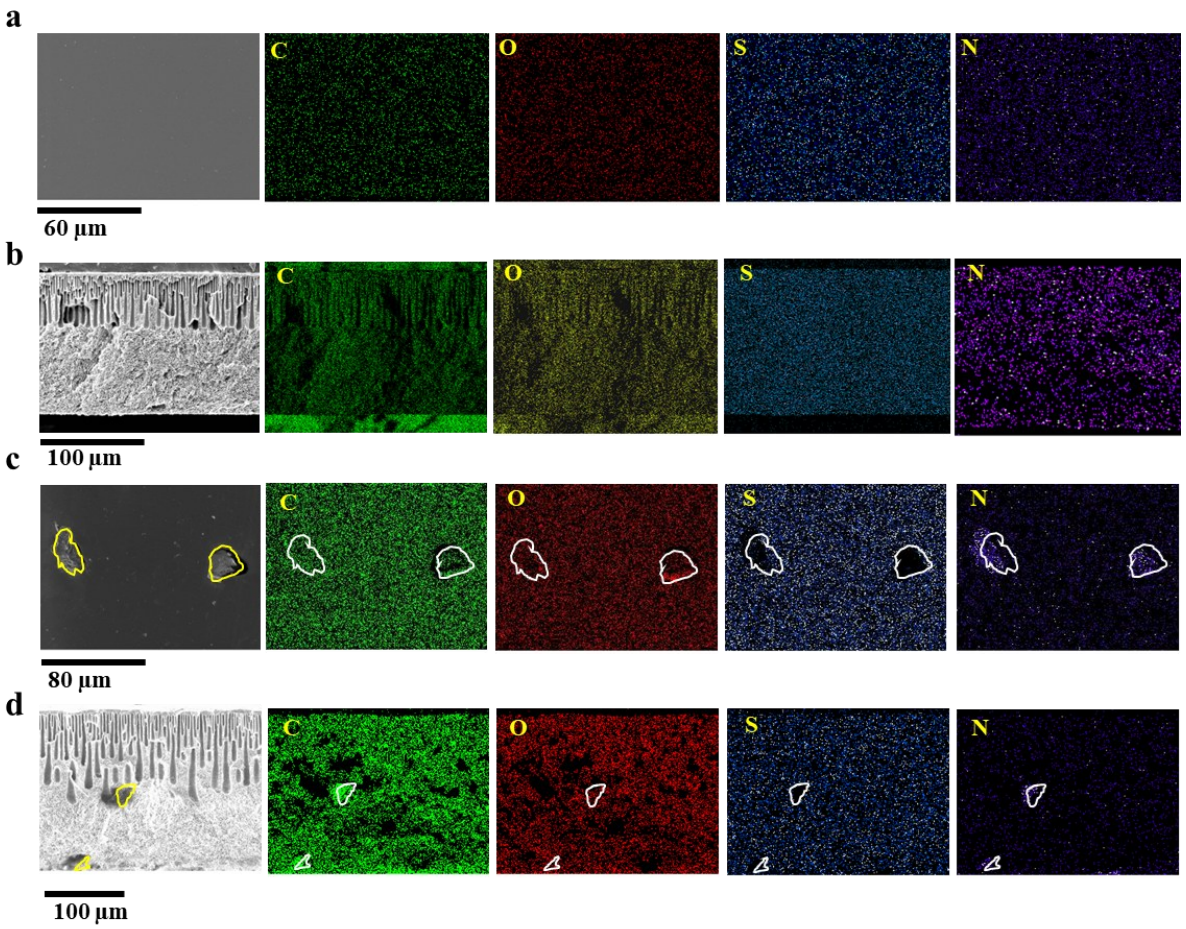


Figure 5.6 SEM-EDX images of the NIPS-CCD Eva membrane with the elemental map of C, O, S, and N. Surface and cross-sectional mapping of membranes prepared by (a, b) PES blend COF solution and (c, d) PES in-situ COF solution, respectively.

Elemental mappings of the resultant PES membranes revealed this inhomogeneity, as shown in Figure 5.6 c, d, where crumpled sheets with varying shapes were observed. These sheets, identified as DABA-TFP due to their strong unique nitrogen signal, indicated that the freeze-dried DABA-TFP nanosheets failed to disperse homogeneously in the PES solution. During the washing and subsequent freeze-dry processes after synthesis, the COF nanosheets self-assemble, forming crumpled sheets larger than 20 μm [21]. This agglomeration likely compromised the uniformity of redispersion, potentially affecting the membrane performance.

Surface roughness plays a crucial role in determining the antifouling properties of membranes [24]. Figure 5.7 presents 3D AFM images of different membranes, illustrating variations in surface morphology. The non-uniform distribution of DABA-TFP COF in the PES blend COF solution resulted in increased surface roughness, as indicated by the higher root mean square ($R_q$) value of the DABA-TFP Eva THF membrane prepared with the PES blend COF solution (2.3 nm, Figure 5.7 b) compared to that prepared with pure PES solution (1.6 nm, Figure 5.7 a4). Despite the relatively higher surface roughness of the membrane prepared using the PES in-situ COF solution ($R_q$=1.9 nm, Figure 5.7 c) compared to the pure PES membrane prepared by the same method, this value remains significantly lower than that of the membrane fabricated with the PES blend COF solution. This suggests that the PES in-situ COF solution exhibits a relatively higher degree of homogeneity. Additionally, the fabrication method also influenced the surface roughness. As shown in Figure 5.7 a1-a4, the formation of a dense skin layer induced by the evaporation step significantly reduced surface roughness. A smoother surface is expected to enhance antifouling performance by minimizing pollutant adhesion, thereby improving membrane longevity and efficiency.

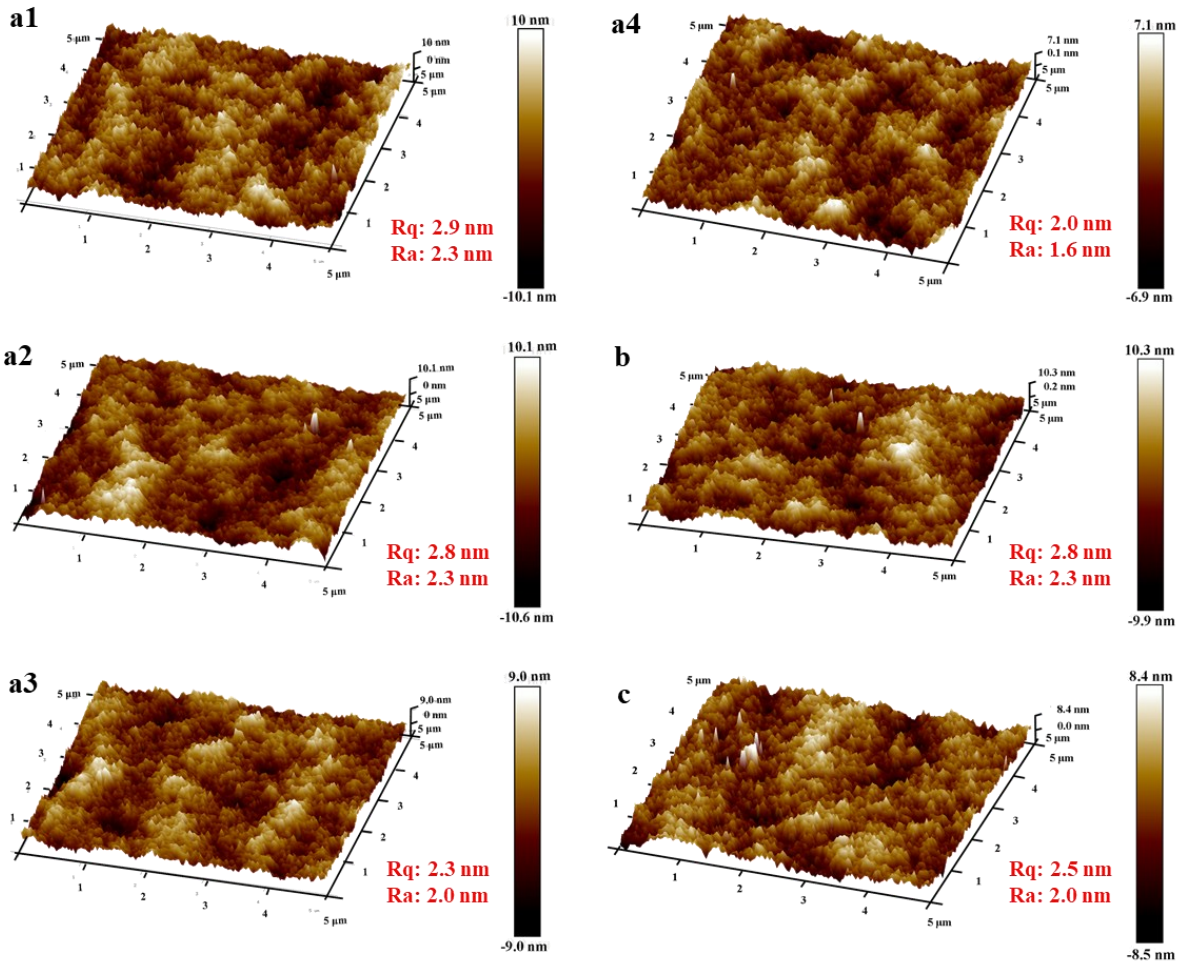



Figure 5.7 Surface roughness of membranes. (a) Pure PES membranes fabricated by NIPS (a1), NIPS-CCD (a2), NIPS-CCD Eva (a3), and NIPS-CCD Eva THF (a4). (b) PES blend COF membrane fabricated by NIPS-CCD Eva THF membrane. (c) PES in-situ COF membrane fabricated by NIPS-CCD Eva THF method.

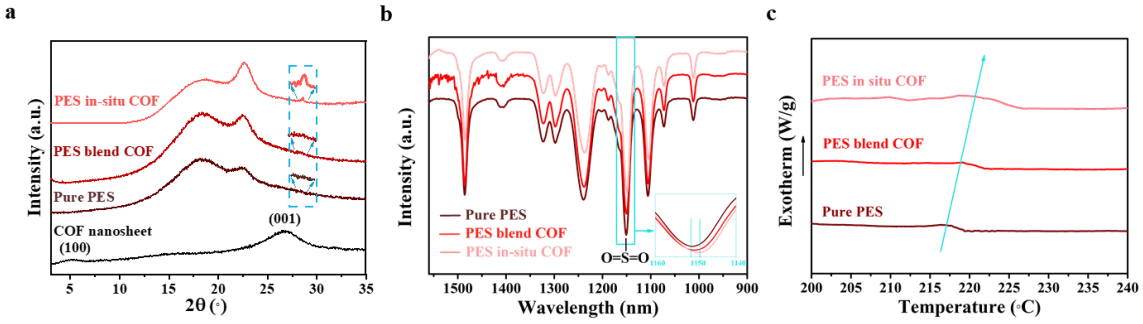



Figure 5.8 Surface chemistry and wettability of the membranes. (a) XRD patterns, (b) FTIR, (c) DSC of pure PES, PES blend COF and PES in-situ COF membranes fabricated by NIPS-CCD Eva method.

The powder X-ray diffraction (PXRD) pattern of the pure PES membrane in Figure 5.8 a shows two

broad peaks at 2θ=17.8° and 2θ=22.5°, indicating the semi-crystalline features of PES [25, 26]. The single solution-phase method used for synthesising the DABA-TFP nanosheets yielded consistent XRD diffractograms with those of a previous report [27]. These nanosheets exhibited moderate crystallinity with two feature peaks at 2θ=4.9° and 2θ=26.8°, corresponding to the (100) and (001) planes, respectively. When examining the composite, significant structural changes were observed for the PES in-situ COF membrane. The PXRD patterns highlighted by a blue dotted frame indicated a notable shift from 2θ=26.8° to 28.6° of the DABA-TFP (001) peak corresponding to the 2D layered hexagonal architecture in the polymeric network [28, 29]. The peak shifting indicated the higher number of stacked sheets and alignment of the consecutive layers bound via the π–π interactions of COF and PES. [30]. This peak shift was also accompanied by an increase in intensity and a decrease in the FWHM, suggesting that tighter molecular packing likely arose from strengthened hydrogen bonding interactions between DABA-TFP and PES [31]. Scherrer's equation supports this interpretation, indicating that a narrower FWHM correlates with shorter stacking distances and enhanced molecular interactions [32, 33].

In contrast, the unchanged intensity of the COF peak in the spectrum of the PES blend COF membrane points to weaker interactions. Further elucidation of these interactions was provided by FTIR analysis, as shown in Figure 5.8 b, which revealed a shift in the peak at 1150 $cm^{-1}$, corresponding to the symmetric tensile vibration of the O=S=O group in PES post-COF inclusion [34]. This shift implies significant intermolecular interactions, with the sulfone groups of PES acting as hydrogen bond acceptors and the -$SO_3H$ groups of DABA-TFP serving as donors, indicating that the two components interact primarily via hydrogen bonding. Moreover, the formation of hydrogen bonding led to an enhanced steric hindrance for segment movement and thus a slight increase in the glass transition temperature ($T_g$) of the PES-COF membrane (Figure 5.8 c) [35].

The surface free energy of membrane was evaluated by measuring the contact angles of different liquid probes on the surface of membranes. As listed in Table 5.3, the contact angle of the pure PES membrane was 75.6°. It decreased to 62.4° for the PES blend COF membrane and further decreased to 51.6° for the PES in-situ COF membrane. This trend is reasonable because the sulfonic acid functionality (-$SO_3H$) of DABA-TFP offers a high affinity for water molecules, and the dispersion of DABA-TFP nanosheets was better in PES in-situ COF membranes. This hypothesis was further supported by the surface energy value presented in Table 5.4 where a more than 18% higher $\boldsymbol{\gamma_S}$ of PES in-situ COF membrane was calculated. This increased surface free energy is expected to offer a higher permeation flux and antifouling resistance, which will be further discussed below.

Table 5.3 Static contact angle data of three liquid probes of different membranes fabricated by NIPS-C CD Eva method

| Membrane | $\theta_W$(°) Water | $\theta_G$(°) Glycerol | $\theta_D$(°) Diiodomethane |
|---|---|---|---|

| | | | |
|---|---|---|---|
| Pure PES | 75.6 | 51.2 | 29.2 |
| PES blend COF | 62.4 | 46.5 | 17.4 |
| PES in-situ COF | 51.6 | 40.1 | 9.8 |

Table 5.4 Surface energy components of different membranes fabricated by NIPS-CCD Eva method

| Membrane | $\gamma_S^{LW}$(mJ m$^{-2}$) | $\gamma_S^{\pm}$(mJ m$^{-2}$) | $\gamma_S^-$(mJ m$^{-2}$) | $\gamma_S$(mJ m$^{-2}$) |
|---|---|---|---|---|
| Pure PES | 44.6 | 1.8 | 2.2 | 48.5 |
| PES blend COF | 48.5 | 0.9 | 10.0 | 54.5 |
| PES in-situ COF | 49.3 | 0.9 | 18.1 | 57.3 |

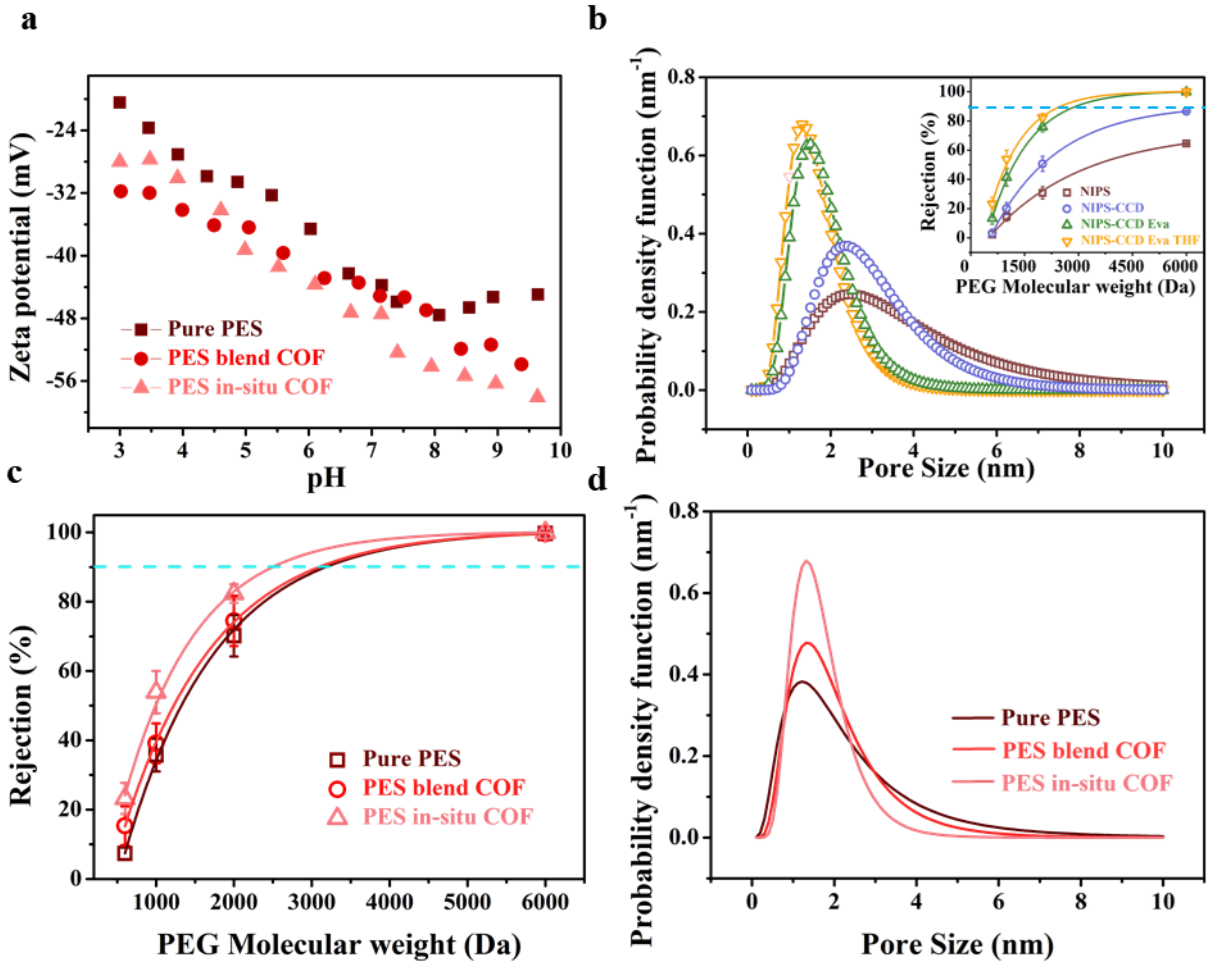



Figure 5.9 Zeta potential and pore size analyses of the membranes. (a) Zeta potential of pure PES, (b) PES blend COF and PES in-situ COF membranes fabricated by NIPS-CCD Eva method. (c) The MWCO curve and (d) the pore size distribution of membranes prepared by pure PES, PES blend COF, and PES in-situ solutions by NIPS-CCD Eva THF method.

Zeta potential analysis across a pH range of 3 to 9.5 for the pure PES and PES-COF membranes demonstrated that all the membranes maintained a negative charge, with variations correlating with the pH (Figure 5.9 a). Due to the adsorption of hydroxide ions by the pristine PES, the pure PES membrane exhibited negative charges in the test pH range. For both the PES blend COF and PES in-situ COF membranes, enhanced negative zeta potentials were obtained within the acidic domain (pH < 5). This can be attributed to the dissociation of sulfonic acid groups from the DABA-TFP nanosheets. As the pH surpassed 5, the zeta potential of the pure PES membrane decreased more substantially. This observation is in accordance with findings by Salgin et al., who suggested more pronounced anion adsorption in the pH range of 6.0~8.0 for pure PES [36].

At higher pH, the negatively charged sulfuric acid groups continued to disassociate, yielding a more negative zeta potential from both the PES blend COF and PES in-situ COF membranes, further confirming the presence of additional sulfonic acid groups on the membrane surface. Throughout the entire pH range, the zeta potential of the membranes derived from the PES in-situ COF solution was more negative than that of their physically blended counterparts. This disparity likely stemmed from the superior segregation of DABA-TFP nanosheets at the membrane surface during phase inversion. This could be a consequence of the greater mobility of these small nanosheets in the in-situ dissolving approach, which facilitates their preferential positioning at the membrane surface.

The MWCOs and pore size distributions of membranes fabricated by different methods were compared based on PES in-situ COF casting solutions, as shown in Figure 5.9 b. Due to the use of pure water as a coagulant, the PES in situ COF membrane fabricated by the NIPS method had the largest MWCO. When an ethanol/water mixture was used for coagulation, delayed demixing created smaller pores on the NIPS surface, which improved the PEG rejection of the NIPS-CCD membrane. A more evident change in the MWCO was found for the PES membranes prepared with the evaporation step, i.e., the NIPS-CCD Eva and NIPS-CCD Eva THF membranes, with smaller MWCOs of 2930 Da and 2503 Da, corresponding to mean pore diameters of 1.74 nm and 1.56 nm, respectively [37]. The dense selective layer also had a narrow pore size distribution, as shown in Figure 5.9 b. These results indicate that the evaporation of the solvent/volatile cosolvent effectively reduced the pore size of the selective layer and narrowed the pore size distribution, leading to a more compact separation layer. As the NIPS-CCD EVA THF method resulted in the best PEG rejection of the PES in-situ COF membrane, we further investigated the influence of the casting solution on the MWCO of the PES membranes. As shown in Figure 5.9 c, the MWCOs of the pure PES membrane, PES blend COF membrane and PES in-situ COF membrane were all in the range of 2503 to 3177 Da, which substantiated the importance of the evaporation step in the formation of smaller pores. Among these conditions, the PES in-situ COF membranes showed the smallest MWCO and narrowest pore size distribution (shown in Figure 5.9 d), which again corresponds to our hypothesis that better segregation of COF nanosheets on the membrane surface was achieved from the PES in-situ

COF casting solution.

### 5.4.2 Antifouling and separation performance

The pure water permeance of the membranes was measured with a crossflow setup at 1 bar, and the stable permeances are illustrated in Figure 5.10 a. The outstanding PWPs at 264, 315, and 302 LMHBar$^{-1}$ were obtained from PES in-situ COF membranes fabricated by the NIPS-CCD, NIPS-CCD Eva, and NIPS-CCD Eva THF methods, respectively. These values are more than 2 times greater than those of the PES blend COF membranes and 4 times greater than those of the pure PES membranes. Aside from the substantial increase in water permeance by the addition of hydrophilic DABA-TFP nanosheets, the PWP is more dramatically affected by the microstructure. For instance, the PWPs of PES in-situ COF membranes fabricated by the NIPS-CCD, NIPS-CCD Eva, and NIPS-CCD Eva THF methods were more than 30 times greater than those of their counterparts prepared by NIPS. This significant improvement is due to the highly interconnected water transport channels from the CCD structure.

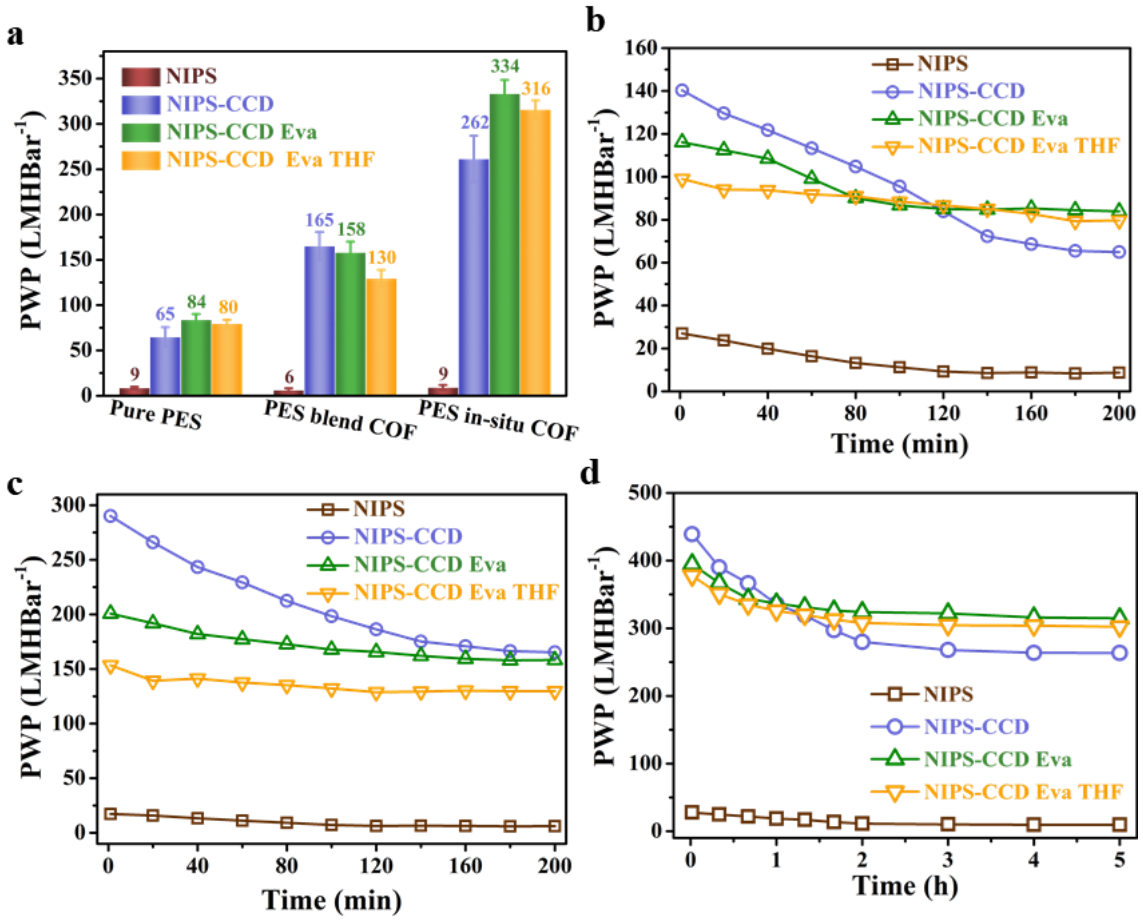



Figure 5.10 Pure water permeance of membranes (a) Pure water permeance (PWP) of membranes. PWP declination of (b) pure PES membranes, (c) PES blend COF membranes and (d) PES in-situ COF membranes over the initial 5 hours

Figure 5.10 b-d highlights the decrease in the PWP over time due to membrane compaction [38]. All membranes exhibited initial decreases in permeance for approximately 2 hours before reaching steady values. Due to the formation of a dense skin layer by solvent evaporation, the effect of skin layer compaction on the NIPS-CCD Eva and NIPS-CCD Eva THF membranes diminished in comparison to that on the NIPS and NIPS-CCD membranes, which exhibited a more porous and loose separation layer (Figure 5.10 d). It has been stated that a denser skin layer is preferred to mitigate compaction by providing less compaction capacity than that has loose structures when the membranes have similar sublayers [39, 40]. Therefore, the NIPS-CCD Eva and NIPS-CCD Eva THF membranes experienced significantly lower permeance reductions, approximately 20%. These values were 2 to 3 times lower than those of the NIPS-CCD and NIPS membranes. Similar trends were observed for both pure PES membranes (Figure 5.10 b) and PES blend-COF membranes (Figure 5.10 c), suggesting that membrane compaction is primarily influenced by fabrication techniques rather than the composition of the casting solution.

The antifouling properties of the membranes were evaluated by BSA fouling, as shown in Figure 5.11 a. After 3 consecutive fouling cycles, an ultrahigh flux recovery ratio (FRR) of 81.3% was obtained from the PES in-situ COF membrane fabricated by the NIPS-CCD Eva THF PES method. This value is comparable with the FRR value reported in other state-of -the-art membranes, which mostly ranging from 75%~90% [41-44].The FRR ratio decreased to 73.8% and 50.6% for the PES blend COF and the pure PES membrane fabricated with the same method, respectively. The change in FRR is in good agreement with the hydrophilicity of the membranes. The ionic -$SO_3H$ group of DABA-TFP effectively created a hydration layer on the PES membrane surface, which exerted a stereo repulsive force on the proteins [45]. Moreover, the electrostatic charge repulsion between the negatively charged surface of the PES membrane and BSA may also be responsible for the good antifouling property [46]. Notably, although the surface of the pure PES membrane is also negatively charged, the formation of a fouling cake due to the decreased hydrophilicity of the pure PES membrane greatly decreases the charge effect. Notably, surface roughness, traditionally regarded as a prominent factor in exacerbating membrane fouling, was found to have a reduced impact on the fouling behaviour in the present study. This observation was attributed to the consistent smoothness across all membranes reflected in the AFM results (Figure 5.7).

The separation performance of the membrane was assessed by $MgSO_4$ and various negative dyes, including Allura Red AC (AR), methyl blue (MB), and rose bengal (RB), and the results are depicted in Figure 5.11 b-d for the pure PES membranes PES blend COF and PES in-situ COF membrane. Aligned with the MWCO results (Figure 5.9 b-d), all membranes fabricated by the NIPS-CCD EVA THF method showed the greatest rejection due to the smallest surface pores formed by (co)solvent evaporation. When comparing the effect of COF addition, both the PES in-situ COF and PES blend COF membranes (Figure 5.11 d and c) outperformed the pure PES membrane shown in Figure 5.11 b. Using the membranes prepared by the NIPS-CCD EVA THF method as an example, RB rejections of 93.41%, 90.18%, and

87.00% were obtained for the PES in-situ COF, PES blend COF, and pure PES membranes, respectively. This indicated that the promotion of membrane rejection is partially attributed to the electrostatic repulsive force between the negatively charged dyes and the negatively charged membrane surface. Owing to the synergistic effect of charge repulsion and size sieving, the best rejection of MB (97.99%) and RB (93.41%) was obtained from the PES in-situ COF membrane fabricated by the NIPS-CCD Eva THF technique. Notably, all PES membranes prepared in this study showed superior rejection of dyes over PEGs. This is attributed to electrostatic exclusion from the surface of the PES membranes [47]. Moreover, the rejection of salts exhibited in Figure 5.11 b-d by all the membranes was less than 9%, indicating the promising potential of this membrane for dye/salt fractionation.

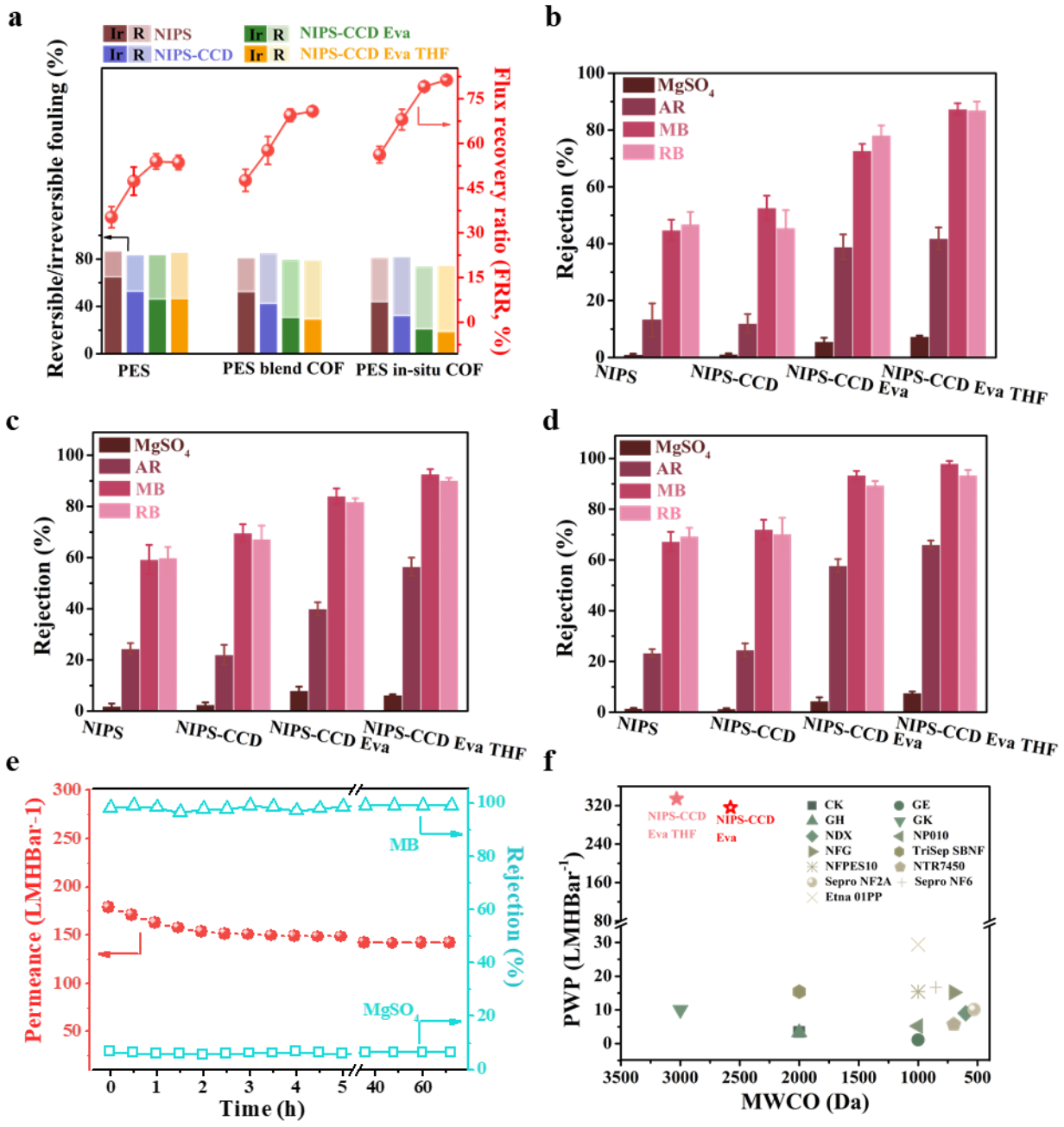


Figure 5.11 Antifouling and dye/salt separation performance of membranes. (a) Membranes' antifouling performance over 3-cycle of BSA filtration. Rejection to $MgSO_4$ and negative dyes of (b) pure PES membranes, (c) PES blend COF membranes and (d) PES in-situ COF membranes. (e) Long-term separation performance of PES in-situ COF membrane fabricated by NIPS-CCD Eva THF method. (f) Comparison with commercial LNF membranes.

As the PES in-situ COF membrane fabricated by the NIPS-CCD EVA THF method demonstrated the best dye rejection, this membrane was selected for long-term dye-salt separation. For testing, a synthetic dye/salt solution comprising 50 ppm methyl blue and 1 g $L^{-1}$ $MgSO_4$ was used. As shown in Figure 5.11 e, a modest reduction in permeance from 178.5 $LMHBar^{-1}$ to approximately 155.5 $LMHBar^{-1}$ was found within the first two hours. Subsequently, the permeance stabilised at a high level of 141.8 $LMHBar^{-1}$ after a three-day test, implying good antifouling properties when treating textile wastewater. Moreover, the rejection of MB and $MgSO_4$ by the membrane almost remained constant at ~98% and ~6%, respectively, revealing the high separation performance of the as-fabricated membrane over long-term testing.

A comparison of the as-prepared membranes with commercial membranes on the basis of permeance and MWCO is shown in Figure 5.11 f and summarised in Table 5.5. A similar comparison with academically reported LNF/tight ultrafiltration (TUF) membranes is summarised in Table 5.6. The PWP of all the commercially available membranes was less than 20 $LMHBar^{-1}$, with MWCO values ranging from 500~2000 Da. For laboratory-scale LNF/TUF membranes designed for dye/slat separation or dye removal, the permeance typically varies from 1 to 179 $LMHBar^{-1}$. These values are considerably lower than those of the as-prepared PES-COF membranes developed in this study, which exhibit a stable permeance exceeding 300 $LMHBar^{-1}$. This significant performance advantage demonstrates the potential of fabricated membranes for efficiently purifying textile wastewater and reclaiming valuable substances.

Table 5.5 Comparison with the performance of commercially available LNF membranes (The selected examples represents key studies identified through a Web of Science search or Google browser u sing keywords such as "commercial loose nanofiltration membrane", and "commercial tight ultraf iltration membrane")

| *Code* | Materials | Supplier | MWCO (Da) | Permeance ($LMHBar^{-1}$) | Ref. |
|---|---|---|---|---|---|
| *NIPS-CCD Eva* | PES/DABA-TFP | / | 2930[a] | 334 | This study |
| *NIPS-CCD Eva THF* | PES/DABA-TFP | / | 2503[a] | 316 | This study |
| *NP010* | Polyether Sulfone | Microdyn Nadir | 1000[b] | 5.1 | [15] |

| | | | | | |
|---|---|---|---|---|---|
| *NFPES10* | Polyether Sulfone | Microdyn Nadir | 1000[a] | 15.4 | [13] |
| *NTR7450* | Sulfonated Polyether Sulfone | Nitto Denko | 600~800[a] | 5.7 | [13] |
| *GE* | Composite Polyamide | Osmonics | 1000[a] | 1.1 | [12] |
| *GH* | Polyamide-TFC | Osmonics | 2000[a] | 3.3 | [12] |
| *GK* | Polyamide-TFC | Osmonics | 3000[a] | 10 | [48] |
| *NDX* | Polyamide | Synder Filtration | 500~700[b] | 7.9~10.1 | [49] |
| *NFG* | Polyamide-TFC | Synder Filtration | 600~800[a] | 14.7~15.7 | [50] |
| *Sepro NF 2A* | Polyamide | Ultura | 530[a] | 10.1 | [51] |
| *Sepro NF 6* | Polyamide | Ultura | 850[a] | 16.7 | [51] |
| *ETNA01PP* | Fluoropolymer | Alfa Laval | 1000[b] | 29.4 | [51] |
| *TriSep SBNF* | Cellulose acetate/ triacetate | Microdyn Nadir | 2000[b] | 12.0~17.7 | [52] |
| *CK* | Cellulose | Osmonics | 2000[a] | 3.45 | [53, 54] |

[a]: Tested by using PEGs as tracer.

[b]: Data from the manufacturer without mentioning the tracer.

Table 5.6 Summary of previously reported LNF/TUF membranes (The selected literature represents key studies identified through a Web of Science search using keywords such as “loose nanofiltration membrane”, and “tight ultrafiltration membrane”)

| *Material* | Solvent | Additive | Permeance ($LMHBar^{-1}$) | Separation target | MWCO* | Ref. |
|---|---|---|---|---|---|---|
| *PSf* | DMAc/ Acetone | Zno/PEG | 72 | dye/salt | 371 (dye) | [55] |

| | | | | | | |
|---|---|---|---|---|---|---|
| *PES/SPSf* | DMAc | Adipic acid | 72.2 | dyes | 7250(PEG) | [56] |
| *sPPSU* | NMP | PEG | 82.5~117.6 | dye/salt | 1000~2000(PEG) | [57] |
| *PES* | DMAc | Ce-Anth-MOF | 10 | PEGs | 1800(PEG) | [58] |
| *PVDF* | DMAc | GO | 24.8 | dye/Salt | 6450(PEG) | [59] |
| *PAAS-m-PAN* | EtOH/NMP | / | 144 | dye | 697(dye) | [60] |
| *PSE* | DMF | PVP | 70.7 | dyes | 697(dye) | [61] |
| *PSF* | NMP | ZIF-8 | 250 | dyes/salt | 697(dye) | [62] |
| *PSf/SMA* | DPGDB | β-CD/TMC | 127 | BSA/dye | 697(dye) | [63] |
| *PES* | DMAc | $MoS_2$ | 72~80 | PEG | 8000(PEG) | [64] |
| *PES* | DMAc | PDA@$MoS_2$/PVP | 42 | PEG/dyes/Salt | 5500(PEG)<br>513(Dye) | [65] |
| *PES* | DMAc | O-$MoS_2$/PVP | 75.24 | PEG/dye | 8408(PEG)<br>1018(dye) | [66] |
| *PES* | DMAc | $MoS_2$-PSBMA | 22.9 | dye/salt | 992(dye) | [67] |
| *PES* | NMP | $CeO_2$ | 20 | dye/salt | 697(dye)<br>1117(dye) | [68] |
| *PES* | DMAc | GO-PSBMA | 8.8 | dye/salt | 577(dye) | [69] |
| *PVDF* | NMP/THF | / | 1.8 | dye | 327(dye) | [70] |
| *PVDF* | DMF | / | 1.35~13.5 | dyes | 697(dye) | [71] |
| *PI/SiO2* | / | $SiO_2$ | 128 | dye/salt | 697(dye) | [72] |
| *PAA-PI* | / | / | 1 | dye/salt in solvent | 1017(dye) | [73] |
| *PES* | NMP | BNNS | 52 | dyes | 1017(dye) | [74] |
| *PES* | NMP | SPSf/PEG | 20 | dyes, organic carbon | 466(dye) | [75] |
| *PES* | DMSO | $TiO_2$ | 33.4 | dye | 814(dye) | [76] |

| | | | | | | |
|---|---|---|---|---|---|---|
| *PVDF* | NMP/THF (9:1) | / | ACN 146<br>Tol 0.94<br>DMF2.16 | solvents/dyes | 1017(dye) | [77] |
| *PES* | DMSO | / | Uf:7.05<br>NF: 2.03 | dyes, BSA | 1017(dye) | [78] |
| *PVDF* | DMAc/THF | LiCl | 14.2 | dye/salt | 320(dyye) | [79] |
| *PSf* | NMP | PES-COOH/PEG | 159.6 | dye/salt | 697(dye) | [80] |
| *PSF-COOH* | DMF | NIPS | 154 | dye/salt | 697(dye) | [81] |
| *PES* | DMAc | mHT/PVP | 6.4 | dye/salt | 992(dye) | [82] |
| *PES* | DMAc | $SiO_2$-PSS/PVP | 93 | dye/salt | 655(PEG) | [83] |
| *PES* | DMAc | CS-MMT/PVP | 7.6 | dye/salt | 576(dye)<br><992(dye) | [84] |
| *PES* | DMAc | ZHT/PVP | 20.1 | dye/salt | 576(dye) | [85] |

## 5.4.3 Mechanical properties of membrane

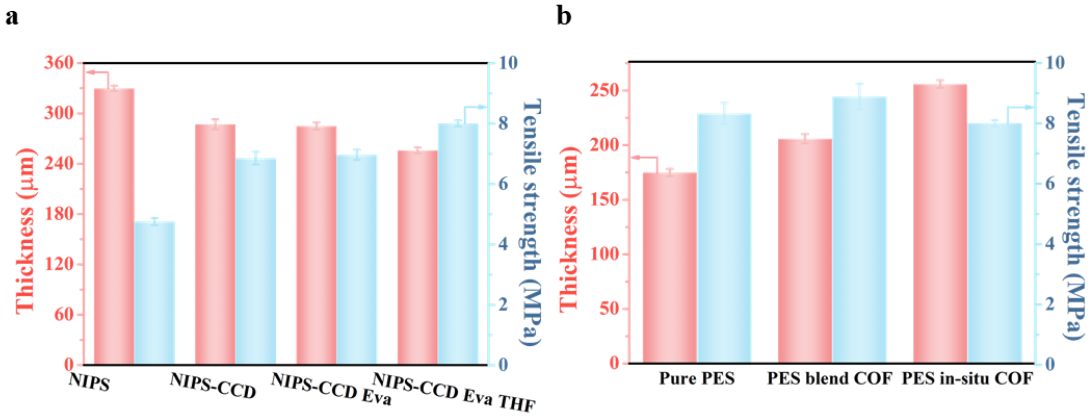



Figure 5.12 Mechanical performance of membranes. (a) Thickness and tensile strength of PES in-situ COF membranes prepared by different methods. (b) Thickness and tensile strength of pure PES, PES blend COF and PES in-situ COF membranes prepared by NIPS-CCD Eva THF method.

The mechanical properties of the membrane are summarised in Figure 5.12 and Table 5.7. Membranes fabricated with different methods exhibited distinct mechanical properties due to their microstructural differences. Compared with the NIPS-CCD membrane, the NIPS membranes are the thickest, with the

highest elongation ratio but lowest tensile strength. This is consistent with previous reports and can be mainly explained by the incorporation of strong, rigid CCD microchannels in the supporting structure of the membranes [22, 86]. Comparing the NIPS-CCD, NIPS-CCD Eva and NIPS-CCD Eva THF membranes in Figure 5.12 a, the membrane thickness decreased after evaporation, while the tensile strength increased after evaporation. This suggests a denser skin layer led to a higher mechanical strength. A high tensile strength of greater than 8 MPa was obtained for the pure PES membrane and PES-COF membranes prepared with the NIPS-CCD Eva THF, regardless of which method was used to blend the COF and PES. With the same fabrication procedure, the tensile properties of the membrane were also greatly influenced by the COF blending strategy. Taking the membranes fabricated by the NIPS-CCD EVA THF method as an example, as shown in Figure 5.12 b, the PES blend COF membrane has the highest elongation ratio and highest tensile strength at 18.07% and 8.89 MPa, respectively, while the PES in-situ COF membrane has the lowest elongation ratio and tensile strength at 13.52% and 8.01 MPa, respectively. The enhancement in mechanical strength and elongation ratio of the PES blend COF membrane can be attributed to the integration of COF nanosheets within the PES membrane. Unlike typical inorganic fillers that often compromise the flexibility of polymer chains [87], the excellent compatibility of DABA-TFP COF with PES allows it to act as a binder in polymer composites, reinforcing the overall polymer structure. When considering the PES in-situ COF membrane, the reduced elongation ratio indicates a more rigid structure resulting from molecular interactions between PES and COF subsequent to hydrogen bonding [88].

Table 5.7 Mechanical strength of membranes

| Solution | Membrane | Thickness (μm) | Elongation (%) | Tensile Strength (MPa) |
|---|---|---|---|---|
| Pure PES | NIPS | 290 ± 3.26 | 19.63 ± 2.42 | 5.48 ± 0.21 |
| | NIPS-CCD | 196 ± 5.45 | 16.12 ± 3.72 | 6.92 ± 0.43 |
| | NIPS-CCD Eva | 188 ± 3.31 | 16.61 ± 3.11 | 7.18 ± 0.37 |
| | NIPS-CCD Eva THF | 175 ± 2.87 | 16.92 ± 2.18 | 8.33 ± 0.35 |
| PES blend COF | NIPS | 300 ± 4.45 | 20.26 ± 2.92 | 6.00 ± 0.31 |
| | NIPS-CCD | 256 ± 3.25 | 17.53 ± 4.25 | 7.48 ± 0.56 |
| | NIPS-CCD Eva | 226 ± 3.44 | 17.59 ± 3.95 | 7.70 ± 0.48 |
| | NIPS-CCD Eva THF | 206 ± 4.21 | 18.07 ± 2.95 | 8.89 ± 0.42 |
| PES in-situ COF | NIPS | 330 ± 3.11 | 15.37 ± 2.58 | 4.76 ± 0.12 |
| | NIPS-CCD | 287 ± 6.01 | 13.31 ± 3.21 | 6.86 ± 0.21 |
| | NIPS-CCD Eva | 285 ± 4.21 | 13.39 ± 2.03 | 6.97 ± 0.17 |

| | | | |
|---|---|---|---|
| NIPS-CCD Eva THF | 256 ± 3.52 | 13.52 ± 2.52 | 8.01 ± 0.10 |

## 5.5 Conclusion

In summary, this study presents an advantageous method for incorporating DABA-TFP nanosheets into a PES matrix to fabricate high-performance LNF membranes. The homogeneous integration of the COF/PES mixture was successfully achieved using an in-situ dissolving approach, resulting in membranes with superior uniformity, selectivity, and permeability. By introducing a solvent evaporation step, the membrane's skin layer was effectively densified, achieving a pore size of 1.56~1.74 nm, which is well-suited for LNF applications. These membranes exhibited excellent antifouling properties, maintaining a fouling recovery ratio (FRR) of 81.3% after three BSA fouling cycles. They also demonstrated high separation efficiency, with over 90% rejection of dyes such as Rose Bengal (RB) and methylene blue (MB), while maintaining high salt permeability, with $MgSO_4$ rejection below 8%. The unique porous and interconnected CCD structure contributed to an ultrahigh PWP exceeding 300 $LMH \cdot bar^{-1}$, significantly surpassing that of commercial LNF membranes and most reported membranes in this category by 10~100 times. Given the high uniformity and enhanced separation performance achieved in this study, the in-situ dissolving strategy holds great potential for the development of a broad range of COF-based membranes with precise structural control, tuneable selectivity, and scalable fabrication for advanced water purification and molecular separation applications.

## References

[1] N. Elmerhi, S. Kumar, M. Abi Jaoude, D. Shetty, Covalent Organic Framework-derived Composite Membranes for Water Treatment, Chemistry – An Asian Journal 19(2) (2024) e202300944. https://doi.org/https://doi.org/10.1002/asia.202300944.
[2] A.P. Cote, A.I. Benin, N.W. Ockwig, M. O'Keeffe, A.J. Matzger, O.M.J.s. Yaghi, Porous, crystalline, covalent organic frameworks, Science 310(5751) (2005) 1166-1170. https://doi.org/10.1126/science.1120411.
[3] X. Feng, D. Peng, J. Zhu, Y. Wang, Y.J.S. Zhang, P. Technology, Recent advances of loose nanofiltration membranes for dye/salt separation, Seperation and Purification Technology 285 (2022) 120228. https://doi.org/10.1016/j.seppur.2021.120228.
[4] L. Valentino, M. Matsumoto, W.R. Dichtel, B.J.J.E.s. Mariñas, technology, Development and performance characterization of a polyimine covalent organic framework thin-film composite nanofiltration membrane, Environmental Science & Technology 51(24) (2017) 14352-14359. https://doi.org/10.1021/acs.est.7b04056.
[5] M.S. Denny, J.C. Moreton, L. Benz, S.M. Cohen, Metal–organic frameworks for membrane-based separations, Nature Reviews Materials 1(12) (2016) 16078. https://doi.org/10.1038/natrevmats.2016.78.
[6] V. Vatanpour, S. Paziresh, A melamine-based covalent organic framework nanomaterial as a nanofiller in polyethersulfone mixed matrix membranes to improve separation and antifouling performance, Journal of Applied Polymer Science 139(1) (2022) 51428. https://doi.org/https://doi.org/10.1002/app.51428.
[7] X. Zhu, D. Jańczewski, S. Guo, S.S.C. Lee, F.J. Parra Velandia, S.L.-M. Teo, T. He, S.R. Puniredd, G.J. Vancso, Polyion Multilayers with Precise Surface Charge Control for Antifouling, ACS Applied Materials & Interfaces 7(1) (2015) 852-861. https://doi.org/10.1021/am507371a.
[8] K. Duan, J. Wang, Y. Zhang, J. Liu, Covalent organic frameworks (COFs) functionalized mixed matrix membrane for effective CO2/N2 separation, Journal of Membrane Science 572 (2019) 588-595.

https://doi.org/https://doi.org/10.1016/j.memsci.2018.11.054.
[9] X. Cao, H. Xu, S. Dong, J. Xu, Z. Qiao, S. Zhao, J. Wang, Z. Wang, Preparation of high-performance and pressure-resistant mixed matrix membranes for CO2/H2 separation by modifying COF surfaces with the groups or segments of the polymer matrix, Journal of Membrane Science 601 (2020) 117882. https://doi.org/https://doi.org/10.1016/j.memsci.2020.117882.
[10] C. Conidi, A. Cassano, E. Drioli, A membrane-based study for the recovery of polyphenols from bergamot juice, Journal of Membrane Science 375(1) (2011) 182-190. https://doi.org/https://doi.org/10.1016/j.memsci.2011.03.035.
[11] Microdyn Nadir NP030-P-Ultrafiltration Membrane. https://www.lenntech.com/Data-sheets/Microdyn-Nadir-D-NP030-P-V1-L.pdf, (accessed 11 Nov 2023).
[12] GE Ultrfiltration Membrane. https://www.sterlitech.com/ultrafiltration-uf-membrane.html#GE, (accessed 11 Nov 2023).
[13] K. Boussu, B. Van der Bruggen, A. Volodin, C. Van Haesendonck, J.A. Delcour, P. Van der Meeren, C. Vandecasteele, Characterization of commercial nanofiltration membranes and comparison with self-made polyethersulfone membranes, Desalination 191(1) (2006) 245-253. https://doi.org/10.1016/j.desal.2005.07.025.
[14] M. Moochani, A. Moghadassi, S.M.N. Hosseini, E. Bagheripour, F.J.K.J.o.C.E. Parvizian, Fabrication of novel polyethersulfone based nanofiltration membrane by embedding polyaniline-co-graphene oxide nanoplates, Korean Journal of Chemical 33 (2016) 2674-2683. https://doi.org/10.1007/s11814-016-0132-4.
[15] Microdyn Nadir NP010 P Nanofiltration Membrane. https://www.lenntech.com/Data-sheets/Microdyn-Nadir-Product-Catalogue-L.pdf, (accessed 11 Nov 2023).
[16] Q. Wu, W. Xie, H. Wu, L. Wang, S. Liang, H. Chang, B.J.R.a. Liu, Effect of volatile solvent and evaporation time on formation and performance of PVC/PVC-g-PEGMA blended membranes, RSC advances 9(59) (2019) 34486-34495. https://doi.org/10.1039/C9RA05454E.
[17] I. Pinnau, W.J. Koros, Structures and gas separation properties of asymmetric polysulfone membranes made by dry, wet, and dry/wet phase inversion, Journal of Applied Polymer Science 43(8) (1991) 1491-1502. https://doi.org/10.1002/app.1991.070430811.
[18] A.K. Hołda, B. Aernouts, W. Saeys, I.F.J. Vankelecom, Study of polymer concentration and evaporation time as phase inversion parameters for polysulfone-based SRNF membranes, Journal of Membrane Science 442 (2013) 196-205. https://doi.org/10.1016/j.memsci.2013.04.017.
[19] J. Shen, G. Liu, K. Huang, Q. Li, K. Guan, Y. Li, W. Jin, UiO-66-polyether block amide mixed matrix membranes for CO2 separation, Journal of Membrane Science 513 (2016) 155-165. https://doi.org/https://doi.org/10.1016/j.memsci.2016.04.045.
[20] Y. Ying, M. Tong, S. Ning, S.K. Ravi, S.B. Peh, S.C. Tan, S.J. Pennycook, D. Zhao, Ultrathin two-dimensional membranes assembled by ionic covalent organic nanosheets with reduced apertures for gas separation, Journal of the American Chemical Society 142(9) (2020) 4472-4480.
[21] T. Huang, H. Jiang, J.C. Douglin, Y. Chen, S. Yin, J. Zhang, X. Deng, H. Wu, Y. Yin, D.R. Dekel, M.D. Guiver, Z. Jiang, Single Solution-Phase Synthesis of Charged Covalent Organic Framework Nanosheets with High Volume Yield, Angewandte Chemie International Edition 62(4) (2023) e202209306. https://doi.org/10.1002/anie.202209306.
[22] H. Peng, K. Li, Nanostructured membranes with interconnected pores via a combination of phase inversion and solvent crystallisation approach, Journal of Membrane Science 680 (2023) 121738. https://doi.org/10.1016/j.memsci.2023.121738.
[23] P. Vandezande, X. Li, L.E.M. Gevers, I.F.J. Vankelecom, High throughput study of phase inversion parameters for polyimide-based SRNF membranes, Journal of Membrane Science 330(1) (2009) 307-318. https://doi.org/10.1016/j.memsci.2008.12.068.
[24] D. Howell, B. Behrends, A review of surface roughness in antifouling coatings illustrating the importance of cutoff length, Biofouling 22(6) (2006) 401-410.
[25] J. Bian, X.W. Wei, H.L. Lin, L. Wang, Z.P. Guan, Comparative study on the exfoliated expanded graphite nanosheet-PES composites prepared via different compounding method, 124(5) (2012) 3547-3557. https://doi.org/https://doi.org/10.1002/app.35531.
[26] B. Nandan, L.D. Kandpal, G.N. Mathur, Crystallization and melting behavior of poly(ether ether ketone)/poly(aryl ether sulfone) blends, 90(11) (2003) 2906-2918. https://doi.org/https://doi.org/10.1002/app.13012.
[27] C.R. DeBlase, K.E. Silberstein, T.-T. Truong, H.D. Abruña, W.R.J.J.o.t.A.C.S. Dichtel, β-Ketoenamine-linked covalent organic frameworks capable of pseudocapacitive energy storage, Journal of the American Chemical Society 135(45) (2013) 16821-16824. https://doi.org/10.1021/ja409421d.

[28] C.R. DeBlase, K.E. Silberstein, T.-T. Truong, H.D. Abruña, W.R. Dichtel, β-Ketoenamine-linked covalent organic frameworks capable of pseudocapacitive energy storage, Journal of the American Chemical Society 135(45) (2013) 16821-16824.
[29] S. Kandambeth, A. Mallick, B. Lukose, M.V. Mane, T. Heine, R. Banerjee, Construction of crystalline 2D covalent organic frameworks with remarkable chemical (acid/base) stability via a combined reversible and irreversible route, Journal of the American Chemical Society 134(48) (2012) 19524-19527.
[30] A. Singh, R. Gogoi, K. Sharma, R. Kumar, P.F. Siril, Continuous flow synthesis of disordered covalent organic framework for ultra-high removal of industrial pollutants in flow, Separation and Purification Technology 307 (2023) 122739. https://doi.org/10.1016/j.seppur.2022.122739.
[31] V.Y. Rudyak, A.A. Gavrilov, D.V. Guseva, S.-H. Tung, P.V. Komarov, Accounting for π–π stacking interactions in the mesoscopic models of conjugated polymers, Molecular Systems Design & Engineering 5(6) (2020) 1137-1146. https://doi.org/10.1039/D0ME00034E.
[32] Y. Zhu, W. Wu, M. Gao, J. Yan, B. Wang, Molecular Compatibility and Hydrogen Bonding Mechanism of PES/PEI Blends, Polymers 14 (2022) 3046. https://doi.org/10.3390/polym14153046.
[33] D. Zhao, J. Huang, Y. Zhong, K. Li, L. Zhang, J. Cai, High-Strength and High-Toughness Double-Cross-Linked Cellulose Hydrogels: A New Strategy Using Sequential Chemical and Physical Cross-Linking, Advanced Functional Materials 26(34) (2016) 6279-6287. https://doi.org/10.1002/adfm.201601645.
[34] X. Zhu, Z. Yang, Z. Gan, X. Cheng, X. Tang, X. Luo, D. Xu, G. Li, H. Liang, Toward tailoring nanofiltration performance of thin-film composite membranes: Novel insights into the role of poly(vinyl alcohol) coating positions, Journal of Membrane Science 614 (2020) 118526. https://doi.org/https://doi.org/10.1016/j.memsci.2020.118526.
[35] J.F. Blanco, Q.T. Nguyen, P. Schaetzel, Novel hydrophilic membrane materials: sulfonated polyethersulfone Cardo, Journal of Membrane Science 186(2) (2001) 267-279. https://doi.org/https://doi.org/10.1016/S0376-7388(01)00331-3.
[36] S. Salgın, U. Salgın, N. Soyer, Streaming Potential Measurements of Polyethersulfone Ultrafiltration Membranes to Determine Salt Effects on Membrane Zeta Potential, International Journal of Electrochemical Science 8(3) (2013) 4073-4084. https://doi.org/10.1016/S1452-3981(23)14454-3.
[37] K. Banjerdteerakul, H. Peng, K. Li, COF-based nanofiltration membrane for effective treatment of wastewater containing pharmaceutical residues, Journal of Membrane Science 681 (2023) 121780. https://doi.org/10.1016/j.memsci.2023.121780.
[38] K.M. Persson, V. Gekas, G. Trägårdh, Study of membrane compaction and its influence on ultrafiltration water permeability, Journal of Membrane Science 100(2) (1995) 155-162. https://doi.org/10.1016/0376-7388(94)00263-X.
[39] H. Yasuda, J.T. Tsai, Pore size of microporous polymer membranes, 18(3) (1974) 805-819. https://doi.org/https://doi.org/10.1002/app.1974.070180316.
[40] C. Xu, Z. Wang, Y. Hu, Y. Chen, Thin-Film Composite Membrane Compaction: Exploring the Interplay among Support Compressive Modulus, Structural Characteristics, and Overall Transport Efficiency, Environmental Science & Technology 58(19) (2024) 8587-8596. https://doi.org/10.1021/acs.est.4c01639.
[41] Y. Yang, F. Zhao, Z. Zhang, Y. Liu, Z. Li, X. Wei, T. Wang, C. Fan, Z. Jiang, Electrostatic interaction enhanced surface segregation towards heterogeneous antifouling membrane for oil/water separation, Chemical Engineering Science 306 (2025) 121283. https://doi.org/https://doi.org/10.1016/j.ces.2025.121283.
[42] E. Shokri, B. Khanghahi, E. Effati, Fabrication and characterizations of degradable PVC/PLA-HAp ultrafiltration membrane with enhanced antifouling properties, Journal of Applied Polymer Science 140(17) (2023) e53767. https://doi.org/https://doi.org/10.1002/app.53767.
[43] E. Virga, J. de Grooth, K. Žvab, W.M. de Vos, Stable polyelectrolyte multilayer-based hollow fiber nanofiltration membranes for produced water treatment, ACS Applied Polymer Materials 1(8) (2019) 2230-2239.
[44] A. Johari, M. Razmjouei, A. Mansourizadeh, D. Emadzadeh, Fabrication of blend hydrophilic polyamide imide (Torlon®)-sulfonated poly (ether ether ketone) hollow fiber membranes for oily wastewater treatment, Polymer Testing 91 (2020) 106733.
[45] Y. Zhao, X. Yang, Z. Cheng, C.H. Lau, J. Ma, L. Shao, Surface manipulation for prevention of migratory viscous crude oil fouling in superhydrophilic membranes, Nature Communications 14(1) (2023) 2679. https://doi.org/10.1038/s41467-023-38419-3.
[46] M. Yang, P. Hadi, X. Yin, J. Yu, X. Huang, H. Ma, H. Walker, B.S. Hsiao, Antifouling nanocellulose membranes: How subtle adjustment of surface charge lead to self-cleaning property, Journal of Membrane Science 618 (2021) 118739. https://doi.org/10.1016/j.memsci.2020.118739.
[47] J. Lin, W. Ye, M.-C. Baltaru, Y.P. Tang, N.J. Bernstein, P. Gao, S. Balta, M. Vlad, A. Volodin, A. Sotto,

P. Luis, A.L. Zydney, B. Van der Bruggen, Tight ultrafiltration membranes for enhanced separation of dyes and Na2SO4 during textile wastewater treatment, Journal of Membrane Science 514 (2016) 217-228. https://doi.org/10.1016/j.memsci.2016.04.057.
[48] M. Cissé, F. Vaillant, D. Pallet, M. Dornier, Selecting ultrafiltration and nanofiltration membranes to concentrate anthocyanins from roselle extract (Hibiscus sabdariffa L.), Food Research International 44(9) (2011) 2607-2614. https://doi.org/10.1016/j.foodres.2011.04.046.
[49] Industrial Nanofiltration Membranes - NDX. https://synderfiltration.com/2014/wp-content/uploads/2017/12/NDX-Specsheet-TFC-500-700Da-Industrial-1.pdf, (accessed 20 Mar 2024).
[50] NFG (TFC 600-800Da) Sanitary NF Membrane. https://synderfiltration.com/2014/wp-content/uploads/2018/11/NFG-TFC-600-800Da-Sanitary-Specsheet.pdf, (accessed 20 Mar 2024).
[51] J. Lin, C.Y. Tang, W. Ye, S.-P. Sun, S.H. Hamdan, A. Volodin, C.V. Haesendonck, A. Sotto, P. Luis, B. Van der Bruggen, Unraveling flux behavior of superhydrophilic loose nanofiltration membranes during textile wastewater treatment, Journal of Membrane Science 493 (2015) 690-702. https://doi.org/10.1016/j.memsci.2015.07.018.
[52] Cellulose Acetate (CA) NF Membrane. https://water-membrane-solutions.mann-hummel.com/content/dam/water-membrane-solutions/download/technical-data-sheets/trisep/trisep-sbnf-flat-sheet-membrane-data-sheet.pdf/_jcr_content/renditions/original./trisep-sbnf-flat-sheet-membrane-data-sheet.pdf, (accessed 20 Mar 2024).
[53] A.W. Mohammad, Y.H. Teow, W.L. Ang, Y.T. Chung, D.L. Oatley-Radcliffe, N. Hilal, Nanofiltration membranes review: Recent advances and future prospects, Desalination 356 (2015) 226-254. https://doi.org/10.1016/j.desal.2014.10.043.
[54] C. Baudequin, Z. Mai, M. Rakib, I. Deguerry, R. Severac, M. Pabon, E. Couallier, Removal of fluorinated surfactants by reverse osmosis – Role of surfactants in membrane fouling, Journal of Membrane Science 458 (2014) 111-119. https://doi.org/10.1016/j.memsci.2014.01.063.
[55] P.T.P. Aryanti, F.A. Nugroho, I.N. Widiasa, P.D. Sutrisna, I.G.J.J.o.A.P.S. Wenten, Preparation of highly selective PSf/ZnO/PEG400 tight ultrafiltration membrane for dyes removal, Journal of Applied Polymer Science 139(33) (2022) e52779. https://doi.org/10.1002/app.52779.
[56] M. Hu, S. Yang, X. Liu, R. Tao, Z. Cui, C. Matindi, W. Shi, R. Chu, X. Ma, K. Fang, M. Titus, B.B. Mamba, J. Li, Selective separation of dye and salt by PES/SPSf tight ultrafiltration membrane: Roles of size sieving and charge effect, Separation and Purification Technology 266 (2021) 118587. https://doi.org/10.1016/j.seppur.2021.118587.
[57] Y. Feng, G. Han, T.-S. Chung, M. Weber, N. Widjojo, C. Maletzko, Effects of polyethylene glycol on membrane formation and properties of hydrophilic sulfonated polyphenylenesulfone (sPPSU) membranes, Journal of Membrane Science 531 (2017) 27-35. https://doi.org/10.1016/j.memsci.2017.02.040.
[58] E.S. Mansor, E.A. Ali, A.M. Shaban, Tight ultrafiltration polyethersulfone membrane for cheese whey wastewater treatment, Chemical Engineering Journal 407 (2021) 127175. https://doi.org/10.1016/j.cej.2020.127175.
[59] C. Wang, Y. Chen, K. Yang, X. Hu, Y. Zhang, Fabrication of tight GO/PVDF hollow fiber membranes with improved permeability for efficient fractionation of dyes and salts in textile wastewater, Polymer Bulletin 79(1) (2022) 443-462. https://doi.org/10.1007/s00289-020-03513-9.
[60] G. Jiang, S. Zhang, Y. Zhu, S. Gao, H. Jin, L. Luo, F. Zhang, J. Jin, Hydrogel-embedded tight ultrafiltration membrane with superior anti-dye-fouling property for low-pressure driven molecule separation, Journal of Materials Chemistry A 6(7) (2018) 2927-2934. https://doi.org/10.1039/C7TA09898G.
[61] J.-Y. Zhou, M.-J. Yin, Z.-P. Wang, Y. Shen, N. Wang, Z. Qin, Q.-F. An, Tailoring of polysulfate/polyvinylpyrrolidone membrane structure via NIPS coupled physical aging technique for high-performance dye/salt separation, Separation and Purification Technology 283 (2022) 120163. https://doi.org/10.1016/j.seppur.2021.120163.
[62] H. Yu, D. Cai, S. Li, C. Gao, L.J.J.o.M.S. Xue, Tight UF membranes with ultrahigh water flux prepared by in-situ growing ZIF particles in NIPS process for greatly enhanced dye removal efficiency, Journal of Membrane Science 666 (2023) 121136. https://doi.org/10.1016/j.memsci.2022.121136.
[63] J.M. Tesha, D.S. Dlamini, S. Qaseem, Z. Cui, J. Li, Tight ultrafiltration: Layer deposition of Trimesoyl chloride/β-Cyclodextrin onto Polysulfone/Poly (styrene-co-maleic anhydride) membrane for water treatment, Journal of Environmental Chemical Engineering 8(3) (2020) 103733. https://doi.org/10.1016/j.jece.2020.103733.
[64] H. Tian, X. Wu, K. Zhang, Tailoring Morphology and Properties of Tight Utrafiltration Membranes by Two-Dimensional Molybdenum Disulfide for Performance Improvement, Membranes 12 (2022) 1071. https://doi.org/10.3390/membranes12111071.

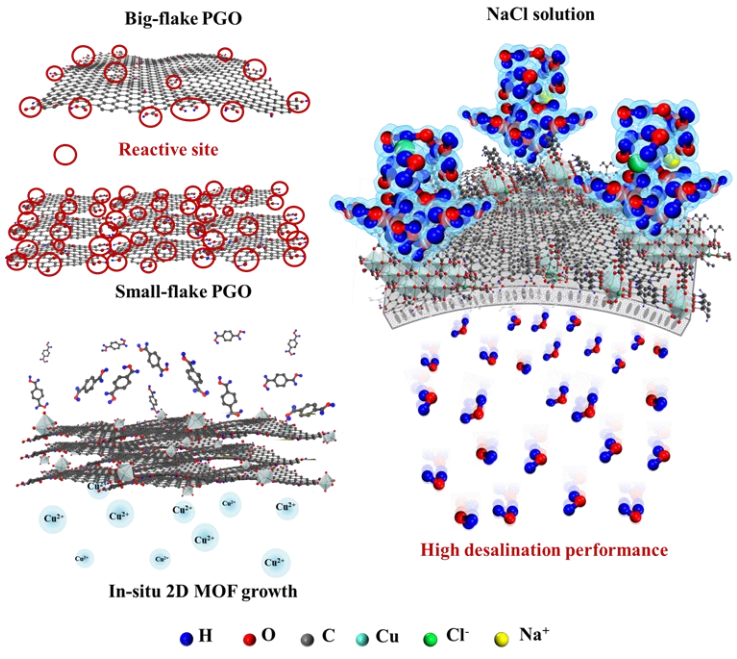
[65] H. Tian, X. Wu, K. Zhang, Polydopamine-Assisted Two-Dimensional Molybdenum Disulfide (MoS2)-Modified PES Tight Ultrafiltration Mixed-Matrix Membranes: Enhanced Dye Separation Performance, Membranes 11 (2021) 96. https://doi.org/10.3390/membranes11020096.
[66] H. Tian, S. Yang, X. Wu, K. Zhang, Two-dimensional molybdenum disulfide oxide (O-MoS2) enhanced tight ultrafiltration membrane with improved molecular separation performance and antifouling properties, Colloids and Surfaces A: Physicochemical and Engineering Aspects 656 (2023) 130328. https://doi.org/10.1016/j.colsurfa.2022.130328.
[67] X. Liang, P. Wang, J. Wang, Y. Zhang, W. Wu, J. Liu, B. Van der Bruggen, Zwitterionic functionalized MoS2 nanosheets for a novel composite membrane with effective salt/dye separation performance, Journal of Membrane Science 573 (2019) 270-279. https://doi.org/10.1016/j.memsci.2018.12.015.
[68] T. Tavangar, M. Karimi, M. Rezakazemi, K.R. Reddy, T.M. Aminabhavi, Textile waste, dyes/inorganic salts separation of cerium oxide-loaded loose nanofiltration polyethersulfone membranes, Chemical Engineering Journal 385 (2020) 123787. https://doi.org/10.1016/j.cej.2019.123787.
[69] J. Zhu, M. Tian, J. Hou, J. Wang, J. Lin, Y. Zhang, J. Liu, B. Van der Bruggen, Surface zwitterionic functionalized graphene oxide for a novel loose nanofiltration membrane, Journal of Materials Chemistry A 4(5) (2016) 1980-1990. https://doi.org/10.1039/C5TA08024J.
[70] M. Mertens, T. Van Dyck, C. Van Goethem, A.Y. Gebreyohannes, I.F.J. Vankelecom, Development of a polyvinylidene difluoride membrane for nanofiltration, Journal of Membrane Science 557 (2018) 24-29. https://doi.org/10.1016/j.memsci.2018.04.020.
[71] M.G. Buonomenna, L.C. Lopez, P. Favia, R. d'Agostino, A. Gordano, E. Drioli, New PVDF membranes: The effect of plasma surface modification on retention in nanofiltration of aqueous solution containing organic compounds, Water Research 41(19) (2007) 4309-4316. https://doi.org/10.1016/j.watres.2007.06.033.
[72] Z. Liu, R. Qiang, L. Lin, X. Deng, X. Yang, K. Zhao, J. Yang, X. Li, W. Ma, M. Xu, Thermally modified polyimide/SiO2 nanofiltration membrane with high permeance and selectivity for efficient dye/salt separation, Journal of Membrane Science 658 (2022) 120747. https://doi.org/10.1016/j.memsci.2022.120747.
[73] C. Wei, Z. He, L. Lin, Q. Cheng, K. Huang, S. Ma, L. Chen, Negatively charged polyimide nanofiltration membranes with high selectivity and performance stability by optimization of synergistic imidization, Journal of Membrane Science 563 (2018) 752-761. https://doi.org/10.1016/j.memsci.2018.06.046.
[74] Z.-X. Low, J. Ji, D. Blumenstock, Y.-M. Chew, D. Wolverson, D. Mattia, Fouling resistant 2D boron nitride nanosheet – PES nanofiltration membranes, Journal of Membrane Science 563 (2018) 949-956. https://doi.org/10.1016/j.memsci.2018.07.003.
[75] J. Gao, Z. Thong, K.Y. Wang, T.-S. Chung, Fabrication of loose inner-selective polyethersulfone (PES) hollow fibers by one-step spinning process for nanofiltration (NF) of textile dyes, Journal of Membrane Science 541 (2017) 413-424. https://doi.org/10.1016/j.memsci.2017.07.016.
[76] M.T. Tsehaye, J. Wang, J. Zhu, S. Velizarov, B. Van der Bruggen, Development and characterization of polyethersulfone-based nanofiltration membrane with stability to hydrogen peroxide, Journal of Membrane Science 550 (2018) 462-469. https://doi.org/10.1016/j.memsci.2018.01.022.
[77] M. Mertens, C. Van Goethem, M. Thijs, G. Koeckelberghs, I.F.J. Vankelecom, Crosslinked PVDF-membranes for solvent resistant nanofiltration, Journal of Membrane Science 566 (2018) 223-230. https://doi.org/10.1016/j.memsci.2018.08.051.
[78] N. Evenepoel, S. Wen, M. Tilahun Tsehaye, B. Van der Bruggen, Potential of DMSO as greener solvent for PES ultra- and nanofiltration membrane preparation, 135(28) (2018) 46494. https://doi.org/10.1002/app.46494.
[79] C. Wang, Y. Chen, X. Hu, P. Guo, Scalable dual-layer PVDF loose nanofiltration hollow fiber membranes for treating textile wastewater, Journal of Water Process Engineering 46 (2022) 102579. https://doi.org/10.1016/j.jwpe.2022.102579.
[80] D. Yao, F. Zhang, G. Feng, Y. Zhang, J. Meng, High-flux PSF/PES-COOH hollow fiber loose nanofiltration membrane for high-efficiency dye-salt separation, Journal of Environmental Chemical Engineering 10(4) (2022) 108180. https://doi.org/10.1016/j.jece.2022.108180.
[81] Z. Liu, L. Wang, Z. Mi, S. Jin, D. Wang, X. Zhao, H. Zhou, C. Chen, A carboxyl potassium salt polysulfone (PSF-COOK)-embedded mixed matrix membrane with high permeability and anti-fouling properties for the effective separation of dyes and salts, Applied Surface Science 490 (2019) 7-17. https://doi.org/https://doi.org/10.1016/j.apsusc.2019.06.063.
[82] L. Yu, J. Deng, H. Wang, J. Liu, Y. Zhang, Improved Salts Transportation of a Positively Charged Loose Nanofiltration Membrane by Introduction of Poly(ionic liquid) Functionalized Hydrotalcite Nanosheets, ACS Sustainable Chemistry & Engineering 4(6) (2016) 3292-3304. https://doi.org/10.1021/acssuschemeng.6b00343.

[83] L. Xing, N. Guo, Y. Zhang, H. Zhang, J. Liu, A negatively charged loose nanofiltration membrane by blending with poly (sodium 4-styrene sulfonate) grafted SiO2 via SI-ATRP for dye purification, Separation and Purification Technology 146 (2015) 50-59. https://doi.org/10.1016/j.seppur.2015.03.030.
[84] J. Zhu, M. Tian, Y. Zhang, H. Zhang, J. Liu, Fabrication of a novel "loose" nanofiltration membrane by facile blending with Chitosan–Montmorillonite nanosheets for dyes purification, Chemical Engineering Journal 265 (2015) 184-193. https://doi.org/10.1016/j.cej.2014.12.054.
[85] J. Wang, Y. Zhang, J. Zhu, J. Hou, J. Liu, B. Van der Bruggen, Zwitterionic functionalized layered double hydroxides nanosheets for a novel charged mosaic membrane with high salt permeability, Journal of Membrane Science 510 (2016) 27-37. https://doi.org/10.1016/j.memsci.2016.03.016.
[86] B. Wang, J. Ji, K. Li, Crystal nuclei templated nanostructured membranes prepared by solvent crystallization and polymer migration, Nature Communications 7(1) (2016) 12804. https://doi.org/10.1038/ncomms12804.
[87] Y. Shen, A.C.J.C.e.j. Lua, Preparation and characterization of mixed matrix membranes based on PVDF and three inorganic fillers (fumed nonporous silica, zeolite 4A and mesoporous MCM-41) for gas separation, 192 (2012) 201-210.
[88] S. Wu, J. Liang, Y. Shi, M. Huang, X. Bi, Z. Wang, J.J.J.o.M.S. Jin, Design of interchain hydrogen bond in polyimide membrane for improved gas selectivity and membrane stability, 618 (2021) 118659.

# Chapter 6: Confined Growth of 2D MOF Nanosheets within Porous Graphene Oxide Membranes for Long-term Stable Desalination

## 6.1 Abstract

Integration of MOFs and graphene oxide (GO) is a promising strategy to simultaneously achieve both enhanced structural stability of the GO membrane and improved separation efficiency by leveraging the versatile functionality and porosity of the MOF. However, precise and targeted growth of MOFs without interrupting the inherent laminar architecture of GO membrane remains challenging. This study presents a MOF@porous graphene oxide (PGO) composite membrane, where the confined growth of two-dimensional copper 1,4-benzene dicarboxylate (CuBDC) within the PGO matrix enhances structural integrity while preserving water transport pathways. Coordination between $Cu^{2+}$ and oxygen-containing groups on PGO nanosheets mitigates swelling, ensuring long-term stability. The resultant membrane achieves a water flux of 124 kg $m^{-2}$ $h^{-1}$ in conventional pervaporation mode and 89 kg $m^{-2}$ $h^{-1}$ in energy-efficient water carrier pervaporation mode, both while maintaining a NaCl rejection rate above 99.9%. This outstanding performance is attributed to CuBDC's hydrophilicity-induced high capillary pressure, well-preserved $sp^2$ regions, and a shortened transport pathway of the composite membrane. Overall, this study presents a promising strategy for the controlled integration of crystalline frameworks with other advanced 2D materials, enabling the precise design of next-generation frameworks-based composite membranes for various separation applications.




**Keywords:** PGO membrane stabilization, Confined growth, Coordination interaction, Laminar

frameworks, Desalination

## 6.2 Introduction

MOF/COF composite membranes have demonstrated exceptional potential across various separation applications by harnessing the inherent chemistry and structural benefits of porous frameworks while mitigating issues related to intercrystalline defects [1-3]. Among the most promising two-dimensional (2D) materials, graphene oxide (GO) and its derivatives stand out because of their ease of synthesis, chemical stability, and strong antifouling properties, making them highly suitable for membrane-based separations [4, 5]. A single GO nanosheet features by the coexistence of $sp^3$ domains hybridized with oxygen-containing groups and $sp^2$ regions inherited from graphene [6, 7]. The self-assembly of GO nanosheets can be obtained by stacking, leading to a laminar membrane structure. Theoretically, the abundant functional groups on the lamellar planes and edges of the nanolayers impart hydrophilicity, promoting the preferential adsorption of water molecules. Moreover, the non-oxide zones between adjacent GO nanosheets act as 2D capillaries that enables near-frictionless flow of water while impeding transport of larger hydrated species [8, 9]. Despite these advantages, the widespread deployment of GO membranes in aqueous environments remains significantly constrained by their inherent poor stability in aqueous solutions.

The oxygen-containing functional groups in GO membranes pose significant challenges to their structural stability in aqueous environments. These groups readily undergo hydration, generating negative charges that lead to strong electrostatic repulsion between adjacent layers. This repulsion can increase the interlayer spacing, diminish selectivity, and potentially cause delamination of the GO membrane within several hours [10, 11]. Extensive research has sought to mitigate the swelling effect through methods, such as partial reduction [12], covalent crosslinking [13, 14] and crosslinking with multivalent cations [15]. GO reduction is typically achieved via chemical/photo treatments to remove oxygen-containing groups. However, it drastically decrease membrane permeability because of the smaller interlayer spacing in reduced GO [16]. Covalent cross-linking with organic compounds is another method for improving GO membrane stability. This increases interlayer d-spacing, enhancing permeance but at the expense of reduced rejection [11]. Cation-GO crosslinking, which is based on the cations-π interactions and cation oxidizing group interactions, can stabilize the GO structure with controlled interlayer spacing. However, the stability of this interaction is compromised by the leakage of cations when ions with stronger interactions are present [15].

The intrinsic highly tuneable functionalities of MOFs endow them with high potential for stabilizing GO membrane by coordinating with functional groups to mitigate delamination and improve mechanical stability [10, 17, 18]. Furthermore, the intrinsically porous architecture with a tailorable

pore size is expected to increase the number of mass transport pathways and enhance the molecular sieving capability of the resultant membranes [19]. Alemayehu et al. demonstrated the fabrication of an Al-MOF/GO composite membrane using a co-stacking strategy, achieving stable nanofiltration performance over a 80-h continuous dead-end test [20]. Owing to its simplicity, this approach has been widely employed in the construction of GO/MOF composite membranes [21]. Nevertheless, the co-stacking strategy hinges on the independent synthesis of GO and MOFs, followed by their vacuum-assisted assembly. When coordination interactions between metal ions and functional groups on GO are realized after assembly, the dominant interfacial forces are considered as the electrostatic interactions and π−π stacking due to the intrinsic stability of MOFs after synthesis [20, 21]. This inherently weak interlayer adhesion significantly undermines the stabilization efficacy of MOFs within GO membranes, thereby limiting their long-term durability. Moreover, the vacuum-assisted stacking process leads to a random distribution of MOFs within the GO membrane, resulting in a failure to selectively patch lateral defects with the intrinsically porous architecture of the MOFs [18].

The in-situ growth of MOFs within GO membranes represents a highly promising strategy for establishing robust coordination interactions. Recently, Moghadam et al. reported the fabrication of a hybrid PGO/ZIF-8 membrane through a two-step in-situ growth approach, achieving targeted coordination between $Zn^{2+}$ from ZIF-8 and hydroxyl functional groups on GO [22]. This precise coordination not only imparted good structural robustness, enabling the membrane to withstand a 50-h continuous crossflow test, but also enhanced its molecular selectivity. Despite this advancement, the incorporation of three-dimensional (3D) MOFs within the laminar framework of GO has raised fundamental concerns [23]. The laminar structure of GO membranes is particularly advantageous for mass transport in separation processes that are not driven by hydraulic pressure, such as pervaporation and membrane distillation. In these systems, the narrow nanochannels between 2D laminae generate substantial capillary pressure once liquid/vapour interface is established. This provides a key driving force for the efficient transport of water across a large portion of the membrane's nanochannels [24, 25]. However, the integration of MOFs with a 3D configuration inevitably disrupts the ordered laminar framework of GO, significantly compromising structural uniformity and hence effecting capillary pressure. To address this limitation, tailoring the in-situ growth of 2D MOF nanosheets represents a compelling strategy for enhancing GO membrane stability while preserving its advantageous laminar structure. However, achieving this goal remains challenging because of the lack of precise control over targeted nucleation and oriented growth kinetics of 2D MOFs within the interlayer space of GO membranes.

In this work, we fabricate a MOF@GO composite membrane by a confined growth of a water-stable 2D MOF, copper 1,4-benzene dicarboxylate (CuBDC) [26], within the laminar structure of a porous graphene oxide (PGO) membrane (Figure 6.1). The PGO membranes are formed via vacuum coating

via two types of PGO flakes: big-flake PGO (bPGO), with an aspect ratio of 0.8~1.5 μm, and small-flake PGO (sPGO) with size range of 300~400 nm, obtained by fragmenting bPGO through a facile tip-sonication process (Figure 6.1 a, b). These PGO flakes are coated onto alumina hollow fibres (HFs) with various coating times of 40s, 80s, and 120s, resulting in membranes labelled bPGO40s, bPGO80s, bPGO120s, and sPGO40s, sPGO80s, sPGO120s, respectively. The corresponding membrane thicknesses are detailed in Table 6.1. CuBDC nanosheets are synthesized in-situ in the vacuum-coated PGO HF membrnes via a contra-diffusion method (Figure 6.1 a). The oxygen-containing groups of the PGO nanosheets highlighted with red circles in Figure 6.1 b offer reactive sites to coordinate with metal ions, promoting the in-situ formation of metal cluster and facilitating robust interactions between the MOF and PGO. The CuBDC loading is significantly increased in the sPGO-based composite membrane because of the increased density of reactive sites (Figure 6.1 c). The targeted coordination of reactive sites with CuBDC significantly enhances the structural robustness of the composite membrane, ensuring the stabilization of the PGO membrane during desalination tests conducted via, reverse osmosis (RO), pervaporation and energy-efficient water carrier pervaporation (analogous to direct contact membrane distillation).

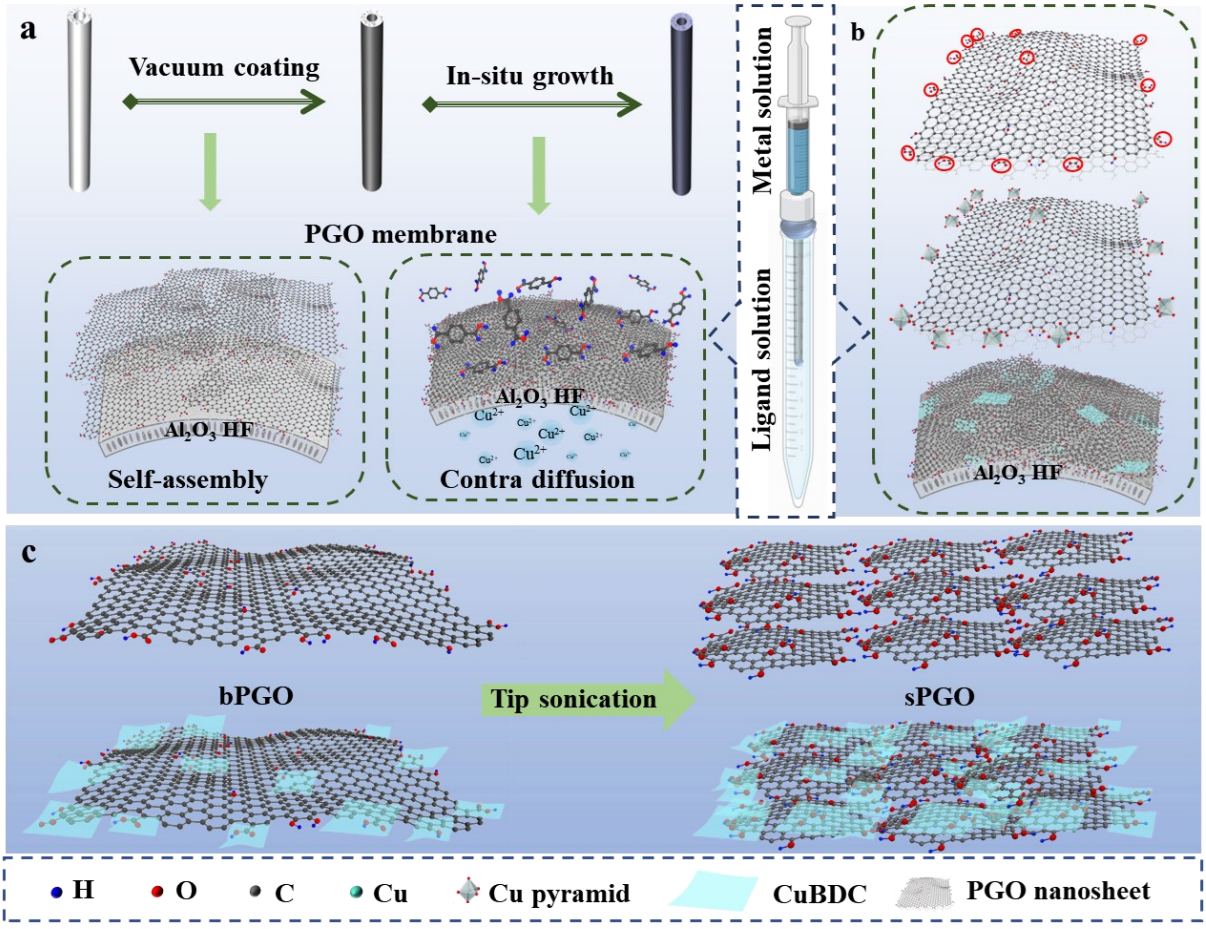



Figure 6.1 Schematic illustration of the membrane fabrication process. (a) Fabrication process of the

CuBDC@PGO composite membrane, (b) CuBDC-PGO interaction via coordination between oxygen-containing groups and the Cu pyramid, and (c) schematic illustration of the increase in reactive sites resulting from the fragmentation of bPGO into sPGO and the corresponding increase in CuBDC loading.

Notably, the composite membranes exhibit superior desalination performance in pervaporation. The improvement in water permeance and salt rejection can be attributed to the regulated growth of the CuBDC nanosheets, which imparts increased hydrophilicity and porosity to the membrane. The resulting laminar structure of the composite membrane with well-defined microchannels as well as its hydrophilic nature is expected to exhibit ultrahigh capillary pressure for aqueous solutions, enhancing mass transfer during the pervaporation process. This results in an exceptional flux of up to 124 kg $m^{-2}$ $h^{-1}$. In a low-energy water carrier pervaporation system (Figure 6.3), the membrane sustains a high flux of 89 kg $m^{-2}$ $h^{-1}$ over an extended testing period. Overall, this study constructively employs a contra-diffusion strategy for the in-situ growth of 2D MOFs, that are precisely patched the defects and aligned with the laminar framework of PGO membranes. This integration yields a structurally robust and water-stable composite architecture, offering a promising pathway for enhancing the stability and performance of 2D frameworks in molecular separation technologies.

## 6.3 Material and Methods

### 6.3.1 Material and membrane fabrication

To synthesize CuBDC, copper nitrate trihydrate ($Cu(NO_3)_2 \bullet 3H_2O$, Sigma Aldrich, 99%), and terephthalic acid ($H_2BDC$, Sigma Aldrich, 98%) were utilized without further purification. Graphite powder (99% carbon basis, 325 mesh) used for PGO synthesis was purchased from Sigma Aldrich. Details of other chemicals can be found in Section 3.1.

### 6.3.2 Preparation of alumina hollow fibre and disc as substrate

The alumina-based substrate was prepared following the methodology outlined in Section 3.2.

### 6.3.3 PGO nanosheets preparation

Two types of PGO nanosheets, big-flake PGO (bPGO) and small-flake PGO (sPGO), were prepared according to methods described in Section 3.3.3.

### 6.3.4 Membrane fabrication

PGO HF membranes were fabricated via a vacuum coating method, and subsequent CuBDC patching was achieved via a contra diffusion strategy with the experimental details given in Section 3.3.

### 6.3.5 Characterizations

Characterizations conducted in this chapter include SEM, EDX, FTIR, XPS, TGA, DLS, Raman, thermal conductivity, AFM, and XRD, with detailed descriptions available in Section 3.4.

### 6.3.6 Desalination tests

#### 6.3.6.1 Desalination performance test via RO

Desalination performance via conventional RO is introduced in detail in Section 3.4.12

#### 6.3.6.2 Desalination performance test via pervaporation

The PV performance of all samples was evaluated using a custom-built setup (Figure 6.2). In this setup, the membrane was sealed at one end and connected to a vacuum pump at the other end, providing an effective membrane area of 1.73 cm². A NaCl solution with a concentration of 3.5 wt% was circulated over the outer surface of the membrane under continuous stirring at 70 °C. A liquid nitrogen cold trap was used downstream between the membrane and the vacuum pump to collect the permeate.

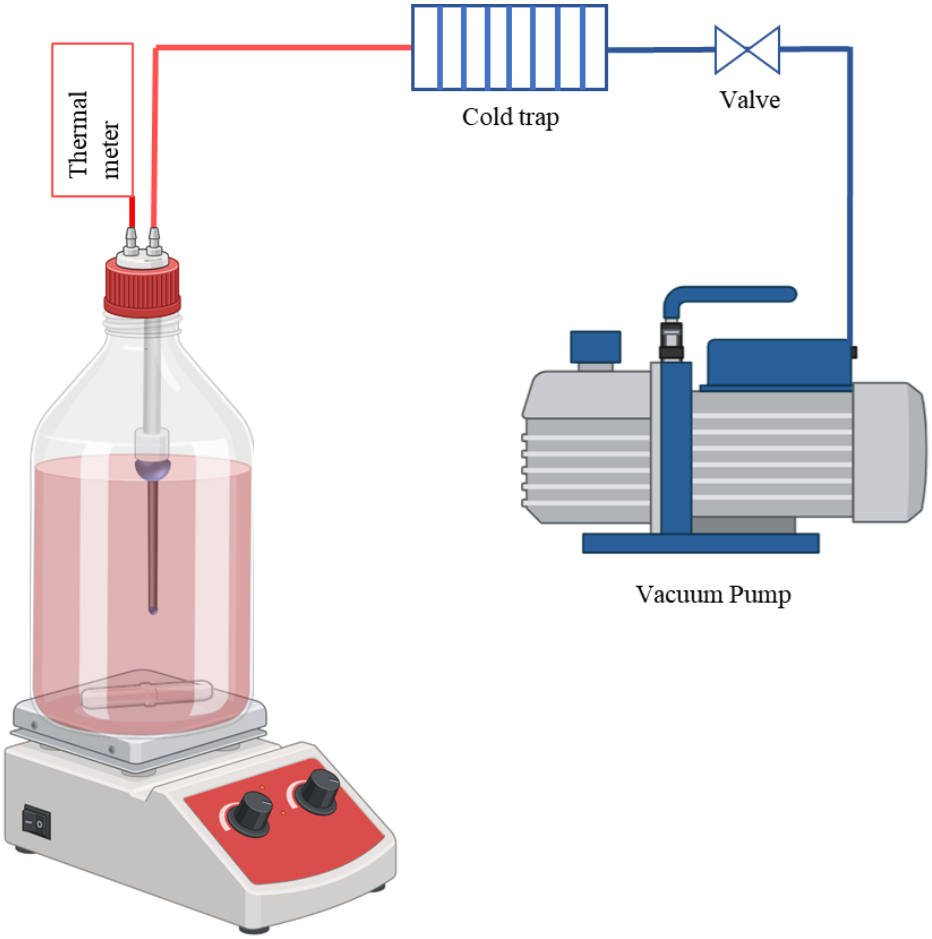



Figure 6.2 Illustration of the pervaporation setup. The effective membrane area is approximately

1.73 $cm^2$.

6.3.6.3 Desalination performance test via water carrier pervaporation

Water carrier pervaporation was conducted using a laboratory-made setup. As illustrated in Figure 6.3, an HF module, assembled by potting two pieces of 13-cm HF membranes (with a total effective area of 17.97 $cm^2$) with Araldite adhesive, was connected to two flow streams. The feed stream (indicated by the red arrows) containing 3.5 wt% NaCl circulated over the outer surface of the membrane at a flow rate of 35 mL $min^{-1}$, whereas a cold deionized water stream (blue arrows) continuously circulated through the membrane lumen. Both streams were driven by peristaltic pumps, with the feed stream temperature controlled at 60 °C via a hot plate. The pressure on the feed side was regulated to 1 bar via a valve (V). The inlet and outlet temperatures of the feed stream were monitored with thermocouples ($T_{f1}$, $T_{f2}$), and the pressure was tracked by pressure sensors ($P_{f1}$, $P_{f2}$). Similarly, the permeate side temperatures at the inlet ($T_{p1}$) and outlet ($T_{p2}$) were also monitored and recorded. The flow rates on both the feed and permeate sides were measured as $F_f$ and $F_p$, respectively. The PV performance was assessed based on the change in weight and conductivity of the permeate tank.

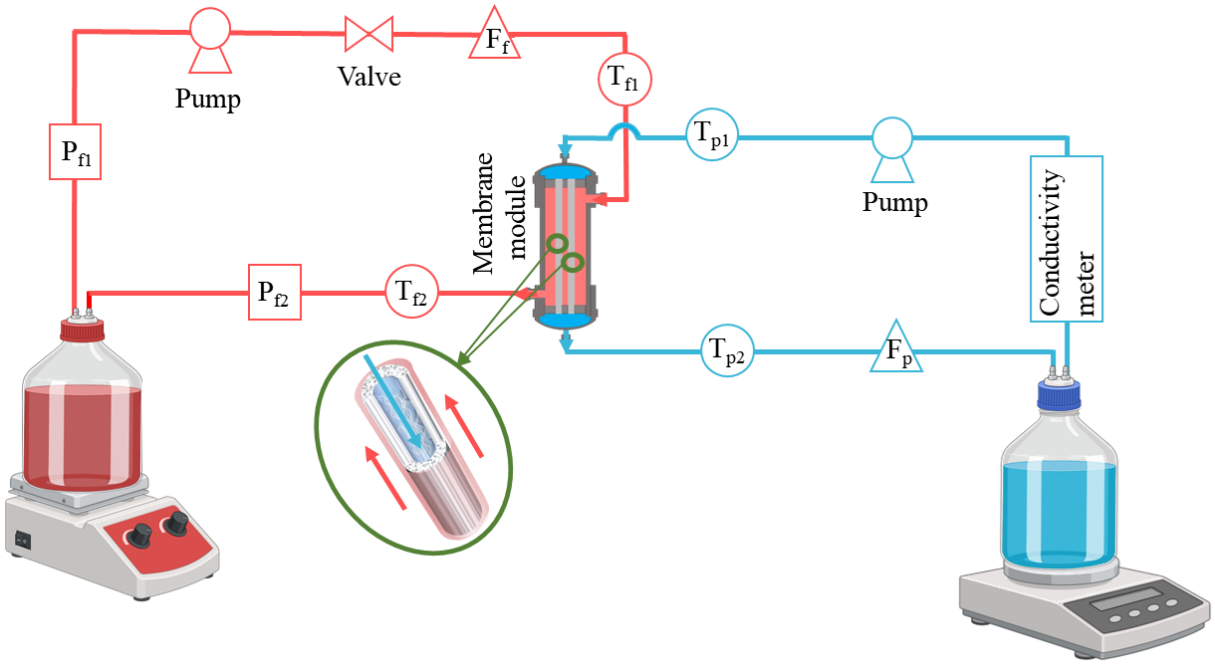



Figure 6.3 Illustration of water carrier pervaporation (analogous to direct contact membrane distillation (DCMD)). The membrane module contains two pieces of HF membranes, providing an effective test area of 17.97 $cm^2$.

## 6.4 Results and Discussion

### 6.4.1 Fabrication and characterizations of the membranes

As depicted by Figure 6.1 a, PGO nanosheets with atomically thin 2D structure readily self-assembled into a layered structure film under vacuum filtration. Notably, there was no significant difference between the surface and cross-sectional morphologies of bPGO and sPGO membranes, as shown in Figure 6.4. As the coating time increased, the membrane thickness increased from approximately 40 nm to 130 nm. The ultrathin nature of the membranes allowed the underlying protuberances of the alumina substrate to remain visible. The subsequent CuBDC loading was achieved by in-situ growth using a contra-diffusion technique. Under contra diffusion of the metal and ligand solutions from the lumen and shell side of the PGO-HF membrane, respectively, the metal cluster were formed first by pyramidally coordinating $Cu^{2+}$ with five O atoms. The metal pyramids then coordinatively linked with the carboxyl groups of terephthalic acid (Figure 6.1 a, b), forming CuBDC in the PGO membrane. The oxygen-containing groups on the PGO nanosheets played a dual role in this process: they either directly participated in metal cluster formation or coordinated with preformed clusters, both of which facilitated the subsequent growth of the MOF (Figure 6.1 b) [18, 27].

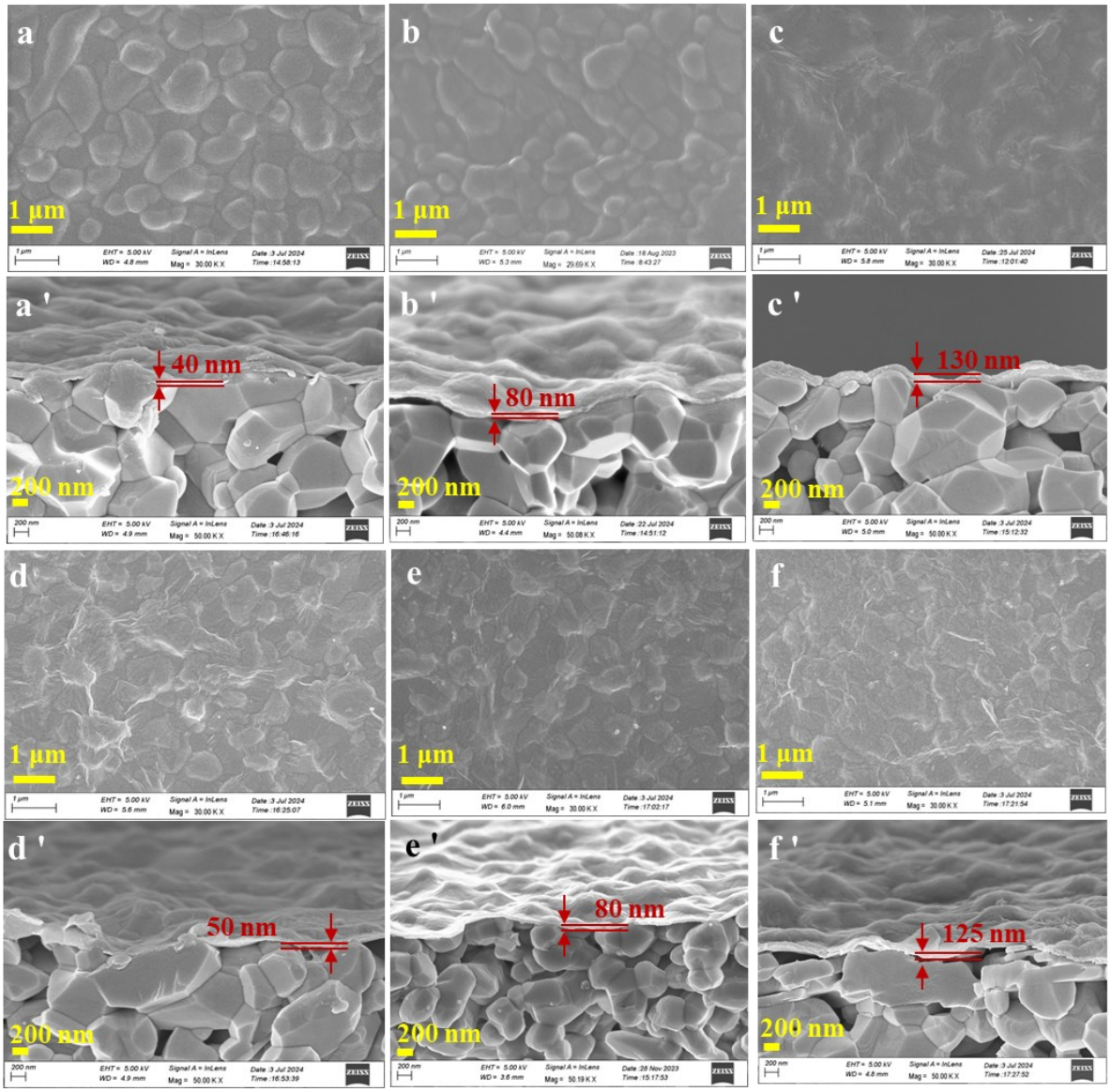



Figure 6.4 Morphology of the PGO membranes. (a-f) Surface and cross-sectional morphologies of (a, a') bPGO40s, (b, b') bPGO80s, (c, c') bPGO120s, (d, d') sPGO40s, (e, e') sPGO80s, and (f, f') sPGO120s.

The surface and cross-sectional structures of the CuBDC@bPGO composite membranes were observed using SEM (Figure 6.5 a-c). Highlighted in light blue, the CuBDC nanosheets on the bPGO membrane displayed a tetragonal or nearly tetragonal shape with lateral dimensions ranging from 0.4~2 µm. The square edges were also observed in the cross-sectional images highlighted by blue circles, as shown in Figure 6.5 a', b', confirming the successful growth of CuBDC within the interlayers of the bPGO membrane. This is further reflected by the 12.5~5.4% growth in the membrane thickness relative to the pristine bPGO membrane as shown in Table 6.1.

Table 6.1 Comparison of membrane thickness before and after the growth of CuBDC

| Membrane | Thickness (nm) | Increase ratio (%) |
|---|---|---|

| | | |
|---|---|---|
| bPGO40s | 40 | / |
| CuBDC@bPGO40s | 45 | 12.5 |
| bPGO80s | 80 | / |
| CuBDC@bPGO80s | 90 | 12.5 |
| bPGO120s | 130 | / |
| CuBDC@bPGO120s | 150 | 15.4 |
| sPGO40s | 50 | / |
| CuBDC@sPGO40s | 80 | 60 |
| sPGO80s | 80 | / |
| CuBDC@sPGO80s | 120 | 50 |
| sPGO120s | 125 | / |
| CuBDC@sPGO120s | 200 | 60 |

The CuBDC loading in the composite membrane was enhanced in the sPGO-based membranes because of the increased number of reactive sites. As observed in Figure 6.5 d-f, CuBDC nanosheets with a consistent tetragonal morphology nearly achieve complete surface coverage. This higher loading led to a 50~60% increase in membrane thickness for CuBDC@sPGO (Table 6.1), indicating increased loading on both the surface and within the interlayer of the sPGO membrane. The increased MOF loading is attributed to the increased number of reactive sites. As illustrated in Figure 6.1 b, c, oxygen-containing functional groups, which coordinate with the MOF, are located primarily at the edge and defect sites of the PGO layer [28, 29]. Mild tip-sonication reduced the flake size of bPGO nanosheets from 0.8~1.5 μm to approximately 300~400 nm for sPGO, as shown by the AFM images and flake size distributions of the bPGO and sPGO nanosheets measured by DLS, as shown in Figure 6.5 g. This reduction increased the number of exposed edges per unit area, providing more coordination sites and thereby promoting higher MOF loading.

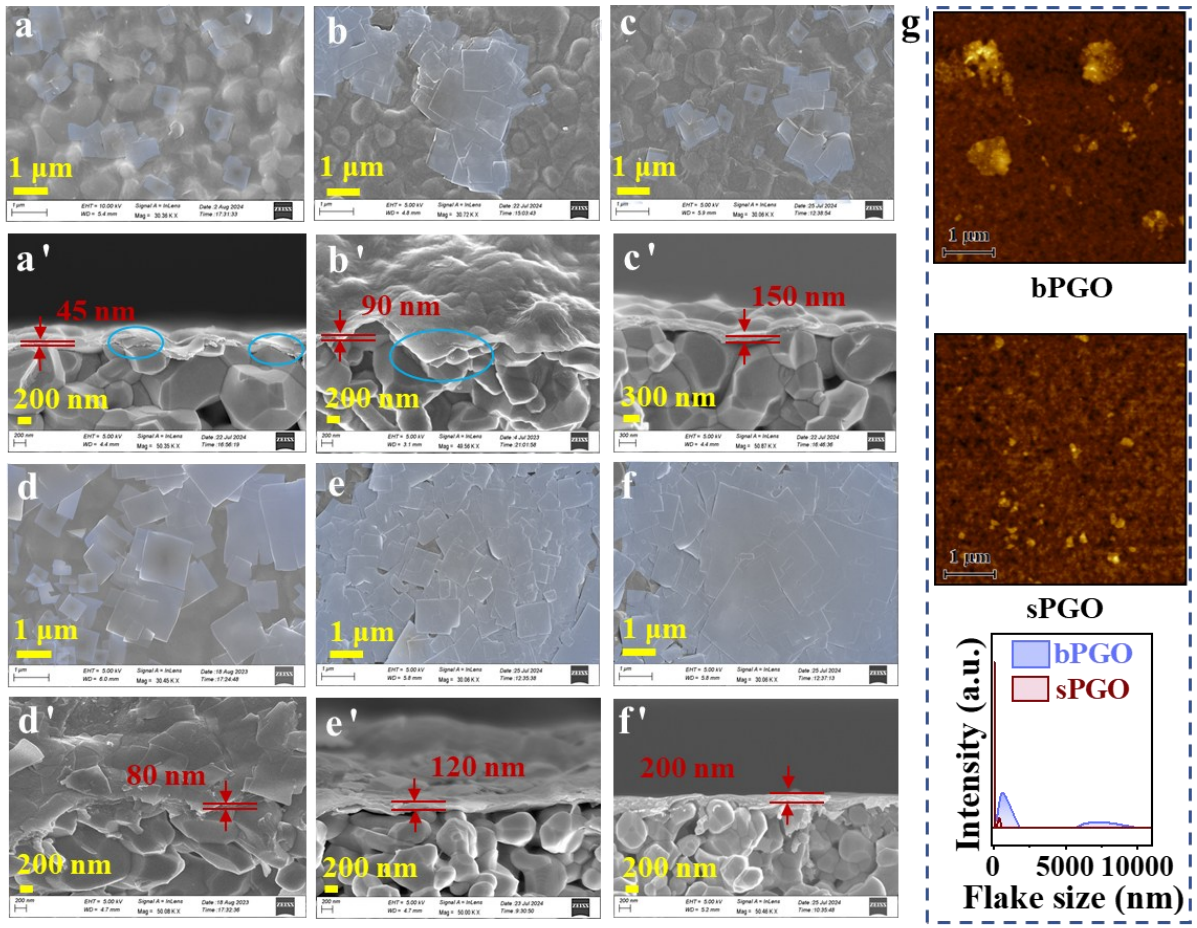



Figure 6.5 Morphology of the membranes and the flake size of the bPGO nanosheet. a-f) Surface and cross-sectional morphologies of (a, a') CuBDC@bPGO40s, (b, b') CuBDC@bPGO80s, (c, c') CuBDC@bPGO120s, (d, d') CuBDC@sPGO40s, (e, e') CuBDC@sPGO80s, and (f, f') CuBDC@sPGO120s; g) AFM image of the bPGO and sPGO flakes and the flake size distributions of the bPGO and sPGO nanosheets measured via dynamic light scattering (DLS).

The formation of the CuBDC@PGO composite membrane was further confirmed by elemental mapping, as shown in Figure 6.6. While C element was uniformly distributed in all the samples, Cu was detected only in the CuBDC@PGO composite membranes, with a relatively high density in CuBDC@sPGO. Because the membrane is thin, the Al signal from the alumina support appears on the surface of the untreated PGO membrane and in areas without Cu in the composite membranes.

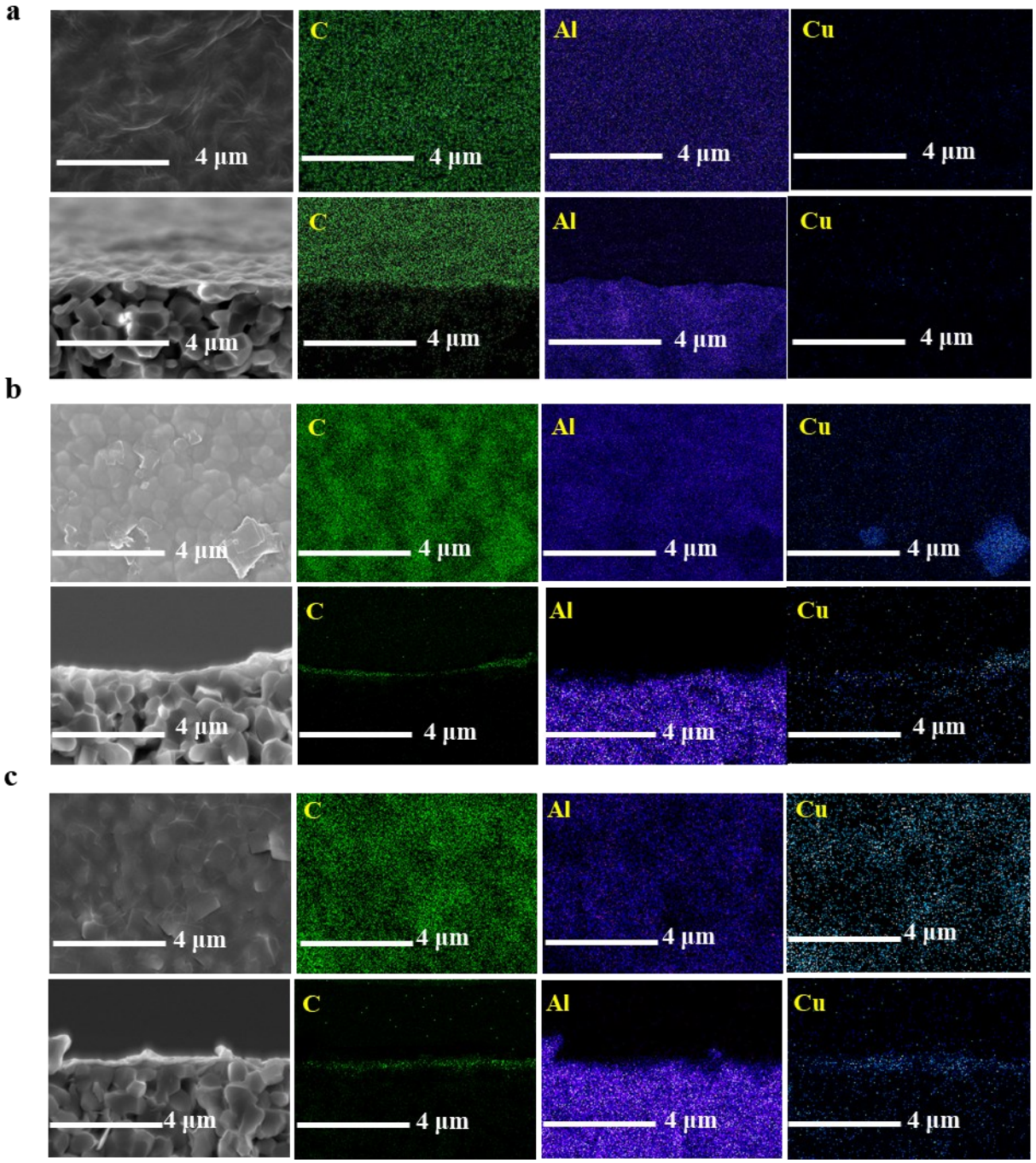



Figure 6.6 Surface and cross-sectional EDX mapping analysis of the (a) bPGO40s (b) CuBDC@bPGO40s and (c) CuBDC@sPGO40s membranes.

The confined growth of 2D CuBDC nanosheets within the laminar framework of the PGO membrane was confirmed by SEM imaging. As shown in Figure 6.7 a, a mechanical exfoliation method with the assistance of adhesive tape was utilized to reveal the inner microstructure of the CuBDC@sPGO40s membrane. After exfoliated, the membrane was partially attached to the tape (Figure 6.7 b), while the remaining structure was retained on the HF surface (Figure 6.7 c), thereby exposing the inner structure of the composite membrane. CuBDC nanosheets were found to be well aligned along the inner sPGO

basal planes, highlighted in light blue, on randomly selected areas of both the layers adhered to the tape and those remaining on the HF surface. Compared with the nanosheets formed on the outer surface of the membrane, these internally confined nanosheets exhibited lower density and smaller lateral dimensions, ranging from 0.2 to 0.6 μm. This observation provides strong evidence of the confined growth of the CuBDC nanosheets within the PGO membrane structure.

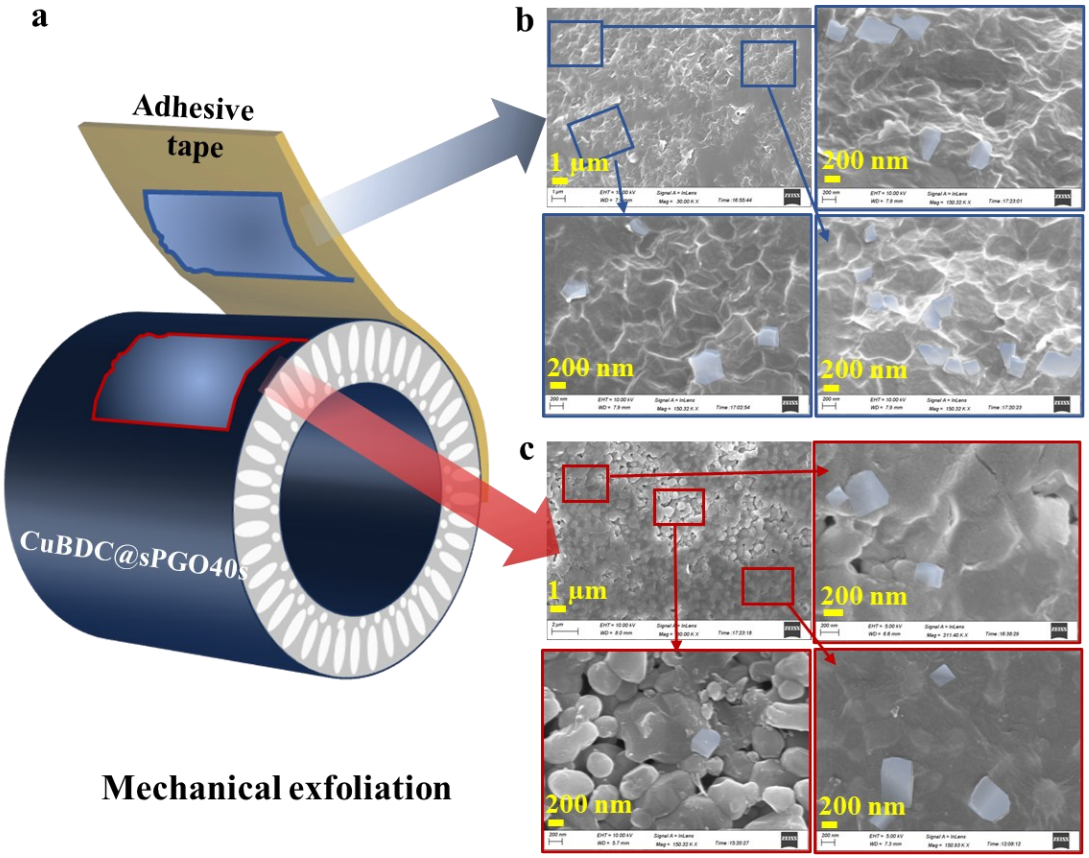



Figure 6.7 Inner microstructure of the CuBDC@sPGO40s membrane. (a) Illustration of mechanical exfoliation assisted by adhesive tape. (b) Microstructure of the membrane adhered to the tape; regions outlined in blue frames are shown at higher magnification, as indicated by the corresponding arrows. (c) Microstructure of the membrane remained on the HF surface; regions outlined in red frames are shown at higher magnification, as indicated by the corresponding arrows.

In the contra diffusion process, the PGO layer served as both a loading platform, providing the reactive sites for MOF loading, and a barrier, preventing bulk CuBDC formation. Typically, bulk CuBDC forms rapidly, leading to densely packed lamellae when metal and ligand solutions are mixed directly [26]. The proposed strategy successfully confines CuBDC intergrowth through a combination of limited nutrient supply inherent to the contra-diffusion technique, spatial constraints imposed by the layered structure of PGO, and the absence of reactive sites in the $sp^2$ regions [30]. These factors collectively ensure the preservation of the laminar architecture, which is critical for maintaining the functionality and stability

of the membrane.

The XPS spectra shown in Figures 6.8 and 6.9 reveal the elemental composition and bonding interactions within the membranes. The full-range spectrum (Figure 6.8) shows an increased O 1s peak intensity in the sPGO membrane, indicating an increase in the oxygen content from 25 at% to 29 at% (Table 6.2). This increase is further confirmed by the Raman spectra shown in Figure 6.9 d, where the increase in the $I_D/I_G$ ratio from 0.95 to 1.08 reflects a greater density of oxygen-containing functional groups, which serve as reactive sites for CuBDC coordination. Consequently, the CuBDC@sPGO membrane has a significantly greater copper content (22 at%), nearly four times greater than that of CuBDC@bPGO (5 at%), as shown in Table 6.2.

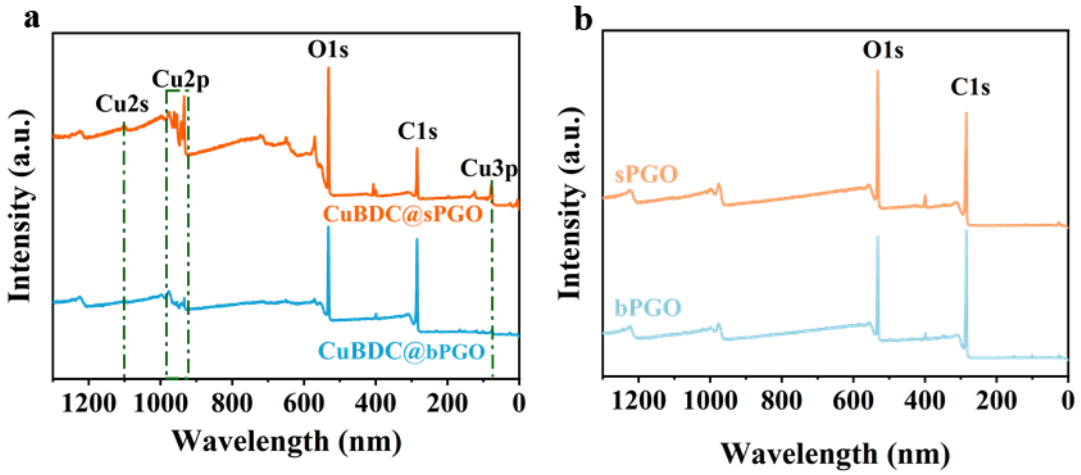



Figure 6.8 Full-rang XPS spectra of the membrane. (a) and (b) CuBDC@PGO40s and pristine PGO40s membrane, respectively.

Table 6.2 Atomic percentages of C, O, and Cu elements in the fabricated membranes.

| Membrane | Carbon (Atomic percentage, at%) | Oxygen (Atomic percentage, at%) | Copper (Atomic percentage, at%) |
|---|---|---|---|
| bPGO | 75 | 25 | / |
| sPGO | 71 | 29 | / |
| CuBDC@bPGO | 67 | 25 | 5 |
| CuBDC@sPGO | 38 | 37 | 21 |

High-resolution XPS spectra (Figure 6.9 a-c) confirmed the interaction between the CuBDC and PGO membranes. As shown in Figure 6.9 a, the O 1s spectra of the composite membranes show three characteristic peaks, with a new peak at 530.9 eV corresponding to O anions in the crystalline CuBDC network [29]. This peak is more intense in the spectrum of CuBDC@sPGO, suggesting enhanced

coordination between the Cu and oxygen functional groups. Additionally, shifts in C=O (from 531.3 eV to 532.1 eV) and C–O (from 532.6 eV to 532.8 eV) for PGO imply electron transfer from oxygen-containing groups to Cu(II), confirming coordination interactions [28]. This observation supports our hypothesis that the metal clusters of CuBDC interact with the PGO membrane through coordination interactions. In addition, the composite membranes also retain intense C–C/C=C peaks, as shown in Figure 6.9 b, indicating that the $sp^2$-hybridized domains remain intact after MOF loading, which is consistent with the Raman spectra (Figure 6.9 d,). This is potentially related to the well-preserved laminar structure stacked by π–π stacking in the fabricated membranes [31].

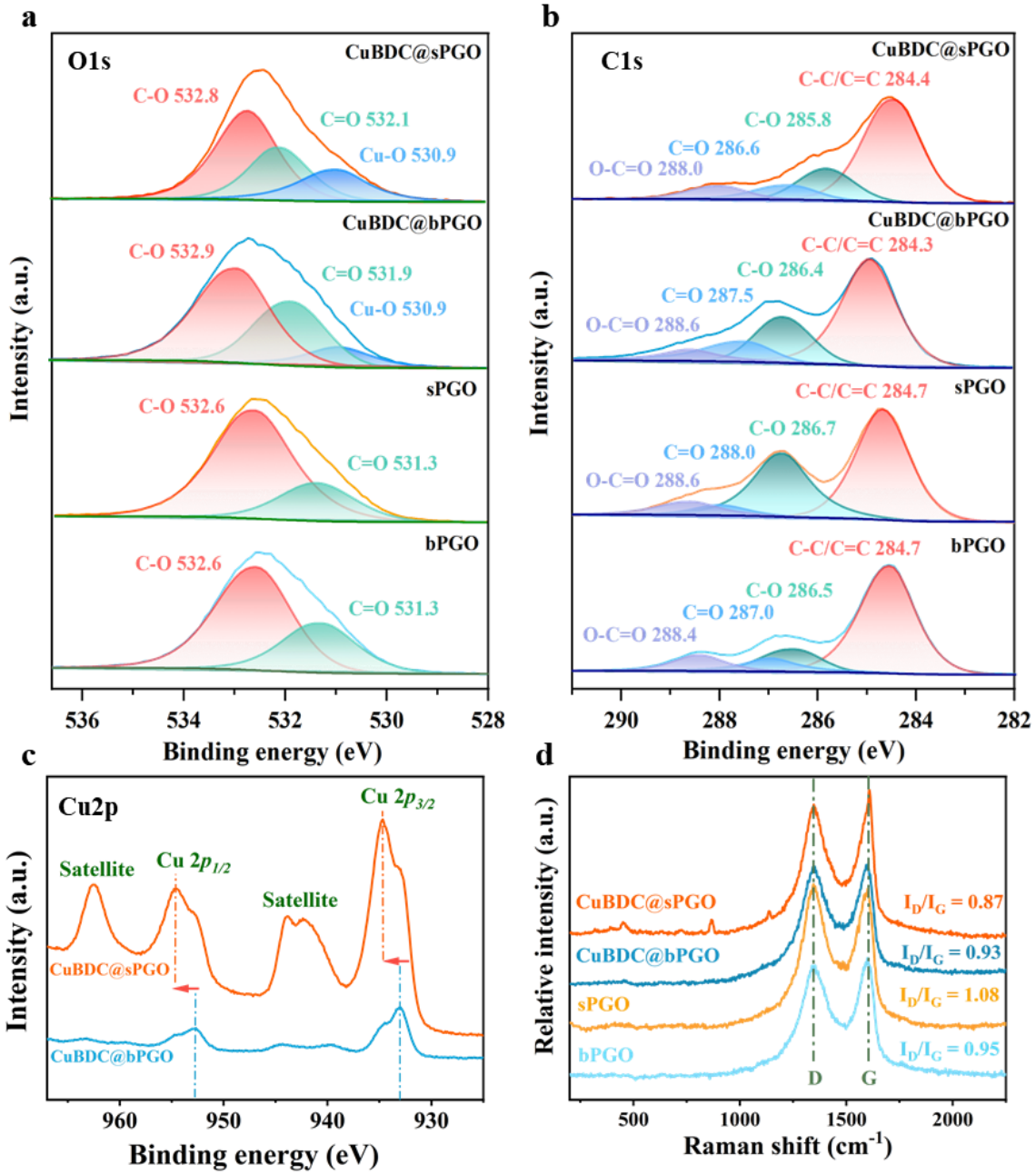



Figure 6.9 High-resolution XPS and Raman spectra. High-resolution XPS (a) O1s, (b) C1s, and (c) Cu2p

and (d) Raman spectra of the bPGO40s, sPGO40s, CuBDC@bPGO40s and CuBDC@sPGO40s membranes.

The Cu2p spectra (Figure 6.9 c) of CuBDC@PGO display two characteristic peaks at 934.5 eV ($Cu2p_{3/2}$) and 953.7 eV ($Cu2p_{1/2}$) [32], along with "shake-up" satellite peaks, confirming Cu(II) coordination within the layered structured membranes via coordination with carboxyl groups from both the terephthalate ($BDC^{2-}$) and the PGO membrane [33]. The intensity of the Cu(II) signal in CuBDC@bPGO is approximately one-fourth that of the sPGO-based membrane, correlating directly with oxygen content (Table 6.2). This suggests that CuBDC primarily interacts with PGO via coordination with oxygen functional groups rather than mere physical confinement within interlayer spaces. Theoretically, this coordination occurs through two mechanisms: (1) direct $Cu^{2+}$ coordination with hydroxyl groups, forming metal clusters, and (2) subsequent interaction of the clusters with carboxyl groups. The observed slight shift in Cu(II) peaks to higher binding energy (Figure 6.9 c) supports electron cloud migration from Cu to O atoms, enhancing membrane stability against hydration [34, 35].

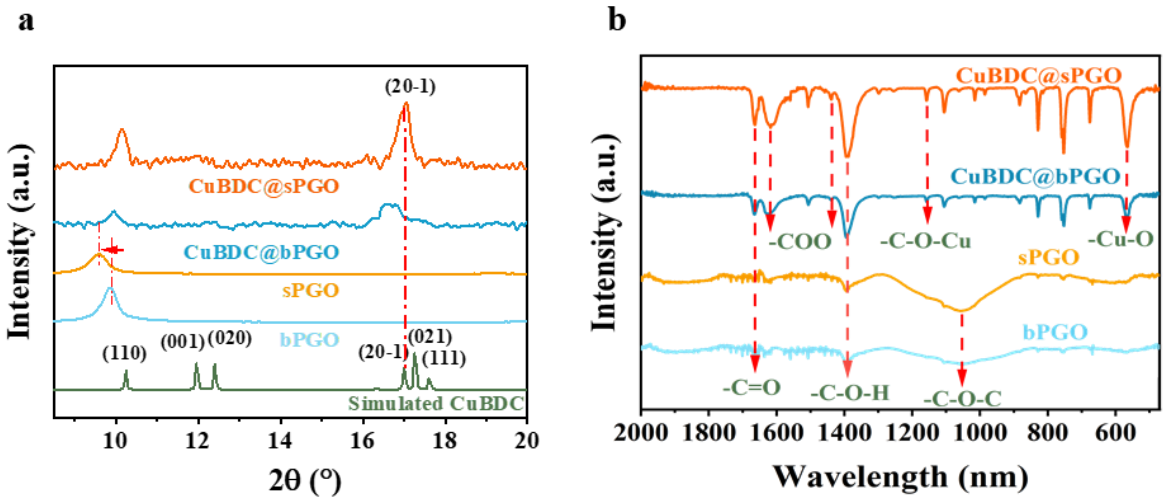



Figure 6.10 XRD and FTIR patterns of the membrane. (e) XRD patterns of the simulated CuBDC and bPGO40s, sPGO40s, CuBDC@bPGO40s and CuBDC@sPGO40s membranes. (f) FTIR spectra of the bPGO40s, sPGO40s, CuBDC@bPGO40s and CuBDC@sPGO40s membranes.

XRD patterns confirmed that structural changes were induced by the incorporation of CuBDC. The diffraction peak shown in Figure 6.10 a shifting from 9.83° (bPGO) to 9.56° (sPGO) indicates a slight increase in the interlayer d-spacing, attributed to enhanced electrostatic repulsion and edge-to-edge interactions among small PGO flakes [36, 37]. The peak at approximately 10° in the spectrum of CuBDC@sPGO lies between the PGO feature peak and the CuBDC (110) peak at 10.25°, suggesting that the peak overlaps due to CuBDC coordination. The broad peak at 16.25~7.85° corresponds to CuBDC. According to the Scherrer equation, this broad peak with a wider full width at half maximum (FWHM)

suggests a smaller CuBDC crystal size, indicating its confined growth within the PGO interlayers, as confirmed by SEM images [38]. Notably, the (20-1) CuBDC peak is prominent, whereas the (001) and (020) peaks disappear, implying that the CuBDC nanosheets are preferentially confined within the laminar structure of PGO [33, 39, 40].

The FTIR spectra shown in Figure 6.10 b further confirmed the formation of CuBDC and its interaction with PGO. The peaks at 1616 $cm^{-1}$ and 1422 $cm^{-1}$ correspond to asymmetric and symmetric -$COO^-$ stretching, confirming that CuBDC forms via $BDC^{2-}$ linker coordination with $Cu^{2+}$ [40]. The presence of a -Cu-O stretching peak at 562 $cm^{-1}$ supports CuBDC incorporation, whereas a newly emerged peak at 1116 $cm^{-1}$ (-C-O-Cu stretching) signifies Cu coordination with oxygen functional groups in the sPGO membrane [33]. These interactions enhance interlayer adhesion, bridging voids between adjacent nanosheets and improving membrane stability [41].

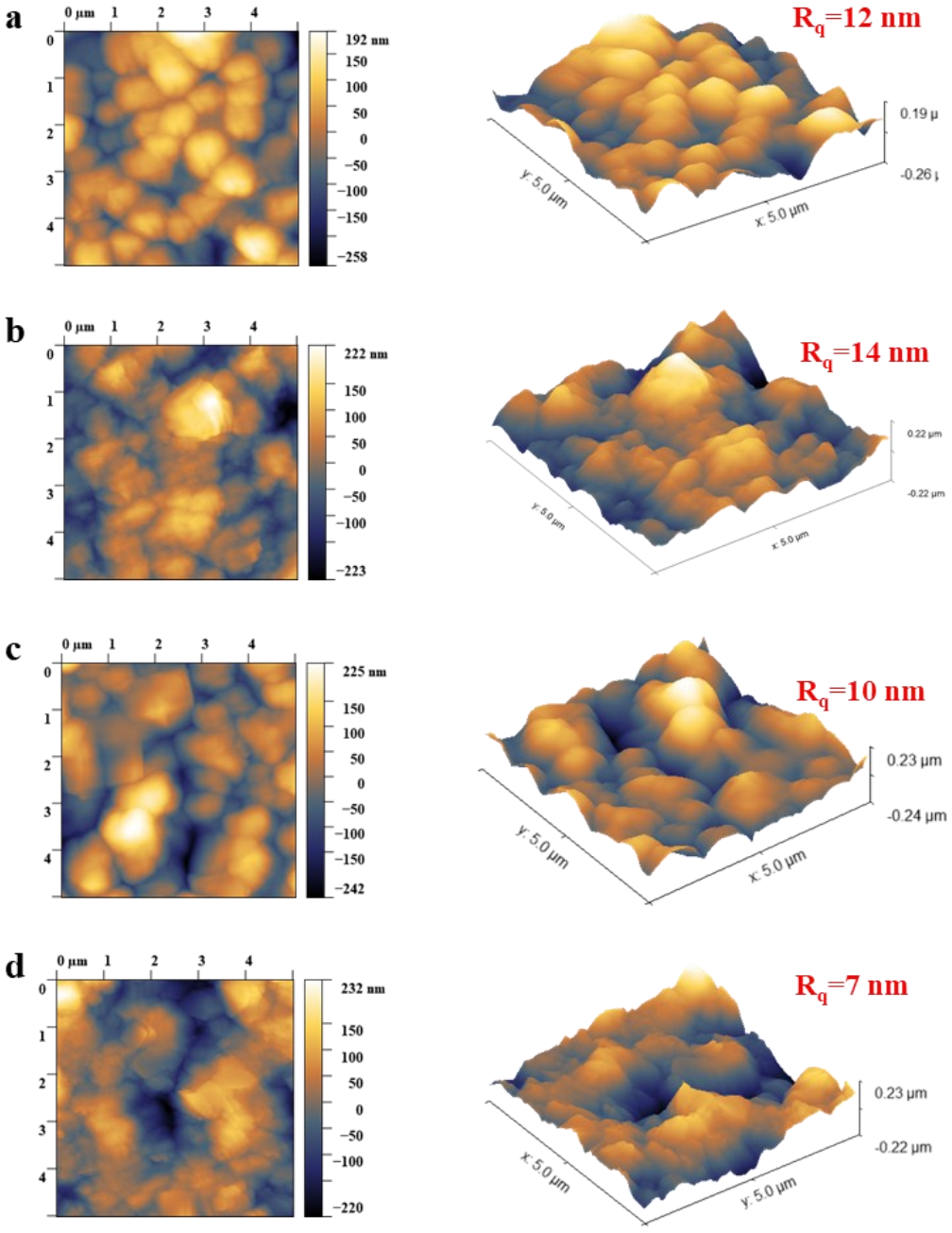



Figure 6.11 Surface roughness of the membranes. 2D and 3D surface roughness of the (a) bPGO40s, (b) sPGO40s, (c) CuBDC@bPGO40s and (d) CuBDC@sPGO40s membranes.

Surface roughness plays a crucial role in membrane fouling behaviour [42]. AFM analysis (Figure 6.11) reveals a rougher surface for sPGO ($R_q$ = 14 nm, Figure 6.11 b) than bPGO ($R_q$ = 12 nm, Figure 6.11 a) supported on the alumina substrate. The increased roughness of the sPGO membrane is attributed to the increased density of nanosheet edges. Upon CuBDC incorporation, the roughness decreases to 10 nm (CuBDC@bPGO, Figure 6.11 c) and 7 nm (CuBDC@sPGO, Figure 6.11 c) because of the smooth morphology of the CuBDC nanosheets. The reduced roughness is expected to enhance antifouling

performance by minimizing contact points for contaminants and reducing pollutant accumulation [43].

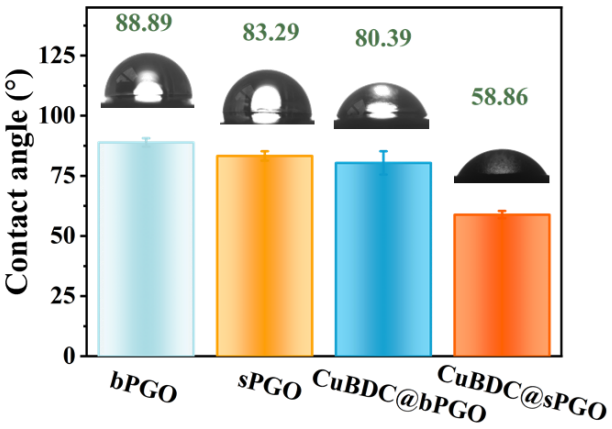



Figure 6.12 Water contact angles of the membranes.

A smoother surface correlates with lower water contact angles [44]. As shown in Figure 6.12, CuBDC@sPGO has a contact angle of 58.86°, indicating enhanced hydrophilicity. This increased water affinity arises from both the hydrophilic nature of CuBDC [45] and the reduction in surface roughness. In contrast, pristine PGO membranes display a higher contact angle (~90°) due to the coexistence of hydrophobic $sp^2$ regions and hydrophilic $sp^3$ domains [46]. Improved surface hydrophilicity enhances water flux by facilitating water adsorption and reduces fouling by forming a protective hydration layer [47, 48].

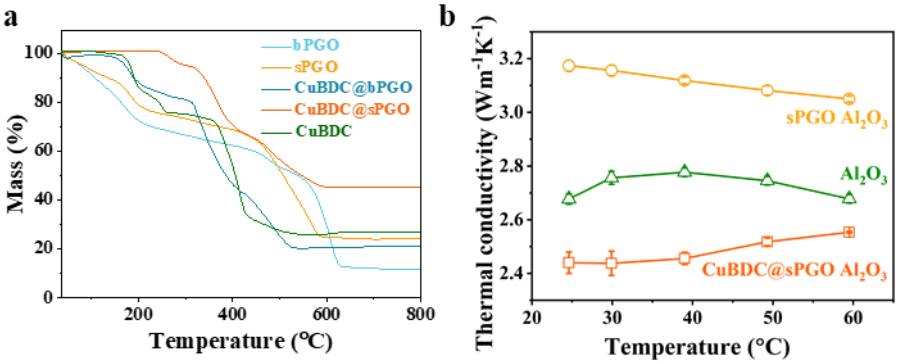



Figure 6.13 Thermal properties of the membranes. (a) TGA plot of the CuBDC, bPGO, sPGO, CuBDC@bPGO, and CuBDC@sPGO membranes measured under $N_2$ atmosphere. (b) Thermal conductivity of the $Al_2O_3$ HF substrate, sPGO HF membrane and CuBDC@sPGO membrane.

Figure 6.13 a illustrates the thermal stability of the membranes. The CuBDC@sPGO composite membrane remains stable up to 220°C, whereas CuBDC@bPGO degrades below 140°C because of the lower CuBDC loading. Pristine PGO membranes exhibit early weight loss, attributed to the pyrolysis of oxygen-containing functional groups, indicating poor thermal stability [49]. The improved stability of

CuBDC@sPGO is due to the coordination of $Cu^{2+}$ with oxygen functional groups, which strengthens the interlayer interactions. The higher stability of CuBDC@sPGO over CuBDC@bPGO highlights the importance of increasing the number of reactive sites on the PGO layers for effective stabilization.

Table 6.3 Parameters used for calculating the thermal conductivity of the fabricated membranes

| Samples | Temperature (°C) | ρ (g $m^3$) | α ($m^2$ $s^{-1}$) | $C_p$ (J $g^{-1}$ $K^{-1}$) | K (W $m^{-1}$ $K^{-1}$) |
|---|---|---|---|---|---|
| $Al_2O_3$ | 24.6 | 1108422.296 | 0.000002776 | 0.87 | 2.676973 |
| | 29.9 | 1108422.296 | 0.000002769 | 0.898 | 2.756161 |
| | 39 | 1108422.296 | 0.000002671 | 0.938 | 2.777039 |
| | 49.3 | 1108422.296 | 0.000002543 | 0.974 | 2.745431 |
| | 59.5 | 1108422.296 | 0.000002416 | 1 | 2.677948 |
| sPGO $Al_2O_3$ | 25.4 | 1162146.965 | 0.000002975 | 0.918 | 3.173881 |
| | 30 | 1162146.965 | 0.000002889 | 0.94 | 3.155996 |
| | 39.2 | 1162146.965 | 0.00000273 | 0.983 | 3.118726 |
| | 49.6 | 1162146.965 | 0.000002572 | 1.031 | 3.081702 |
| | 58.6 | 1162146.965 | 0.000002455 | 1.069 | 3.049933 |
| CuBDC @sPGO $Al_2O_3$ | 25.9 | 948541.6758 | 0.000002852 | 0.902 | 2.440127 |
| | 29.9 | 948541.6758 | 0.000002728 | 0.942 | 2.43754 |
| | 39.3 | 948541.6758 | 0.00000261 | 0.992 | 2.455888 |
| | 49.5 | 948541.6758 | 0.000002481 | 1.07 | 2.518065 |
| | 59 | 948541.6758 | 0.000002393 | 1.125 | 2.553593 |

Thermal conductivity is a key factor in evaluating membrane performance when it is used for direct contact membrane distillation (DCMD). Laser flash apparatus (LFA) measurements (Figure 6.13 b, Table 6.3) show that all the tested samples had significantly lower thermal conductivities than the commercial alumina membranes (18 W $m^{-1}K^{-1}$) [50]. This highlights the advantageous porous structure of the alumina substrate. The average thermal conductivity of the alumina support was approximately 2.7-2.8 W $m^{-1}$ $K^{-1}$, which increased to 3.2-3.0 W $m^{-1}$ $K^{-1}$ after coating the sPGO membrane and decreased to 2.4-2.6 W $m^{-1}$ $K^{-1}$ in the case of the CuBDC@sPGO composite membrane. The slight increase in thermal conductivity after coating with sPGO arises from the low-density $sp^2$ domains and increased photon

scattering [51]. However, the porous structure of MOFs endows them with an ultralow thermal conductivity, which is generally less than 0.5 W $m^{-1} K^{-1}$ [52]. A membrane with low thermal conductivity offers promising thermal insulation, reducing heat transfer across the membrane and ensuring high thermal efficiency in practical applications such as DCMD for seawater desalination [53].

### 6.4.2 Desalination performance

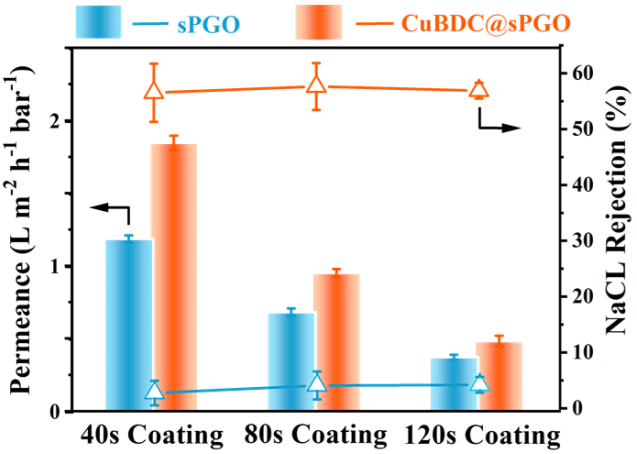



Figure 6.14 Desalination performance of the membranes tested by RO.

The desalination performance of the fabricated membranes was evaluated using conventional RO and pervaporation processes with a 35 g $L^{-1}$ NaCl feed solution. Figure 6.14 illustrates the RO performance of the sPGO40s, sPGO80s, and sPGO120s membranes before and after CuBDC incorporation. As can be seen, increasing CuBDC loading in the sPGO-based composite membranes significantly enhanced NaCl rejection, increasing from less than 5% to approximately 55%. This improvement is attributed to the formation of narrower transport channels enabled by the small aperture (~5 Å) of the CuBDC pores [54]. Targeted CuBDC growth along the edges and defects of PGO nanosheets effectively refine the inherently large, non-uniform pore structure of the sPGO membrane. In addition, compared with their pristine sPGO counterparts, the composite membranes exhibited increased permeance. The optimized membrane achieved a maximum permeance of 1.8 L $m^{-2} \cdot h^{-1} \cdot bar^{-1}$, representing a 164% increase over the sPGO40s membrane. These findings demonstrate the successful enhancement of both flux and salt rejection through confined growth of 2D MOF nanosheets within the sPGO framework.

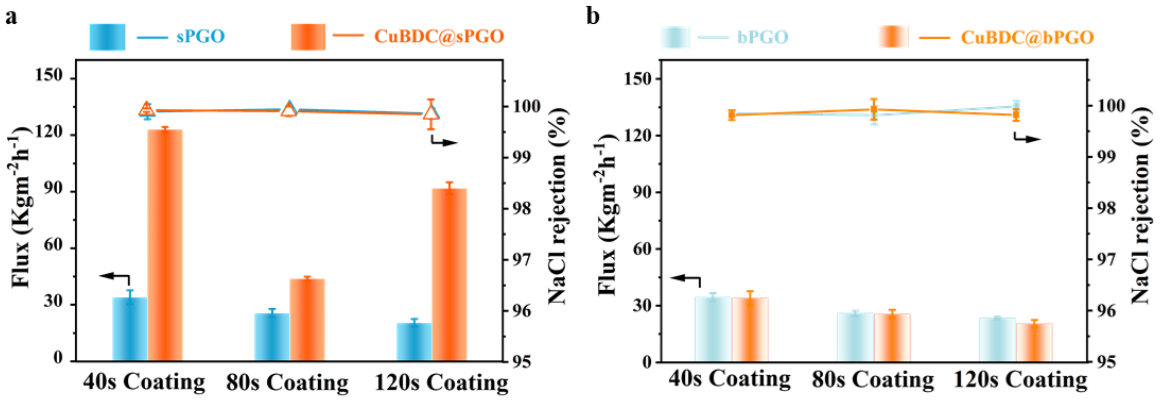



Figure 6.15 Pervaporation performance of (a) the pristine sPGO and CuBDC@sPGO membranes and (b) the pristine bPGO and CuBDC@bPGO membranes

The composite membranes also exhibited excellent desalination performance in pervaporation mode (Figure 6.2), achieving 99.9% salt rejection and a flux of 124 kg $m^{-2} \cdot h^{-1}$ with CuBDC@sPGO40s, nearly four times higher than that of pristine sPGO40s (Figure 6.15 a). This exceptional flux surpasses most state-of-the-art pervaporation membranes, which typically range from 4~80 kg $m^{-2}$ $h^{-1}$ [55-57]. Similarly, the thicker CuBDC@sPGO80s and CuBDC@sPGO120s composite membranes presented higher water fluxes than their pristine counterparts did, ranging from 35~90 kg $m^{-2}$ $h^{-1}$. The water flux of the sPGO membranes was consistent with the previously reported GO membrane pervaporation performance (Table 6.4). Compared with the bPGO membranes shown in Figure 6.15 b, the sPGO membranes exhibited slightly greater flux because of their smaller flakes, which shorten the water transport path [58-60]. Notably, the water fluxes of the bPGO and CuBDC@bPGO composite membranes were comparable (Figure 6.15 b), largely due to the relatively low CuBDC loading in CuBDC@bPGO membranes, hence showing negligible effects on permeation flux.

Table 6.4 Comparison of state-of-the-art desalination membranes via PV (The selected literature represents key studies identified through a Web of Science search using keywords such as “desalination membrane” and “desalination via pervaporation”)

| *Membrane* | Substrate | Feed | Temperature (K) | Flux (Kg $m^{-2}$ $h^{-1}$) | Salt rejection (%) | Ref. |
|---|---|---|---|---|---|---|
| *CuBDC@sPGO40s* | Alumina HF | 35,000 ppm NaCl | 343 | 127±1.29 | 99.93 | This study |
| *GO-PVA* | PVDF | 100,000 ppm NaCl | 338 | 28 | 99.99 | [61] |
| *GO-PVA* | Cellulose | 200,000 ppm NaCl | 358 | 98.1 | 99.99 | [62] |
| *GO-PI* | / | 35,000 ppm NaCl | 363 | 15.6 | 99.80 | [63] |

| | | | | | | |
|---|---|---|---|---|---|---|
| *GO* | PAN | 35,000 ppm NaCl | 363 | 65.1 | 99.80 | [64] |
| *GO* | PAN | 35,000 ppm NaCl | 303 | 14.3 | 99.80 | [64] |
| *GO* | PTFE | 35,000 ppm NaCl | 343 | 124 | 99.99 | [65] |
| *1,4-Diaminobutane-GO* | α-Al2O3 | Simulated seawater | 363 | 19.7 | 99.9 | [66] |
| *GO-Polyimide* | / | Simulated seawater | 363 | 36.1 | 99.9 | [67] |
| *GO-Polyimide* | / | Simulated seawater | 363 | 15.6 | 99.8 | [63] |
| *GO-Polyamide* | PAN | Simulated seawater | 343 | 26.7 | 99.99 | [68] |
| *GO-Chitosan* | / | 50,000 ppm NaCl | 354 | 30 | 99.99 | [69] |
| *GO-SA* | / | Simulated seawater | 333 | 8.1 | 99.41 | [70] |
| *GO-PEI* | / | 200,000 ppm NaCl | 338 | 8.4 | 99.90 | [71] |
| *GO-PEI* | MCE | 100,000 ppm NaCl | 363 | 86 | 99.99 | [72] |
| *GO@CuBTC/PVDF* | / | Simulated seawater | 348 | 36.8 | 99.68 | [73] |
| *Graphene oxide framework* | Alumina HF | Simulated seawater | 363 | 11.4 | 99.6 | [74] |
| *PA-mCNT* | PAN | Simulated seawater | 343 | 104 | 99.99 | [75] |
| *MXene* | PAN | 35,000 ppm NaCl | 338 | 85.4 | 99.5 | [76] |
| *MOF-303/MXene-PVA* | PAN | 35,000 ppm NaCl | 308 | 15.9 | 99.84 | [77] |
| *MIL-101(Cr)@GO-PVA* | / | 40,000 ppm NaCL | 333 | 9.7 | 99.9 | [78] |
| *GO-g-PVA* | PAN | 35,000 ppm NaCl | 308 | 4.5 | 99.99 | [79] |
| *PVA/NC* | PAN | 200,000 ppm NaCl | 343 | 103.1 | 99.8 | [80] |
| *BTCA-TAPB-* | Alumina | 35,000 ppm NaCl | 353 | 40 | 99.9 | [81] |

*COF*

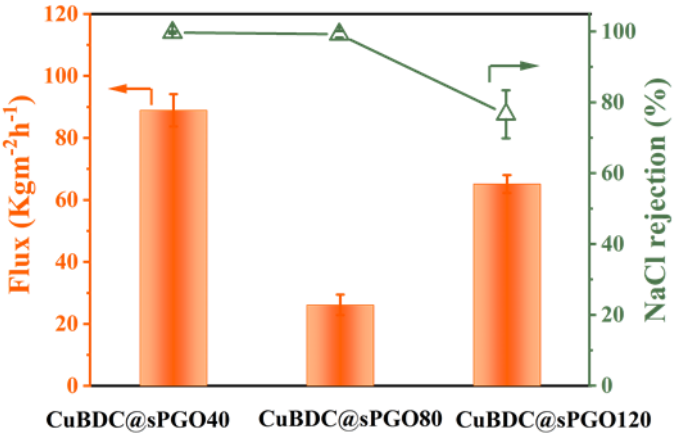



Figure 6.16 Desalination performance of the water carrier pervaporation system.

Despite the excellent desalination performance demonstrated by conventional pervaporation, its large-scale application remains significantly impeded because of the high energy demand required to maintain a continuous vacuum on the permeate side. To address this limitation, a water carrier pervaporation system (illustrated in Figure 6.3), which is analogous to the energy-efficient direct contact membrane distillation (DCMD) process, was employed to further evaluate the desalination performance of the CuBDC@sPGO40s composite membrane. As shown in Figure 6.16, a high flux of 89 kg $m^{-2}$ $h^{-1}$ with a promising salt rejection of over 99.9% was achieved. This flux nearly doubles compared with those of previously reported membranes, which mostly exhibited fluxes below 50 kg $m^{-2}$ $h^{-1}$ (Table 6.5). Owing to the increased thickness, the flux of the sPGO composite membrane fabricated using sPGO80s was reduced to less than 30 kg $m^{-2}$ $h^{-1}$. In contrast, the flux of the CuBDC@sPGO120s membrane was nearly twice that of the sPGO80s-based membrane, with a decreased salt rejection of less than 80%. This can be attributed to the nonuniform distribution of CuBDC nanosheets within the thicker sPGO membrane, which arises from the differing diffusion rates of the metal and ligand solutions, an effect that is negligible in thinner sPGO matrices. Notably, the custom-designed membrane module, as depicted in Figure 6.3, offers an effective testing area more than ten times larger than that of RO and conventional pervaporation systems. This expanded testing area was utilized in the water carrier pervaporation test, highlighting the potential of the sPGO40s- and sPGO80s-based composite membrane for larger-scale desalination applications.

Table 6.5 Comparison of WCPV membranes with state-of-the-art desalination membranes via direct c ontact membrane distillation (The selected literature represents key studies identified through a Web of Science search using keywords such as “direct contact membrane distillation”, “GO mem brane for DCMD” “DCMD for desalination”)

| *Membrane* | Substrate | Feed | Temperature difference (ΔK) | Flux ($Kgm^{-1}h^{-1}$) | Salt rejection (%) | Ref. |
|---|---|---|---|---|---|---|
| *CuBDC@sPGO40s* | Alumina HF | 35,000 ppm NaCl | 50 | 88.9±5.21 | 99.70 | This study |
| *GO-PVA/SSA* | PP | 35,000 ppm NaCL | 40 | 3.4 | 99.60 | [82] |
| *GO/PVA&PP-PVDF* | / | / | 40 | 52 | ~100.00 | [83] |
| *Powered activated carbon* | PVDF-HFP | 35,000 ppm NaCl | / | 77 | 99.00 | [84] |
| *PET* | / | 75,000 ppm NaCl | 50 | 1.9 | 91.39 | [85] |
| *Silica-PDA-PVDF* | / | 35,000 ppm NaCl | 50 | 37.0 | ~100 | [86] |
| *SiNPs/PFOTS* | / | 250,000 ppm NaCl | 40 | 17.5 | ~100 | [87] |
| *PDA-PEI* | PVDF | 40,000 ppm NaCl | 40 | 15 | 99.99 | [88] |
| *KOH modified PVDF* | / | 24,000 ppm NaCl | 50 | 45 | 99.99 | [89] |
| *MOF-808/PVDF/PAN* | / | 35,000 ppm NaCl | 30 | 4.4 | 99.97 | [90] |
| *UiO-66-$NH_2$/PVA* | PTFE | 35,000 ppm NaCl | 50 | 21.3 | 99.99 | [91] |
| *Silica-CA* | PTFE | 24,000 ppm NaCl | 33 | 20 | ~100.00 | [92] |
| *CNT -PVDF* | / | 30,000 ppm NaCl | 60 | 74.7 | 99.99 | [93] |
| *PVDF* | / | 35,000 ppm NaCl | 40 | 38.0 | 99.99 | [94] |
| *Quartz fibre-* | / | 40,000 ppm NaCl | 40 | 18.3 | 99.00 | [95] |

| | | | | | | |
|---|---|---|---|---|---|---|
| *PVDF-HFP* | | | | | | |
| *ZnO/PVDF* | / | Simulated seawater | 40 | 15.7 | 99.90 | [96] |
| *PLA@SiO₂* | / | 35,000 ppm NaCl | 40 | 14.3 | 99.99 | [97] |
| *12LF-NC* | Nylon/nitrocellulose | 100,000 ppm NaCl | 40 | 10.1 | ~100 | [98] |
| *9LF-NC* | Nylon/nitrocellulose | 35,000 ppm NaCl | 40 | 14.0 | ~100 | [98] |
| *Vinyl-POSS-PTFE* | / | 35,000 ppm NaCl | 40 | 40 | 99.99 | [99] |
| *AlFu-PVA-SSA* | PTFE | 35,000 ppm NaCl | ~35 | 45.1 | 99.9 | [100] |

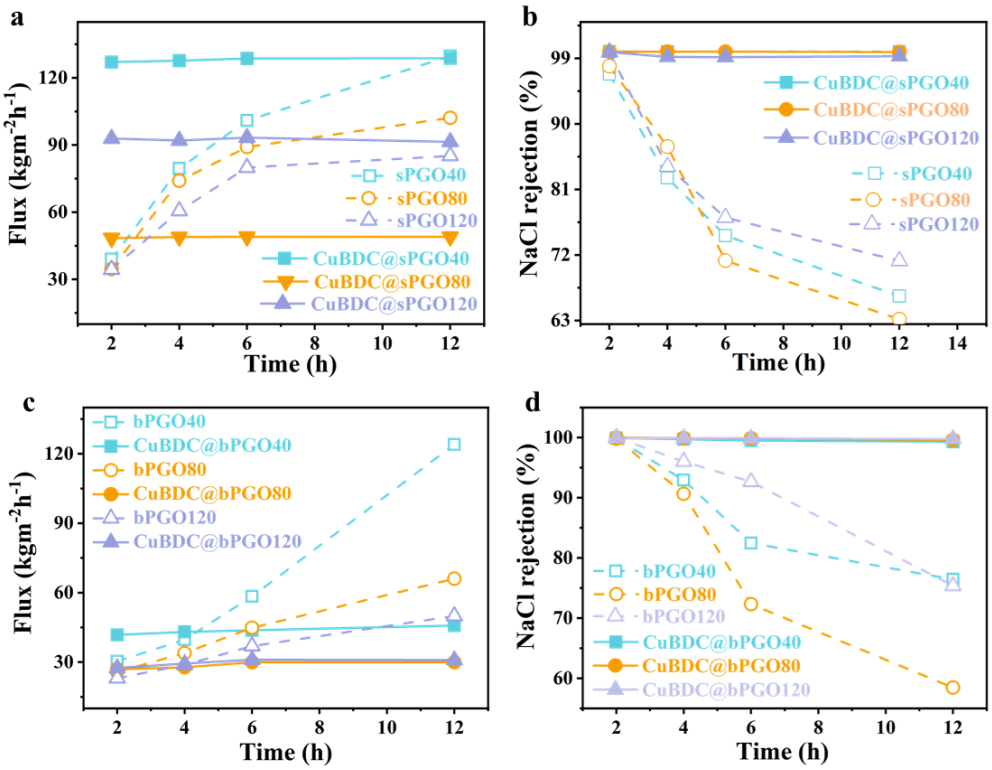



Figure 6.17 Desalination performance of the membranes tested for an extended duration. (a) Flux and (b) NaCl rejection of the sPGO and CuBDC@sPGO composite membranes. (c) Flux and (d) NaCl rejection performance of bPGO and CuBDC@bPGO composite membranes.

The PGO membranes patched with CuBDC selectively tested via either conventional pervaporation or water carrier pervaporation exhibited stable performances over extended duration. As shown in Figure

6.17 a and b, the CuBDC@sPGO composite membranes demonstrated substantial stability compared with the sPGO membrane in terms of both water flux and NaCl rejection over a 12-h continuous test. For the bPGO-based membranes, despite the low CuBDC loading, the structural integrity of the CuBDC@bPGO composite membranes remained stable, retaining their framework over a 12-h continuous test. In contrast, the pristine sPGO and bPGO membranes experienced structural failure within 2-4 hours (Figure 6.17 c and 6.17 d) leading to a gradual increase in flux accompanied by a significant decline in salt rejection.

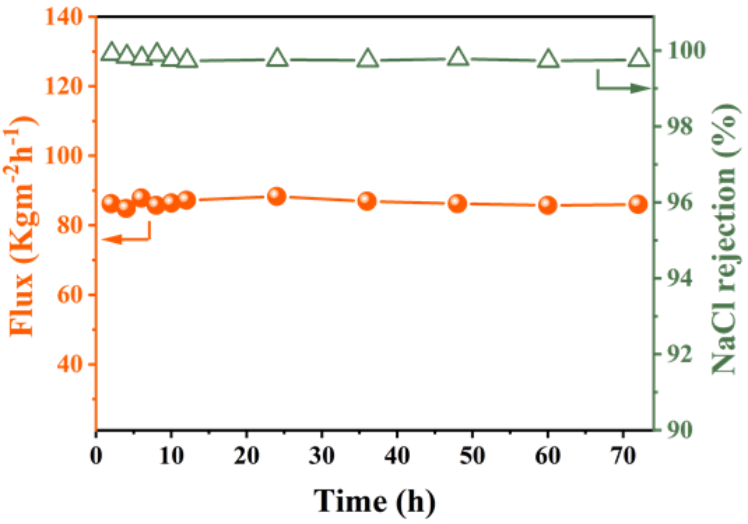



Figure 6.18 Stability test of the CuBDC@sPGO40s composite membrane operated in water carrier pervaporation mode.

Notably, the CuBDC@sPGO40s membrane which exhibited the best desalination performance maintained stable performance over up to a 72-h continuous water carrier pervaporation test (Figure 6.18), further demonstrating its robustness and suitability for long-term desalination applications. This stability is attributed to coordination between the oxygen-containing functional groups on the PGO flakes and the $Cu^{2+}$ clusters in the CuBDC, as confirmed by structural characterization. These interactions mitigate hydration of oxygen-containing groups, suppressing PGO layer swelling and enhancing membrane integrity under aqueous conditions. This highlights the potential of the CuBDC@sPGO composite membrane for energy-efficient, high-performance pervaporation-based desalination.

It is interesting to note that the water flux obtained using the RO mode is significantly lower than that obtained via pervaporation. This is due to differences in the driving forces. During RO operation, i.e. pressure-driven operation, water transport occurs via hydraulic pressure, which is relatively low compared with the capillary pressure present in pervaporation. Water in the interlayer nanochannels of the GO membrane does not experience a phase transition in RO mode, leading to slow transport over long and tortuous paths. Conversely, in pervaporation, a liquid-vapour interface forms in the

nanochannels, generating high capillary pressure (~1440 bar for GO membranes) [24] which drives water efficiently across a large portion of nanochannel of the GO membrane. In addition, water vapour flux within the remaining nanochannels further influences overall water fluxes operated between conventional pervaporation and water carrier pervaporation. In conventional pervaporation (vacuum applied), high water flux is achieved through convective vapour flow, whereas in water carrier pervaporation (or DCMD) mode, vapour transport is primarily diffusive and thus is lower. In any case, the substantial difference in water flux between the RO and pervaporation modes is due primarily to the stronger driving force in pervaporation, which is absent in the RO mode.

## 6.5 Conclusion

In summary, we successfully fabricated a CuBDC@PGO composite membrane with excellent structural stability and competitive desalination performance using a contra-diffusion strategy. This was achieved through the confined growth of CuBDC nanosheets within the laminar PGO framework. Comprehensive structural and elemental analyses (XPS, XRD, and FTIR) confirmed strong coordinative interactions between the oxygen-containing groups of PGO and $Cu^{2+}$ ions in CuBDC. Reducing the bPGO flake size increased the density of reactive sites, increasing MOF loading and structural integrity. These interactions imparted remarkable stability, enabling the composite membranes to maintain high separation performance for extended desalination operations.

The CuBDC@sPGO40s composite membrane demonstrated enhanced performance in RO, with improved permeance and NaCl rejection. In pervaporation, an exceptional flux of 124 kg $m^{-2} \cdot h^{-1}$ was observed, nearly four times higher than that of the pristine sPGO membrane, while 99.9% salt rejection was maintained. In addition, it showed competitive performance in water carrier pervaporation, underscoring its potential for leveraging low-grade energy sources in desalination.

This study not only addresses key challenges in developing high-performance MOF/GO composite membranes with a laminar structure but also presents a promising approach for fabricating robust, energy-efficient membranes. These findings open new avenues for advanced desalination and water purification technologies.

## References

[1] Y. Ying, D. Liu, W. Zhang, J. Ma, H. Huang, Q. Yang, C. Zhong, High-Flux Graphene Oxide Membranes Intercalated by Metal–Organic Framework with Highly Selective Separation of Aqueous Organic Solution, ACS Applied Materials & Interfaces 9(2) (2017) 1710-1718. https://doi.org/10.1021/acsami.6b14371.
[2] M. Chen, M. Trubyanov, P. Zhang, D. Rodríguez-San-Miguel, F. Zamora, K.S. Novoselov, D.V. Andreeva, Control of gas selectivity and permeability through COF-GO composite membranes for sustainable decarbonization and hydrogen production, Carbon 219 (2024) 118855.

https://doi.org/https://doi.org/10.1016/j.carbon.2024.118855.
[3] L. Chen, W. Wang, Q. Fang, K. Zuo, G. Hou, Q. Ai, Q. Li, L. Ci, J. Lou, High performance hierarchically nanostructured graphene oxide/covalent organic framework hybrid membranes for stable organic solvent nanofiltration, Applied Materials Today 20 (2020) 100791. https://doi.org/https://doi.org/10.1016/j.apmt.2020.100791.
[4] J.Y. Chong, B. Wang, K. Li, Graphene oxide membranes in fluid separations, Current Opinion in Chemical Engineering 12 (2016) 98-105. https://doi.org/https://doi.org/10.1016/j.coche.2016.04.002.
[5] J. Alam, A.K. Shukla, M. Alhoshan, L. Arockiasamy Dass, M.R. Muthumareeswaran, A. Khan, F.A. Ahmed Ali, Graphene oxide, an effective nanoadditive for a development of hollow fiber nanocomposite membrane with antifouling properties, 37(7) (2018) 2597-2608. https://doi.org/https://doi.org/10.1002/adv.21935.
[6] S. Pei, H.-M. Cheng, The reduction of graphene oxide, Carbon 50(9) (2012) 3210-3228. https://doi.org/https://doi.org/10.1016/j.carbon.2011.11.010.
[7] H.C. Schniepp, J.-L. Li, M.J. McAllister, H. Sai, M. Herrera-Alonso, D.H. Adamson, R.K. Prud'homme, R. Car, D.A. Saville, I.A. Aksay, Functionalized Single Graphene Sheets Derived from Splitting Graphite Oxide, The Journal of Physical Chemistry B 110(17) (2006) 8535-8539. https://doi.org/10.1021/jp060936f.
[8] R.K. Joshi, P. Carbone, F.C. Wang, V.G. Kravets, Y. Su, I.V. Grigorieva, H.A. Wu, A.K. Geim, R.R. Nair, Precise and Ultrafast Molecular Sieving Through Graphene Oxide Membranes, 343(6172) (2014) 752-754. https://doi.org/doi:10.1126/science.1245711.
[9] R.R. Nair, H.A. Wu, P.N. Jayaram, I.V. Grigorieva, A.K. Geim, Unimpeded Permeation of Water Through Helium-Leak–Tight Graphene-Based Membranes, 335(6067) (2012) 442-444. https://doi.org/doi:10.1126/science.1211694.
[10] F. Moghadam, M. Zhai, T. Zouaoui, K. Li, Hybrid graphene oxide membranes with regulated water and ion permeation channels via functional materials, Current Opinion in Chemical Engineering 40 (2023) 100907. https://doi.org/https://doi.org/10.1016/j.coche.2023.100907.
[11] K.H. Thebo, X. Qian, Q. Zhang, L. Chen, H.-M. Cheng, W. Ren, Highly stable graphene-oxide-based membranes with superior permeability, Nature Communications 9(1) (2018) 1486. https://doi.org/10.1038/s41467-018-03919-0.
[12] H. Liu, H. Wang, X.J.A.M. Zhang, Facile fabrication of freestanding ultrathin reduced graphene oxide membranes for water purification, 27(2) (2015) 249-254.
[13] W.-S. Hung, C.-H. Tsou, M. De Guzman, Q.-F. An, Y.-L. Liu, Y.-M. Zhang, C.-C. Hu, K.-R. Lee, J.-Y. Lai, Cross-Linking with Diamine Monomers To Prepare Composite Graphene Oxide-Framework Membranes with Varying d-Spacing, Chemistry of Materials 26(9) (2014) 2983-2990. https://doi.org/10.1021/cm5007873.
[14] N. Meng, W. Zhao, E. Shamsaei, G. Wang, X.K. Zeng, X.C. Lin, T.W. Xu, H.T. Wang, X.W. Zhang, A low-pressure GO nanofiltration membrane crosslinked via ethylenediamine, Journal of Membrane Science 548 (2018) 363-371. https://doi.org/10.1016/j.memsci.2017.11.044.
[15] L. Chen, G. Shi, J. Shen, B. Peng, B. Zhang, Y. Wang, F. Bian, J. Wang, D. Li, Z. Qian, G. Xu, G. Liu, J. Zeng, L. Zhang, Y. Yang, G. Zhou, M. Wu, W. Jin, J. Li, H. Fang, Ion sieving in graphene oxide membranes via cationic control of interlayer spacing, Nature 550(7676) (2017) 380-383. https://doi.org/10.1038/nature24044.
[16] K. Goh, W. Jiang, H.E. Karahan, S. Zhai, L. Wei, D. Yu, A.G. Fane, R. Wang, Y.J.A.F.M. Chen, All-carbon nanoarchitectures as high-performance separation membranes with superior stability, 25(47) (2015) 7348-7359.
[17] Z. Yu, Y. Peng, F. Yang, Z. Guo, An ultra-high permeability membrane composed of graphene oxide nanosheets supported by a MOF framework utilized for dye separation, Journal of Materials Chemistry A 12(25) (2024) 14986-14990. https://doi.org/10.1039/D4TA02969K.
[18] W.-H. Zhang, M.-J. Yin, Q. Zhao, C.-G. Jin, N. Wang, S. Ji, C.L. Ritt, M. Elimelech, Q.-F. An, Graphene oxide membranes with stable porous structure for ultrafast water transport, Nature Nanotechnology 16(3) (2021) 337-343.
[19] D. Bradshaw, A. Garai, J. Huo, Metal–organic framework growth at functional interfaces: thin films and composites for diverse applications, Chemical Society Reviews 41(6) (2012) 2344-2381.
[20] H.G. Alemayehu, C. Liu, J. Hou, J. Yang, M. Fang, Z. Tang, L. Li, Highly stable membrane comprising MOF nanosheets and graphene oxide for ultra-permeable nanofiltration, Journal of Membrane Science 652 (2022) 120479. https://doi.org/https://doi.org/10.1016/j.memsci.2022.120479.
[21] Z. Wang, J. Zhu, S. Xu, Y. Zhang, B. Van der Bruggen, Graphene-like MOF nanosheets stabilize graphene oxide membranes enabling selective molecular sieving, Journal of Membrane Science 633 (2021) 119397. https://doi.org/https://doi.org/10.1016/j.memsci.2021.119397.

[22] F. Moghadam, C. Zhang, Z. Li, J. Li, M. Zhai, K. Li, Structurally Stable Hollow-Fiber-Based Porous Graphene Oxide Membranes with Improved Rejection Performance by Selective Patching of Framework Defects with Metal–Organic Framework Crystals, ACS Applied Materials & Interfaces 17(1) (2025) 1803-1812. https://doi.org/10.1021/acsami.4c13400.
[23] X. Zhang, H. Wang, R. Yao, L. Wang, P. Zhao, Y. Li, L. Wang, Q. Wang, Q. Lyu, Z. Fan, Growing ZIF-L seeds in graphene oxide interlayers towards synthesizing efficient cation sieving membranes, Journal of Membrane Science 701 (2024) 122718. https://doi.org/https://doi.org/10.1016/j.memsci.2024.122718.
[24] J.Y. Chong, B. Wang, K. Li, Water transport through graphene oxide membranes: the roles of driving forces, Chemical Communications 54(20) (2018) 2554-2557. https://doi.org/10.1039/C7CC09120F.
[25] H. Chen, Y. Mao, B. Mo, Y. Pan, R. Xu, W. Ji, G. Chen, G. Liu, W. Jin, Plasma-assisted facile fabrication of omniphobic graphene oxide membrane with anti-wetting property for membrane distillation, Journal of Membrane Science 668 (2023) 121207. https://doi.org/https://doi.org/10.1016/j.memsci.2022.121207.
[26] C.G. Carson, K. Hardcastle, J. Schwartz, X. Liu, C. Hoffmann, R.A. Gerhardt, R. Tannenbaum, Synthesis and Structure Characterization of Copper Terephthalate Metal–Organic Frameworks, 2009(16) (2009) 2338-2343. https://doi.org/https://doi.org/10.1002/ejic.200801224.
[27] A.M. Varghese, K.S.K. Reddy, G.N. Karanikolos, An In-Situ-Grown Cu-BTC Metal–Organic Framework / Graphene Oxide Hybrid Adsorbent for Selective Hydrogen Storage at Ambient Temperature, Industrial & Engineering Chemistry Research 61(18) (2022) 6200-6213. https://doi.org/10.1021/acs.iecr.1c04710.
[28] W. Li, Y. Zhang, P. Su, Z. Xu, G. Zhang, C. Shen, Q. Meng, Metal–organic framework channelled graphene composite membranes for H2/CO2 separation, Journal of Materials Chemistry A 4(48) (2016) 18747-18752. https://doi.org/10.1039/C6TA09362K.
[29] B. Venu, V. Shirisha, B. Vishali, G. Naresh, R. Kishore, I. Sreedhar, A. Venugopal, A Cu-BTC metal–organic framework (MOF) as an efficient heterogeneous catalyst for the aerobic oxidative synthesis of imines from primary amines under solvent free conditions, New Journal of Chemistry 44(15) (2020) 5972-5979. https://doi.org/10.1039/C9NJ05997K.
[30] L.-H. Xu, Y. Li, S.-H. Li, M.-Y. Lv, Z.-P. Zhao, Space-confined growth of 2D MOF sheets between GO layers at room temperature for superior PDMS membrane-based ester/water separation, Journal of Membrane Science 656 (2022) 120605. https://doi.org/https://doi.org/10.1016/j.memsci.2022.120605.
[31] V. Georgakilas, M. Otyepka, A.B. Bourlinos, V. Chandra, N. Kim, K.C. Kemp, P. Hobza, R. Zboril, K.S. Kim, Functionalization of Graphene: Covalent and Non-Covalent Approaches, Derivatives and Applications, Chemical Reviews 112(11) (2012) 6156-6214. https://doi.org/10.1021/cr3000412.
[32] A.A. Ensafi, S.E. Moosavifard, B. Rezaei, S.K. Kaverlavani, Engineering onion-like nanoporous CuCo2O4 hollow spheres derived from bimetal–organic frameworks for high-performance asymmetric supercapacitors, Journal of Materials Chemistry A 6(22) (2018) 10497-10506. https://doi.org/10.1039/C8TA02819B.
[33] G. Zhan, L. Fan, F. Zhao, Z. Huang, B. Chen, X. Yang, S.-f. Zhou, Fabrication of Ultrathin 2D Cu-BDC Nanosheets and the Derived Integrated MOF Nanocomposites, 29(9) (2019) 1806720. https://doi.org/https://doi.org/10.1002/adfm.201806720.
[34] B. Mao, D.G. Calatayud, V. Mirabello, B.J. Hodges, J.A.R. Martins, S.W. Botchway, J.M. Mitchels, S.I. Pascu, Interactions between an Aryl Thioacetate-Functionalized Zn(II) Porphyrin and Graphene Oxide, 26(5) (2016) 687-697. https://doi.org/https://doi.org/10.1002/adfm.201504147.
[35] F. Yang, M. Wu, Y. Wang, S. Ashtiani, H.J.A.a.m. Jiang, interfaces, A GO-induced assembly strategy to repair MOF nanosheet-based membrane for efficient H2/CO2 separation, 11(1) (2018) 990-997.
[36] N.F.D. Aba, J.Y. Chong, B. Wang, C. Mattevi, K. Li, Graphene oxide membranes on ceramic hollow fibers – Microstructural stability and nanofiltration performance, Journal of Membrane Science 484 (2015) 87-94. https://doi.org/https://doi.org/10.1016/j.memsci.2015.03.001.
[37] T. Yang, H. Lin, K.P. Loh, B. Jia, Fundamental Transport Mechanisms and Advancements of Graphene Oxide Membranes for Molecular Separation, Chemistry of Materials 31(6) (2019) 1829-1846. https://doi.org/10.1021/acs.chemmater.8b03820.
[38] N. Mahdjoub, N. Allen, P. Kelly, V. Vishnyakov, SEM and Raman study of thermally treated TiO2 anatase nanopowders: Influence of calcination on photocatalytic activity, Journal of Photochemistry and Photobiology A: Chemistry 211(1) (2010) 59-64. https://doi.org/https://doi.org/10.1016/j.jphotochem.2010.02.002.
[39] T. Rodenas, I. Luz, G. Prieto, B. Seoane, H. Miro, A. Corma, F. Kapteijn, F.X. Llabrés i Xamena, J. Gascon, Metal–organic framework nanosheets in polymer composite materials for gas separation, Nature Materials 14(1) (2015) 48-55. https://doi.org/10.1038/nmat4113.

[40] F. Yang, M. Wu, Y. Wang, S. Ashtiani, H. Jiang, A GO-Induced Assembly Strategy To Repair MOF Nanosheet-Based Membrane for Efficient H2/CO2 Separation, ACS Applied Materials & Interfaces 11(1) (2019) 990-997. https://doi.org/10.1021/acsami.8b19480.
[41] L. Chen, G. Shi, J. Shen, B. Peng, B. Zhang, Y. Wang, F. Bian, J. Wang, D. Li, Z.J.N. Qian, Ion sieving in graphene oxide membranes via cationic control of interlayer spacing, 550(7676) (2017) 380-383.
[42] M. Zhai, H. Peng, K. Li, High-performance loose nanofiltration membranes with excellent antifouling properties for dye/salt separation, Journal of Membrane Science 708 (2024) 123028. https://doi.org/https://doi.org/10.1016/j.memsci.2024.123028.
[43] H. Peng, K. Li, Nanostructured membranes with interconnected pores via a combination of phase inversion and solvent crystallisation approach, Journal of Membrane Science 680 (2023) 121738. https://doi.org/https://doi.org/10.1016/j.memsci.2023.121738.
[44] P. Ragesh, V. Anand Ganesh, S.V. Nair, A.S. Nair, A review on 'self-cleaning and multifunctional materials', Journal of Materials Chemistry A 2(36) (2014) 14773-14797. https://doi.org/10.1039/C4TA02542C.
[45] P. Song, G. Natale, J. Wang, T. Bond, H. Hejazi, H.d.l.H. Siegler, I. Gates, Q. Lu, 2D and 3D Metal–Organic Framework at the Oil/Water Interface: A Case Study of Copper Benzenedicarboxylate, 6(2) (2019) 1801139. https://doi.org/https://doi.org/10.1002/admi.201801139.
[46] J. Wang, P. Zhang, B. Liang, Y. Liu, T. Xu, L. Wang, B. Cao, K. Pan, Graphene Oxide as an Effective Barrier on a Porous Nanofibrous Membrane for Water Treatment, ACS Applied Materials & Interfaces 8(9) (2016) 6211-6218. https://doi.org/10.1021/acsami.5b12723.
[47] I.N. Floros, E.P. Kouvelos, G.I. Pilatos, E.P. Hadjigeorgiou, A.D. Gotzias, E.P. Favvas, A.A. Sapalidis, Enhancement of Flux Performance in PTFE Membranes for Direct Contact Membrane Distillation, 12(2) (2020) 345.
[48] S. Zhao, C. Jiang, J. Fan, S. Hong, P. Mei, R. Yao, Y. Liu, S. Zhang, H. Li, H. Zhang, C. Sun, Z. Guo, P. Shao, Y. Zhu, J. Zhang, L. Guo, Y. Ma, J. Zhang, X. Feng, F. Wang, H. Wu, B. Wang, Hydrophilicity gradient in covalent organic frameworks for membrane distillation, Nature Materials 20(11) (2021) 1551-1558. https://doi.org/10.1038/s41563-021-01052-w.
[49] S. Azizighannad, S. Mitra, Stepwise Reduction of Graphene Oxide (GO) and Its Effects on Chemical and Colloidal Properties, Scientific Reports 8(1) (2018) 10083. https://doi.org/10.1038/s41598-018-28353-6.
[50] Z.S. Tai, M.H. Abd Aziz, M.H.D. Othman, M.I.H. Mohamed Dzahir, N.A. Hashim, K.N. Koo, S.K. Hubadillah, A.F. Ismail, M. A Rahman, J. Jaafar, Ceramic Membrane Distillation for Desalination, Separation & Purification Reviews 49(4) (2020) 317-356. https://doi.org/10.1080/15422119.2019.1610975.
[51] X. Mu, X. Wu, T. Zhang, D.B. Go, T. Luo, Thermal Transport in Graphene Oxide – From Ballistic Extreme to Amorphous Limit, Scientific Reports 4(1) (2014) 3909. https://doi.org/10.1038/srep03909.
[52] S. Alharbi, J.C. Crepeau, B. Rezaie, K.J.J.o.E.T. Kumar, Temperature Dependence of Thermal Conductivity for Water Using the Transient Hot-Wire Method, 31 (2022) 78 - 97.
[53] H. Liu, Z. Huang, K. Liu, X. Hu, J. Zhou, Interfacial Solar-to-Heat Conversion for Desalination, 9(21) (2019) 1900310. https://doi.org/https://doi.org/10.1002/aenm.201900310.
[54] R. Dai, X. Zhang, M. Liu, Z. Wu, Z. Wang, Porous metal organic framework CuBDC nanosheet incorporated thin-film nanocomposite membrane for high-performance forward osmosis, Journal of Membrane Science 573 (2019) 46-54. https://doi.org/https://doi.org/10.1016/j.memsci.2018.11.075.
[55] Y. Mao, Q. Huang, B. Meng, K. Zhou, G. Liu, A. Gugliuzza, E. Drioli, W. Jin, Roughness-enhanced hydrophobic graphene oxide membrane for water desalination via membrane distillation, Journal of Membrane Science 611 (2020) 118364. https://doi.org/https://doi.org/10.1016/j.memsci.2020.118364.
[56] S. Al-Gharabli, Z. Abu El-Rub, E. Hamad, W. Kujawski, Z. Flanc, K. Pianka, J. Kujawa, Surfaces with Adjustable Features-Effective and Durable Materials for Water Desalination, Int J Mol Sci 22(21) (2021). https://doi.org/10.3390/ijms222111743.
[57] Z.A. Pouya, M.A. Tofighy, T. Mohammadi, Synthesis and characterization of polytetrafluoroethylene/oleic acid-functionalized carbon nanotubes composite membrane for desalination by vacuum membrane distillation, Desalination 503 (2021) 114931. https://doi.org/https://doi.org/10.1016/j.desal.2021.114931.
[58] J.Y. Chong, B. Wang, C. Mattevi, K. Li, Dynamic microstructure of graphene oxide membranes and the permeation flux, Journal of Membrane Science 549 (2018) 385-392. https://doi.org/https://doi.org/10.1016/j.memsci.2017.12.018.
[59] F.U.J.D. Nigiz, Graphene oxide-sodium alginate membrane for seawater desalination through pervaporation, 485 (2020) 114465.
[60] K.-K. Yan, L. Jiao, S. Lin, X. Ji, Y. Lu, L.J.D. Zhang, Superhydrophobic electrospun nanofiber membrane

coated by carbon nanotubes network for membrane distillation, 437 (2018) 26-33.
[61] L. Li, J. Hou, Y. Ye, J. Mansouri, Y. Zhang, V. Chen, Suppressing Salt Transport through Composite Pervaporation Membranes for Brine Desalination, 7(8) (2017) 856.
[62] J. Sun, X. Qian, Z. Wang, F. Zeng, H. Bai, N. Li, Tailoring the microstructure of poly(vinyl alcohol)-intercalated graphene oxide membranes for enhanced desalination performance of high-salinity water by pervaporation, Journal of Membrane Science 599 (2020) 117838. https://doi.org/https://doi.org/10.1016/j.memsci.2020.117838.
[63] A. Huang, B. Feng, Synthesis of novel graphene oxide-polyimide hollow fiber membranes for seawater desalination, Journal of Membrane Science 548 (2018) 59-65. https://doi.org/https://doi.org/10.1016/j.memsci.2017.11.016.
[64] B. Liang, W. Zhan, G. Qi, S. Lin, Q. Nan, Y. Liu, B. Cao, K. Pan, High performance graphene oxide/polyacrylonitrile composite pervaporation membranes for desalination applications, Journal of Materials Chemistry A 3(9) (2015) 5140-5147. https://doi.org/10.1039/C4TA06573E.
[65] Y. Song, R. Li, F. Pan, Z. He, H. Yang, Y. Li, L. Yang, M. Wang, H. Wang, Z. Jiang, Ultrapermeable graphene oxide membranes with tunable interlayer distances via vein-like supramolecular dendrimers, Journal of Materials Chemistry A 7(31) (2019) 18642-18652. https://doi.org/10.1039/C9TA05909A.
[66] Y. Qian, X. Zhang, C. Liu, C. Zhou, A. Huang, Tuning interlayer spacing of graphene oxide membranes with enhanced desalination performance, Desalination 460 (2019) 56-63. https://doi.org/https://doi.org/10.1016/j.desal.2019.03.009.
[67] B. Feng, K. Xu, A. Huang, Synthesis of graphene oxide/polyimide mixed matrix membranes for desalination, RSC Advances 7(4) (2017) 2211-2217. https://doi.org/10.1039/C6RA24974D.
[68] X. Zhao, Z. Tong, X. Liu, J. Wang, B. Zhang, Facile Preparation of Polyamide–Graphene Oxide Composite Membranes for Upgrading Pervaporation Desalination Performances of Hypersaline Solutions, Industrial & Engineering Chemistry Research 59(26) (2020) 12232-12238. https://doi.org/10.1021/acs.iecr.0c01417.
[69] X. Qian, N. Li, Q. Wang, S. Ji, Chitosan/graphene oxide mixed matrix membrane with enhanced water permeability for high-salinity water desalination by pervaporation, Desalination 438 (2018) 83-96. https://doi.org/https://doi.org/10.1016/j.desal.2018.03.031.
[70] F. Ugur Nigiz, Graphene oxide-sodium alginate membrane for seawater desalination through pervaporation, Desalination 485 (2020) 114465. https://doi.org/https://doi.org/10.1016/j.desal.2020.114465.
[71] E. Halakoo, X. Feng, Layer-by-layer assembly of polyethyleneimine/graphene oxide membranes for desalination of high-salinity water via pervaporation, Separation and Purification Technology 234 (2020) 116077. https://doi.org/https://doi.org/10.1016/j.seppur.2019.116077.
[72] Z. Wang, J. Sun, N. Li, Y. Qin, X. Qian, Z. Xie, Tuning interlayer structure to construct steady dual-crosslinked graphene oxide membranes for desalination of hypersaline brine via pervaporation, Separation and Purification Technology 286 (2022) 120459. https://doi.org/https://doi.org/10.1016/j.seppur.2022.120459.
[73] D.D. Kachhadiya, Z.V.P. Murthy, Graphene oxide modified CuBTC incorporated PVDF membranes for saltwater desalination via pervaporation, Separation and Purification Technology 290 (2022) 120888. https://doi.org/https://doi.org/10.1016/j.seppur.2022.120888.
[74] B. Feng, K. Xu, A. Huang, Covalent synthesis of three-dimensional graphene oxide framework (GOF) membrane for seawater desalination, Desalination 394 (2016) 123-130. https://doi.org/https://doi.org/10.1016/j.desal.2016.04.030.
[75] Y. Liu, Z. Tong, H. Zhu, X. Zhao, J. Du, B. Zhang, Polyamide composite membranes sandwiched with modified carbon nanotubes for high throughput pervaporation desalination of hypersaline solutions, Journal of Membrane Science 641 (2022) 119889. https://doi.org/https://doi.org/10.1016/j.memsci.2021.119889.
[76] G. Liu, J. Shen, Q. Liu, G. Liu, J. Xiong, J. Yang, W. Jin, Ultrathin two-dimensional MXene membrane for pervaporation desalination, Journal of Membrane Science 548 (2018) 548-558. https://doi.org/https://doi.org/10.1016/j.memsci.2017.11.065.
[77] Y. Zhang, H. Yuan, X. Chen, Z. Jiang, J. Lu, F. Xin, Incorporating MXene@MOF-303 Composites into Poly(vinyl alcohol) (PVA) to Fabricate Pervaporation Membranes for Desalination, ACS Applied Polymer Materials 6(14) (2024) 8277-8290. https://doi.org/10.1021/acsapm.4c01071.
[78] D. Unlu, Water Desalination by Pervaporation Using MIL-101(Cr) and MIL-101(Cr)@GODoped PVA Hybrid Membranes, Water, Air, & Soil Pollution 234(2) (2023) 96. https://doi.org/10.1007/s11270-023-06128-8.
[79] Z. Zeng, H. Yuan, J. Lu, Preparation and characterization of PVA-g-GO/PVA/PAN composite membrane for pervaporation desalination, 101(4) (2023) 2199-2211. https://doi.org/https://doi.org/10.1002/cjce.24619.
[80] D. Qin, R. Zhang, B. Cao, P. Li, Fabrication of high-performance composite membranes based on

hierarchically structured electrospun nanofiber substrates for pervaporation desalination, Journal of Membrane Science 638 (2021) 119672. https://doi.org/https://doi.org/10.1016/j.memsci.2021.119672.
[81] Z. Li, J. Fan, L. Wang, X. Yang, L. Guo, H. Chen, D. Gong, G. Yang, Q. Xu, S. Zou, G. Zeng, Two-dimensional lamellar stacking COF membrane with charge repulsion effect for ions separation, Journal of Membrane Science 699 (2024) 122645. https://doi.org/https://doi.org/10.1016/j.memsci.2024.122645.
[82] G. Yang, D. Ng, Z. Huang, J. Zhang, S. Gray, Z. Xie, Janus hollow fibre membranes with intrusion anchored structure for robust desalination and leachate treatment in direct contact membrane distillation, Desalination 551 (2023) 116423. https://doi.org/https://doi.org/10.1016/j.desal.2023.116423.
[83] Z. Zhu, M. Song, F. Qu, Y. Zhou, Y. Yang, J. Qi, J. Li, Engineering Multinanochannel Polymer-Intercalated Graphene Oxide Membrane for Strict Volatile Sieving in Membrane Distillation, Environmental Science & Technology 58(2) (2024) 1399-1409. https://doi.org/10.1021/acs.est.3c08452.
[84] C. Regmi, Y.K. Kshetri, S.R. Wickramasinghe, Carbon-Based Nanocomposite Membranes for Membrane Distillation: Progress, Problems and Future Prospects, 14(7) (2024) 160.
[85] A.B. Yeszhanov, I.V. Korolkov, O. Güven, G.B. Melnikova, S.S. Dosmagambetova, A.N. Borissenko, A.K. Nurkassimov, M.T. Kassymzhanov, M.V. Zdorovets, Effect of hydrophobized PET TeMs membrane pore-size on saline water treatment by direct contact membrane distillation, RSC Advances 14(6) (2024) 4034-4042. https://doi.org/10.1039/D3RA07475G.
[86] W. Zhang, Y. Lu, J. Liu, X. Li, B. Li, S. Wang, Preparation of re-entrant and anti-fouling PVDF composite membrane with omniphobicity for membrane distillation, Journal of Membrane Science 595 (2020) 117563. https://doi.org/https://doi.org/10.1016/j.memsci.2019.117563.
[87] H. Feng, H. Li, M. Li, X. Zhang, Construction of omniphobic PVDF membranes for membrane distillation: Investigating the role of dimension, morphology, and coating technology of silica nanoparticles, Desalination 525 (2022) 115498. https://doi.org/https://doi.org/10.1016/j.desal.2021.115498.
[88] N.G.P. Chew, S. Zhao, C. Malde, R. Wang, Superoleophobic surface modification for robust membrane distillation performance, Journal of Membrane Science 541 (2017) 162-173. https://doi.org/https://doi.org/10.1016/j.memsci.2017.06.089.
[89] M. Mohammadi Ghaleni, A. Al Balushi, S. Kaviani, E. Tavakoli, M. Bavarian, S. Nejati, Fabrication of Janus Membranes for Desalination of Oil-Contaminated Saline Water, ACS Applied Materials & Interfaces 10(51) (2018) 44871-44879. https://doi.org/10.1021/acsami.8b16621.
[90] J.E. Efome, D. Rana, T. Matsuura, F. Yang, Y. Cong, C.Q. Lan, Triple-Layered Nanofibrous Metal–Organic Framework-Based Membranes for Desalination by Direct Contact Membrane Distillation, ACS Sustainable Chemistry & Engineering 8(17) (2020) 6601-6610. https://doi.org/10.1021/acssuschemeng.9b06791.
[91] L. Chen, F. Li, L. Jiang, F. He, Y. Wei, UiO-66-NH2/PVA composite Janus membrane with a dense hydrophilic surface layer for strong resistance to fouling and wettability in membrane distillation, Journal of Water Process Engineering 48 (2022) 102887. https://doi.org/https://doi.org/10.1016/j.jwpe.2022.102887.
[92] D. Hou, Z. Wang, K. Wang, J. Wang, S. Lin, Composite membrane with electrospun multiscale-textured surface for robust oil-fouling resistance in membrane distillation, Journal of Membrane Science 546 (2018) 179-187. https://doi.org/https://doi.org/10.1016/j.memsci.2017.10.017.
[93] M. Essalhi, M. Khayet, S. Tesfalidet, M. Alsultan, N. Tavajohi, Desalination by direct contact membrane distillation using mixed matrix electrospun nanofibrous membranes with carbon-based nanofillers: A strategic improvement, Chemical Engineering Journal 426 (2021) 131316. https://doi.org/https://doi.org/10.1016/j.cej.2021.131316.
[94] S. Munirasu, F. Banat, A.A. Durrani, M.A. Haija, Intrinsically superhydrophobic PVDF membrane by phase inversion for membrane distillation, Desalination 417 (2017) 77-86. https://doi.org/https://doi.org/10.1016/j.desal.2017.05.019.
[95] S. Kalam, A. Dutta, X. Du, X. Li, T. Tong, J. Lee, A non-substrate-specific technique of antifouling and antiwetting Janus membrane fabrication for membrane distillation, Desalination 573 (2024) 117195. https://doi.org/https://doi.org/10.1016/j.desal.2023.117195.
[96] T. Pan, J. Liu, N. Deng, Z. Li, L. Wang, Z. Xia, J. Fan, Y. Liu, ZnO Nanowires@PVDF nanofiber membrane with superhydrophobicity for enhanced anti-wetting and anti-scaling properties in membrane distillation, Journal of Membrane Science 621 (2021) 118877. https://doi.org/https://doi.org/10.1016/j.memsci.2020.118877.
[97] M.M. Sayed, H.M. Mousa, A.H. El-Shazly, A. Zkria, T. Yoshitake, M. ElKady, Novel post-heat treatment green biodegradable PLA@SiO2 nanocomposite membrane for water desalination, Journal of Environmental Chemical Engineering 12(6) (2024) 114378. https://doi.org/https://doi.org/10.1016/j.jece.2024.114378.
[98] Y. Zhang, J.Y. Chong, Y. Zhao, R. Xu, A. Asakawa, R. Wang, Facile hydrophobic modification of

hydrophilic membranes by fluoropolymer coating for direct contact membrane distillation, Journal of Membrane Science 672 (2023) 121432. https://doi.org/https://doi.org/10.1016/j.memsci.2023.121432.
[99] J. Ju, K. Fejjari, Y. Cheng, M. Liu, Z. Li, W. Kang, Y. Liao, Engineering hierarchically structured superhydrophobic PTFE/POSS nanofibrous membranes for membrane distillation, Desalination 486 (2020) 114481. https://doi.org/https://doi.org/10.1016/j.desal.2020.114481.
[100] Z. Huang, G. Yang, J. Zhang, S. Gray, Z. Xie, Dual-layer membranes with a thin film hydrophilic MOF/PVA nanocomposite for enhanced antiwetting property in membrane distillation, Desalination 518 (2021) 115268. https://doi.org/https://doi.org/10.1016/j.desal.2021.115268.

# Chapter 7: Conclusion and Future Plan

## 7.1 Conclusion

Membrane separation has gained significant attention in industrial applications because of its energy efficiency, operational simplicity, and environmental friendliness. However, the further development of membrane technologies is severely hindered by inherent material limitations. Polymeric membranes, the most widely adopted membrane materials in industry, face three main challenges: (1) the well-known Robeson trade-off between permeability and selectivity, which constrains overall separation efficiency; (2) susceptibility to fouling, which compromises membrane longevity; and (3) limited stability under high temperatures and harsh operating conditions.

To address these limitations, crystalline frameworks, represented primarily by MOFs and COFs, have emerged as promising alternatives. Synthesized through reticular chemistry, these crystalline frameworks are built from modular units. In MOFs, these units typically consist of metal ions or clusters connected by organic linkers. In COFs, the units are organic molecules connected by strong covalent bonds. They exhibit high porosity with regulated pore sizes and tuneable chemical functionalities. An in-depth understanding of the synthesis mechanisms is crucial to fully exploit their potential in the fabrication of high-performance membranes for various separation applications.

To fully exploit the regulated porous structure and versatile chemistry, we demonstrate a dual-source seeding approach to produce continuous, water-stable MOF-303 membranes on alumina hollow fibres and preferentially tailor crystallographic orientation. By controlling the nucleation site density during secondary growth, MOF-303 membranes with a crystallographic preferred orientation (CPO) on the (011) plane were fabricated. The MOF-303 membrane with CPO on (011) provides straight one-dimensional permeation channels, ensuring high water permeance in nanofiltration and the dehydration of alcohols via pervaporation. The high crystallinity and controlled orientation facilitate a promising water permeance of 15 L $m^{-2}$ $h^{-1}$ $bar^{-1}$ and a high precise molecular weight cut-off (MWCO ≈ 269) for dye nanofiltration. Additionally, the utilization of metal source from the alumina HF results in robust attachment between the substrate and the MOF membrane, leading to high structural integrity over long-term tests. These results provide a concept for developing ultra-permeable MOF membranes with good selectivity and structural integrity for pervaporation and nanofiltration.

Given the persistent challenge of mitigating intrinsic nonselective defects that arise during the synthesis of continuous crystalline framework membranes, we incorporated COF nanosheets as nano-fillers in PES loose nanofiltration membranes by taking advantage of their chemical compatibility with polymers.

A homogeneous casting solution was achieved via in-situ dissolution of PES into a single solution phase-synthesized DABA-TFP colloid. The membrane was fabricated using the recently developed NIPS-CCD method, which combines nonsolvent-induced phase separation (NIPS) with combined crystallization and diffusion (CCD). The anionic DABA-TFP COF not only imparted a negative charge to the membrane but also increased the membrane hydrophilicity. Performance tests involving dye-salt separation revealed a MWCO for dyes of approximately 800-1000 Da while maintaining high salt permeability. Notably, the water permeance of the COF-enhanced PES membranes was 10~100 times greater than that of commercial LNF membranes, with a fouling recovery ratio exceeding 80%. This study offers a promising approach for manufacturing COF-incorporated membranes for loose nanofiltration applications.

The versatile chemistry of crystalline frameworks also enables their integration with other advanced 2D frameworks. We fabricated a MOF@porous graphene oxide (PGO) composite membrane via the confined growth of a water-stable 2D MOF, copper 1,4-benzene dicarboxylate (CuBDC), within the laminar structure of a porous graphene oxide (PGO) membrane. The PGO membranes were formed via vacuum coating using two types of PGO flakes: big-flake PGO (bPGO) and small-flake PGO (sPGO), which were obtained by fragmenting bPGO through a facile tip-sonication process. CuBDC nanosheets were synthesized in-situ via a contra-diffusion method based on vacuum-coated PGO HF membranes, where oxygen-coating groups were provided on the edges or defects of the PGO basal plane. The CuBDC loading was significantly increased in the sPGO-based composite membrane because of the increased density of reactive sites. This targeted coordination of reactive sites with CuBDC significantly enhanced the structural robustness of the composite membrane, ensuring the stabilization of the PGO membrane during desalination tests conducted via reverse osmosis (RO), pervaporation and water carrier pervaporation (analogous to energy-saving direct contact membrane distillation, i.e., DCMD). High water fluxes of 124 kg $m^{-2}$ $h^{-1}$ and 89 kg $m^{-2}$ $h^{-1}$ were achieved in conventional pervaporation mode and in the water carrier pervaporation mode, respectively, both while maintaining a NaCl rejection rate above 99.9%.

## 7.2 Future Plan

Building on the foundations established in this thesis, several potential directions can be pursued in future research.

A versatile technique for controlling CPO should be explored. The DS strategy reported in this thesis successfully regulates the preferred MOF orientation by adjusting the crystal growth stages without relying on external confinement or an inducer. However, the versatility of this method for other crystalline frameworks should be further validated. Moreover, finer regulation aimed at further reducing

the lateral growth stage is essential to shorten mass transport channels, especially for anisotropic crystals possessing one-dimensional channels.

The well-regulated stacking of 2D MOF/COF nanosheets should be pursued. Imperfect stacking in 2D membranes remains a persistent challenge in 2D framework membranes, causing a reduction in or blockage of mass transport channels, thus compromising permeance [1]. Addressing this problem is crucial for fabricating highly permeable membranes with precise molecular sieving capacities. Three strategies can be considered to overcome this challenge: 1) fabricating ultrathin 2D membranes, especially monolayer COFs/MOFs membranes, 2) introducing an additional correction step following synthesis, and 3) modifying the building units to facilitate precise, controlled layer-by-layer stacking.

The fabrication of smart membranes is also a worthwhile research direction. The research presented in this thesis has demonstrated enhanced separation performance by manipulating the fundamental properties of MOF/COF membranes. Further exploration of their chemical versatility and functional adaptability could open pathways toward smart membrane fabrication. One potential approach is the incorporation of photoactive linkers or nanoparticles into MOF/COF membranes to create photothermally responsive membranes for solar-driven desalination. Likewise, thermos-responsive COFs or MOFs that can change surface hydrophilicity/hydrophobicity with temperature are also promising for the fabrication of adaptive desalination membranes.

Expending the application scope of framework membranes represents another research direction. To date, most reported framework-based membranes have been evaluated for salt rejection, remediation of traditional organic pollutants and heavy ions removal. However, their relatively high fabrication cost necessitates high-value applications or separations unattainable with conventional membranes. Potential applications include: 1) the removal of advanced emerging organic containments, such as per- and polyfluoroalkyl substances, 2) chiral separation relevant to pharmaceuticals and fine chemicals; and 3) challenging crude oil separation.

Finally, the machine learning-guided deign could warrant a thorough investigation of the framework membrane. Given the vast combinations of metal nodes/linkers (MOFs) or organic building blocks (COFs), traditional trial-and-error synthesis and testing methods are time-consuming and resource-intensive. The power of artificial intelligence (AI)-human collaboration has been proven in the prediction and synthesis of crystalline frameworks [2]. Extending machine learning to membrane research should be considered for its potential to 1) predict key properties in membrane separation (e.g., pore size, surface porosity, diffusion coefficient, selectivity and mechanical stability), 2) optimize MOF/COF membranes for targeted separations, and 3) design synthetic routes for novel MOF/COFs-based membrane.

## References

[1] D.W. Burke, Z. Jiang, A.G. Livingston, W.R. Dichtel, 2D Covalent Organic Framework Membranes for Liquid-Phase Molecular Separations: State of the Field, Common Pitfalls, and Future Opportunities, Advanced Materials 36(1) (2024) 2300525. https://doi.org/https://doi.org/10.1002/adma.202300525.
[2] Z. Zheng, N. Rampal, T.J. Inizan, C. Borgs, J.T. Chayes, O.M. Yaghi, Large language models for reticular chemistry, Nature Reviews Materials (2025). https://doi.org/10.1038/s41578-025-00772-8.

# List of Publication

## Journal Publications

**M. J. Zhai**, F. Moghadam, T. Gosiamemang, J. Y.Y. Heng and K. Li* Facile orientation control of MOF-303 hollow fibre membranes by a dual-source seeding method. *Nature Communication*. (Published) PageLink: https://doi.org/10.1038/s41467-024-54730-z

**M. J. Zhai,** H. Peng, K. Li*, High-performance loose nanofiltration membranes with excellent antifouling properties for dye/salt separation. *Journal of Membrane Science.* (Published) PageLink: https://doi.org/10.1016/j.memsci.2024.123028

**M. J. Zhai,** F. Moghadam, G. R. Wang, K. Li * Confined growth of 2D MOF nanosheets within porous graphene oxide membranes for long-term stable desalination. *(To be submitted to Nature Communication)*

F. Moghadam, **M. J. Zhai,** T. Zouaoui, K. Li*, Hybrid graphene oxide membranes with regulated water and ion permeation channels via functional materials. Current Opinion in Chemical Engineering. (Published) PageLink: https://doi.org/10.1016/j.coche.2023.100907.

F. Moghadam, C. Zhang, Z. Li, J. Li, **M. Zhai,** K. Li, Structurally Stable Hollow-Fiber-Based Porous Graphene Oxide Membranes with Improved Rejection Performance by Selective Patching of Framework Defects with Metal–Organic Framework Crystals, ACS Applied Materials & Interfaces 17(1) (2025) 1803-1812. https://doi.org/10.1021/acsami.4c13400.

## Conference Presentation

Oral Presentation:

(1) **Mengjiao Zhai**; Controllable fabrication of stable CuBDC@GO hollow fiber membrane for membrane distillation, Euromembrane 2024, Prague, Czech, 2024.09.08-2024.09.12. (Session Chair)

(2) **Mengjiao Zhai**; Ultra-permeable MOF-303 hollow fiber membranes with controlled crystals orientation,13th International Congress on Membranes and Membrane Process, Tokyo, Japan, 2023.07.09-2023.07.14.

(3) **Mengjiao Zhai**; Ultra-permeable MOF-303 hollow fiber membranes fabricated by a novel two-step in-situ growth technique, Euromembrane 2022, Naples, Italy, 2022.11.20-2022.11.24.

# Permissions for the Reproduction of Copyright Materials

Table Summary of the copyright permissions

| Caption | Source of work | Copyright information | Permission request date |
|---|---|---|---|
| Figure 2.3b | S. Yuan, L. Huang, Z. Huang, D. Sun, J.-S. Qin, L. Feng, J. Li, X. Zou, T. Cagin, H.-C. Zhou, Continuous Variation of Lattice Dimensions and Pore Sizes in Metal–Organic Frameworks, *Journal of the American Chemical Society* 142(10) (2020) 4732-4738. https://doi.org/10.1021/jacs.9b13072. | Copyright © 2020, American Chemical Society | 23/03/2025 |
| Figure 2.6 b | H. Yoo, N. Shin, Fabrication of well-intergrown ZIF-8 films via sequential ZnO seed layer overlaying, *Applied Surface Science* 625 (2023) 157211. https://doi.org/https://doi.org/10.1016/j.apsusc.2023.157211. | Copyright © 2023 Elsevier B.V. | 23/03/2025 |
| Figure 2.8a | H. Lu, S. Zhu, Interfacial Synthesis of Free-Standing Metal–Organic Framework Membranes, *European Journal of Inorganic Chemistry* 2013(8) (2013) 1294-1300. | Copyright © 2013 WILEY - VCH Verlag GmbH & Co. KGaA, Weinheim | 23/03/2025 |
| Figure 2.8b | K. Huang, Q. Li, G. Liu, J. Shen, K. Guan, W. Jin, A ZIF-71 Hollow Fiber Membrane Fabricated by Contra-Diffusion, ACS Applied Materials & Interfaces 7(30) (2015) 16157-16160. https://doi.org/10.1021/acsami.5b04991. | Copyright © 2015, American Chemical Society | 23/03/2025 |
| Figure 2.10a | Y. Liu, H. Chen, T. Li, Y. Ren, H. Wang, Z. Song, J. Li, Q. Zhao, J. Li, L. Li, Balancing the Crystallinity and Film Formation of Metal–Organic Framework Membranes through In Situ Modulation for Efficient Gas Separation, Angewandte Chemie International Edition 62(37) (2023) e202309095. https://doi.org/https://doi.org/10.1002/anie.202309095. | Copyright © 2023 Wiley - VCH GmbH | 23/03/2025 |
| Figure 2.11a | Y. Sun, D. Yan, Y. Wu, F.-Y. Shih, C. Zhang, H. Luo, S.-H. Lin, Y. Liu, Fabrication of Twin-Free Ultrathin NH2-MIL-125(Ti) Membrane with c-Preferred Orientation Using Transition-Metal Trichalcogenides as Titanium Source, ACS Materials Letters | Copyright © 2022, American Chemical Society | 23/03/2025 |

| | | | |
|---|---|---|---|
| | 4(1) (2022) 55-60. https://doi.org/10.1021/acsmaterialslett.1c00452. | | |
| Figure 2.11b | C. Zhang, J. Yan, T. Ji, D. Du, Y. Sun, L. Liu, X. Zhang, Y. Liu, Fabrication of highly (110)-Oriented ZIF-8 membrane at low temperature using nanosheet seed layer, Journal of Membrane Science 641 (2022) 119915. https://doi.org/https://doi.org/10.1016/j.memsci.2021.119915. | Copyright © 2021 Elsevier B.V. All rights reserved. | 23/03/2025 |
| Figure 2.12a | G. Li, K. Zhang, T. Tsuru, Two-Dimensional Covalent Organic Framework (COF) Membranes Fabricated via the Assembly of Exfoliated COF Nanosheets, ACS Applied Materials & Interfaces 9(10) (2017) 8433-8436. https://doi.org/10.1021/acsami.6b15752. | Copyright © 2017, American Chemical Society | 23/03/2025 |
| Figure 2.12b | G. Zhang, J. Li, N. Wang, H. Fan, R. Zhang, G. Zhang, S. Ji, Enhanced flux of polydimethylsiloxane membrane for ethanol permselective pervaporation via incorporation of MIL-53 particles, Journal of Membrane Science 492 (2015) 322-330. https://doi.org/https://doi.org/10.1016/j.memsci.2015.05.070 | Copyright © 2015 Elsevier B.V. All rights reserved. | 23/03/2025 |
| Figure 2.12c | H. Fan, Q. Shi, H. Yan, S. Ji, J. Dong, G. Zhang, Simultaneous Spray Self-Assembly of Highly Loaded ZIF-8–PDMS Nanohybrid Membranes Exhibiting Exceptionally High Biobutanol-Permselective Pervaporation, Angewandte Chemie International Edition 53(22) (2014) 5578-5582. https://doi.org/https://doi.org/10.1002/anie.201309534. | Copyright © 2014 WILEY - VCH Verlag GmbH & Co. KGaA, Weinheim | 23/03/2025 |
| Figure 2.12d | D. Cheng, L. Zhao, N. Li, S.J.D. Smith, D. Wu, J. Zhang, D. Ng, C. Wu, M.R. Martinez, M.P. Batten, Z. Xie, Aluminum fumarate MOF/PVDF hollow fiber membrane for enhancement of water flux and thermal efficiency in direct contact membrane distillation, Journal of Membrane Science 588 (2019) 117204. https://doi.org/https://doi.org/10.1016/j.memsci.2019.117204. | Copyright © 2019 Elsevier B.V. All rights reserved. | 23/03/2025 |